# Modélisation multi-échelle des milieux poreux réactifs à haute température appliquée aux protections thermique spatiale et à la pyrolyse de la biomasse.

Hermes Scandelli

HESAM UNIVERSITÉ

Arts et Métiers Sciences et Technologies

**ÉCOLE DOCTORALE SCIENCES ET MÉTIERS DE L'INGÉNIEUR**
**Laboratoire I2M - Campus de Bordeaux**

# THÈSE

*présentée par* : **Hermes SCANDELLI**
*soutenue le* : **14 Octobre 2022**

*pour obtenir le grade de* : **Docteur d'HESAM Université**

*préparée à* : **École Nationale Supérieure d'Arts et Métiers**
*Spécialité* : **Mécanique et Matériaux**

# Multiscale modeling of reactive porous materials interacting with high-temperature flows in support of the biomass, space, and fire communities

**THÈSE dirigée par :**
**Mme Azita AHMADI-SENICHAULT**

**et co-encadrée par :**
**M. Jean LACHAUD**

**Jury**

| | | |
|---|---|---|
| **M. Wahbi JOMAA** | Professeur, Université de Bordeaux | Président |
| **M. Thierry MAGIN** | Professeur, The von Karman Institute for Fluid Dynamics | Rapporteur |
| **M. Frédéric MARIAS** | Professeur, Université de Pau et des Pays de l'Adour | Rapporteur |
| **M. Gillian LEPLAT** | Ingénieur de recherche, ONERA - The French Aerospace Lab | Examinateur |
| **M. Stéphane GALERA** | Ingénieur de recherche, CNES | Examinateur |
| **M. Franck RICHARD** | Maître de conférences, Université de Poitiers | Examinateur |
| **Mme Azita AHMADI** | Professeur, Arts et Métiers ParisTech | Directrice de thèse |
| **M. Jean LACHAUD** | Maître de conférences, Université de Bordeaux | Co-encadrant de thèse |
| **M. Gregory PINAUD** | Ingénieur de recherche, ArianeGroup | Invité |
| **M. Heiko RITTER** | Ingénieur de recherche, ESA | Invité |

THÈSE

*Considerate la vostra semenza*
*fatti non foste a viver come bruti*
*ma per seguir virtute e canoscenza*
(D. Alighieri)

# Table des matières

# Liste des tableaux

# Table des figures

# Chapitre 1

# Synthèse de la Thèse

## Nomenclature

*Latin Letters*

| | |
|---|---|
| $\mathcal{A}$ | facteur pré-exponentiel de la loi d'Arrhenius $[s^{-1}]$ |
| $A$ | élément/espèce générique |
| $\mathcal{C}$ | tenseur de rigidité du quatrième ordre $[kg\ m^{-1}\ s^{-2}]$ |
| $c_p$ | chaleur spécifique à pression constante $[J\ kg^{-1}\ K^{-1}]$ |
| $\boldsymbol{D}$ | champ de déplacement $[m]$ |
| $\mathcal{E}$ | énergie d'activation de la loi d'Arrhenius $[J\ mol^{-1}]$ |
| $e$ | énergie interne spécifique $[J\ kg^{-1}]$ |
| $E_{sm}$ | module de Young $[kg\ m^{-1}\ s^{-2}]$ |
| $\boldsymbol{\mathcal{F}}$ | flux de diffusion effectif $[kg\ m^{-2}\ s^{-1}]$ |
| $\boldsymbol{f}$ | force volumique générique $[m\ s^{-2}]$ |
| $g$ | énergie libre de Gibbs spécifique $[J\ kg^{-1}]$ |
| $h$ | enthalpie absolue spécifique $[J\ kg^{-1}]$ |
| $\underline{\underline{h}}v$ | tenseur de transfert de chaleur volumétrique $[W\ m^{-3}\ K^{-1}]$ |
| $h_v$ | coefficient de transfert de chaleur volumétrique $[W\ m^{-3}\ K^{-1}]$ |
| $\underline{\underline{I}}$ | tenseur d'identité |
| $\underline{\underline{K}}$ | tenseur de perméabilité $[m^2]$ |
| $\underline{\underline{k}}$ | tenseur de la conductivité thermique $[W\ m^{-1}\ K^{-1}]$ |
| $k$ | coefficient de la conductivité thermique $[W\ m^{-1}\ K^{-1}]$ |
| $k_{eq}, k_{fw}, k_{bw}$ | constantes de vitesse chimique à l'équilibre, en avant, et en arrière |
| $l, L$ | longueur caractéristique à l'échelle microscopique et macroscopique $[m]$ |
| $\mathcal{M}$ | masse molaire $[kg\ mol^{-1}]$ |
| $m, n$ | paramètres de la loi d'Arrhenius |
| $n$ | nombre de moles |
| $N_g$ | nombre d'espèces gazeuses |

## Nomenclature

| | |
|---|---|
| $N_{p,i}$ | nombre de sous-phases dans la phase solide i |
| $N_s$ | nombre de phases solides |
| $N_t$ | nombre de réactifs et de produits dans une réaction chimique |
| $\mathcal{P}_i, \mathcal{P}_{i,j}$ | phase solide $i$ et sous-phase $j$ de la phase solide $i$. |
| $p$ | pression $[Pa]$ |
| $\boldsymbol{\mathcal{Q}}$ | flux de chaleur de diffusion effectif $[J\ m^{-2}\ s^{-1}]$ |
| $\mathcal{R}$ | constante universelle des gaz parfaits $[J\ kg^{-1}\ K^{-1}]$ |
| $r$ | rayon générique d'une sphère $[m]$ |
| $R$ | constante spécifique des gaz parfaits $[J\ mol^{-1}\ K^{-1}]$ |
| $\mathcal{S}$ | surface spécifique $[m^2\ m^{-3}]$ |
| $s$ | entropie spécifique $[J\ kg^{-1}\ K^{-1}]$ |
| $t$ | temps $[s]$ |
| $T$ | température $[K]$ |
| $\boldsymbol{v}$ | vitesse de convection $[m\ s^{-1}]$ |
| $v$ | volume spécifique $[m^3\ kg^{-1}]$ |
| $V$ | volume de prise des moyennes $[m^3]$ |
| $V_i$ | volume de la phase i $[m^3]$ |
| $\boldsymbol{x}$ | coordonnées microscopiques $[m]$ |
| $\boldsymbol{X}$ | coordonnées macroscopiques $[m]$ |
| $X$ | fraction molaire |
| $y$ | fractions massiques des espèces |
| $z$ | fractions massiques des éléments |

*Greek Letters*

| | |
|---|---|
| $\underline{\underline{\alpha}}$ | tenseur de l'expansion thermique $[K^{-1}]$ |
| $\alpha$ | coefficient d'expansion thermique $[K^{-1}]$ |
| $\underline{\underline{\beta}}$ | tenseur de correction du glissement $[Pa]$ |
| $\gamma$ | indicateur de phase |
| $\underline{\underline{\epsilon}}$ | tenseur de déformation |
| $\epsilon$ | fraction de volume |
| $\theta$ | angle d'orientation de la vitesse |
| $\Theta$ | densité du site actif $[mol\ m^{-3}]$ |
| $\lambda$ | libre parcours moyen $[m]$ |
| $\mu$ | coefficient de viscosité volumique $[Pa\ s]$ |
| $\mu_{sm}, \lambda_{sm}$ | constantes de Lame $[kg\ m^{-1}\ s^{-2}]$ |
| $\nu$ | coefficient stoechiométrique |
| $\nu_{sm}$ | coefficient de Poisson |
| $\underline{\underline{\xi}}$ | tenseur de contribution de la pyrolyse |
| $\xi$ | coefficient de contribution de la pyrolyse |
| $\pi_k$ | taux de production de l'espèce/élément $k$ par pyrolyse $[kg\ m^{-3}\ s^{-1}]$ |

## Nomenclature

| | |
|---|---|
| $\Pi$ | taux global de production de gaz de pyrolys $[kg\ m^{-3}\ s^{-1}]$ |
| $\rho$ | densité $[kg\ m^{-3}]$ |
| $\underline{\underline{\sigma}}$ | tenseur des contraintes $[kg\ m^{-1}\ s^{-2}]$ |
| $\underline{\underline{\tau}}$ | tenseur des contraintes visqueuses $[N\ m^{-2}]$ |
| $\tau$ | avancement total des réactions de pyrolyse |
| $\chi_{i,j}$ | avancement de la réaction de pyrolyse de la sous-phase $j$ dans la phase $i$. |
| $\boldsymbol{\omega}$ | vorticité $[s^{-1}]$ |
| $\omega_i$ | taux de production des espèces $i$ $[mol\ m^{-3}\ s^{-1}]$ |
| $\omega_i^h$ | réactions hétérogènes taux de production de masse des espèces $i$ $[kg\ m^{-3}\ s^{-1}]$ |
| $\Omega_h$ | taux global de production de masse des réactions hétérogènes $[kg\ m^{-3}\ s^{-1}]$ |

*Subscripts and Superscripts*

| | |
|---|---|
| 0 | temps initial |
| bw | arrière |
| cl | cluster |
| eff | effective |
| eq | équilibre |
| f | fluide |
| fw | avant |
| g | gasz |
| $i$, $j$, $k$ | indices utilisés dans les opérateurs somme/produit |
| s | solide |
| sm | matériau solide |

*Formalism*

| | |
|---|---|
| $\underline{\underline{A}}$ | tenseur du second ordre A |
| $\boldsymbol{A}$ | vecteur A |
| $A$ | scalaire A |
| $\langle\ \rangle$ | moyenne intrinsèque |
| $\partial_t$ | dérivée partielle à t |
| $\partial_{\boldsymbol{x}}$ | opérateur gradient |
| $\partial_{\boldsymbol{x}}\cdot$ | opérateur divergence |
| $tr()$ | opérateur trace |
| $\sum_{j=1}^{N_t}$ | opérateur de somme dont l'indice j varie de $j=1$ à $j=N_t$ |
| $\prod_{j=1}^{N_t}$ | opérateur produit dont l'indice j varie de $j=1$ à $j=N_t$ |
| $*$ | variable non dimensionnelle |

*Adimensional Groups*

| | |
|---|---|
| Kn | nombre de Knudsen |

## Nomenclature

| | |
|---|---|
| Pe | nombre de Peclet |
| Re | nombre de Reynolds |

*Acronims*

| | |
|---|---|
| CMT | Computed Micro-Tomography |
| LTE | Local Thermal Equilibrium |
| LTNE | Local Thermal Non-Equilibrium |
| MSL | Mars Science Laboratory |
| PATO | Porous material Analysis Toolbox based on OpenFoam |
| TACOT | Theoretical Ablative Composite for Open Testing |
| TPS | Thermal Protection System |

## 1.1 Les Matériaux Poreux

Un **milieu poreux** est constitué d'une structure solide, la **matrice**, et d'espaces vides, les **pores**. Ces derniers sont généralement remplis par un fluide, comme l'air, l'eau, l'huile ou un mélange de différents fluides. Les matériaux poreux se rencontrent presque partout dans la vie quotidienne, qu'ils soient d'origine géologique (par exemple, les roches, le sol), biologique (par exemple, les os, le bois, le liège) ou artificielle (par exemple, les ciments, les céramiques, les polymères). Leur principale caractéristique est qu'ils peuvent être décrits de différentes manières selon l'échelle à laquelle on les observe, comme illustré dans la Fig. 1.1. Les structures du bois, de l'os, de la céramique et du feutre en fibre de carbone sont représentées de deux façons différentes: dans la partie supérieure de la figure, ils sont représentés à l'échelle à laquelle nous avons l'habitude de les voir, i.e. l'échelle macroscopique, ou **échelle du continuum**; tandis que dans la partie inférieure, ils sont zoomés à l'échelle microscopique, ou **échelle des pores**, où leur structure poreuse est révélée. L'interaction entre un milieu poreux perméable et un fluide pénétrant à travers ses pores peut être décrite aux deux échelles en utilisant des simulations numériques. Au niveau microscopique, la description est basée sur la mécanique classiques des fluides et des solides, ce qui peut entraîner certaines difficultés lorsqu'il s'agit de géométries complexes, mais elles s'avèrent essentielles pour visualiser et comprendre la physique de l'interaction. Différemment, à l'échelle macroscopique, le solide et le fluide sont homogénéisés dans un **matériau continu poreux équivalent** et où les phénomènes de transfert sont décrits par des **équations directrices moyennes**. Les deux échelles sont reliées entre elles par des **processus de mise à l'échelle**. Les plus populaires dans le domaine des milieux poreux sont: la théorie de l'homogénéisation [14],la technique de prise de moyenne volumique [15], et les méthodes stochastiques [16]. Différentes approches conduisent à la formulation de modèles de continuum équivalents, à condition de considérer le même niveau d'approximations mathématiques et les mêmes hypothèses physiques [17], notamment les hypothèses de

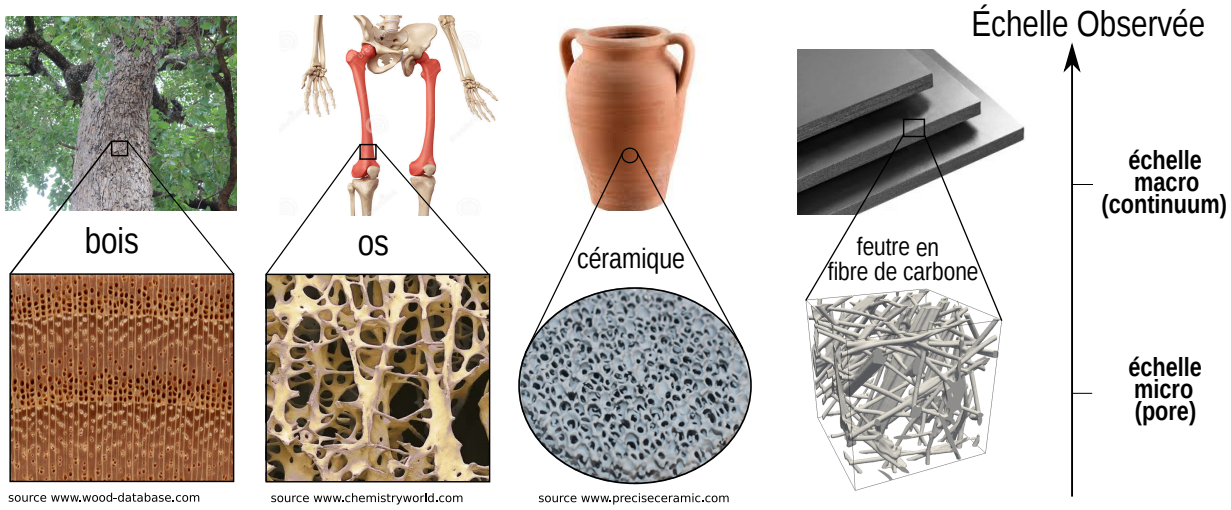


FIGURE 1.1 – Représentations à l'échelle micro (pores) et macro (continuum) de quatre matériaux poreux: bois, os, céramique et feutre en fibre de carbone.

**séparation d'échelle** et l'existence d'un **volume élémentaire représentatif** (REV) [1] où les variations à petite échelle sont atténuées. Cette situation est illustré dans la Fig. 1.2. À l'échelle du continuum, les détails de la structure microscopique des pores et de leur interaction avec l'écoulement soient perdus. Toutefois, les informations moyennes sont contenues dans les **propriétés effectives**. Des exemples de ces dernières sont le tenseur de perméabilité, le coefficient de transfert thermique, la conductivité thermique effective et le tenseur des contraintes. Compte tenu de leur importance physique, leur estimation correcte est essentielle pour la précision du modèle. Selon les besoins et les conditions, différentes méthodes de détermination peuvent être suivies. Les expérimentations sont largement utilisées dans la littérature [18–25], cependant, bien que le domaine de la microfluidique progresse très rapidement, l'influence de la structure microscopique sur le comportement de l'interaction fluide-matériau poreux ne peut pas encore être directement observée pour les matériaux complexes. À cette fin, des simulations numériques sont nécessaires. La géométrie d'un milieu poreux peut être obtenue soit par une représentation mathématique idéalisée [21, 26–30] ou à partir d'une image numérique reconstruite [31–38]. Dans le premier cas, la structure des pores doit être décrite d'un point de vue statistique [39] et la géométrie reconstruite par de petits objets primitifs dans un domaine fini [30]. Autrement, si une image numérique est disponible, des simulations sont effectuées sur la géométrie exacte. Cela permet de visualiser directement le comportement des quantités de transport et des gradients dans tout le domaine au niveau des pores et d'observer clairement comment ces derniers sont affectés par les caractéristiques microscopiques du matériau. Les simulations numériques nécessitent un ensemble approprié de conditions aux limites, bien que cela ne soit pas toujours simple, surtout lorsqu'il s'agit de domaines numériques qui ne sont pas assez grands pour être considérés comme REV [40, 41]. Enfin, la troisième façon de déterminer les propriétés effectives est d'utiliser les corrélations. Elles sont obtenues par une compréhension globale de la physique, dérivée de l'analyse expérimentale ou théorique du pro-

1. En référence à la technique de prise de moyenne volumique.

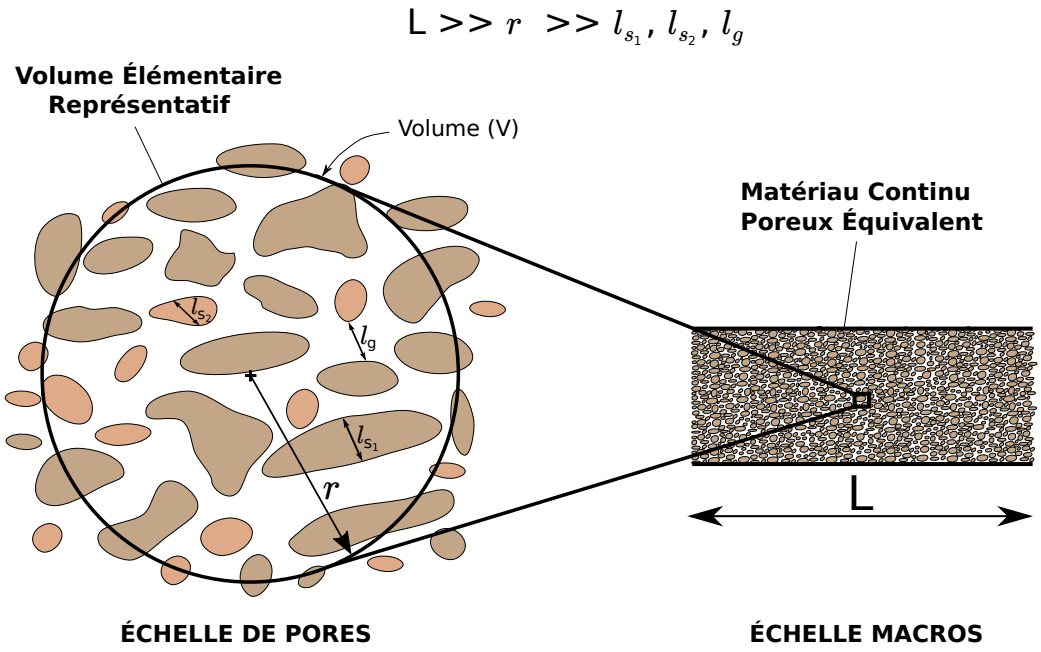


FIGURE 1.2 – Concept générique du processus de mise à l'échelle. Le processus repose sur les hypothèses de séparation d'échelle ($L >> r >> l_{s1}, l_{s2}, l_g$) et sur l'existence d'un REV où les variations à petite échelle sont atténuées.

blème [28, 34, 38, 42–44]. Leur applicabilité est généralement limitée à des géométries connues et dans des intervalles de conditions spécifiques (tels que des intervalles de Reynolds ou de Peclet spécifiques).

## 1.2 Matériaux Poreux Réactifs dans des Écoulements à Haute Température

Diverses technologies et applications techniques sont basées sur les matériaux poreux. Les convertisseurs catalytiques pour le traitement des eaux [45], les dispositifs de filtrage [46], les capteurs microfluidiques [47], la récupération améliorée du pétrole [48], pour ne citer que quelques exemples. Dans ce travail, l'attention est orientée vers le sous-ensemble des matériaux poreux réactifs interagissant avec des écoulements à haute température, un thème avec un large champ d'applications allant de la conception d'un bouclier thermique poreux d'un véhicule spatial entrant dans une atmosphère, à la simulation de la combustion d'une allumette. Malgré la nette différence en termes de conditions externes, ces applications sont décrites par les mêmes phénomènes physiques d'un point de vue matériel, comme schématisé dans la Fig. 1.3. Comme les matériaux et les conditions externes sont différents, les gammes de température et les mécanismes chimiques ne sont pas les mêmes dans les deux cas. Quelques exemples de ces différences sont montrés en bleu pour la combustion de l'allumette et en rouge pour le matériau ablatif poreux en carbone/phénolique. Cependant, la même phénoménologie générique s'applique aux deux cas. Les lois de conservation au sein des matériaux sont les mêmes et le même modèle mathématique peut être utilisé pour décrire leurs comportements. Le sujet des

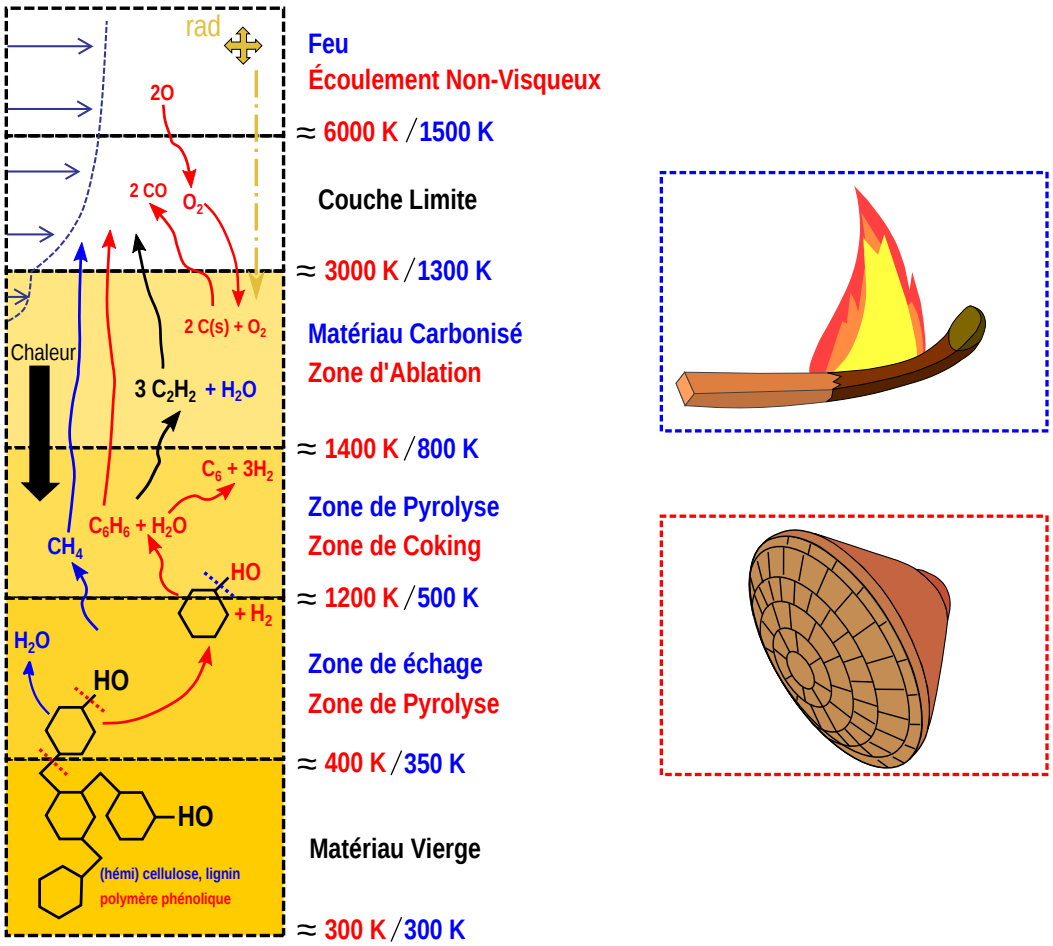


FIGURE 1.3 – Illustration simplifiée des phénomènes physiques d'un point de vue matériel d'une allumette qui brûle (bleu) et d'un matériau poreux en carbone/phénolique qui s'ablate (rouge). Le texte en jaune et noir s'applique aux deux.

matériaux poreux réactifs interagissant avec des écoulements à haute température est d'une grande importance, notamment pour les communautés de la biomasse, de l'espace et de la sécurité incendie. Au cours des dernières décennies, ces communautés scientifiques ont abordé le sujet en se focalisant sur plusieurs aspects fondamentaux. Une brève introduction aux trois communautés et un examen de leurs principaux points forts sont maintenant présentés.

1. La **communauté de la biomasse**. Actuellement, les effets du changement climatique sont tout à fait évidents (*effet de serre*, *réchauffement global*, *Earth overshoot day*[2]) et adopter de solutions vertes devient de plus en plus importante. La Fig.1.4 montre la consommation annuelle mondiale d'énergie par source. Les données datent de 2016, mais des tendances similaires se

2. Date de l'année où la demande de l'humanité en ressources et services écologiques dépasse ce que la Terre peut régénérer au cours de l'année.

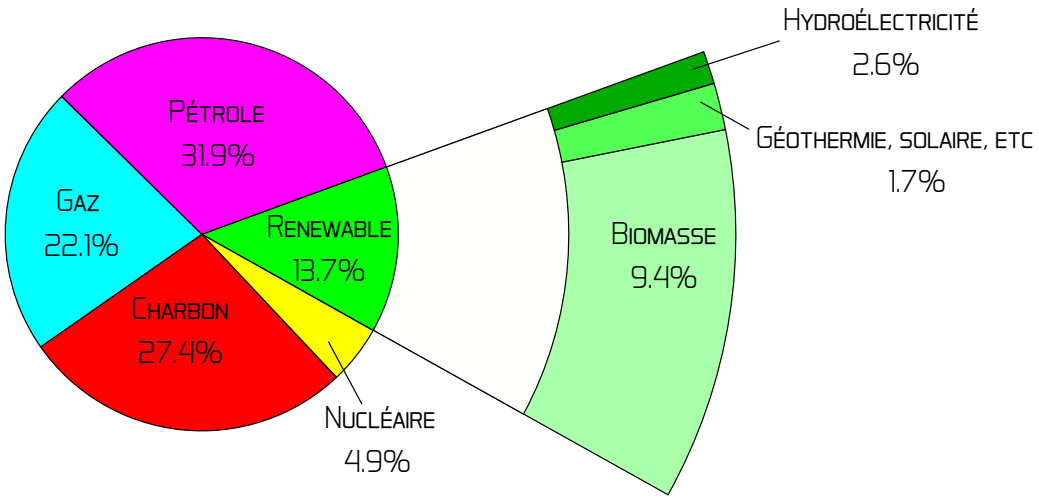


FIGURE 1.4 – Consommation mondiale d'énergie par source en 2016. *Source https://www.iea.org/*. La biomasse, avec 9.4% de la consommation totale d'énergie, est la source d'énergie renouvelable la plus utilisée.

dégagent aujourd'hui. On peut observer que la biomasse est la source d'énergie renouvelable la plus utilisée. Le terme *biomasse* désigne généralement une matière d'origine végétale qui peut être convertie thermiquement en molécules de bio-hydrocarbures de grande valeur [49, 50]. Le phénomène thermochimique à l'origine de ce processus est **pyrolyse**, qui transforme les espèces chimiques sous l'effet de la chaleur et produit des rendements différents selon les conditions imposées [51,52]. L'objectif principal de la communauté de la biomasse est de développer des modèles qui peuvent être utilisés pour améliorer les techniques (température, taux de chauffage, temps, etc.) pour transformer la biomasse lignocellulosique en molécules de bio-hydrocarbures à haute valeur ajoutée. Le premier modèle de pyrolyse est attribué à Bamford, Crank et Malan [53]. Selon ce modèle, la pyrolyse est modélisée comme une réaction de premier ordre suivant une loi d'Arrhenius, et une équation différentielle ordinaire est résolue pour estimer la perte de masse en fonction du temps. Cela permet de capturer la perte de masse de la pyrolyse à un coût de calcul réduit. Suite à ces travaux, plusieurs modèles ont été développés au fil des années, chacun caractérisé par un niveau de précision différent dans la description des réactions chimiques. Le niveau le plus simple correspond au *mécanismes de réaction unique* [54], dans lequel une seule réaction de décomposition est considérée. Une plus grande précision est fournie par les *modèles de réaction unique à composants multiples* [55], où la description tient compte de la matière première. Plus complexes sont les *modèles compétitifs* [56] qui introduisent des réactions compétitives pour prédire différentes distributions de produits en fonction des conditions de conversion. Enfin, les modèles les plus précis sont les *modèles compétitifs multi-composants* [57,58], qui tiennent compte efficacement de la dépendance à la charge et de l'effet de la température sur les rendements;

2. La **communauté de sécurité incendie**. La sécurité incendie est l'ensemble des pratiques visant à réduire les destructions causées par le feu. Elle comprend les mesures destinées à prévenir et à détecter un incendie non contrôlé, celles utilisées pour contenir et éteindre le développement

et les effets d'un incendie après qu'il se soit déclaré, et celles destinées à évaluer la libération d'espèces chimiques suffocantes. Un accent particulier a été mis sur les milieux poreux, en raison de leur utilisation fréquente dans de nombreux projets civils et aéronautiques: le bois utilisé pour la construction de maisons, de ponts et de bâtiments génériques [59]; les matériaux composites utilisés comme pièces structurelles dans les systèmes aéronautiques et spatiaux [60]. En raison de la nature inflammable de ces matériaux, il est important de pouvoir prédire leur potentiel à augmenter le risque d'incendie avec la perte conséquente de rigidité, de force et de résistance de la structure [61,62]. Pour cette raison, plusieurs études ont tenté de définir leurs caractéristiques de performance pendant la combustion, telles que leur retardement du feu [63], leurs propriétés d'inflammabilité [64], et leurs émissions gazeuses [65]. Ainsi, la force de la communauté de la sécurité incendie réside dans la capacité à coupler le matériau avec l'environnement et à décrire le comportement du feu pour un matériau donné, y compris les processus d'allumage, de croissance du feu, de propagation et d'extinction [66].

3. La **communauté spatiale**. Les missions extra-orbitales impliquent souvent l'analyse du processus d'entrée dans les atmosphères planétaires à des vitesses hypersoniques [67]. Dans ces conditions, un choc à haute enthalpie se forme devant le véhicule spatial et l'énergie cinétique est progressivement dissipée en chaleur, qui atteignent la surface par diffusion, convection et rayonnement. La température à la surface du matériau peut atteindre 4000 $K$ pour des conditions d'entrée sévères. Pour garantir l'intégrité de la structure, un **système de protection thermique** (TPS) est désigné pour absorber et dissiper la chaleur par des changements de phase, des réactions chimiques et l'enlèvement de matériaux. Les matériaux ablatifs carbonisés représentent une approche traditionnelle de la protection thermique [68,69]. Un exemple célèbre est la nouvelle classe d'ablateurs imprégnés de phénolique (PICA [70], PICA-X, ASTERM [71]) qui consiste en une préforme en fibre de carbone partiellement imprégnée de résine phénolique, résultant en un poids très léger, de bons isolants et une résistance mécanique élevée.
   La modélisation numérique d'un TPS doit pouvoir capturer la dégradation de la matière et la dissipation de chaleur au sein du matériau. Dans le cas contraire, la modélisation peut conduire à des inexactitudes dans l'estimation de l'efficacité de l'ablateur, et donc à une plus grande marge de sécurité dans le processus de conception. Pour cette raison, la communauté spatiale s'est principalement orientée vers la modélisation de la chimie hétérogène et des phénomènes de transport, comme en témoigne la grande quantité de logiciels développés au fil des ans. Dans le cadre d'une comparaison de codes effectuée dans la communauté aérospatiale [72], les modèles mis en œuvre dans vingt-cinq codes de conception et de recherche TPS ont été examinés, comparés et classés en trois catégories différentes: *modèles de type 1*, qui sont mis en œuvre dans tous les codes de conception et décrivent les phénomènes essentiels du problème de pyrolyse-ablation. Ils sont bien adaptés aux conditions 1D, quasi stables et d'équilibre chimique; *type-2*, qui augmentent leur précision en incluant la mise en œuvre de la conservation de la quantité de mouvement pour simuler la direction du flux de pyrolyse pour des mélanges constants d'éléments/espèces; *type-3*, qui complètent la description en incluant les équations de conservation des éléments (ou des espèces) et les modèles d'équilibre chimique (ou à taux fini) associés.

Sur la base de la littérature, un modèle générique a été proposé pour tenter d'englober les exigences

de physique fondamentale des trois applications [73–75]. Ce modèle générique, implémenté dans le **Porous material Analysis Toolbox based in OpenFoam (PATO)** publié en open source, est maintenant utilisé par des équipes universitaires et industrielles des trois communautés. Les capacités de PATO par rapport aux contributions et aux développements des compréhensions de chaque communauté sont présentées dans la Fig. 1.5. Une sélection de quatre codes par communauté est présentée. Le choix s'est porté sur les codes les plus connus, bien que la priorité ait été donnée à quelques implémentations récentes. Le lien entre le tableau et le modèle mathématique peut être fait par la description des termes des différentes équations de conservation (colonne 2) et par les numéros des termes dans la colonne PATO, qui font référence aux numéros des équations et à l'ordre de ces termes dans les équations. Par exemple, dans l'équation de conservation de la masse solide, le terme de pyrolyse est le deuxième terme de l'Eq. (1.25). Chaque code est décrit en termes d'année de publication initiale, de type de méthodes numériques, de dimensions, de disponibilité du code, et en termes de classification du modèle selon les critères introduits par Lachaud et al. 2011 [72]. On peut observer que PATO est le seul code de la communauté TPS à implémenter un modèle de type (3). Différents modèles de type (3) ont été développés par les deux autres communautés. En particulier, ThermaKin [76], Gpyro [77], et MoDeTheC [78] sont trois codes populaires de la communauté du feu, tandis que SPY [52], bioSmoke [79], et les codes développés par Ratte et al, 2009 [80], et Pozzobon et al., 2018 [81], sont les codes de la communauté de la biomasse mettant en œuvre les fonctionnalités les plus avancées à notre connaissance. Dans de nombreux codes, la dynamique de l'eau liquide n'est pas modélisée mais un modèle de vaporisation est implémenté. Le même choix a été fait dans PATO. Cependant, les codes de Ratte et al, 2009 [80], et Pozzobon et al, 2018 [81], implémentent le séchage en utilisant une formulation de Darcy généralisée. Les codes TPS et feu adoptent des modèles intégrés de couche limite réactive comme conditions limites et supposent (à l'exception de PATO) une composition élémentaire constante des gaz de pyrolyse et utilisent l'équilibre chimique, tandis que les modèles de biomasse considèrent la conservation des espèces et la chimie à taux fini. PATO est le seul code qui est directement couplé à des codes d'écoulement externes. Les capacités de mécanique solide ne sont pas prises en compte dans la classification des codes. Cependant, des modèles thermomécaniques sont implémentés dans Amaryllis [82], Char [83] et PATO. En plus, PATO prend en compte le retrait dû à la pyrolyse. SPY et bioSmoke ont inclus des modèles de rétrécissement permettant de comprimer linéairement le maillage au cours de la pyrolyse.

## 1.3 Objectifs de la Thèse

Deux objectifs définissent cette thèse. Le premier est de contribuer à la modélisation du comportement des matériaux poreux réactifs dans les écoulements à haute température, car les modèles actuels de l'état de l'art sont encore limités dans la prédiction de toute la physique cachée derrière l'application. À cette fin, la conservation de la quantité de mouvement, la déformation du solide et la conservation de l'énergie sont étudiées. Ces trois aspects sont principalement renforcés par l'introduction d'effets de régime de glissement, par la prise en compte de la déformation pyromécanique, et en permettant aux phases solides et d'écoulement d'être en non-équilibre thermique local entre elles. Deux applications multi-physiques différentes sont considérées et analysées afin de vérifier l'impact de

| | | | Original | TPS | | | | Feu | | | | Biomasse | | | |
|---|---|---|---|---|---|---|---|---|---|---|---|---|---|---|---|
| | | | [BAM1946] | CMA/FIAT | AMARYLLIS | CHAR | PATO | [HEN85] | ThermaKin | Gpyro | MoDeTheC | [RAT09] | SPY | [POZ2018] | bioSMOKE |
| Aperçu | | | | | | | | | | | | | | | |
| Mise en libre service | | | | x | | | x | | | x | | | | | |
| Open source | | | | x | | | x | | | x | | | | | |
| Année de la première publication | | | 1946 | 1968 | 2009 | 2011 | 2014 | 1985 | 2008 | 2009 | 2014 | 2009 | 2012 | 2014 | 2017 |
| Méthode numérique | | | FD | FD | FE | FE | FV | FD | FE | FV | FV | FD | FD | FV | FV |
| Dimensions | | | 1D | 1D | 3D | 3D | 3D | 1D | 2D | 3D | 3D | 1D | 2D | 3D | 3D |
| Type de modèle (selon la classif cation TPS de 2011) | | 1, 2, or 3 | | 1 | 2 | 2 | 3 | 1 | 3 | 3 | 3 | 3 | 3 | 3 | 3 |
| Conservation de la masse | | | | | | | | | | | | | | | |
| Solide | stockage | 1 | | x | x | x | 1.25:1 | x | x | x | x | x | x | x | x |
| | pyolyse | 1 | x | x | x | x | 1.25:2 | x | x | x | x | x | x | x | x |
| | réact. hét. | 3 | | | | | 1.25:3 | | x | x | | | | | |
| Gaz | stockage | 2 | | | x | x | 1.14:1 | | x | x | x | x | x | x | x |
| | convection | 1 | | x | x | x | 1.14:2 | x | x | x | x | x | x | x | x |
| | - pyolysis | 1 | | x | x | x | 1.14:3 | x | x | x | x | x | x | x | x |
| | - réact. hét. | 1 | | | | | 1.14:3 | | x | x | | | | | |
| Éléments | stockage | 3 | | | | | 1.18:1 | | | | | | | | |
| | convection | 3 | | | | | 1.18:2 | | | | | | | | |
| | dif usion | 3 | | | | | 1.18:3 | | | | | | | | |
| | pyolyse | 3 | | x | x | x | 1.18:4 | | | | | | | | |
| Espèce | stockage | 3 | | | | | 1.21:1 | | x | x | x | x | x | x | x |
| | convection | 3 | | | | | 1.21:2 | | x | x | x | x | x | x | x |
| | dif usion | 3 | | | | | 1.21:3 | | x | x | x | x | x | x | x |
| | pyolyse | 3 | | | | | 1.21:4 | | x | x | x | x | x | x | x |
| | réact. Hét. | 3 | | | | | 1.21:5 | | x | x | x | x | x | x | x |
| Liquide | no motion | n/a | | | | | In 1.25 | | | | | | x | | x |
| | avec motion | n/a | | | | | | | | | | x | | x | |
| Conservation du momentum | | | | | | | | | | | | | | | |
| Solide | déplacement. | n/a | | | x | x | 1.27:1 | | | | | | x | | x |
| | div. stress | n/a | | | x | x | 1.27:2 | | | | | | | | |
| | forces de volume | n/a | | | x | x | 1.27:3 | | | | | | | | |
| | élast. Lin. | n/a | | | x | x | 1.29:1 | | | | | | | | |
| | expans. th. | n/a | | | x | x | 1.29:2 | | | | | | | | |
| | rétr. par pyr. | n/a | | | | | 1.29:3 | | | | | | | | |
| | viscoélastique | n/a | | | | | | | | | | | | | |
| Gaz | vitesse | 2 | | | x | x | 1.15:1 | | x | | x | x | x | x | x |
| | Darcy | 2 | | | x | x | 1.15:2 | | x | | x | x | x | x | x |
| | Klinkenberg | 3 | | | | x | 1.15:3 | | | | | | | | |
| Liquide | Darcy gen. | n/a | | | | | | | | | | x | | x | |
| Conservation de l'énergie | | | | | | | | | | | | | | | |
| Solide | stock. sens. | 1 | x | x | x | x | 1.26:1 | x | x | x | x | x | x | x | x |
| | form. de l'enth. | 1 | x | x | x | x | 1.26:2 | x | x | x | x | x | x | x | x |
| | conduction | 1 | x | x | x | x | 1.26:3 | x | x | x | x | x | x | x | x |
| | trans. de chaleur | n/a | | | | | 1.26:4 | | | | | | | | |
| Gaz | stock. Sens. | 2 | | | x | x | 1.17:1 | | x | x | x | x | x | x | x |
| | form. enth. | 3 | | x | x | x | 1.17:2 | x | x | x | x | x | x | x | x |
| | trav. de pression | 3 | | | x | x | 1.17:3 | | x | x | x | x | x | x | x |
| | convection | 1 | | x | x | x | 1.17:4 | x | x | x | x | x | x | x | x |
| | conduction | n/a | | | | | 1.17:5 | | x | x | x | x | x | x | x |
| | dif usion | 3 | | | | | 1.17:6 | | x | x | x | x | | x | x |
| | trans. de chaleur | n/a | | | | | 1.17:7 | | | | | | | | |
| Liquide | no motion | | | | | | In 1.26 | | | | | | x | | x |
| | avec motion | n/a | | | | | | | | | | x | | x | |
| Caractéristiques supplémentaires | | | | | | | | | | | | | | | |
| Solveur de chimie à taux f nis | | 3 | | | | | x | | | | | x | x | x | x |
| Solveur de chimie d'équilibre | | 3 | | | | | x | | | | | | | | |
| Modèle de couche limite réactive | | 1 | | x | x | x | x | | x | x | x | | | | |
| Solveur(s) d'écoulement intégré(s) | | n/a | | | | | x | | | | | | | | |

FIGURE 1.5 – Comparaison des modèles mathématiques implémentés dans les logiciels de simulation des trois communautés. Crédit J. Lachaud.

ces aspects physiques sur le modèle.
Quel que soit le modèle employé à l'échelle macroscopique pour décrire l'interaction entre un matériau poreux réactif et un écoulement à haute température, l'exactitude de la description dépend de la précision avec laquelle les propriétés effectives sont estimées sur la base de la structure et des propriétés à micro-échelle. Leur dérivation s'avère être une tâche complexe et la littérature ne fournit pas une méthodologie numérique complète à cet effet. Le second objectif de cette thèse est donc d'établir et de valider des stratégies numériques pour estimer les propriétés effectives des milieux poreux anisotropes dans le cas générique d'un volume microscopique non périodique disponible par microtomographie.

## 1.4 Structure de la Thèse

La mémoire est présentée sous la forme d'une compilation d'articles. Le chapitre d'introduction est rédigé en français (Chapitre 1) et en anglais (Chapitre 2). Dans le chapitre d'introduction, la thèse est décrite en exposant le contexte, l'état de l'art, les objectifs, les applications d'intérêt, les modèles physiques, les principaux résultats obtenus, et la conclusion. Les articles sont placés dans six chapitres indépendants:

1. Two-Temperature ablative material response model with application to Stardust and MSL atmospheric entries;
2. Simulation of wood combustion in PATO using a detailed pyrolysis model coupled to fireFoam;
3. Computation of the permeability tensor of non-periodic anisotropic porous media from 3D images;
4. Multiscale modeling of flow in porous thermal protection systems from the continuum to the slip regime;
5. Volumetric heat transfer coefficient: numerical evaluation and introductory analysis to anisotropic effects;
6. Multi-Scale modeling of wood shrinkage during pyrolysis.

Deux parties principales sont définies en fonction de l'objectif fixé. La première partie comprend les articles 1 et 2, tandis que les autres articles sont incorporés dans la seconde partie. Le manuscrit comprend une annexe présentant une dérivation des équations macroscopiques pour le transfert de masse, de quantité de mouvement et d'énergie dans les milieux poreux avec la technique de la moyenne volumique.

Une nomenclature est donnée au début de chaque chapitre. Une bibliographie complète est présentée à la fin du manuscrit, rassemblant les citations de tous les articles.

## 1.5 Modèle Physique

La description numérique d'un matériau poreux interagissant avec un écoulement générique dépend de l'échelle d'intérêt. À l'échelle du continuum, des équations moyennées sont adoptées, tandis qu'à

l'échelle du pore, la conservation de la masse, de la quantité de mouvement et de l'énergie est résolue par les équations de Navier-Stokes.

### 1.5.1 Macro-Échelle

#### 1.5.1.1 Hypothèses et Notations

Le modèle numérique utilisé dans ce travail est basé sur le modèle générique d'équilibre thermique local précédemment implémenté dans PATO [75]. Il suppose l'interaction entre un mélange de gaz réactif multi-espèces ($N_g$ espèces gazeuses) avec un matériau réactif multi-phases ($N_s$ phases solides). Les espèces gazeuses sont supposées être en équilibre thermique local entre elles, ainsi que les phases solides. Cependant, le matériau et le mélange de gaz ne sont plus supposés être en équilibre thermique local dans le travail actuel. Aucune phase liquide n'a été modélisée. Un liquide, s'il est présent (par exemple l'eau), est modélisé comme une phase solide. Les équations du continuum sont obtenues soit par des techniques de mise à l'échelle [3] soit définies de manière heuristique. En référence à la technique de prise de moyenne volumique, les hypothèses fondamentales sont l'existence d'un REV (Fig. 1.2) dans lequel les propriétés peuvent être moyennées par phase et la satisfaction de la séparation d'échelle. La fraction volumique $\epsilon$ d'une phase donnée $i$ est définie comme suit

$$\langle \gamma_i \rangle = \epsilon_i(\boldsymbol{X}, t) = \frac{1}{V} \int_{V_i} \gamma_i(\boldsymbol{X} + \boldsymbol{x}, t) d\boldsymbol{x} \tag{1.1}$$

où la moyenne utilisée est appelée *moyenne intrinsèque*, $V$ est le volume de prise des moyennes, $V_i$ est le volume de la phase $i$, $\gamma_i$ est l'indicateur de phase, avec $\gamma_i = 1$ dans la phase $i$ et $\gamma_i = 0$ en dehors de la phase $i$, $\boldsymbol{X}$ et $\boldsymbol{x}$ désignent respectivement la coordonnée macroscopique et la coordonnée locale dans le volume de prise des moyennes, et $t$ est le temps. La notation $\langle\ \rangle$ désigne la moyenne intrinsèque. Cette dernière s'applique à toutes les variables de phase. Comme toute la section ne concerne que l'échelle du continuum, des notations non marquées sont employées pour simplifier la lecture des équations. Les valeurs moyennes des variables extensives (volume, masse, énergie) dans le domaine sont obtenues à partir de la somme pondérée des valeurs des phases superficielles. Par exemple, la densité totale $\rho$ est donnée par

$$\rho = \epsilon_g \rho_g + \sum_{i=1}^{N_s} \epsilon_i \rho_i \tag{1.2}$$

où l'indice $g$ identifie le mélange de gaz. Les variables intensives (pression, vitesse, température) sont résolues par les équations moyennées et les propriétés effectives (tortuosité, perméabilité, conductivité) doivent être déterminées par des expériences, des simulations numériques ou des corrélations.

**Pour une meilleure clarté, dans tout le manuscrit, la phase solide est indiquée par l'indice $s$; le mélange de gaz à l'intérieur du matériau poreux est indiqué par l'indice $g$; l'écoulement externe, à l'extérieur du matériau, est indiqué par l'indice $f$.**

3. La dérivation des équations directrices pour les matériaux non réactifs et écoulement incompressible est présentée dans l'Annexe.

#### 1.5.1.2 Mélange de Gaz: Propriétés Thermodynamiques

Le gaz est supposé être un mélange de gaz thermiquement parfaits (gaz parfaits dont les chaleurs spécifiques sont fonction de la température uniquement). La pression totale du mélange de gaz, $p_g$, est donnée par la loi de Dalton

$$p_g = \sum_{i=1}^{N_g} p_i \tag{1.3}$$

Un seul gaz obéit à la loi des gaz parfaits

$$p_i v_i = n_i \mathcal{R} T_i \tag{1.4}$$

où $v_i$, $n_i$ et $T_i$ désignent respectivement le volume, le nombre de moles et la température du gaz $i$, et $\mathcal{R}$ est la constante universelle des gaz. Le mélange et les différents gaz partagent la même valeur du volume spécifique, $v_i = v_g$. De plus, les gaz sont supposés être en équilibre thermique local entre eux, $T_i = T_g$. Le mélange de gaz obéit à la loi des gaz parfaits

$$p_g v_g = n_g \mathcal{R} T_g \tag{1.5}$$

Les propriétés thermodynamiques sont dérivées des règles de mélange: les propriétés du mélange sont obtenues comme la somme des propriétés des espèces pondérées par la composition du mélange. La composition du mélange peut être décrite par la fraction molaire ou la fraction massique. La fraction molaire d'une espèce, $X_i$, est définie comme le rapport du nombre de moles de l'espèce $n_i$, divisé par le nombre de moles du mélange $n_g$.

$$X_i = \frac{n_i}{n_g} = \frac{p_i}{p_g} \tag{1.6}$$

La fraction massique d'une espèce, $y_i$, est définie comme le rapport de la masse de l'espèce divisée par la masse totale du mélange. La définition peut également être écrite en termes de rapport de densités

$$y_i = \frac{\rho_i}{\rho_g} \tag{1.7}$$

Une fois que $X_i$ ou $y_i$ sont connus, les règles de mélange peuvent être appliquées. Pour ne donner que quelques exemples, la constante des gaz de mélange $R_g$, la masse molaire $\mathcal{M}_g$, l'enthalpie absolue spécifique $h_g$, l'entropie spécifique $s_g$ et l'énergie interne spécifique $e_g$ sont données par

$$R_g = \sum_{i=1}^{N_g} y_i R_i \tag{1.8}$$

$$\mathcal{M}_g = \sum_{i=1}^{N_g} \frac{\mathcal{M}_i}{y_i} \tag{1.9}$$

$$\rho_g h_g = \sum_{i=1}^{N_g} \rho_i h_i \tag{1.10}$$

$$\rho_g s_g = \sum_{i=1}^{N_g} \rho_i (s_i - R_i ln X_i) \tag{1.11}$$

$$\rho_g e_g = \sum_{i=1}^{N_g} \rho_i h_i - \sum_{i=1}^{N_g} p_i \tag{1.12}$$

La chaleur spécifique du mélange à pression constante $c_{p,g}$ est estimée directement à partir de sa définition

$$c_{p,g} = \Big(\frac{\partial h_g}{\partial T_g}\Big)_p \tag{1.13}$$

La connaissance de la composition du gaz et des propriétés thermodynamiques des espèces est essentielle pour retrouver les propriétés du mélange. Les propriétés thermodynamiques d'une seule espèce peuvent être évaluées (1) par des fonctions issues d'un ensemble donné de polynômes (NASA7 et NASA9 par exemple) ou (2) par des fonctions de partition. Le cas (1) permet une évaluation directe des propriétés. Le cas (2) nécessite l'introduction de concepts de thermodynamique statistique et cela dépasse le cadre de ce travail. Des détails supplémentaires sont donnés dans l'étude de Scoggins et Magin, 2014 [84]. L'évaluation de la composition du gaz suit une procédure différente selon la supposition de l'équilibre ou du non-équilibre chimique. Ceci est détaillé dans la section 1.5.1.4 et dans la section 1.5.1.5.

#### 1.5.1.3 Mélange de Gaz: Équations Directrices

L'équation globale de conservation de la masse, qui est déterminée par la somme des équations de conservation des espèces, est la suivante

$$\partial_t(\epsilon_g \rho_g) + \partial_{\boldsymbol{X}} \cdot (\epsilon_g \rho_g \boldsymbol{v}_g) = -\sum_{i=1}^{N_s} \partial_t(\epsilon_i \rho_i) = \Pi + \Omega_h \tag{1.14}$$

où $\boldsymbol{v}_g$ est la vitesse convective du gaz, et les termes du droit rendent compte des échanges avec les phases solides: pyrolyse $\Pi$ et réactions hétérogènes $\Omega_h$ (décrites dans la section 1.5.1.9). Les équations de conservation des éléments ou des espèces sont nécessaires dans le cas d'équilibre ou de non-équilibre chimique. Ces équations sont abordées dans les sections respectives.
La vitesse moyenne du gaz est obtenue en résolvant l'équation de conservation de la quantité de mouvement. Dans les milieux poreux, la conservation de la quantité de mouvement moyenne est la suivante

$$\boldsymbol{v}_g = -\frac{1}{\epsilon_g}\Big[\frac{1}{\mu_g}\underline{\underline{K}}\Big(1 + \frac{1}{p_g}\underline{\underline{\beta}}\Big)\Big] \cdot \partial_{\boldsymbol{X}} p_g \tag{1.15}$$

où $\mu_g$ est la viscosité dynamique du gaz, $\underline{\underline{K}}$ est le tenseur de perméabilité, et $\underline{\underline{\beta}}$ la correction de glissement pour prendre en compte les effets de glissement. La vitesse moyenne du gaz peut être introduite dans la conservation de la masse du gaz. En utilisant la loi des gaz parfaits, la forme finale de la conservation de la quantité de mouvement est la suivante

$$\partial_t\Big(\frac{\epsilon_g \mathcal{M}_g}{RT_g} p_g\Big) - \partial_{\boldsymbol{X}} \cdot \Big[\frac{p_g \mathcal{M}_g}{RT_g}\frac{1}{\mu_g}\underline{\underline{K}}\Big(1 + \frac{1}{p_g}\underline{\underline{\beta}}\Big) \cdot \partial_{\boldsymbol{X}} p_g\Big] = \Pi + \Omega_h \tag{1.16}$$

Un modèle de non-équilibre thermique local est considéré pour la description énergétique du système. Cela signifie que deux équations sont nécessaires pour décrire le mélange de gaz et les phases solides d'un point de vue énergétique. Pour le mélange, l'équation directrice de l'énergie s'écrit

$$\epsilon_g \rho_g c_{p,g} \partial_t T_g + \sum_{i=1}^{N_g} h_i \partial_t (\epsilon_g \rho_g y_i) - \partial_t (\epsilon_g p_g) = -\partial_{\boldsymbol{X}} \cdot \Big( \epsilon_g \rho_g \boldsymbol{v}_g h_g \Big) + \partial_{\boldsymbol{X}} \cdot \Big( \underline{\underline{k}}_{\text{eff},g} \cdot \partial_{\boldsymbol{X}} T_g \Big) + \\ + \partial_{\boldsymbol{X}} \cdot \sum_{k=1}^{N_g} \boldsymbol{\mathcal{Q}}_k + h_v \Big( T_s - T_g \Big) \tag{1.17}$$

où $\underline{\underline{k}}_{\text{eff}}$ identifie le tenseur de conductivité thermique effective, $\boldsymbol{\mathcal{Q}}_k$ modélise le transport de chaleur par diffusion effective de l'espèce [75], et $h_v$ est le coefficient de transfert de chaleur volumétrique.

#### 1.5.1.4 Mélange de Gaz: Chimie à l'Équilibre

Dans le cas de l'équilibre, les équations de conservation des espèces ne sont pas nécessaires, mais des réactions chimiques peuvent se produire dans la phase gazeuse. Lorsque celles-ci se produisent, les masses des molécules participantes ne sont pas conservées, alors que les masses des nucléi des éléments chimiques constituant ces mêmes molécules sont conservées. Ainsi, les équations de conservation des éléments pour chaque élément du mélange doivent être prises en compte

$$\partial_t (\epsilon_g \rho_g z_k) + \partial_{\boldsymbol{X}} \cdot (\epsilon_g \rho_g z_k \boldsymbol{v}_g) + \partial_{\boldsymbol{X}} \cdot \boldsymbol{\mathcal{F}}_k = \pi_k \tag{1.18}$$

où $z_k$ identifie la fraction massique de l'élément $k$, $\boldsymbol{\mathcal{F}}_k$ modélise le flux de diffusion effectif [75] de l'élément $k$, et le terme de droite, $\pi_k$, représente le taux de production de pyrolyse de l'élément $k$.

La composition du mélange est explicitement définie par la minimisation de l'énergie libre de Gibbs spécifique, $g$, du mélange. Cette dernière, pour une espèce $i$ est définie comme suit [84]

$$g_i = h_i - s_i T_g \tag{1.19}$$

Pour un mélange à l'équilibre, l'énergie de Gibbs est uniquement fonction de la pression et de la température locales. A partir de la définition de l'énergie libre de Gibbs, Eq. (1.19), la forme suivante de la *loi d'action de masse* peut être dérivée [85] et appliquée à une réaction chimique générique

$$\prod_{j=1}^{N_t} p_j^{\nu_j} = k_{eq} \tag{1.20}$$

où $k_{eq}$ est le taux constant d'équilibre pour la réaction chimique donnée et est fonction de la température uniquement, $\prod_{j=1}^{N_t}$ désigne la notation du produit pour tous les termes $N_t$ réactifs et produits, $j$, dans la réaction chimique; $\nu_j$ représente le coefficient stéchiométrique du terme $j$. En combinant la loi d'action de masse pour chaque réaction dans le mélange, la loi de Dalton (Eq. (1.3)), et les équations de conservation des éléments (Eq. (1.18)), on peut obtenir la pression partielle de chaque

espèce. La connaissance de la pression partielle est suffisante pour retrouver la composition du mélange (Eq. (1.6)), donc les propriétés thermodynamiques de la phase gazeuse. Il faut remarquer qu'à l'équilibre, la composition chimique du mélange réactif est fonction de la pression et de la température locales.

#### 1.5.1.5 Mélange de Gaz: Chimie Hors Équilibre

En cas de chimie hors-équilibre, les équations de continuité des espèces doivent être résolues

$$\partial_t(\epsilon_g \rho_g y_i) + \partial_{\boldsymbol{X}} \cdot (\epsilon_g \rho_g y_i \boldsymbol{v}_g) + \partial_{\boldsymbol{X}} \cdot \boldsymbol{\mathcal{F}}_i = \pi_i + \epsilon_g \omega_i \mathcal{M}_i \tag{1.21}$$

où les termes sources de l'équation sont le taux de production massique de l'espèce $i$ dû à la pyrolyse, $\pi_i$, et le taux de production des réactions chimiques de l'espèce $i$, $\omega_i$.

Les taux de production des espèces dues aux réactions chimiques dans le mélange doivent être estimés afin de calculer la composition du mélange. Une réaction élémentaire générique $j$ caractérisée par $N_t$ réactifs et produits, peut être écrite comme suit

$$\sum_{i=1}^{N_t} \nu'_{ij} A_i \rightleftharpoons \sum_{i=1}^{N_t} \nu''_{ij} A_i \tag{1.22}$$

où $A_i$ représente le nom de l'espèce $i$, et $\nu'_{ij}$ et $\nu''_{ij}$ sont les coefficients stœchiométriques des réactifs et des produits respectivement. Tout type de réaction élémentaire peut être exprimé sous cette forme. Le taux de production d'espèces de cette $j$-ième réaction élémentaire s'écrit

$$\omega_{i,j} = (\nu''_{ij} - \nu'_{ij}) \Big[ k_{fw,j} \prod_{i=1}^{N_t} [A_i]^{\nu'_{ij}} - k_{bw,j} \prod_{i=1}^{N_t} [A_i]^{\nu''_{ij}} \Big] \tag{1.23}$$

où $k_{fw,j}$ et $k_{bw,j}$ sont les constantes de vitesse chimique en avant et en arrière. Ces deux coefficients sont reliés par la constante de vitesse d'équilibre $k_{eq,j}$ comme suit

$$k_{bw,j} = \frac{k_{fw,j}}{k_{eq,j}} \tag{1.24}$$

La constante de vitesse à l'équilibre peut parfois être obtenue par l'expérience et peut toujours être calculée à partir de la thermodynamique statistique [85]. Une loi de vitesse d'Arrhenius est généralement utilisée pour spécifier le coefficient de vitesse de réaction directe [84]. La composition du mélange est obtenue en résolvant l'Eq. (1.23) pour toutes les réactions chimiques.

#### 1.5.1.6 Mélange de Gaz: Coefficients de Transport

La dérivation de la viscosité dynamique, de la conductivité thermique du mélange et des coefficients de diffusion dépasse le cadre de cette thèse. Une librairie nommée *Mutation++* est utilisée pour leur calcul. Plus de détails à ce sujet sont disponibles dans l'étude de Scoggins and Magin, 2014 [84].

#### 1.5.1.7 Phase Solide: Équations Directrices

L'évolution moyenne de la masse pour chaque phase solide $i$ est la suivante

$$\partial_t(\epsilon_i \rho_i) = -\pi_i - \omega_i^h \tag{1.25}$$

où les changements de densité pour la phase solide $i$ sont donnés par les contributions de la pyrolyse $\pi_i$ et des réactions hétérogènes $\omega_i^h$.
Sous l'hypothèse de non-équilibre thermique local, une équation de conservation de l'énergie est nécessaire pour la phase solide. Cette équation est la suivante

$$\sum_{i=1}^{N_s} \epsilon_i \rho_i c_{p,i} \partial_t T_s + \sum_{i=1}^{N_s} h_i \partial_t(\epsilon_i \rho_i) = \partial_{\boldsymbol{X}} \cdot \Big( \underline{\underline{k}}_{\text{eff},s} \cdot \partial_{\boldsymbol{X}} T_s \Big) + h_v \Big( T_g - T_s \Big) \tag{1.26}$$

Il faut remarquer que en supposant $T_g = T_s = T$ et en additionnant cette équation avec l'équation énergétique respective pour le mélange de gaz (Eq. (1.17)), le modèle d'équilibre thermique local est retrouvé.
La phase solide est libre de se déformer. Les hypothèses de petite déformation et de matériau solide élastique linéarisé sont considérées ici. L'équation directrice est donnée par

$$\partial_t(\rho_s \, \partial_t(\boldsymbol{D})) = \partial_{\boldsymbol{X}} \cdot \underline{\underline{\sigma}} + \rho \boldsymbol{f} \tag{1.27}$$

où les quantités $\boldsymbol{D}$, $\underline{\underline{\sigma}}$, et $\boldsymbol{f}$ désignent respectivement le champ de déplacement, le tenseur des contraintes, et une force volumique générique. Le lien entre les tenseurs de contrainte ($\underline{\underline{\sigma}}$) et de déformation ($\underline{\underline{\epsilon}}$) est donné par la loi constitutive

$$\underline{\underline{\sigma}} = \mathbb{C} : \Big( \underline{\underline{\epsilon}} - \underline{\underline{\alpha}}(T - T_0) - \underline{\underline{\xi}}(\tau - \tau_0) \Big) \tag{1.28}$$

où $\mathbb{C}$ est le tenseur de rigidité du quatrième ordre [86], $\underline{\underline{\alpha}}$ et $\underline{\underline{\xi}}$ sont les tenseurs des coefficients de dilatation thermique ($\alpha$) et des coefficients de retrait de pyrolyse ($\xi$), $\tau$ représente l'avancement total des réactions de pyrolyse, et l'indice 0 désigne le temps initial. En supposant que le solide est isotrope, la loi constitutive (Eq. (1.28)) se simplifie en

$$\underline{\underline{\sigma}} = 2\mu_{sm}\underline{\underline{\epsilon}} + \lambda_{sm} tr(\underline{\underline{\epsilon}})\underline{\underline{I}} - (2\mu_{sm} + 3\lambda_{sm})\, \alpha\, (T - T_0)\underline{\underline{I}} - (2\mu_{sm} + 3\lambda_{sm})\, \xi\, (\tau - \tau_0)\underline{\underline{I}} \tag{1.29}$$

où $tr()$ désigne l'opérateur de trace, $\mu_{sm}$ et $\lambda_{sm}$ sont les paramètres de Lame, et $\underline{\underline{I}}$ désigne le tenseur d'identité. L'indice $sm$ correspond au matériau solide. Les paramètres de Lame sont exprimés en termes de constantes d'ingénierie, notamment le module d'Young $E_{sm}$ et le coefficient de Poisson $\nu_{sm}$, par les expressions suivantes

$$\lambda_{sm} = \frac{E_{sm}\, \nu_{sm}}{(1 + \nu_{sm})(1 - 2\nu_{sm})} \tag{1.30}$$

$$\mu_{sm} = \frac{E_{sm}}{2(1 + \nu_{sm})} \tag{1.31}$$

#### 1.5.1.8 Phase Solide: Pyrolyse

Chaque phase solide $\mathcal{P}_i$ peut se décomposer selon plusieurs cinétiques de pyrolyse. Il est pratique courante de diviser chaque phase $i$ en $N_{p,i}$ sous-phases pour modéliser différents mécanismes de dégradation. La décomposition d'une sous-phase générique $j$ (à partir de la phase solide $i$) conduit à la production de différents éléments/espèces $A_k$ en fonction des coefficients stœchiométriques $\nu_{i,j,k}$, comme suit

$$\mathcal{P}_{i,j} \longrightarrow \sum_{k=1}^{N_g} \nu_{i,j,k}\ A_k \tag{1.32}$$

Les réactions de pyrolyse sont modélisées par des lois d'Arrhenius. Ainsi, l'avancement de la réaction de pyrolyse $\chi_{i,j}$ de la sous-phase $j$ dans la phase $i$ est défini comme suit

$$\partial_t \chi_{i,j} = (1-\chi_{i,j})^{m_{i,j}}\ T_s^{n_{i,j}} \mathcal{A}_{i,j}\ exp\Big(-\frac{\mathcal{E}_{i,j}}{RT_s}\Big) \tag{1.33}$$

où $\mathcal{A}$ et $\mathcal{E}$ sont le facteur pré-exponentiel et l'énergie d'activation de la loi d'Arrhenius, et $m_{i,j}$ et $n_{i,j}$ sont les paramètres de la loi d'Arrhenius. L'avancement total du processus de pyrolyse, $\tau$, est évalué comme suit

$$\tau = \sum_{i=1}^{N_s}\sum_{j=1}^{N_{p,i}} \frac{\epsilon_{i,0}\rho_{i,0}y_{i,j}}{\sum_{i=1}^{N_s}\sum_{j=1}^{N_{p,i}} \epsilon_{i,0}\rho_{i,0}y_{i,j}}\ (1-\chi_{i,j}) \tag{1.34}$$

où $y_{i,j}$ est la fraction massique de la sous-phase $j$ dans la phase $i$. Le taux de production total de l'espèce/élément $k$ par décomposition du solide est donné par

$$\pi_k = \sum_{i=1}^{N_s}\sum_{j=1}^{N_{p,i}} \nu_{i,j,k}\ \epsilon_{i,0}\ \rho_{i,0}\ y_{i,j}\ \partial_t \chi_{i,j} \tag{1.35}$$

Le taux global de production de gaz de pyrolyse est obtenu en additionnant $\pi$ sur toutes les espèces gazeuses

$$\Pi = \sum_{k=1}^{N_g} \pi_k \tag{1.36}$$

#### 1.5.1.9 Phase Solide: Réactions Hétérogènes

Pour les réactions élémentaires, les taux de production des espèces sont donnés par l'Eq. (1.23). Les réactions non élémentaires peuvent être modélisées à l'aide d'exposants de densité molaire qui ne sont pas égaux à la molécularité, ou des termes supplémentaires peuvent être ajoutés, par exemple pour tenir compte des réactions du troisième corps ou de la chute de pression.
Les réactions hétérogènes traitent des réactions chimiques élémentaires entre des phases solides réactives et des espèces gazeuses. Une approche unifiée a été proposée pour traiter les espèces solides et gazeuses [75]. La densité molaire effective d'une phase solide réactive $i$ peut être modélisée de manière pratique comme suit

$$X_i = \frac{\mathcal{S}_i \Theta_i}{\epsilon_g} \tag{1.37}$$

où $\mathcal{S}_i$ et $\Theta_i$ sont la surface spécifique et la densité du site actif de la phase solide réactive $i$. Cela permet d'introduire des phases solides dans le mécanisme chimique homogène, de résoudre la chimie homogène et hétérogène à taux finis de manière couplée, et de calculer les taux de réaction effectifs avec une plus grande précision et stabilité numérique. Le taux de changement de masse total est donc la somme de tous les taux de réaction effectifs.

$$\Omega_h = \sum_{i=1}^{N_s} \omega_i^h \tag{1.38}$$

### 1.5.2 Micro-Échelle

Pour atteindre le second objectif, à savoir la dérivation des propriétés effectives, des simulations numériques à l'échelle du pore sont effectuées. Seules les micro-équations pertinentes sont présentées, la chimie, la pyrolyse et le transport de masse n'étant pas pris en compte. Les propriétés matérielles intrinsèques sont utilisées à l'échelle du pore.

#### 1.5.2.1 Écoulement Compressible

Aucune discontinuité (aucune onde de choc, aucune surface de contact, aucune ligne de glissement) et aucune force volumique ne sont considérées dans le domaine. Les équations de conservation de la masse, de la quantité de mouvement et de l'énergie sont les suivantes

$$\begin{cases} \partial_t \rho + \partial_{\boldsymbol{x}} \cdot (\rho \boldsymbol{v}) = 0 \\ \partial_t (\rho \boldsymbol{v}) + \partial_{\boldsymbol{x}} \cdot \Big(\rho \boldsymbol{v} \otimes \boldsymbol{v} + p \underline{\underline{I}}\Big) = \partial_{\boldsymbol{x}} \cdot \underline{\underline{\tau}} \\ \partial_t (\rho e) + \partial_{\boldsymbol{x}} \cdot (\rho \boldsymbol{v} e) = -p \partial_{\boldsymbol{x}} \cdot \boldsymbol{v} + (\underline{\underline{\tau}} \partial_{\boldsymbol{x}}) \cdot \boldsymbol{v} + \partial_{\boldsymbol{x}} \cdot \Big(k \partial_{\boldsymbol{x}} T\Big) \end{cases} \tag{1.39}$$

où la densité du flux thermique local est modélisée par la loi de Fourier et $k$ représente le coefficient de conductivité thermique. La conservation de l'énergie est exprimée en termes d'énergie interne spécifique $e$, et $\underline{\underline{\tau}}$ est le tenseur des contraintes visqueuses. Dans l'hypothèse d'un fluide Newtonian et de l'hypothèse de Stokes, ce tenseur est exprimé comme suit

$$\underline{\underline{\tau}} = \mu \Big[\partial_{\boldsymbol{x}} \otimes \boldsymbol{v} + (\partial_{\boldsymbol{x}} \otimes \boldsymbol{v})^T\Big] - \frac{2}{3} \mu (\partial_{\boldsymbol{x}} \cdot \boldsymbol{v}) \tag{1.40}$$

#### 1.5.2.2 Écoulement Incompressible

L'hypothèse d'un écoulement incompressible est adoptée dans certains chapitres du manuscrit. Dans ce cas, le système d'Eqs. (1.39) se réduit à

$$\begin{cases} \partial_{\boldsymbol{x}} \cdot \boldsymbol{v} = 0 \\ \rho \partial_t \boldsymbol{v} + \rho \boldsymbol{v} \cdot \partial_{\boldsymbol{x}} \boldsymbol{v} - \mu_g \partial_{\boldsymbol{x}}^2 \boldsymbol{v} = -\partial_{\boldsymbol{x}} p_g \\ \rho\, c_p \partial_t T + \rho\, c_p \boldsymbol{v} \cdot \partial_{\boldsymbol{x}} T = \partial_{\boldsymbol{x}} \cdot \Big(k \partial_{\boldsymbol{x}} T\Big) \end{cases} \tag{1.41}$$

où la dissipation visqueuse est négligée.

#### 1.5.2.3 Déformation Solide

La phase solide est libre de se déformer. Les mêmes hypothèses et équations gouvernantes présentées dans la Section 1.5.1.7 pour l'échelle macro s'appliquent à l'échelle du pore. Dans l'hypothèse de petites déformations et de matériau solide élastique linéarisé, l'équation directrice est la suivante

$$\partial_t(\rho_s\ \partial_t(\boldsymbol{D})) = \partial_{\boldsymbol{x}} \cdot \underline{\underline{\sigma}} + \rho \boldsymbol{f} \tag{1.42}$$

La loi constitutive relie les tenseurs de contrainte ($\underline{\underline{\sigma}}$) et de déformation ($\underline{\underline{\epsilon}}$). En supposant que le solide est isotrope, la loi constitutive est la suivante

$$\underline{\underline{\sigma}} = 2\mu_{sm}\underline{\underline{\epsilon}} + \lambda_{sm} tr(\underline{\underline{\epsilon}})\underline{\underline{I}} - (2\mu_{sm} + 3\lambda_{sm})\ \alpha\ (T - T_0)\underline{\underline{I}} - (2\mu_{sm} + 3\lambda_{sm})\ \xi\ (\tau - \tau_0)\underline{\underline{I}} \tag{1.43}$$

où les paramètres de Lame sont liés aux constantes d'ingénierie par les expressions suivantes

$$\lambda_{sm} = \frac{E_{sm}\ \nu_{sm}}{(1 + \nu_{sm})(1 - 2\nu_{sm})} \tag{1.44}$$

$$\mu_{sm} = \frac{E_{sm}}{2(1 + \nu_{sm})} \tag{1.45}$$

## 1.6 Principaux Résultats

Les principales contributions de cette thèse à la modélisation de matériaux poreux réactifs sous des écoulements à haute enthalpie sont marquées en rouge dans la Fig. 1.6. Cette section donne un aperçu générique de ces contributions en relation avec les deux objectifs définis dans la section 1.3. Une présentation et une description complètes des résultats sont disponibles dans les chapitres respectifs.

### 1.6.1 Première Partie

La première partie du travail étudie l'importance de deux aspects physiques spécifiques dans la description numérique. Ces deux études sont réalisées dans les Chapitres 3 et 4.
Le Chapitre 3 étudie l'hypothèse d'un équilibre thermique local (ETL) entre les phases solides et les gaz de pyrolyse pour les matériaux ablatifs dans des conditions d'entrée typiques. Cette hypothèse est généralement justifiée par le fait que le nombre de Peclet thermique à l'intérieur des pores est petit. Le nombre de Peclet thermique est un nombre adimensionnel qui quantifie le rapport entre les vitesses des processus d'advection et de diffusion thermique.

$$Pe = \frac{\rho_g\, c_p\, |\langle \boldsymbol{v}_g \rangle| l}{k} \tag{1.46}$$

$Pe \ll 1$ est une condition nécessaire à l'équilibre thermique dans les matériaux non réactifs. Cependant, la validité de cette analyse peut tomber dans certaines circonstances. Le nombre de Peclet thermique

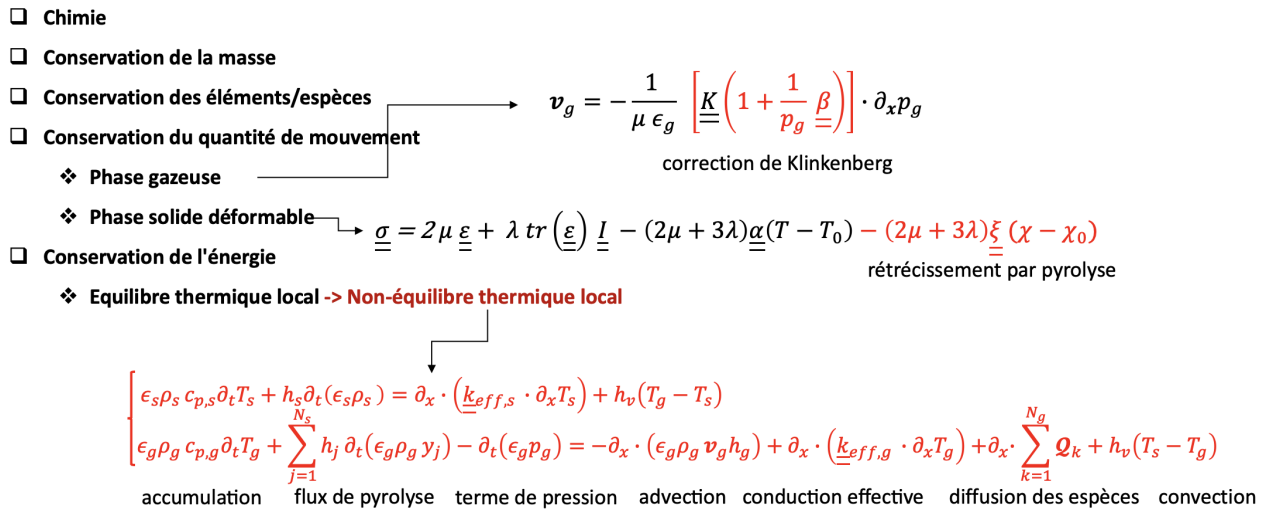


FIGURE 1.6 – Contribution principale de cette thèse (en rouge) à la modélisation des matériaux poreux réactifs sous des écoulements à haute enthalpie.

peut devenir important en raison des vitesses élevées du gaz de pyrolyse, ou des phénomènes physiques supplémentaires non pris en compte dans l'analyse de Peclet peuvent devenir non négligeables, tels que le changement d'enthalpie dû aux réactions chimiques. Un modèle de non-équilibre thermique local (LTNE) est appliqué au Theoretical Ablative Composite for Open Testing (TACOT) dans un large intervalle de conditions afin d'évaluer le véritable domaine de validité de l'hypothèse d'équilibre thermique. Des simulations 1D sont effectuées sur les missions d'entrée dans l'atmosphère Stardust et Mars Science Laboratory. Des modèles d'énergie d'équilibre thermique local et de non-équilibre thermique local sont adoptés. La comparaison entre les deux modèles est effectuée en contrôlant l'évolution de la température au sein du matériau, le taux de soufflage du gaz de pyrolyse, la zone de pyrolyse, le récession de la paroi due à l'ablation, et les concentrations des espèces au sein du matériau. Les mêmes conclusions s'appliquent aux deux cas de mission. Les résultats pour le cas Stardust sont rapportés dans la Fig. 1.7 pour le cas d'équilibre chimique et dans la Fig. 1.8 pour le cas de non-équilibre chimique. Aucune déviation significative des quantités surveillées est observée dans des conditions

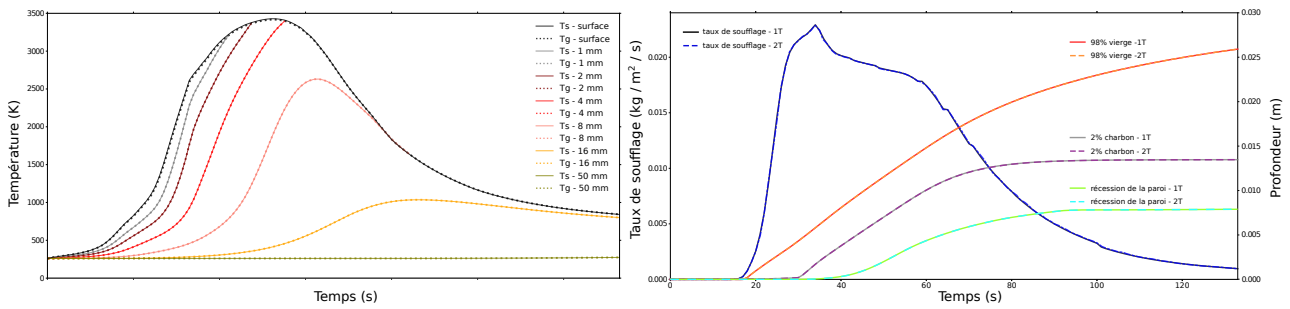


FIGURE 1.7 – Cas Stardust. Données du thermocouple, taux de soufflage, zone de pyrolyse et récession de la paroi dans le temps.

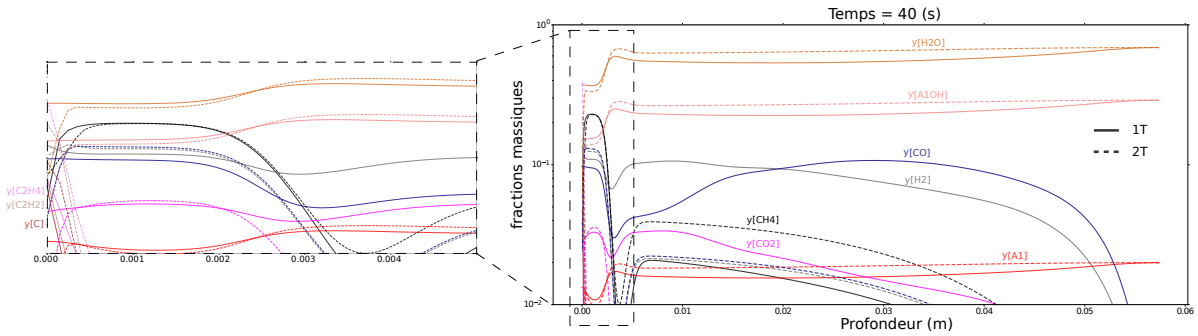


FIGURE 1.8 – Cas Stardust. Distribution des espèces dans le matériau au temps $t = 40\ s$. A gauche: un zoom sur les fractions massiques près de la surface avec l'environnement externe.

d'équilibre chimique. En revanche, dans le cas d'un non-équilibre chimique, une faible différence dans la prédiction de la température entre les deux modèles thermiques suffit à modifier l'évolution des concentrations des espèces au sein du matériau.

La simulation numérique de la propagation du feu nécessite de capturer le couplage entre la pyrolyse du bois, qui conduit à la production de diverses espèces gazeuses, et la combustion de ces espèces dans la flamme, qui produit l'énergie qui entretient le processus de pyrolyse. Comme on peut le voir sur la Fig. 1.5, à l'exception de PATO, aucun code de réponse ne prévoit un couplage direct matériau-écoulement externe. Le Chapitre 4 propose une simulation multi-physique où les matériaux et les écoulements externes sont directement couplés, ce qui permet au code de capturer différents phénomènes physiques. Le cadre numérique couple le modèle de pyrolyse tridimensionnel détaillé de PATO avec fireFoam. La capacité de l'outil de simulation est illustrée sur la combustion d'une bûche de bois. Les résultats, qui sont partiellement rapportés dans la Fig. 1.9, mettent en évidence comment

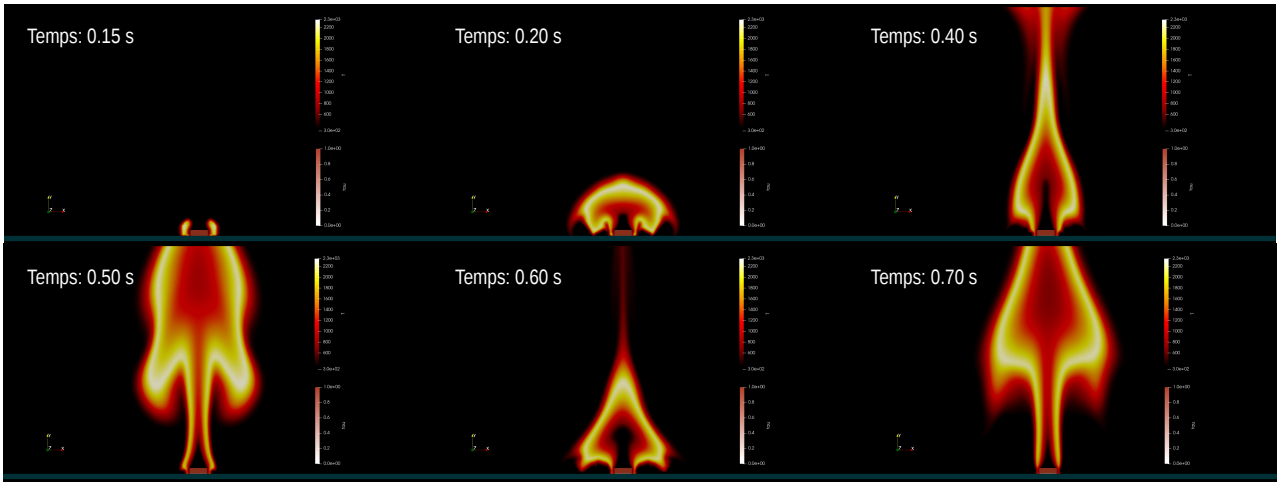


FIGURE 1.9 – Combustion d'une bûche de bois. Six images représentant l'évolution initiale du feu sur la bûche de bois.

l'évolution de la flamme et de sa température pendant la simulation sont affectées par la concentration des espèces gazeuses produites dans le matériau. L'effet de couplage affecte également la bûche de bois: en raison de l'augmentation de la flamme et de la température, le processus de pyrolyse s'accélère et les concentrations des espèces changent en fonction de la vitesse des réactions. La simulation est capable de capturer l'ensemble du processus de pyrolyse, jusqu'à la carbonisation complète du bois et l'extinction de l'incendie qui en résulte. De plus, l'effet de puffing est observé pendant l'évolution de la simulation: le feu présente des fluctuations périodiques qui se succèdent avec une fréquence numérique qui est approximativement la même que celle théorique.

### 1.6.2 Deuxième Partie

Les propriétés macroscopiques effectives jouent un rôle fondamental dans le modèle de continuum, comme le souligne la première partie de la thèse: dans le Chapitre 3 l'analyse du modèle LTNE est strictement liée à la valeur choisie pour le coefficient de transfert de chaleur volumétrique $h_v$; dans le Chapitre 4 l'avancement du processus de pyrolyse, donc le comportement de la flamme, sont strictement liés à la valeur choisie pour le tenseur de perméabilité, $\underline{\underline{K}}$. La deuxième partie du travail vise à établir et valider des stratégies numériques pour estimer les propriétés effectives dans le cas générique de milieux poreux anisotropes non périodiques. À cette fin, quatre études complémentaires sont réalisées dans les Chapitres 5, 6, 7 et 8. Le schéma conceptuel de ces études est illustré dans la Fig. 1.10. Le Chapitre 5 est le point de départ de l'analyse, qui considère les écoulements creeping,

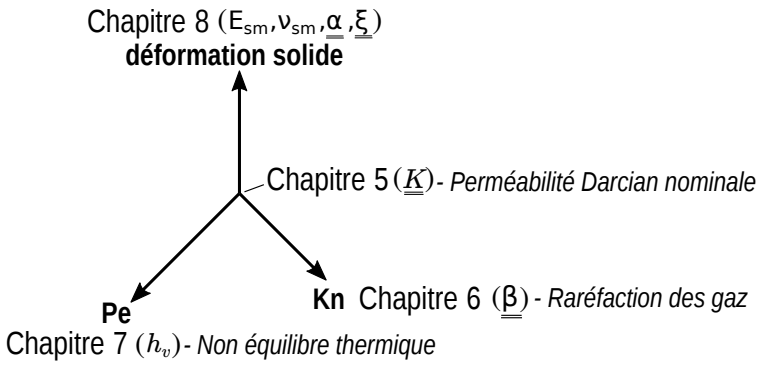


FIGURE 1.10 – Carte conceptuelle des études de la deuxième partie du manuscrit.

continus et isothermes interagissant avec des matrices solides rigides non réactives. Dans ces conditions, le tenseur de perméabilité, $\underline{\underline{K}}$, est la seule propriété efficace à caractériser à l'échelle macro. A partir de ce point de départ, les autres chapitres sont introduits en considérant des conditions plus générales pour l'écoulement et les phases solides. Le Chapitre 6 étend l'analyse aux écoulements raréfiés dans le régime de glissement. Un nombre adimensionnel est introduit. Le nombre de Knudsen est défini comme le rapport du libre parcours moyen $\lambda$ sur la longueur caractéristique de l'écoulement $l$.

$$Kn = \frac{\lambda}{l} \tag{1.47}$$

Ce nombre adimensionnel représente l'importance de l'effet de raréfaction. Plus sa valeur est élevée, plus l'effet de raréfaction est important. Dans le régime de glissement, $0.01 < Kn < 0.1$, les descriptions des micro et macro échelles sont légèrement modifiées. À l'échelle micro, une condition limite de glissement pour le champ de vitesse doit être ajoutée, tandis qu'à l'échelle du continuum, le tenseur de correction du glissement, $\underline{\underline{\beta}}$, doit être défini. Le Chapitre 7 considère les écoulements non isothermes. Trois propriétés effectives différentes sont introduites dans l'analyse: les tenseurs de conductivité thermique du fluide et du solide, $\underline{\underline{k}}_{\text{eff}}$, et le coefficient de transfert thermique volumétrique, $h_v$. Seul ce dernier est analysé dans cette étude et défini numériquement pour différentes valeurs du nombre de Peclet thermique (Eq. (1.46)) comprises entre 0 et 1000. Le Chapitre 8 généralise le problème pour les phases solides déformables. L'analyse des propriétés effectives est enrichie par le module de Young $E_{sm}$, le coefficient de Poisson $\nu_{sm}$, le tenseur de dilatation thermique $\underline{\underline{\alpha}}$, et le tenseur de retrait de pyrolyse $\underline{\underline{\xi}}$. Chaque chapitre effectue une analyse approfondie des différentes méthodes numériques pour estimer les propriétés effectives, en accordant une attention particulière aux effets des conditions aux limites sur les résultats numériques. Dans le but d'atteindre l'objectif et de consolider l'analyse pour les milieux poreux anisotropes non périodiques génériques, les stratégies numériques résultantes sont appliquées aux deux images 3D à haute résolution de la micro-tomographie numérisée (CMT) montrées à la Fig. 1.11. Le domaine (a) est un échantillon de Calcarb vierge [87], une préforme en

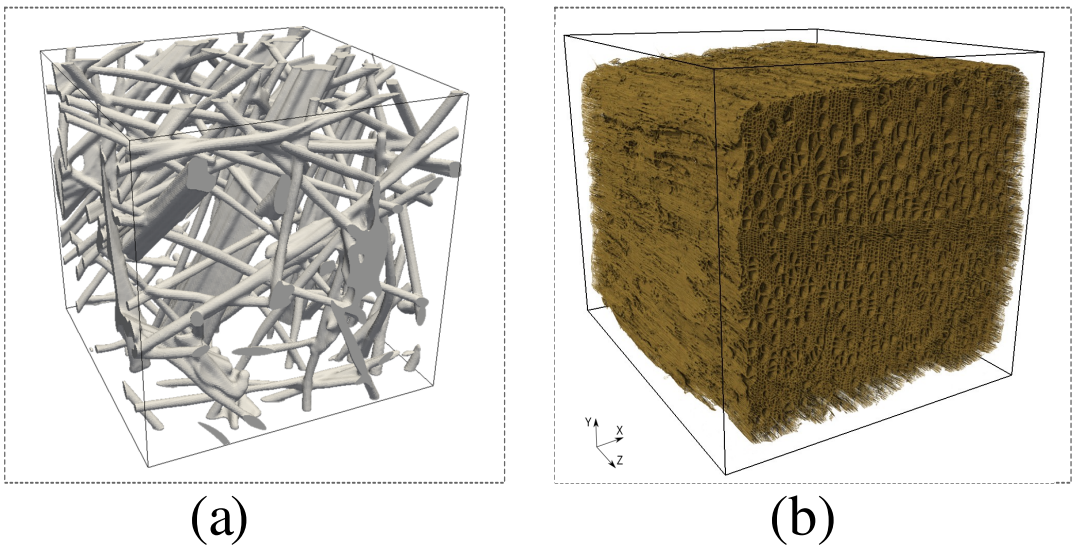


FIGURE 1.11 – Images de tomographie 3D à haute résolution considérées pour la détermination des propriétés effectives. Le domaine de Calcarb (a) est analysé dans les Chapitres 5, 6, et 7. L'échantillon de allumette en bois dur (b) est étudié au Chapitre 8.

fibre de carbone utilisée dans les matériaux de bouclier thermique [68, 69, 88]. Le domaine (b) est un échantillon de allumette en bois dur. Le tenseur de perméabilité du domaine (a) est déterminé au

Chapitre 5. Écrit par rapport aux axes principaux, le tenseur est le suivant

$$\underline{\underline{K}} = \begin{bmatrix} 1.74\ 10^{-10} & 0 & 0 \\ 0 & 1.49\ 10^{-10} & 0 \\ 0 & 0 & 1.11\ 10^{-10} \end{bmatrix} m^2 \tag{1.48}$$

Une différence relative d'environ 42 % est trouvée par rapport à la prédiction obtenue par Borner et al, 2017 [9]. Cette différence est attribuée aux différentes hypothèses de travail: alors que le Chapitre 5 détermine le tenseur complet, le travail de Borner et al, 2017 [9], suppose que le tenseur de perméabilité est initialement aligné avec les axes principaux et caractérisé par des composantes égales dans le plan. Le tenseur de correction du glissement du domaine (a) est déterminé dans le Chapitre 6. Écrit par rapport aux axes principaux, le tenseur est le suivant

$$\underline{\underline{\beta}} = \begin{bmatrix} 971.5 & 0 & 0 \\ 0 & 948.1 & 0 \\ 0 & 0 & 901.4 \end{bmatrix} Pa \tag{1.49}$$

Une différence relative d'environ 8 % est trouvée par rapport à la prédiction obtenue par Borner et al, 2017 [9], où les mêmes hypothèses faites pour le tenseur de perméabilité valent pour le tenseur de correction du glissement. Le coefficient de transfert de chaleur volumétrique du domaine (a) est déterminé dans le Chapitre 7 sous les mêmes conditions définies expérimentalement par Liu et al, 2022 [89]. Le coefficient est estimé à $h_v = 1.6\ 10^8\ Wm^{-3}K^{-1}$, alors que la valeur trouvée dans l'analyse expérimentale est $h_v = 10^9\ Wm^{-3}K^{-1}$. Les deux valeurs diffèrent d'un ordre de grandeur. Plusieurs raisons peuvent conduire à cette différence: l'ensemble de données Calcarb considéré pour la simulation numérique est trop petit et non représentatif; la valeur numérique attribuée au tenseur de conductivité effective ne tient pas compte des effets de dispersion et de tortuosité; la valeur de $h_v$ est si élevée qu'un équilibre thermique local est atteint entre les deux phases, ce qui rend son estimation expérimentale assez complexe. La déformation mécanique thermoélastique-pyrolyse d'une section transversale dans le plan $xy$ du domaine (b) est caractérisée dans le Chapitre 8. La déformation numérique résultante est comparée à la déformation subie expérimentalement par la même tranche après une pyrolyse complète. Cette comparaison est présentée dans la Fig. 1.12. En raison de l'hypothèse d'isotropie, la forme carrée originale est préservée. Malgré cette différence dans les formes finales, le modèle numérique est capable de prédire la valeur de la surface finale avec une erreur relative de 4.1%.

La détermination des propriétés effectives n'est pas le seul résultat obtenu. Différentes analyses et observations physiques sont effectuées dans la deuxième partie du manuscrit.
Le Chapitre 5 aborde la problématique de la définition d'une limite physique à la validité de l'hypothèse du régime de creeping de l'écoulement. Cette limite est généralement mesurée en termes de nombre de Reynolds, un nombre adimensionnel qui caractérise l'importance relative des forces d'inertie et visqueuses dans un fluide

$$Re = \frac{\rho_g |\langle \boldsymbol{v}_g \rangle| l}{\mu_g} \tag{1.50}$$

Pour $Re \ll 1$, les forces visqueuses dominent et l'écoulement est dit en régime de creeping [90, 91]. Ce critère est trop générique et il dépend de la valeur choisie pour la longueur caractéristique. Ce

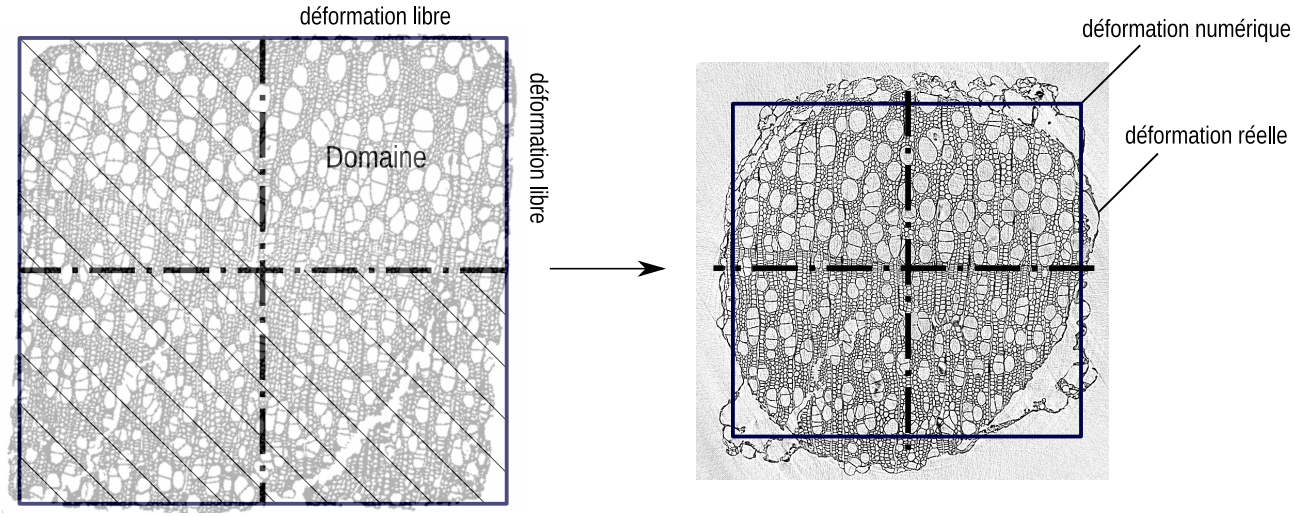


FIGURE 1.12 – Déformation pyro-mécanique d'une tranche 2D du domaine (b) dans le plan $xy$. La déformation numérique résultante est comparée à la déformation réelle soumise expérimentalement par la même section transversale après une pyrolyse complète.

choix n'est pas trivial car les microstructures poreuses sont très diverses et mieux caractérisées par des longueurs différentes. Pour cette raison, le Chapitre 5 définit un nouveau critère de délimitation du régime de creeping basé sur le champ de vorticité, $\boldsymbol{\omega}$, qui décrit la tendance d'un écoulement à tourner

$$\boldsymbol{\omega} = \partial_{\boldsymbol{x}} \times \boldsymbol{v} \tag{1.51}$$

Pour un écoulement incompressible, les gradients de vitesse aux frontières génèrent la vorticité, qui se diffuse ensuite sur l'ensemble du domaine. En raison du comportement linéaire de la vitesse, la vorticité augmente proportionnellement à la magnitude de la vitesse dans le régime de reptation. Cependant, dès que le régime de creeping chute, des non-linéarités dans le champ de vitesse changent cette tendance simple. Le critère consiste à garder sous observation la vorticité sans dimension, définie comme suit

$$\boldsymbol{\omega}^* = \boldsymbol{\omega} \frac{\ell}{\langle v \rangle} \tag{1.52}$$

dont la valeur moyenne reste constante dans le régime rampant. Un des principaux avantages de cette méthode est le fait qu'il est possible d'identifier dans le domaine la zone où la vorticité présente ses valeurs maximales, c'est-à-dire, où les effets de non-linéarité affectent davantage l'écoulement. Ce critère est appliqué pour caractériser l'image CMT de Calcarb présentée dans la Fig. 1.11. La zone influençant le comportement de l'écoulement à l'intérieur du domaine entier est reportée dans la Fig. 1.13. Cette zone est caractérisée par une longueur caractéristique $l_{cl} \sim 80\ \mu m$. Ainsi, la limite physique du régime de reptation pour l'image CMT de Calcarb est trouvée être

$$Re_{cl} < 0.5 \longrightarrow creeping\ \ regime$$

Le Chapitre 6 souligne l'importance de considérer le régime de glissement dans le cadre de la conception des TPS. Cet aspect est mis en évidence dans la Fig. 1.14, où les trajectoires d'entrée des missions

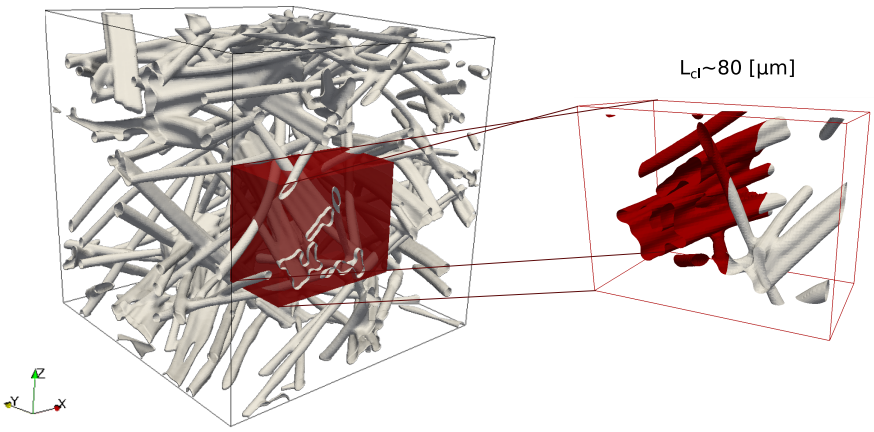


FIGURE 1.13 – Domaine Calcarb caractérisé dans le Chapitre 5. La zone rouge met en évidence une petite zone qui influence le comportement de l'écoulement dans l'ensemble du domaine.

Stardust [92] et Mars Science Laboratory [93] (MSL) sont considérées. Il est possible d'observer comment, au cours de ces trajectoires d'entrée, différents régimes de raréfaction sont traversés par la dynamique d'écoulement dans le milieu poreux. Au sein du matériau, la température du mélange gazeux diminue jusqu'à des valeurs de l'ordre de 273 $K$, tandis que la pression peut être considérée comme constante. Les deux zones surlignées (bleu pour Stardust et rouge pour MSL) donnent une indication des régimes de raréfaction traversés par la dynamique d'écoulement dans le TPS. La figure montre que, pour les deux missions, le régime continu ($Kn < 0.01$) est partiellement traversé par le matériau lorsque les conditions de chauffage atteignent leur maximum. Une plus grande partie des trajectoires est couverte par le régime de glissement ($0.01 < Kn < 0.1$). D'après la Fig. 2.14, il est possible de conclure que l'ensemble des régimes de glissement et de continuum est capable de couvrir entièrement la partie des trajectoires d'entrée caractérisée par les effets d'ablation.
Le Chapitre 7 propose une nouvelle définition du terme de transfert de chaleur volumétrique coefficient capable de rendre compte de manière générique des effets anisotropes

$$h_v = \langle \boldsymbol{v}_g \rangle^T \cdot \underline{\underline{h}}_v \cdot \langle \boldsymbol{v}_g \rangle \ \frac{1}{||\boldsymbol{v}_g||^2} \tag{1.53}$$

où un tenseur de transfert de chaleur volumétrique, $\underline{\underline{h}}_v$, est introduit. Lorsque $x$, $y$ et $z$ correspondent aux axes principaux, $\underline{\underline{h}}_v$ se réduit à un tenseur diagonal

$$\underline{\underline{h}}_v = \begin{bmatrix} h_{v,x} & 0 & 0 \\ 0 & h_{v,y} & 0 \\ 0 & 0 & h_{v,z} \end{bmatrix} \tag{1.54}$$

où $h_{v,x}$, $h_{v,y}$, et $h_{v,z}$ sont les coefficients de transfert de chaleur volumétrique lorsque la vitesse est alignée sur les directions $x$, $y$, et $z$ respectivement. Cette définition est appliquée pour caractériser les effets anisotropes pour un réseau périodique centré sur des mailles carrées avec une porosité $\epsilon = 0.5$. Les résultats sont illustrés dans la Fig. 1.15, où pour différents nombres de Peclet, le vecteur vitesse moyen est mis en rotation dans le plan $xy$. $\theta$ définit l'angle entre le vecteur vitesse moyenne et l'axe

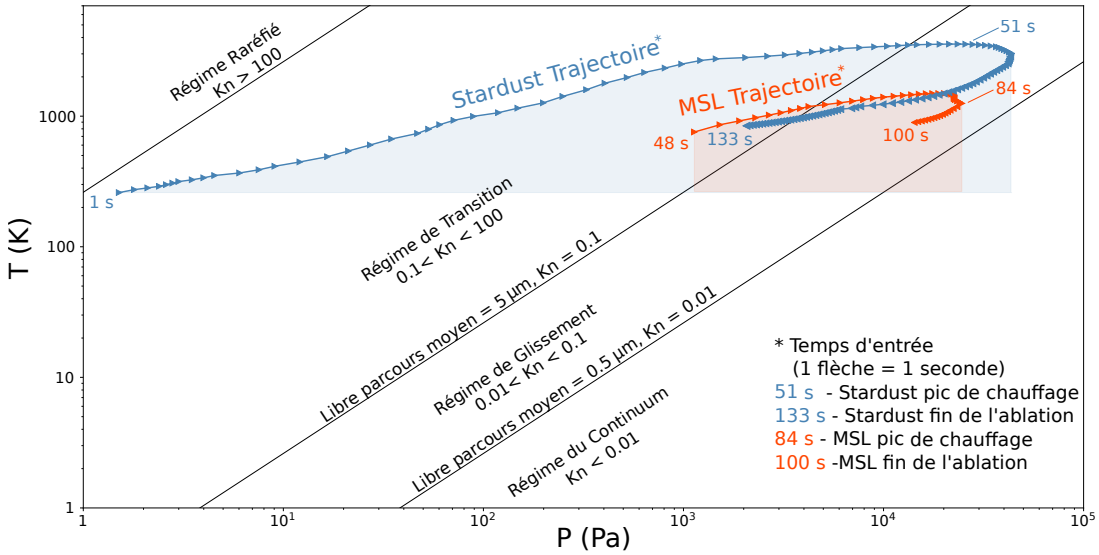


FIGURE 1.14 – Régimes d'écoulement raréfiés rencontrés le long des trajectoires d'entrée de Stardust et MSL dans le milieu poreux. Les valeurs de température-pression de paroi sont prises au point de stagnation le long des trajectoires d'entrée.

x. Dans ce cas, l'Eq. (1.53) se réduit à

$$h_v = cos^2(\theta)\ \ h_{v,x} + sin^2(\theta)\ \ h_{v,y} \tag{1.55}$$

Les résultats montrent que le tenseur de transfert de chaleur volumétrique est capable de capturer la forme du comportement anisotrope, mais pas exactement son amplitude, qui semble dépendre du nombre de Peclet. Pour $Pe = 66.7$, la corrélation capture parfaitement les effets anisotropes. Sur la figure, une variation linéaire du coefficient en fonction de $\theta$ est également représentée. On constate que la formulation tensorielle de la propriété conduit à une bonne capture des effets d'anisotropie.
Le Chapitre 8 dérive une fonction physique *pyrolyse-rétrécissement* pour tenir compte de la contribution de la pyrolyse sur le champ de déplacement. La dérivation de cette fonction est basée sur l'idée d'écrire la contribution de la pyrolyse au champ de déformation sous la même forme que la contribution thermique, puisque les deux contributions conduisent à des déformations volumétriques. La fonction de pyrolyse-rétrécissement est définie comme suit

$$\xi = \frac{1}{3}\frac{V_0 - V_{\text{end}}}{V_0} \tag{1.56}$$

La valeur de $\xi$ doit être définie à partir d'observations expérimentales.

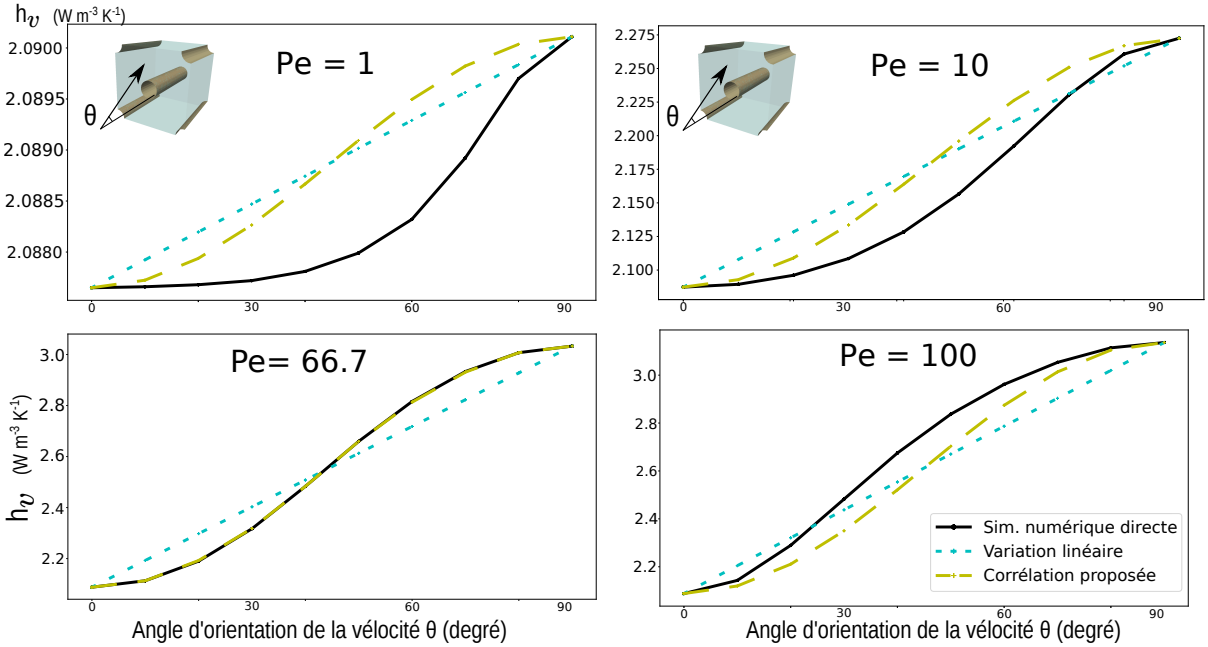


FIGURE 1.15 – Estimation des effets de l'anisotropie pour le cas du réseau périodique 2D de 5 cylindres. Une porosité constante $\epsilon = 0.5$ et différents nombres de Peclet sont considérés. Le tenseur de transfert de chaleur volumétrique capture la forme du comportement anisotrope, mais pas son amplitude.

## 1.7 Conclusions et Perspectives

### 1.7.1 Résultats

Diverses technologies et applications techniques sont centrées sur les matériaux poreux. Dans ce travail, l'attention est orientée vers le sous-ensemble des matériaux poreux réactifs interagissant avec des écoulements à haute température, un thème d'une grande pertinence notamment pour les communautés de la biomasse, de l'espace et de la sécurité incendie. L'objectif de ce projet de thèse a été de contribuer au développement d'un cadre théorique et numérique générique pour évaluer et modéliser les échanges de masse, de quantité de mouvement et de chaleur entre une structure solide élastique et réactive interagissant avec un écoulement à haute température. L'étude se compose de deux parties interdépendantes reposant sur une approche multi-échelle: (1) des simulations numériques multi-physiques sont réalisées à l'échelle macroscopique pour étudier l'impact de certains effets physiques dans la description numérique; (2) des simulations numériques directes sont réalisées à l'échelle microscopique sur des images digitize afin de définir des stratégies numériques pour l'évaluation des propriétés effectives.

La première partie du travail visait à étudier, à l'échelle du continuum, les effets sur les résultats numériques de l'hypothèse d'équilibre thermique local et de la description découplée matériau-écoulement externe. L'analyse ciblé sur deux applications spécifiques: la conception d'un TPS pour véhicule spatial et la description de la propagation d'un incendie. Pour le cas des matériaux ablatifs dans des conditions

d'entrée typiques, les résultats montrent qu'en équilibre chimique, le modèle d'équilibre thermique local est capable de prédire correctement l'évolution des paramètres de conception au sein du matériau. Cependant, en cas de non-équilibre chimique, l'hypothèse d'équilibre thermique local perd de sa précision dans la capture de la distribution des espèces au sein du matériau. Pour la deuxième application, la combustion d'une bûche de bois était considérée. Les résultats montrent que la simulation numérique de la propagation du feu nécessite de capturer le couplage entre la pyrolyse du bois et la combustion de différentes espèces gazeuses. L'hypothèse d'une description découplée matériau-écoulement externe est forte car les deux régions s'influencent fortement l'une l'autre: l'évolution de la flamme et sa température sont affectées par la concentration des espèces gazeuses produites dans le matériau, et en même temps, sous l'effet de l'élévation de la flamme et de la température, le processus de pyrolyse s'accélère et les concentrations des espèces changent en fonction de la vitesse des réactions.
La deuxième partie du travail était concentré sur la définition de stratégies numériques basées sur la simulation numérique à l'échelle des pores (PS-NS) pour prédire avec précision les propriétés effectives. L'importance de cette analyse réside dans le fait que l'exactitude des modèles macroscopiques dépend de la précision avec laquelle les propriétés effectives sont déterminées, et la littérature ne fournit pas de méthodologie numérique complète. A cette fin, une analyse approfondie était réalisée pour définir les stratégies numériques. Le terme stratégie numérique fait référence à la définition du domaine numérique et de l'ensemble des conditions aux limites, à la sélection des équations directrices et à la spécification de l'opération numérique pour déterminer une propriété effective spécifique. Comme propriétés effectives, le tenseur de perméabilité, le tenseur de correction du glissement, le coefficient de transfert de chaleur volumétrique, le module d'Young, le coefficient de Poisson et les termes de correction de l'expansion thermique et de la pyrolyse étaient considérés. Les stratégies numériques ont été définis sur des cas-tests simples, validées par des résultats de la littérature, et appliquées à la caractérisation de deux images de micro-tomographie numérique (CMT) 3D à haute résolution, les images de Calcarb et de pin blanc.

### 1.7.2 Perspectives

Ce travail est une contribution à l'effort continu de trois communautés pour mieux décrire les interactions entre les matériaux pyrolysés et les écoulements à haute température. Classées selon les thèmes abordés dans les six articles, les principales perspectives sont maintenant présentées.

Chapitre 3 aborde l'analyse du processus d'entrée dans les atmosphères planétaires. Ce travail met en évidence un manque particulier de mécanismes chimiques fiables. Dans l'optique d'une modélisation plus réaliste, des efforts accrus doivent être consentis pour le développement de modèles de chimie hors équilibre.

Chapitre 4 propose l'analyse d'une combustion de bûches de bois par la mise en œuvre et l'utilisation d'un code couplé matériau-écoulement externe. Malgré la nature avancée de la simulation, différents aspects physiques ont été négligés. La phase solide est considérée comme rigide, le rayonnement n'est pas pris en compte, la combustion est modélisée avec un modèle laminaire simplifié à taux finis, et le

mécanisme de pyrolyse est décrit avec un modèle de base à réactions multi-composants.

Le Chapitre 5 étudie la proportionnalité directe entre le débit et le gradient de pression des écoulements creeping et continus. Le Chapitre 6 étend l'étude à $0.1 < Kn < 0.01 <$ pour tenir compte des effets raréfiés dans le régime de glissement. L'extension à des nombres de Reynolds élevés manque pour compléter l'analyse, et notamment pour étudier comment la proportionnalité entre le débit et le gradient de pression change à cause des effets inertiels.

Chapitre 7 se concentre sur l'évaluation du coefficient de transfert de chaleur volumétrique en faisant deux hypothèses principales. Les écoulements sont supposés incompressibles,ce qui signifie que la thermodynamique n'est pas prise en compte et que des variables constantes sont supposées dans le domaine. Il s'agit d'une hypothèse forte par rapport aux applications d'intérêt, où les températures peuvent atteindre des milliers de degrés et où les écoulements compressibles doivent être considérés. La deuxième hypothèse concerne le tenseur de conductivité thermique effective. Cette propriété est définie uniquement en termes de diffusion moléculaire, tandis que les effets de dispersion et de tortuosité sont négligés dans l'étude. La détermination numérique du tenseur de conductivité thermique nécessite la définition d'une nouvelle stratégie numérique.

Chapitre 8 étend l'analyse aux phases solides déformables. L'étude est basée sur les hypothèses de petite déformation, de matériau solide élastique linéarisé et de matériaux isotropes. Ces hypothèses sont très fortes si l'on considère que l'application principale concerne la déformation du bois. L'extension aux modèles orthotropes et aux comportements de plasticité doit maintenant être envisagée.

# Chapitre 2

# Summary of the Thesis

## Nomenclature

*Latin Letters*

| | |
|---|---|
| $\mathcal{A}$ | Arrhenius law pre-exponential factor $[s^{-1}]$ |
| $A$ | generic element/species |
| $\mathcal{C}$ | fourth-order stiffness tensor $[kg\ m^{-1}\ s^{-2}]$ |
| $c_p$ | specific heat at constant pressure $[J\ kg^{-1}\ K^{-1}]$ |
| $\boldsymbol{D}$ | displacement field $[m]$ |
| $\mathcal{E}$ | Arrhenius law activation energy $[J\ mol^{-1}]$ |
| $e$ | specific internal energy $[J\ kg^{-1}]$ |
| $E_{sm}$ | Young modulus $[kg\ m^{-1}\ s^{-2}]$ |
| $\boldsymbol{\mathcal{F}}$ | effective diffusion flux $[kg\ m^{-2}\ s^{-1}]$ |
| $\boldsymbol{f}$ | generic volume force $[m\ s^{-2}]$ |
| $g$ | specific Gibbs free energy $[J\ kg^{-1}]$ |
| $h$ | specific absolute enthalpy $[J\ kg^{-1}]$ |
| $\underline{\underline{h}}_v$ | volumetric heat transfer tensor $[W\ m^{-3}\ K^{-1}]$ |
| $h_v$ | volumetric heat transfer coefficient $[W\ m^{-3}\ K^{-1}]$ |
| $\underline{\underline{I}}$ | identity tensor |
| $\underline{\underline{K}}$ | permeability tensor $[m^2]$ |
| $\underline{\underline{k}}$ | thermal conductivity tensor $[W\ m^{-1}\ K^{-1}]$ |
| $k$ | thermal conductivity coefficient $[W\ m^{-1}\ K^{-1}]$ |
| $k_{eq}, k_{fw}, k_{bw}$ | equilibrium, forward, and backward chemical rate constants |
| $l, L$ | characteristic lengths at the microscopic and macroscopic scales $[m]$ |
| $\mathcal{M}$ | molar mass $[kg\ mol^{-1}]$ |
| $m, n$ | Arrhenius law parameters |
| $n$ | number of moles |
| $N_g$ | number of gaseous species |

## Nomenclature

| | |
|---|---|
| $N_{p,i}$ | number of sub-phases in the solid phase i |
| $N_s$ | number of solid phases |
| $N_t$ | number of reactants and products in a chemical reaction |
| $\mathcal{P}_i, \mathcal{P}_{i,j}$ | solid phase $i$ and sub-phase $j$ of solid phase $i$ |
| $p$ | pressure $[Pa]$ |
| $\boldsymbol{\mathcal{Q}}$ | effective diffusion heat flux $[J\ m^{-2}\ s^{-1}]$ |
| $\mathcal{R}$ | universal perfect gas constant $[J\ kg^{-1}\ K^{-1}]$ |
| $r$ | representative elementary volume dimension $[m]$ |
| $R$ | specific perfect gas constant $[J\ mol^{-1}\ K^{-1}]$ |
| $\mathcal{S}$ | specific surface $[m^2\ m^{-3}]$ |
| $s$ | specific entropy $[J\ kg^{-1}\ K^{-1}]$ |
| $t$ | time $[s]$ |
| $T$ | temperature $[K]$ |
| $\boldsymbol{v}$ | convective velocity $[m\ s^{-1}]$ |
| $v$ | specific volume $[m^3\ kg^{-1}]$ |
| $V$ | averaging volume $[m^3]$ |
| $V_i$ | volume of phase i $[m^3]$ |
| $\boldsymbol{x}$ | microscopic coordinates $[m]$ |
| $\boldsymbol{X}$ | macroscopic coordinates $[m]$ |
| $X$ | molar fraction |
| $y$ | species mass fraction |
| $z$ | element mass fraction |

*Greek Letters*

| | |
|---|---|
| $\underline{\underline{\alpha}}$ | thermal expansion tensor $[K^{-1}]$ |
| $\alpha$ | thermal expansion coefficient $[K^{-1}]$ |
| $\underline{\underline{\beta}}$ | slip correction tensor $[Pa]$ |
| $\gamma$ | phase indicator |
| $\underline{\underline{\epsilon}}$ | strain tensor |
| $\epsilon$ | volume fraction |
| $\theta$ | angle of velocity orientation |
| $\Theta$ | active site density $[mol\ m^{-3}]$ |
| $\lambda$ | mean free path $[m]$ |
| $\mu$ | dynamic viscosity $[Pa\ s]$ |
| $\mu_{sm}, \lambda_{sm}$ | Lame's constants $[kg\ m^{-1}\ s^{-2}]$ |
| $\nu$ | stoichiometric coefficient |
| $\nu_{sm}$ | Poisson ratio |
| $\underline{\underline{\xi}}$ | pyrolysis contribution tensor |
| $\xi$ | pyrolysis contribution coefficient |
| $\pi_k$ | pyrolysis mass production rate of element/species $k$ $[kg\ m^{-3}\ s^{-1}]$ |

## Nomenclature

| | |
|---|---|
| $\Pi$ | global mass production rate of the pyrolysis reactions $[kg\ m^{-3}\ s^{-1}]$ |
| $\rho$ | density $[kg\ m^{-3}]$ |
| $\underline{\underline{\sigma}}$ | stress tensor $[kg\ m^{-1}\ s^{-2}]$ |
| $\underline{\underline{\tau}}$ | viscous stress tensor $[N\ m^{-2}]$ |
| $\tau$ | total advancement of the pyrolysis reactions |
| $\chi_{i,j}$ | advancement of the pyrolysis reaction of sub-phase $j$ within phase $i$ |
| $\boldsymbol{\omega}$ | vorticity $[s^{-1}]$ |
| $\omega_i$ | production rate of species $i$ $[mol\ m^{-3}\ s^{-1}]$ |
| $\omega_i^h$ | heterogeneous reactions mass production rate of species $i$ $[kg\ m^{-3}\ s^{-1}]$ |
| $\Omega_h$ | global mass production rate of the heterogeneous reactions $[kg\ m^{-3}\ s^{-1}]$ |

*Subscripts and Superscripts*

| | |
|---|---|
| 0 | initial time |
| bw | backward |
| cl | cluster |
| eff | effective |
| eq | equilibrium |
| f | fluid |
| fw | forward |
| g | gas |
| $i$, $j$, $k$ | indexes used in the sum/product operators |
| s | solid |
| sm | solid material |

*Formalism*

| | |
|---|---|
| $\underline{\underline{A}}$ | second order tensor A |
| $\boldsymbol{A}$ | vector A |
| $A$ | scalar A |
| $\langle\ \rangle$ | intrinsic average |
| $\partial_t$ | partial derivative to t |
| $\partial_{\boldsymbol{x}}$ | gradient operator |
| $\partial_{\boldsymbol{x}}\cdot$ | divergence operator |
| $tr()$ | trace operator |
| $\sum_{j=1}^{N_t}$ | sum operator with index j varying from $j=1$ to $j=N_t$ |
| $\prod_{j=1}^{N_t}$ | product operator with index j varying from $j=1$ to $j=N_t$ |
| $*$ | non-dimensional variable |

*Adimensional Groups*

| | |
|---|---|
| Kn | Knudsen number |

## Nomenclature

| | |
|---|---|
| Pe | Peclet number |
| Re | Reynolds number |

*Acronyms*

| | |
|---|---|
| CMT | Computed Micro-Tomography |
| LTE | Local Thermal Equilibrium |
| LTNE | Local Thermal Non-Equilibrium |
| MSL | Mars Science Laboratory |
| PATO | Porous material Analysis Toolbox based on OpenFoam |
| TACOT | Theoretical Ablative Composite for Open Testing |
| TPS | Thermal Protection System |

## 2.1 Porous Materials

A **porous medium** consists of a solid structure, the **matrix**, and empty spaces, the **pores**. The latter are usually filled by some fluid, such as air, water, oil or a mixture of different fluids. Porous materials are encountered almost everywhere in daily life, having both geological (e.g. rocks, soil), biological (e.g. bones, wood, cork), and man-made nature (e.g. cements, ceramics, polymer) origins. Their main characteristic is that they can be described in different ways depending on the scale at which they are looked at, as illustrated in Fig. 2.1. Wood, bone, ceramic, and carbon fiber felt structures are represen-

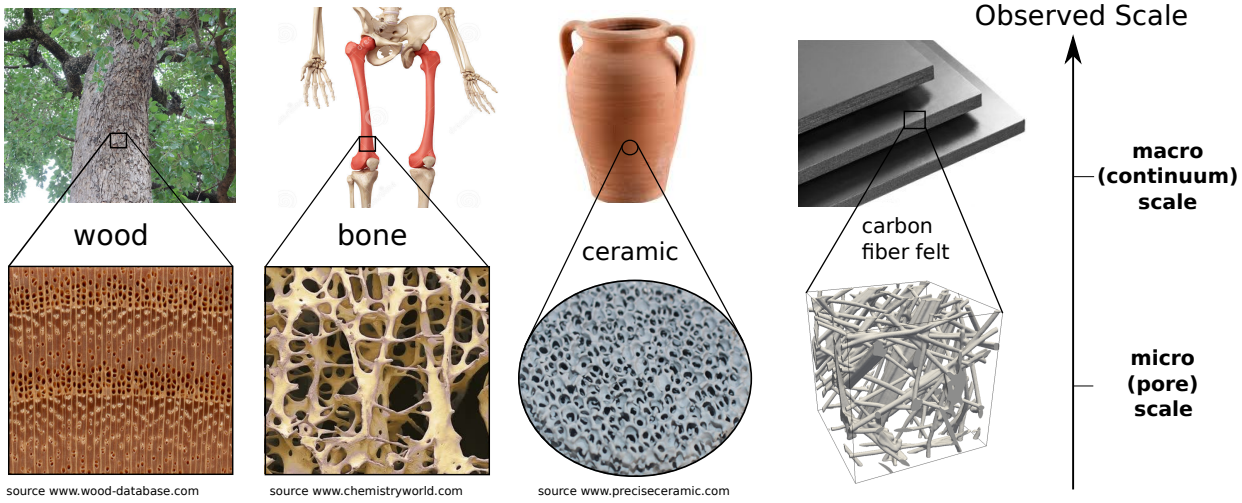


FIGURE 2.1 – Micro (pore) scale and macro (continuum) scale representations of four porous materials: wood, bone, ceramic, and carbon fiber felt.

ted in two different ways: in the upper part of the figure they are showed at the scale at which we are used to seeing them, i.e. the macroscopic scale, or **continuum scale**; while in the lower part they are zoomed in at the microscopic scale, or **pore-scale**, where their porous structure is revealed. The interaction between a permeable porous medium and a fluid penetrating through its pores can be studied at both scales using numerical simulations. At the microscopic level the description is based on classical fluid-solid mechanics, which may lead to some difficulties when dealing with complex geometries, but they prove to be essential for visualizing and understanding the physics of the interaction. Differently, at the macroscopic scale, the solid and fluid are homogenized in an **equivalent porous continuum material** and transfer phenomena are described by **averaged governing equations**. The two scales are linked together by **upscaling processes**. The most popular ones in the field of porous media are: the homogenization theory [14], the volume-averaging technique [15], and stochastic methods [16]. The different approaches lead to the formulation of equivalent continuum models, provided that the same level of mathematical approximations and the same physical hypotheses are considered [17], mainly the assumptions of **scale separation** and the existence of a **representative elementary volume** (REV) [1] where small scale variations are smoothed. This is illustrated in Fig. 2.2. At the continuum-scale,

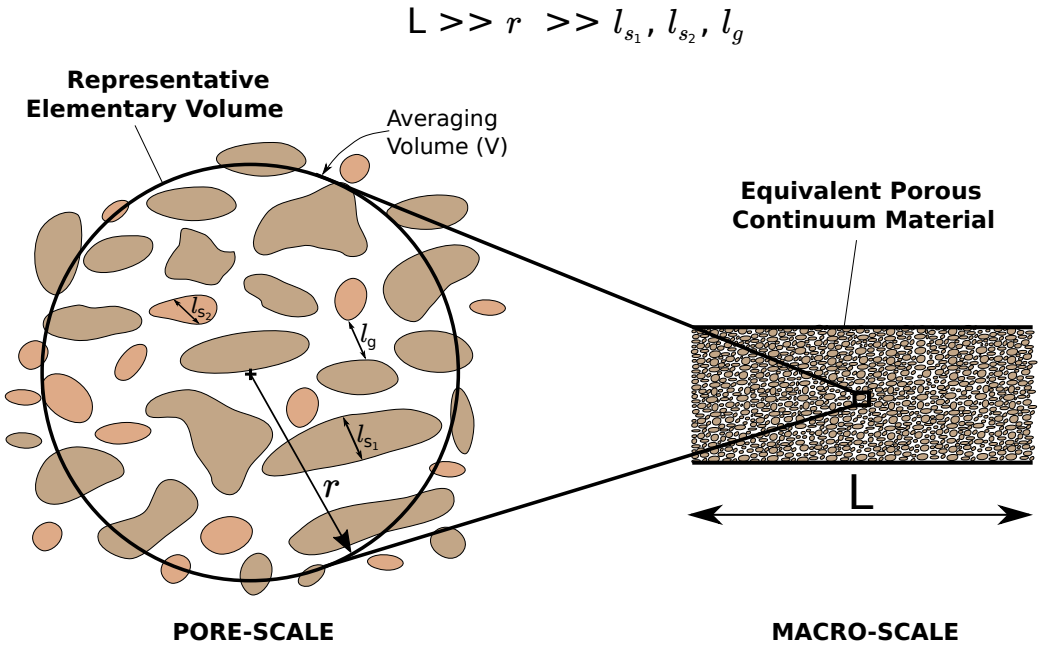


FIGURE 2.2 – Generic concept of the upscaling process. The process relies on the hypotheses of scale separation ($L >> r >> l_{s1}, l_{s2}, l_g$) and the existence of a REV where the small scale variations are smoothed.

details of the microscopic structure of the pores and their interaction with the flow are lost. However, the average information is contained within the **effective properties**. Examples of the latter are the permeability tensor, heat transfer coefficient, effective thermal conductivity and stress tensors. Given

1. With reference to the volume averaging technique.

their physical importance, their correct estimation is essential for model accuracy. Depending on the needs and conditions, different ways of determination can be followed. Experiments are widely used in the literature [18–25], however, although the filed of microfluidics is progressing vert fast, the influence of the microscopic structure on the behavior of the fluid-porous material interaction cannot yet be directly observed for complex materials. To this end, numerical simulations are needed. The geometry of a porous medium can be obtained either by an idealized mathematical representation [21, 26–30] or from a reconstructed digital image [31–38]. In the former case, the pore structure must be described from a statistical point of view [39] and the geometry reconstructed by small primitive objects within a finite domain [30]. Differently, if a digital image is available, simulations are performed on the exact geometry. This allows direct visualisation of the behaviour of transport quantities and gradients throughout the domain at the pore level and a clear observation of how the latter are affected by the microscopic characteristics of the material. Numerical simulations need an appropriate set of boundary conditions, although this is not always straightforward, especially when dealing with numerical domains that are not big enough to be considered as REV [40, 41]. Finally, the third way to determine effective properties is to use correlations. They are obtained through a comprehensive understanding of physics, derived from experimental or theoretical analysis of the problem [28, 34, 38, 42–44]. Their applicability is usually limited to known geometries and within specific ranges of conditions (such as specific Reynolds or Peclet intervals).

## 2.2 Reactive Porous Materials in High-Temperature Flows

Various technologies and engineering applications are centered on porous materials. Catalytic converters for water treatment [45], filtering devices [46], microfluidic sensors [47], enhanced oil recovery [48], to name a few. In this work, attention is oriented towards the subset of reactive porous materials interacting with high-temperature flows, a theme with a breadth of applications ranging from the design of a porous heat shield of a space vehicle entering an atmosphere, to the simulation of the burning of a match. Despite the clear difference in terms of external conditions, these applications are described by the same physical phenomena from a material point of view, as schematized in Fig. 2.3. As different materials and external conditions are considered, the temperature ranges and chemical mechanisms are not the same for both cases. Some examples of these differences are showed in blue for the burning match and in red for the ablative porous carbon/phenolic material. However, the same generic phenomenology applies to both. The conservation laws within the materials are the same and the same mathematical model may be used to describe their behaviors. The topic of reactive porous materials interacting with high-temperature flows is of great relevance particularly for the biomass, space, and fire-safety communities. Over the past decades, these scientific communities have addressed the subject by targeting several fundamental aspects. A brief introduction to the three communities and a review of their key strengths is now presented.

1. The **biomass community**. Nowadays, the effects of climate change are quite evident (*greenhouse effect*, *global warming*, *Earth overshoot day*[2]) and embracing green solutions is becoming in-

2. Calendar date of the year when the humanity's demand for ecological resources and services exceeds what Earth

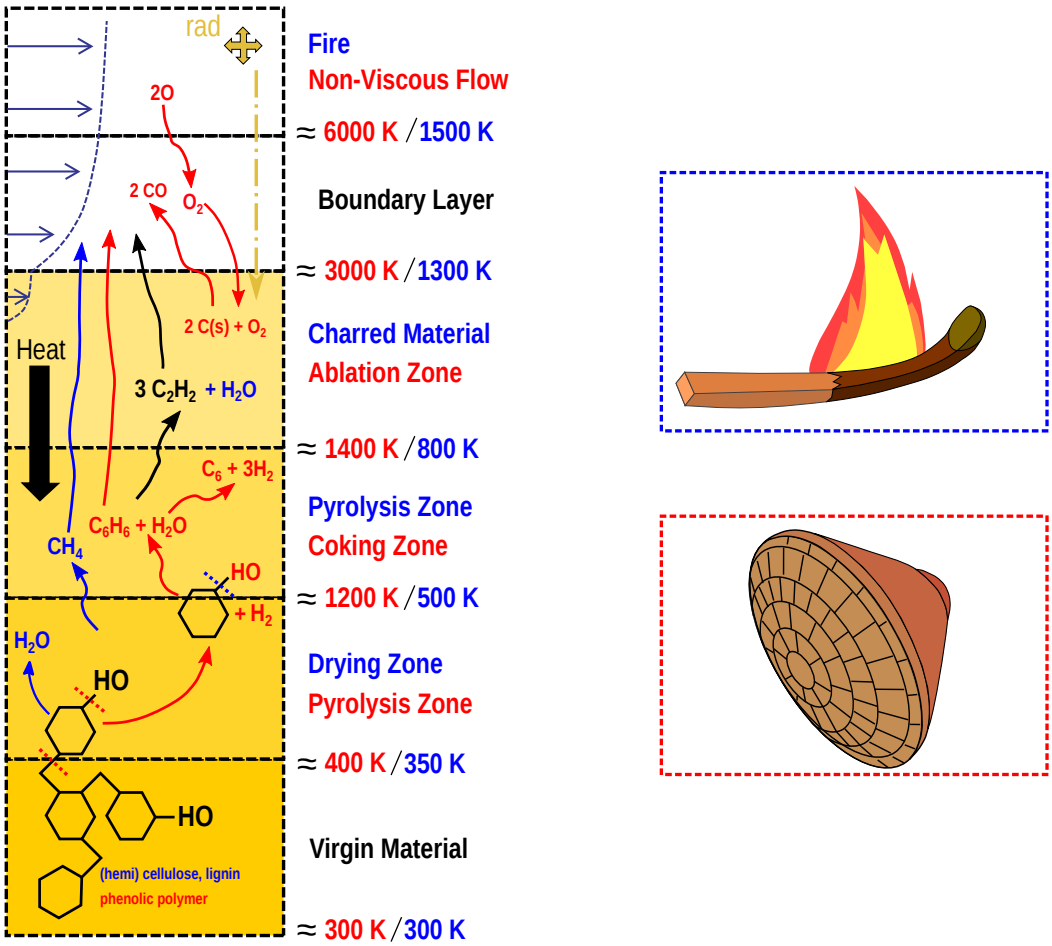


FIGURE 2.3 – Simplified illustration of the physical phenomena from a material point of view of a burning match (blue) and of a ablating porous carbon/phenolic material (red). The text in yellow and black applies to both.

creasingly important [94, 95]. Fig.2.4 shows the world annual energy consumption by source [3]. It can be observed that biomass is the most widely used source of renewable energy. The term *biomass* generally refers to a plant-derived material that can be thermally converted into high-value bio-hydrocarbon molecules [49,50]. The thermo-chemical phenomena behind this process is **pyrolysis**, which transforms substances under the effect of heat and produces different chemical species according to the imposed conditions [51, 52]. The main objective of the biomass community is to develop models that can be used to improve the techniques (temperature, heating rate, time, etc) to transform lignocellulosic biomass in high-value bio-hydrocarbon molecules. The first pyrolysis model is attributed to Bamford, Crank and Malan [53]. According to this

can regenerate in that year.

3. Data are from 2016, but similar trends hold nowadays.

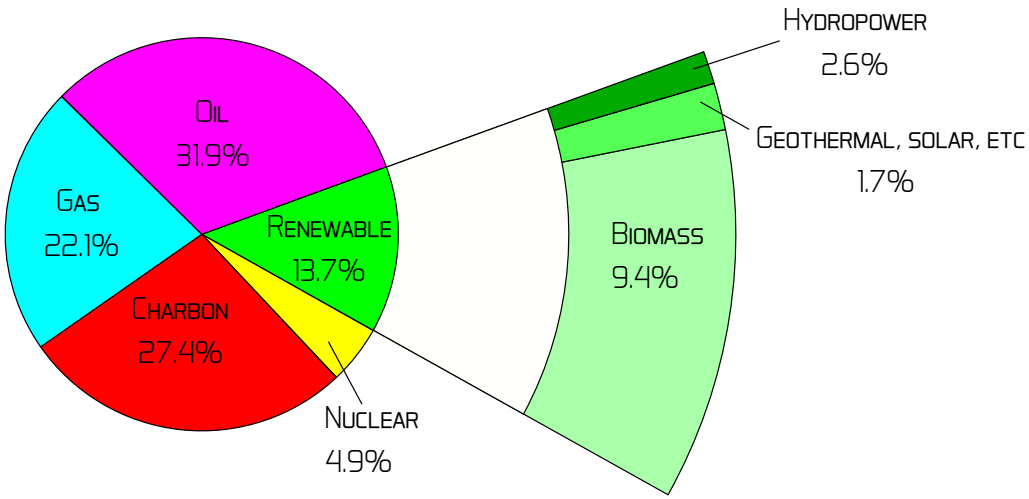


FIGURE 2.4 – World energy consumption by source in 2016. *Source https://www.iea.org/*. Biomass, with 9.4% of the total energy consumption, is the most used source of renewable energy.

model, pyrolysis is modeled as a first-order reaction following an Arrhenius law, and an ordinary differential equation is solved to estimate the mass loss as a function of time. This allows capturing the pyrolysis mass loss at a reduced computational cost. Following this work, several models have been developed over the years, each characterized by a different level of accuracy in describing chemical reactions. The simplest level corresponds to *single reaction mechanisms* [54], in which only a single decomposition reaction is considered. Greater accuracy is provided by the *multi-component single reaction models* [55], where the description accounts for the feed-stock. At higher complexity are the *competitive models* [56] that introduce competitive reactions to predict different product distributions depending on the conversion conditions. Finally, the most accurate models are the *competitive multi-component models* [57, 58], which efficiently account for feed-stock dependence and the effect of temperature on yields;

2. The **fire-safety community**. Fire safety is the set of practices intended to reduce the destruction caused by fire. It includes measures to prevent and detect an uncontrolled fire, those used to contain and extinguish the development and effects of a fire after it has broken out, and those to assess the release of suffocating chemical species. Particular emphasis has been placed on porous media, due to their frequent use in many civil and aeronautical projects: timber used for the construction of houses, bridges, and generic buildings [59]; composite materials used as structural parts in aircrafts and spacecraft systems [60]. Because of the flammable nature of these materials, it is important to be able to predict their potential in increasing fire hazard with the consequent loss of stiffness, strength, and resistance of the structure [61, 62]. For this reason, several studies have attempted to define their performance characteristics during combustion, such as their fire retardancy [63], their flammability properties [64], and their gaseous emissions [65]. Thus, the strength of the fire safety community lies in the ability to couple the material with the environment and describe the fire behavior for a given material, including the processes of ignition, fire growth, propagation and extinction [66].

3. The **space community**. Extra-orbital missions often involve the analysis of the entry process into planetary atmospheres at hypersonic speeds [67]. Under these conditions, a high enthalpy curved detached shock (bow shock) forms in front of the spacecraft and the kinetic energy is progressively dissipated into heat, which reaches the surface by diffusion, convection, and radiation. The temperature at the surface of the material can increase up to 4000 $K$ for severe entry conditions. To ensure the integrity of the structure, a **Thermal Protection System** (TPS) is designed to absorb and dissipate the heat through phase changes, chemical reactions, and material removal. Charring ablative materials represent a traditional approach to thermal protection [68, 69]. A famous example is the new class of phenolic impregnated ablators (PICA [70], PICA-X, ASTERM [71]) that consists of a carbon fiber preform partially impregnated with phenolic resin, resulting in very light weight, good insulators, and high mechanical strength.
   Numerical modelling of a TPS must be able to capture the material removal and the heat dissipation within the material. If not, the modelling may lead to inaccuracies in the estimation of the efficiency of the ablator, and thus to a greater margin of safety in the design process. For this reason, the space community has turned its attention primarily to the modeling of heterogeneous chemistry and transport phenomena, as evidenced by the vast amount of software developed over the years. In the frame of a code comparison carried out in the aerospace community [72], the models implemented in twenty-five TPS design and research codes were reviewed, compared, and classified into three different categories: *type-1 models*, which are implemented in all design codes and describe the core phenomena of the pyrolysis-ablation problem. They are well adapted for 1D, quasi steady-state, and chemical equilibrium conditions; *type-2 models*, which increase their accuracy by including the implementation of the momentum conservation to simulate the direction of the pyrolysis flux for constant element/species mixtures; *type-3 models*, which complete the description by including element (or species) conservation equations and the associated chemical equilibrium (or finite-rate) models.

Based on the open literature, a generic model has been proposed as an attempt to encompass the fundamental physics requirements of the three applications [73–75]. This generic model, implemented in the **Porous material Analysis Toolbox based in OpenFoam (PATO)** released open source, is now used by academia and industry teams of the three communities. The capabilities of PATO with respect to the contributions and developments of each community understandings are presented in Fig. 2.5. A selection of four codes per community is showed. An effort was made to select codes amongst the most well-known, although priority was given to a couple of recent implementations. The link between the table and the mathematical model can be made through the description of the terms of the different conservation equation (column 2) and through the numbers of the terms in the PATO column, which refer to the equation numbers and order of these terms in the equations. For example, in the solid mass conservation equation, the pyrolysis term is the second term in Eq. (2.25). Each code is described in terms of the year of the initial publication, the type of the numerical methods, the dimensions, the availability of the code, and in terms of the model classification based on the criterion introduced by Lachaud et al., 2011 [72]. It can be observed that PATO is the only code from the TPS community to implement a type (3) model. Different type (3) models have been developed by the two other communities. In particular, ThermaKin [76], Gpyro [77], and MoDeTheC [78] are

| | | | Original | TPS | | | | Fire | | | | Biomass | | | |
|---|---|---|---|---|---|---|---|---|---|---|---|---|---|---|---|
| | | | BAM1946 | CMA/FIAT | AMARYLLIS | CHAR | PATO | HEN85 | Thermakin | Gpyro | MoDeTheC | RAT09 | SPY | POZ2018 | bioSMOKE |
| Overview | | | | | | | | | | | | | | | |
| Free release | | | | x | | | x | | | x | | | | | |
| Open source | | | | x | | | x | | | x | | | | | |
| Year of initial publication | | | 1946 | 1968 | 2009 | 2011 | 2014 | 1985 | 2008 | 2009 | 2014 | 2009 | 2012 | 2014 | 2017 |
| Numerical method | | | FD | FD | FE | FE | FV | FD | FE | FV | FV | FD | FD | FV | FV |
| Dimensions | | | 1D | 1D | 3D | 3D | 3D | 1D | 2D | 3D | 3D | 1D | 2D | 3D | 3D |
| Type of model (according to TPS classif cation of 2011) | | 1, 2, or 3 | | 1 | 2 | 2 | 3 | 1 | 3 | 3 | 3 | 3 | 3 | 3 | 3 |
| Mass conservation | | | | | | | | | | | | | | | |
| Solid | storage | 1 | | x | x | x | 2.25:1 | x | x | x | x | x | x | x | x |
| | pyolysis | 1 | x | x | x | x | 2.25:2 | x | x | x | x | x | x | x | x |
| | het. react. | 3 | | | | | 2.25:3 | | x | x | | | | | |
| Gas | storage | 2 | | | x | x | 2.14:1 | | x | x | x | x | x | x | x |
| | convection | 1 | | x | x | x | 2.14:2 | x | x | x | x | x | x | x | x |
| | - pyolysis | 1 | | x | x | x | 2.14:3 | x | x | x | x | x | x | x | x |
| | - het. react. | 1 | | | | | 2.14:3 | | x | x | | | | | |
| Elements | storage | 3 | | | | | 2.18:1 | | | | | | | | |
| | convection | 3 | | | | | 2.18:2 | | | | | | | | |
| | dif usion | 3 | | | | | 2.18:3 | | | | | | | | |
| | pyrolysis | 3 | | x | x | x | 2.18:4 | | | | | | | | |
| Species | storage | 3 | | | | | 2.21:1 | | x | x | x | x | x | x | x |
| | convection | 3 | | | | | 2.21:2 | | x | x | x | x | x | x | x |
| | dif usion | 3 | | | | | 2.21:3 | | x | x | x | x | x | x | x |
| | pyrolysis | 3 | | | | | 2.21:4 | | x | x | x | x | x | x | x |
| | het. react. | 3 | | | | | 2.21:5 | | x | x | x | x | x | x | x |
| Liquid | no motion | n/a | | | | | ln 2.25 | | | | | | x | | x |
| | with motion | n/a | | | | | | | | | | x | | x | |
| Momentum conservation | | | | | | | | | | | | | | | |
| Solid | displacem. | n/a | | | x | x | 2.27:1 | | | | | | x | | x |
| | stress. div. | n/a | | | x | x | 2.27:2 | | | | | | | | |
| | body. forc. | n/a | | | x | x | 2.27:3 | | | | | | | | |
| | lin. elast. | n/a | | | x | x | 2.29:1 | | | | | | | | |
| | th. expens. | n/a | | | x | x | 2.29:2 | | | | | | | | |
| | pyr. shrink. | n/a | | | | | 2.29:3 | | | | | | | | |
| | viscoelastic | n/a | | | | | | | | | | | | | |
| Gas | velocity | 2 | | | x | x | 2.15:1 | | x | | x | x | x | x | x |
| | Darcy | 2 | | | x | x | 2.15:2 | | x | | x | x | x | x | x |
| | Klinkenberg | 3 | | | | x | 2.15:3 | | | | | | | | |
| Liquid | Darcy gen. | n/a | | | | | | | | | | x | | x | |
| Energy conservation | | | | | | | | | | | | | | | |
| Solid | sens. stor. | 1 | x | x | x | x | 2.26:1 | x | x | x | x | x | x | x | x |
| | form. enth. | 1 | x | x | x | x | 2.26:2 | x | x | x | x | x | x | x | x |
| | conduction | 1 | x | x | x | x | 2.26:3 | x | x | x | x | x | x | x | x |
| | heat. trans. | n/a | | | | | 2.26:4 | | | | | | | | |
| Gas | sens. stor. | 2 | | | x | x | 2.17:1 | | x | x | x | x | x | x | x |
| | form. enth. | 3 | | x | x | x | 2.17:2 | x | x | x | x | x | x | x | x |
| | press. work | 3 | | | x | x | 2.17:3 | | x | x | x | x | x | x | x |
| | convection | 1 | | x | x | x | 2.17:4 | x | x | x | x | x | x | x | x |
| | conduction | n/a | | | | | 2.17:5 | | x | x | x | x | x | x | x |
| | dif usion | 3 | | | | | 2.17:6 | | x | x | x | x | | x | x |
| | heat. trans. | n/a | | | | | 2.17:7 | | | | | | | | |
| Liquid | no motion | | | | | | ln 2.26 | | | | | | x | | x |
| | with motion | n/a | | | | | | | | | | x | | x | |
| Additional features | | | | | | | | | | | | | | | |
| Finite-rate chemistry solver | | 3 | | | | | x | | | | | x | x | x | x |
| Equilibium chemistry solver | | 3 | | | | | x | | | | | | | | |
| Reactive boundary layer model | | 1 | | x | x | x | x | | x | x | x | | | | |
| Integrated flow solver(s) | | n/a | | | | | x | | | | | | | | |

FIGURE 2.5 – Comparison of the mathematical models implemented in simulation tools of the three communities. Credit J. Lachaud.

three popular codes of the fire community, while SPY [52], bioSmoke [79], and the codes developed by Ratte et al., 2009 [80], and Pozzobon et al., 2018 [81], are the codes of the biomass community implementing the most advanced features to our knowledge. In many codes, the liquid water motion is not modeled but a vaporization model is implemented. The same choice was made in PATO. However, the codes by Ratte et al., 2009 [80], and Pozzobon et al., 2018 [81], implement drying using a generalized Darcy formulation. TPS and fire codes adopt integrated reactive boundary layer models as boundary conditions and assume (with the exception of PATO) constant elemental composition of the pyrolysis gases and use chemical equilibrium, while biomass models consider species conservation and finite-rate chemistry. PATO is the only code that is directly coupled to external flow codes. Solid mechanics capabilities were not considered in the code classification. However, thermo-mechanics models are implemented in Amaryllis [82], Char [83] and PATO. In addition, PATO takes into account pyrolysis shrinkage. SPY and bioSmoke have included shrinkage models allowing to linearly compress the mesh as pyrolysis progresses.

## 2.3 Objectives of the Thesis

Two objectives define this thesis. The first is to contribute to modelling the behaviour of reactive porous materials in high-temperature flows, as current state-of-the-art models are still limited in predicting all the hidden physics behind the application. To this end, momentum conservation, solid deformation, and conservation of energy are investigated. These three aspects are mainly strengthened by the introduction of slip regime effects, by accounting for pyro-mechanical deformation, and by allowing solid and flow phases to be in local thermal non-equilibrium between each other. Two different multi-physics applications are considered and analyzed in order to verify the impact of these physical aspects on the model.
Regardless of the model employed at the macroscopic scale to describe the interaction between a reactive porous material and a high temperature flow, the accuracy of the description depends on the precision with which the effective properties are estimated based on the micro-scale structure and properties. Their derivation proves to be a complex task and the literature does not provide a complete numerical methodology for such purpose. The second objective of this thesis is therefore to establish and validate numerical strategies to estimate the effective properties of anisotropic porous media in the generic case of a non-periodic microscopic volume available through microtomography.

## 2.4 Structure of the Thesis

The dissertation is presented in the form of a compilation of articles. The introductory chapter is written in both French (Chapter 1) and English (Chapter 2). In the introductory chapter the thesis is outlined by exposing the background, state of the art, objectives, applications of interest, physical models, main results obtained, and the conclusion. The articles are placed in six independent chapters:

1. Two-Temperature ablative material response model with application to Stardust and MSL atmospheric entries;

2. Simulation of wood combustion in PATO using a detailed pyrolysis model coupled to fireFoam;
3. Computation of the permeability tensor of non-periodic anisotropic porous media from 3D images;
4. Multiscale modeling of flow in porous thermal protection systems from the continuum to the slip regime;
5. Volumetric Heat Transfer Coefficient: Numerical Evaluation and Introductory Analysis to Anisotropic Effects;
6. Multi-Scale modeling of wood shrinkage during pyrolysis.

Two main parts are defined according to the set objective. The first part encloses articles 1 and 2, while the remaining articles are incorporated in the second part. The manuscript includes an Appendix presenting a derivation of macroscopic equations for the mass, momentum, and energy transfer in porous media with the volume averaging technique.

A nomenclature is given at the beginning of each chapter. A general bibliography is included at the end of the manuscript, collecting citations of all the articles.

## 2.5 Physical Model

The numerical description of a porous material interacting with a generic flow relies on the scale of interest. At the continuum-scale, volume averaged equations are adopted, while at the pore-scale, conservation of mass, momentum, and energy is solved by the Navier-Stokes equations.

### 2.5.1 Macro-Scale

#### 2.5.1.1 Assumptions and Notations

The numerical model used in this work is based on the generic local thermal equilibrium model previously implemented in PATO [75]. It assumes the interaction between a multi-species reactive gas mixture ($N_g$ gaseous species) with a multi-phase reactive material ($N_s$ solid phases). The gaseous species are assumed to be in local thermal equilibrium among themselves, as are the solid phases. However, the material and the gas mixture are no longer assumed to be in local thermal equilibrium in the current worker. No liquid phase has been modeled. Any liquid, if present (e.g. water), is modeled as a solid phase. Continuum equations are obtained either through upscaling theories [4], or defined heuristically. With reference to the volume-averaging technique, the fundamental hypothesis are the existence of a REV (Fig. 2.2) in which properties can be phase averaged and the satisfaction of the scale separation. The volume fraction $\epsilon$ of a given phase $i$ is defines as

$$\langle \gamma_i \rangle = \epsilon_i(\boldsymbol{X}, t) = \frac{1}{V} \int_{V_i} \gamma_i(\boldsymbol{X} + \boldsymbol{x}, t) d\boldsymbol{x} \tag{2.1}$$

4. The derivation of the governing equations for non-reactive materials and incompressible flow is presented in the Appendix.

where the average used is called *intrinsic average*, $V$ is the averaging volume, $V_i$ is the volume of phase $i$ within the averaging volume, $\gamma_i$ is the phase indicator, with $\gamma_i = 1$ within phase $i$ and $\gamma_i = 0$ outside phase i, $\boldsymbol{X}$ and $\boldsymbol{x}$ denote the macroscopic coordinate and the local coordinate within the averaging volume, respectively, and $t$ is the time. The $\langle\ \rangle$ notation denotes the intrinsic average. The latter applies for all the phase variables. As the entire section deals only with the continuum-scale, unmarked notations are employed to simplify the reading of the equations. The averaged values of the extensive variables (volume, mass, energy) in the domain are obtained from the weighted sum of the superficial phase values. For example, the total density $\rho$ is given by

$$\rho = \epsilon_g \rho_g + \sum_{i=1}^{N_s} \epsilon_i \rho_i \tag{2.2}$$

where the subscript $g$ identifies the gas mixture. Intensive variables (pressure, velocity, temperature) are solved by the averaged equations and effective properties (tortuosity, permeability, conductivity) must be determined by experiments, numerical simulations, or correlations.

**For further clarity, throughout the manuscript, the solid phase is indicated with the subscript $s$; the gas mixture inside the porous material is indicated with the index $g$; the external flow, outside of the material, is indicated with the subscript $f$.**

#### 2.5.1.2 Gas Mixture: Thermodynamic Properties

The gas is assumed to be a mixture of thermally perfect gases (perfect gases whose specific heats are function of the temperature only). The total pressure of the gas mixture, $p_g$, is given by Dalton's law

$$p_g = \sum_{i=1}^{N_g} p_i \tag{2.3}$$

The single gas obeys the perfect gas law

$$p_i v_i = n_i \mathcal{R} T_i \tag{2.4}$$

where $v_i$, $n_i$, and $T_i$ identify the volume, the number of moles, and temperature of the gas $i$, respectively, and $\mathcal{R}$ is the universal gas constant. The mixture and the single gases share the same value of the specific volume, $v_i = v_g$. Moreover, the gases are supposed to be in local thermal equilibrium among themselves, $T_i = T_g$. The gas mixture obeys the perfect gas law

$$p_g v_g = n_g \mathcal{R} T_g \tag{2.5}$$

Thermodynamic properties are derived from the mixing rules: the properties of the mixture are obtained as the sum of the species properties weighted by the composition of the mixture. The composition of the mixture can be described by the molar fraction or the mass fraction. The molar fraction of a species, $X_i$, is defined as the ratio of the species number of moles $n_i$, divided by the mixture number of moles $n_g$

$$X_i = \frac{n_i}{n_g} = \frac{p_i}{p_g} \tag{2.6}$$

The mass fraction of a species, $y_i$, is defined as the ratio of the species mass divided by the total mixture mass. The definition can also be written in terms of the densities ratio

$$y_i = \frac{\rho_i}{\rho_g} \tag{2.7}$$

Once $X_i$ or $y_i$ are known, the mixing rules can be applied. Just to give a few examples, the mixture gas constant $R_g$, molar mass $\mathcal{M}_g$, specific absolute enthalpy $h_g$, specific entropy $s_g$, and specific internal energy $e_g$ are given by

$$R_g = \sum_{i=1}^{N_g} y_i R_i \tag{2.8}$$

$$\mathcal{M}_g = \sum_{i=1}^{N_g} \frac{\mathcal{M}_i}{y_i} \tag{2.9}$$

$$\rho_g h_g = \sum_{i=1}^{N_g} \rho_i h_i \tag{2.10}$$

$$\rho_g s_g = \sum_{i=1}^{N_g} \rho_i (s_i - R_i ln X_i) \tag{2.11}$$

$$\rho_g e_g = \sum_{i=1}^{N_g} \rho_i h_i - \sum_{i=1}^{N_g} p_i \tag{2.12}$$

The mixture specific heat at constant pressure $c_{p,g}$ is estimated directly from its definition

$$c_{p,g} = \Big(\frac{\partial h_g}{\partial T_g}\Big)_p \tag{2.13}$$

The knowledge of the gas composition and species thermodynamic properties is essential to recover the mixture properties. The thermodynamic properties of a single species can be evaluated (1) by functions from a given set of polynomials (NASA7 and NASA9 for examples) or (2) by partition functions. Case (1) allows a direct evaluation of the properties. Case (2) requires the introduction of concepts of statistical thermodynamics and this is beyond the scope of this work. Further details are given in the study of Scoggins and Magin, 2014 [84]. The evaluation of the gas composition follows different procedure depending on whether equilibrium or chemical non-equilibrium is assumed. This is detailed in Section 2.5.1.4 and in Section 2.5.1.5.

#### 2.5.1.3 Gas Mixture: Governing Equations

The global mass conservation equation, which is determined by the sum of the species conservation equations, reads

$$\partial_t(\epsilon_g \rho_g) + \partial_{\boldsymbol{X}} \cdot (\epsilon_g \rho_g \boldsymbol{v}_g) = -\sum_{i=1}^{N_s} \partial_t(\epsilon_i \rho_i) = \Pi + \Omega_h \tag{2.14}$$

where $\boldsymbol{v}_g$ is the convective gas velocity, and the terms on the second right-hand side account for the exchanges with the solid phases: pyrolysis $\Pi$ and heterogeneous reactions $\Omega_h$ (described in Section 2.5.1.9). The element or species conservation equations are needed in the case of chemical equilibrium or non-equilibrium. These equations are addressed in the respective sections.
The average gas velocity is obtained by solving the momentum-conservation equation. In porous media, the volume averaged momentum conservation reads

$$\boldsymbol{v}_g = -\frac{1}{\epsilon_g}\Big[\frac{1}{\mu_g}\underline{\underline{K}}\Big(1+\frac{1}{p_g}\underline{\underline{\beta}}\Big)\Big]\cdot\partial_{\boldsymbol{X}}p_g \tag{2.15}$$

where $\mu_g$ is the dynamic viscosity of the gas, $\underline{\underline{K}}$ is the permeability tensor, and $\underline{\underline{\beta}}$ the slip correction to account for slip effects. The average gas velocity can be introduced into the gas mass conservation. By using the perfect gas law, the final form of the momentum conservation reads

$$\partial_t\Big(\frac{\epsilon_g\mathcal{M}_g}{RT_g}p_g\Big)-\partial_{\boldsymbol{X}}\cdot\Big[\frac{p_g\mathcal{M}_g}{RT_g}\frac{1}{\mu_g}\underline{\underline{K}}\Big(1+\frac{1}{p_g}\underline{\underline{\beta}}\Big)\cdot\partial_{\boldsymbol{X}}p_g\Big]=\Pi+\Omega_h \tag{2.16}$$

A local thermal non-equilibrium model is considered for the energy description of the system. This means that two equations are needed to describe the mixture and the solid phases from an energy point of view. For the mixture, the energy governing equation writes

$$\epsilon_g\rho_g c_{p,g}\partial_t T_g+\sum_{i=1}^{N_g}h_i\partial_t(\epsilon_g\rho_g y_i)-\partial_t(\epsilon_g p_g)=-\partial_{\boldsymbol{X}}\cdot\Big(\epsilon_g\rho_g\boldsymbol{v}_g h_g\Big)+\partial_{\boldsymbol{X}}\cdot\Big(\underline{\underline{k}}_{\text{eff},g}\cdot\partial_{\boldsymbol{X}}T_g\Big)+$$
$$+\partial_{\boldsymbol{X}}\cdot\sum_{k=1}^{N_g}\boldsymbol{\mathcal{Q}}_k+h_v\Big(T_s-T_g\Big) \tag{2.17}$$

where $\underline{\underline{k}}_{\text{eff}}$ identifies the effective thermal conductivity tensor, $\boldsymbol{\mathcal{Q}}_k$ models heat transport by effective diffusion of the species [75], and $h_v$ is the volumetric heat transfer coefficient.

#### 2.5.1.4 Gas Mixture: Equilibrium Chemistry

In the case of equilibrium, the species conservation equations are not needed, but chemical reactions can occur in the gas phase. When these happen, the masses of the participating molecules are not conserved, while the masses of the nuclei of the chemical elements constituting the same molecules are conserved. Thus, the element conservation equations for each element in the mixture must be considered

$$\partial_t(\epsilon_g\rho_g z_k)+\partial_{\boldsymbol{X}}\cdot(\epsilon_g\rho_g z_k\boldsymbol{v}_g)+\partial_{\boldsymbol{X}}\cdot\boldsymbol{\mathcal{F}}_k=\pi_k \tag{2.18}$$

where $z_k$ identifies the $k$-element mass fraction, $\boldsymbol{\mathcal{F}}_k$ models the effective diffusion flux [75] of the $k$-element, and the term on the second hand-right, $\pi_k$, represents the pyrolysis production rate of the $k$-element.

The composition of the mixture is explicitly defined by the minimization of the specific Gibbs free energy, $g$, of the mixture. The latter, for a pure species $i$ is defined as [84]

$$g_i=h_i-s_iT_g \tag{2.19}$$

For an equilibrium mixture, the Gibbs energy is function of the local pressure and temperature only. From the definition of the Gibbs free energy, Eq. (2.19), the following form of the *law of mass action* can be derived [85] and applied to a generic chemical reaction

$$\prod_{j=1}^{N_t} p_j^{\nu_j} = k_{eq} \tag{2.20}$$

where $k_{eq}$ is the equilibrium constant rate for the given chemical reaction and is a function of the temperature only, $\prod_{j=1}^{N_t}$ denotes the product notation for all the $N_t$ reactants and products terms, $j$, in the chemical reaction; $\nu_j$ represents the stechiometric coefficient of the $j-$term. By combining the law of mass action for each reaction in the mixture, Dalton's law (Eq. (2.3)), and the element conservation equations (Eq. (2.18)), the partial pressure of each species can be obtained. The knowledge of the partial pressure is enough to recover the mixture composition (Eq. (2.6)), thus the thermodynamic properties of the gas phase. It should be remarked that, at equilibrium, the chemical composition of the reactive mixture is a function of local pressure and temperature.

#### 2.5.1.5 Gas Mixture: Non-Equilibrium Chemistry

In the case of chemical non-equilibrium, the species continuity equations must be solved

$$\partial_t(\epsilon_g \rho_g y_i) + \partial_{\boldsymbol{X}} \cdot (\epsilon_g \rho_g y_i \boldsymbol{v}_g) + \partial_{\boldsymbol{X}} \cdot \boldsymbol{\mathcal{F}}_i = \pi_i + \epsilon_g \omega_i \mathcal{M}_i \tag{2.21}$$

where the source terms in the equation are the mass production rate of the $i-$species due to pyrolysis, $\pi_i$, and the production rate of the $i-$species chemical reactions, $\omega_i$.

The species production rates due to the chemical reactions in the mixture must be estimated in order to compute the mixture composition. A generic elementary reaction $j$ characterized by $N_t$ reactants and products, can be written as

$$\sum_{i=1}^{N_t} \nu'_{ij} A_i \rightleftharpoons \sum_{i=1}^{N_t} \nu''_{ij} A_i \tag{2.22}$$

where $A_i$ represents the name of species $i$, and $\nu'_{ij}$ and $\nu''_{ij}$ are the stoichiometric coefficients of the reactants and products respectively. Any type of elementary reaction can be expressed in this form. The species production rate of this $j$-th elementary reaction writes

$$\omega_{i,j} = (\nu''_{ij} - \nu'_{ij}) \Big[ k_{fw,j} \prod_{i=1}^{N_t} [A_i]^{\nu'_{ij}} - k_{bw,j} \prod_{i=1}^{N_t} [A_i]^{\nu''_{ij}} \Big] \tag{2.23}$$

where $k_{fw,j}$ and $k_{bw,j}$ are the forward and backward chemical rate constants. These two coefficients are connected through the equilibrium constant rate $k_{eq,j}$ as follows

$$k_{bw,j} = \frac{k_{fw,j}}{k_{eq,j}} \tag{2.24}$$

The equilibrium constant rate can sometimes be obtained from experiment and can always be calculated from statistical thermodynamics [85]. An Arrhenius rate law is usually used to specify the

forward reaction rate coefficient [84]. The mixture composition is obtained by solving Eq. (2.23) for all chemical reactions.

#### 2.5.1.6 Gas Mixture: Transport Coefficients

The derivation of the dynamic viscosity, mixture thermal conductivity, and the diffusion coefficients is beyond the scope of this thesis. A library named *Mutation++* is used for their computation. More details on this are available in the study of Scoggins and Magin, 2014 [84].

#### 2.5.1.7 Solid Phase: Governing Equations

The average mass evolution for each solid phase $i$ reads

$$\partial_t(\epsilon_i \rho_i) = -\pi_i - \omega_i^h \tag{2.25}$$

where the changes in density for the solid phase $i$ are given by the pyrolysis $\pi_i$ and heterogeneous reactions $\omega_i^h$ contributions.
Under the local thermal non-equilibrium assumption, an energy conservation equation is needed for the solid phase. The equation is as follows

$$\sum_{i=1}^{N_s} \epsilon_i \rho_i c_{p,i} \partial_t T_s + \sum_{i=1}^{N_s} h_i \partial_t(\epsilon_i \rho_i) = \partial_{\boldsymbol{X}} \cdot \Big( \underline{\underline{k}}_{\text{eff},s} \cdot \partial_{\boldsymbol{X}} T_s \Big) + h_v \Big( T_g - T_s \Big) \tag{2.26}$$

It should be remarked that by assuming $T_g = T_s = T$ and summing this equation with the respective energy equation for the gas mixture (Eq. (2.17)), the local thermal equilibrium model is recovered.
The solid phase is free to deform. The assumptions of small strain and linearized elastic solid material are considered here. The governing equation is given by

$$\partial_t(\rho_s \, \partial_t(\boldsymbol{D})) = \partial_{\boldsymbol{X}} \cdot \underline{\underline{\sigma}} + \rho \boldsymbol{f} \tag{2.27}$$

where the quantities $\boldsymbol{D}$, $\underline{\underline{\sigma}}$, and $\boldsymbol{f}$ denote the displacement field, the stress tensor, and a generic volume force, respectively. The link between the stress ($\underline{\underline{\sigma}}$) and the strain ($\underline{\underline{\epsilon}}$) tensors is given by the constitutive law

$$\underline{\underline{\sigma}} = \mathbb{C} : \Big( \underline{\underline{\epsilon}} - \underline{\underline{\alpha}}(T - T_0) - \underline{\underline{\xi}}(\tau - \tau_0) \Big) \tag{2.28}$$

where $\mathbb{C}$ is the fourth order stiffness tensor [86], $\underline{\underline{\alpha}}$ and $\underline{\underline{\xi}}$ are the tensors of the thermal expansion coefficients ($\alpha$) and pyrolysis shrinkage coefficients ($\xi$), $\tau$ stands for the total advancement of the pyrolysis reactions, and the subscript 0 refers to the initial time. Assuming the solid to be isotropic, the constitutive law (Eq. (2.28)) simplifies to

$$\underline{\underline{\sigma}} = 2\mu_{sm} \underline{\underline{\epsilon}} + \lambda_{sm} tr(\underline{\underline{\epsilon}}) \underline{\underline{I}} - (2\mu_{sm} + 3\lambda_{sm}) \, \alpha \, (T - T_0) \underline{\underline{I}} - (2\mu_{sm} + 3\lambda_{sm}) \, \xi \, (\tau - \tau_0) \underline{\underline{I}} \tag{2.29}$$

where $tr()$ denotes the trace operator, $\mu_{sm}$ and $\lambda_{sm}$ are the Lame's parameters, and $\underline{\underline{I}}$ denotes the identity tensor. The subscript $sm$ corresponds to solid material. Lame's parameters are expressed in

terms of the engineering constants, i.e. the Young modulus $E_{sm}$ and the Poisson ratio $\nu_{sm}$, by the following expressions

$$\lambda_{sm} = \frac{E_{sm}\ \nu_{sm}}{(1+\nu_{sm})(1-2\nu_{sm})} \tag{2.30}$$

$$\mu_{sm} = \frac{E_{sm}}{2(1+\nu_{sm})} \tag{2.31}$$

#### 2.5.1.8 Solid Phase: Pyrolysis

Each solid phase $\mathcal{P}_i$ may decompose following several pyrolysis kinetics. It is a common practice to split each phase $i$ into $N_{p,i}$ sub-phases to model different degradation mechanisms. The decomposition of a generic sub-phase $j$ (from the solid phase $i$) leads to the production of different element/species $A_k$ according to the stoichiometric coefficients $\nu_{i,j,k}$, as follows

$$\mathcal{P}_{i,j} \longrightarrow \sum_{k=1}^{N_g} \nu_{i,j,k}\ A_k \tag{2.32}$$

Pyrolysis reactions are modeled by Arrhenius laws. Thus, the advancement of the pyrolysis reaction $\chi_{i,j}$ of sub-phase $j$ within phase $i$ is defined as

$$\partial_t \chi_{i,j} = (1-\chi_{i,j})^{m_{i,j}}\ T_s^{n_{i,j}} \mathcal{A}_{i,j}\ exp\Big(-\frac{\mathcal{E}_{i,j}}{RT_s}\Big) \tag{2.33}$$

where $\mathcal{A}$ and $\mathcal{E}$ are the pre-exponential factor and activation energy of the Arrhenius law, and $m_{i,j}$ and $n_{i,j}$ are the Arrhenius law parameters. The total advancement in the pyrolysis process, $\tau$, is evaluated as follows

$$\tau = \sum_{i=1}^{N_s}\sum_{j=1}^{N_{p,i}} \frac{\epsilon_{i,0}\rho_{i,0}y_{i,j}}{\sum_{i=1}^{N_s}\sum_{j=1}^{N_{p,i}} \epsilon_{i,0}\rho_{i,0}y_{i,j}}\ (1-\chi_{i,j}) \tag{2.34}$$

where $y_{i,j}$ is the mass fraction of sub-phase $j$ within phase $i$. The total production rate of species/element $k$ by decomposition of the solid is given by

$$\pi_k = \sum_{i=1}^{N_s}\sum_{j=1}^{N_{p,i}} \nu_{i,j,k}\ \epsilon_{i,0}\ \rho_{i,0}\ y_{i,j}\ \partial_t \chi_{i,j} \tag{2.35}$$

The overall pyrolysis-gas production rate is obtained by summing $\pi$ over all gaseous species

$$\Pi = \sum_{k=1}^{N_g} \pi_k \tag{2.36}$$

#### 2.5.1.9 Solid Phase: Heterogeneous Reactions

For elementary reactions, species production rates are given by Eq. (2.23). Non-elementary reactions may be modeled using molar density exponents that are not equal to the molecularity, or additional terms can be added, for example to account for third body reactions or pressure drop.

Heterogeneous reactions deal with elementary chemical reactions between reactive solid phases and gas species. A unified approach was proposed to deal with solid and gas species [75]. The effective molar density of a reacting solid phase $i$ may be conveniently modeled as

$$X_i = \frac{\mathcal{S}_i \Theta_i}{\epsilon_g} \tag{2.37}$$

where $\mathcal{S}_i$ and $\Theta_i$ are the specific surface and active site density of the reacting solid phase $i$. This allows introducing solid phases into the homogeneous chemical mechanism, solving homogeneous and heterogeneous finite-rate chemistry in a coupled manner, and computing the effective reaction rates with greater accuracy and numerical stability. The total mass change rate is thus the sum of all effective reaction rates

$$\Omega_h = \sum_{i=1}^{N_s} \omega_i^h \tag{2.38}$$

### 2.5.2 Micro-Scale

To fulfill the second objective, namely the derivation of the effective properties, pore-scale numerical simulations are performed. Only the relevant micro-equations are presented, as chemistry, pyrolysis, and mass transport are not taken into account. Intrinsic material properties are used at the pore-scale.

#### 2.5.2.1 Compressible Flow

No discontinuities (no shock waves, no contact surfaces, no slip lines) and no volume forces are considered in the domain. The mass, momentum, and energy conservation equations are the following

$$\begin{cases} \partial_t \rho + \partial_{\boldsymbol{x}} \cdot (\rho \boldsymbol{v}) = 0 \\ \partial_t (\rho \boldsymbol{v}) + \partial_{\boldsymbol{x}} \cdot \Big(\rho \boldsymbol{v} \otimes \boldsymbol{v} + p \underline{\underline{I}}\Big) = \partial_{\boldsymbol{x}} \cdot \underline{\underline{\tau}} \\ \partial_t (\rho e) + \partial_{\boldsymbol{x}} \cdot (\rho \boldsymbol{v} e) = -p \partial_{\boldsymbol{x}} \cdot \boldsymbol{v} + (\underline{\underline{\tau}} \partial_{\boldsymbol{x}}) \cdot \boldsymbol{v} + \partial_{\boldsymbol{x}} \cdot \Big(k \partial_{\boldsymbol{x}} T\Big) \end{cases} \tag{2.39}$$

where the local heat flux density is modeled with the Fourier law and $k$ denoted the thermal conductivity coefficient. The energy conservation is expressed in terms of the specific internal energy $e$, and $\underline{\underline{\tau}}$ is the viscous stress tensor. Under the assumption of Newtonian fluid and Stokes' hypothesis, this tensor is expressed as

$$\underline{\underline{\tau}} = \mu \Big[\partial_{\boldsymbol{x}} \otimes \boldsymbol{v} + (\partial_{\boldsymbol{x}} \otimes \boldsymbol{v})^T\Big] - \frac{2}{3} \mu (\partial_{\boldsymbol{x}} \cdot \boldsymbol{v}) \tag{2.40}$$

#### 2.5.2.2 Incompressible Flow

The assumption of incompressible flow is adopted in some chapters of the manuscript. In this case, the system of Eqs. (2.39) reduces to

$$\begin{cases} \partial_{\boldsymbol{x}} \cdot \boldsymbol{v} = 0 \\ \rho \partial_t \boldsymbol{v} + \rho \boldsymbol{v} \cdot \partial_{\boldsymbol{x}} \boldsymbol{v} - \mu_g \partial^2_{\boldsymbol{x}} \boldsymbol{v} = -\partial_{\boldsymbol{x}} p_g \\ \rho\, c_p \partial_t T + \rho\, c_p \boldsymbol{v} \cdot \partial_{\boldsymbol{x}} T = \partial_{\boldsymbol{x}} \cdot \left( k \partial_{\boldsymbol{x}} T \right) \end{cases} \tag{2.41}$$

where viscous dissipation is neglected.

#### 2.5.2.3 Solid Deformation

The solid phase is free to deform. The same assumptions and governing equations presented in Section 2.5.1.7 for the macro scale are used at the pore-scale. Under the assumption of small strain and linearized elastic solid material, the governing equation writes

$$\partial_t(\rho_s\, \partial_t(\boldsymbol{D})) = \partial_{\boldsymbol{x}} \cdot \underline{\underline{\sigma}} + \rho \boldsymbol{f} \tag{2.42}$$

The constitutive law links the stress ($\underline{\underline{\sigma}}$) and the strain ($\underline{\underline{\epsilon}}$) tensors. Assuming the solid to be isotropic, the constitutive is as follows

$$\underline{\underline{\sigma}} = 2\mu_{sm}\underline{\underline{\epsilon}} + \lambda_{sm} tr(\underline{\underline{\epsilon}})\underline{\underline{I}} - (2\mu_{sm} + 3\lambda_{sm})\, \alpha\, (T - T_0)\underline{\underline{I}} - (2\mu_{sm} + 3\lambda_{sm})\, \xi\, (\tau - \tau_0)\underline{\underline{I}} \tag{2.43}$$

where Lame's parameters are linked to the engineering constants by the following expressions

$$\lambda_{sm} = \frac{E_{sm}\, \nu_{sm}}{(1 + \nu_{sm})(1 - 2\nu_{sm})} \tag{2.44}$$

$$\mu_{sm} = \frac{E_{sm}}{2(1 + \nu_{sm})} \tag{2.45}$$

## 2.6 Main Results

The main contribution of this thesis to the modeling of reactive porous material under high enthalpy flows are highlighted in red in Fig. 2.6. This section provides a generic overview of these contributions in relation to the two objectives defined in Section 2.3. A complete presentation and description of the results can be found in the respective chapters.

### 2.6.1 First Part

The first part of the work studies the importance of two particular physical aspects in the numerical description. The two studies are carried out in Chapters 3 and 4.

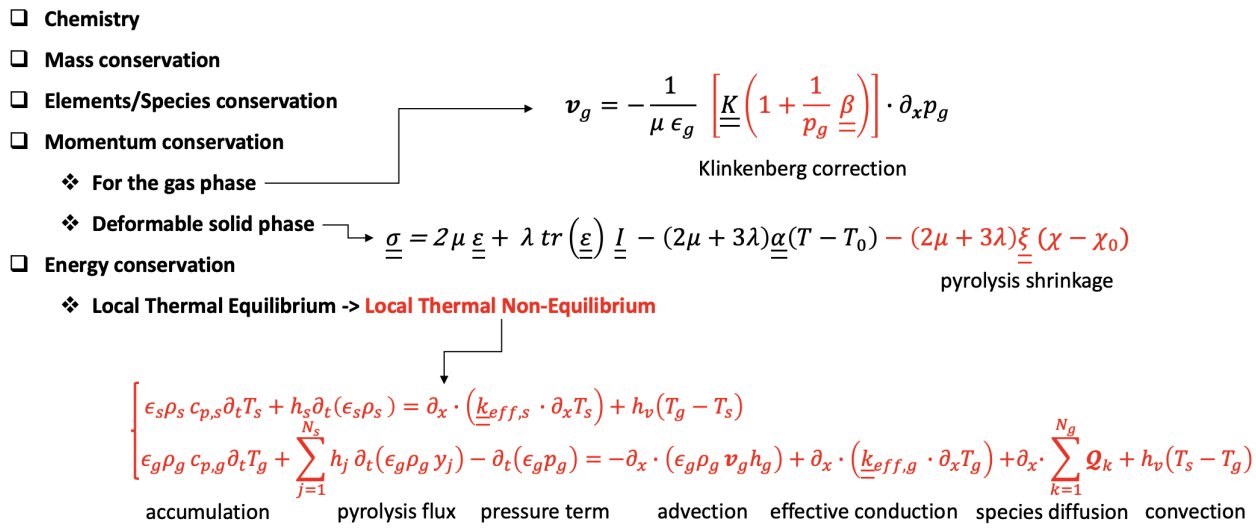


FIGURE 2.6 – Main contribution of this thesis (in red) to the modeling of reactive porous material under high enthalpy flows.

Chapter 3 investigates the assumption of Local Thermal Equilibrium (LTE) between the solid phases and the pyrolysis gases for ablative materials under typical entry conditions. This hypothesis is generically justified by the fact that the thermal Peclet number within the pores is small. The thermal Peclet number is a dimensionless number that quantifies the ratio of the rates of the processes of advection and thermal diffusion

$$Pe = \frac{\rho_g\,c_p\,|\langle\boldsymbol{v}_g\rangle|\,l}{k} \tag{2.46}$$

$Pe \ll 1$ is a necessary condition for thermal equilibrium in non-reactive materials. However, the validity of this analysis may fall under some circumstances. The thermal Peclet number may become large due to high pyrolysis gas velocities, or additional physical phenomena not accounted for in the Peclet analysis may become non-negligible, such as the change of enthalpy due to chemical reactions. A Local Thermal Non-Equilibrium (LTNE) model is applied to the Theoretical Ablative Composite for Open Testing (TACOT) under a wide range of conditions to assess the true range of validity of the thermal equilibrium hypothesis. 1D simulations are performed on the Stardust and Mars Science Laboratory atmospheric entry missions. Local thermal equilibrium and local thermal non-equilibrium energy models are adopted. The comparison between the two models is carried out by monitoring the temperature evolution within the material, pyrolysis gas blowing rate, pyrolysis zone, wall recession due to ablation, and the species concentrations within the material. Same conclusions hold for both mission cases. Results for the Stardust case are reported in Fig. 2.7 for the chemical equilibrium case and in Fig. 2.8 for the chemical non-equilibrium case. No significant deviation in the monitored quantities is observed under chemical equilibrium conditions. In the case of chemical non-equilibrium, instead, a small difference in the temperature prediction between the two thermal models is sufficient to change the evolution of the species concentrations within the material.

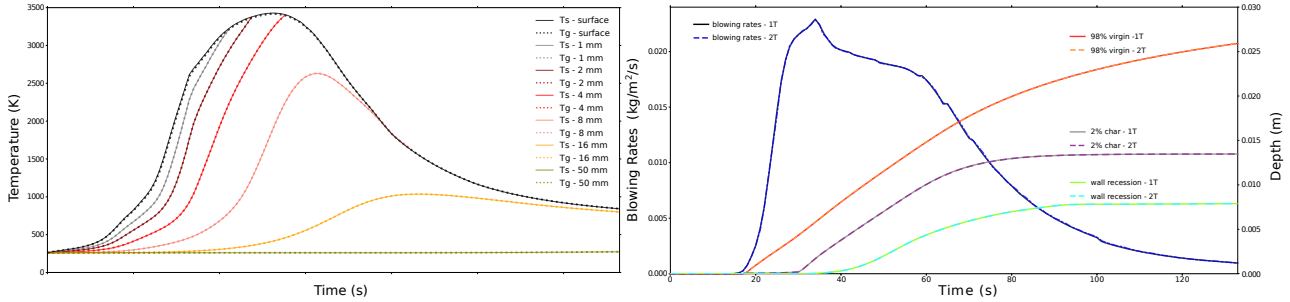


FIGURE 2.7 – Stardust case. Thermocouple data, blowing rates, pyrolysis zone, and wall recession over time.

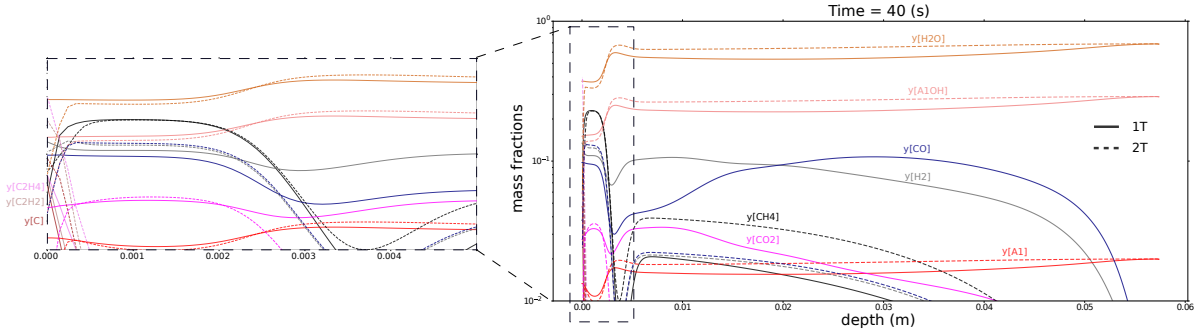


FIGURE 2.8 – Stardust case. Species distribution within the material at time t = 40 s. At the left: a zoom of the mass fractions near the surface with the external environment.

The numerical simulation of fire propagation requires capturing the coupling between wood pyrolysis, which leads to the production of various gaseous species, and the combustion of these species in the flame, which produces the energy that sustains the pyrolysis process. As can be seen in Fig. 2.5, with the exception of PATO, no response code provides for direct material-external flow coupling. Chapter 4 proposes a multi-physical simulation where material and external flows are directly coupled, resulting in the ability of the code to capture different physical phenomena. The numerical framework couples the detailed three-dimensional pyrolysis model of PATO with fireFoam. The capability of the simulation tool is illustrated on the the combustion of a wood log. Results, which are partially reported in Fig. 2.9, highlight how the evolution of the flame and its temperature during the simulation are affected by the concentration of the gaseous species produced in the material. The coupling effect affects the wood log as well: due to the flame and temperature rise, the pyrolysis process accelerates and the concentrations of species change according to the speed of the reactions. The simulation is able to capture the whole pyrolysis process, until the complete charring of the wood and the resulting extinguishment of the fire. Moreover, the puffing effect is observed during the evolution of the simulation: the fire exhibits periodic fluctuations that follow each other with a numerical frequency that is approximately the same as the theoretical one.

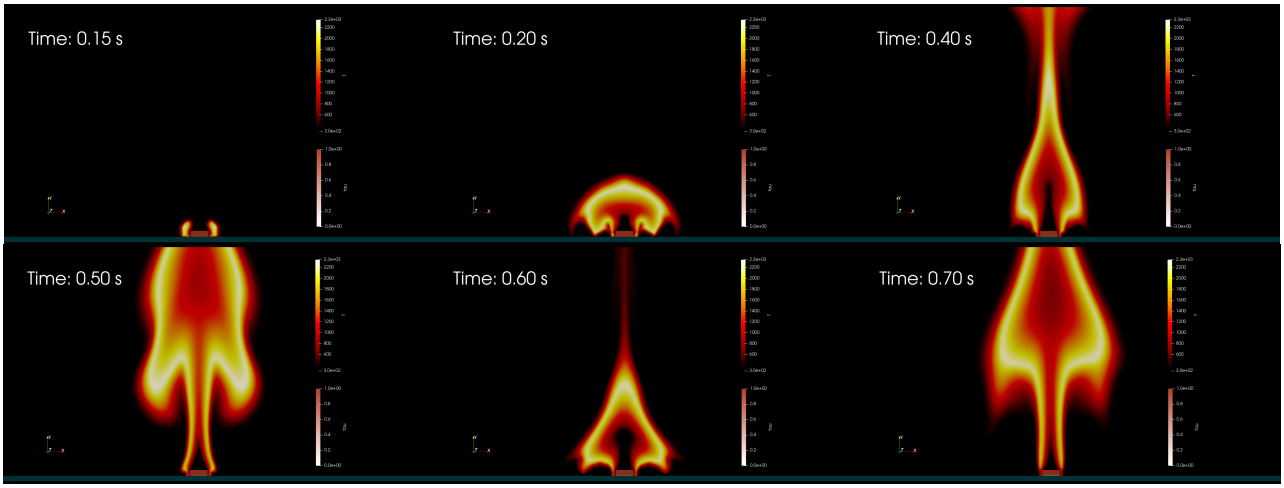


FIGURE 2.9 – Combustion of a wood log. Six different snapshots representing the initial evolution of the fire on the wood log.

### 2.6.2 Second Part

The effective macroscopic properties play a fundamental role in the continuum model, as highlighted in the first part of the thesis: in Chapter 3 the analysis of the LTNE model is strictly related to the value chosen for the volumetric heat transfer coefficient $h_v$; in Chapter 4 the advancement of the pyrolysis process, thus the behaviour of the flame, are strictly connected to the value chosen for the permeability tensor, $\underline{\underline{K}}$. The second part of the work aims to establish and validate numerical strategies to estimate the effective properties in the generic case of non-periodic anisotropic porous media. To this end, four complementary studies are carried out in Chapters 5, 6, 7 and 8. The concept map of these studies is showed in Fig. 2.10. Chapter 5 is the starting point of the analysis, which

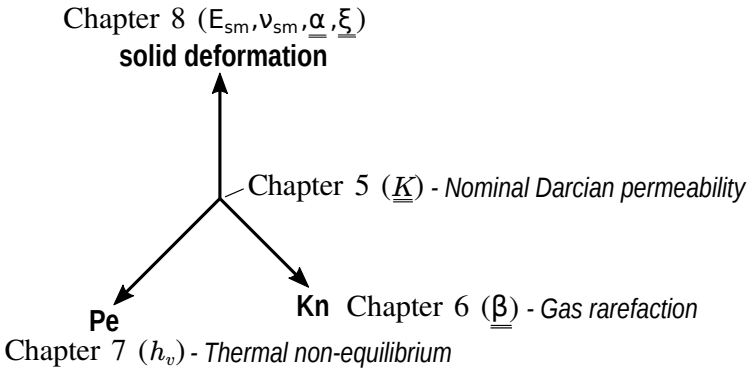


FIGURE 2.10 – Concept map of the studies in the second part of the manuscript.

considers creeping, continuum, and isothermal flows interacting with rigid non-reactive solid matrices. Under these conditions, the permeability tensor, $\underline{\underline{K}}$, is the only effective property to characterize at the macro-scale. From this starting point, the other chapters are introduced by considering more general

conditions for the flow and solid phases. Chapter 6 extends the analysis for rarefied flows in the slip regime. A dimensionless number is introduced. The Knudsen number is defined as the ratio of the mean free path $\lambda$ over the flow characteristic length $l$

$$Kn = \frac{\lambda}{l} \tag{2.47}$$

This dimensionless number represents the importance of the rarefaction effect. The higher its value, the greater the rarefaction effect. In the slip regime, $0.01 < Kn < 0.1$, the micro and macro scales descriptions are slightly modified. At the micro-scale a slip boundary condition for the velocity field must be added, while at the continuum scale the slip correction tensor, $\underline{\underline{\beta}}$, must be defined. Chapter 7 considers non-isothermal flows. Three different effective properties are introduced in the analysis: the fluid and solid thermal conductivity tensors, $\underline{\underline{k}}_{\text{eff}}$, and the volumetric heat transfer coefficient, $h_v$. Only the latter is investigated in the study and numerically defined for different values of the thermal Peclet number (Eq. (2.46)) ranging from 0 to 1000. Chapter 8 generalizes the problem for deformable solid phases. The analysis of the effective properties is enriched with the Young modulus $E_{sm}$, Poisson ratio $\nu_{sm}$, thermal expansion tensor $\underline{\underline{\alpha}}$, and the pyrolysis shrinkage tensor $\underline{\underline{\xi}}$. Each chapter performs an in-depth analysis on the different numerical methods to estimate the effective properties, paying particular attention to the effects of the boundary conditions on the numerical results. To fulfill the objective and consolidate the analysis for generic non-periodic anisotropic porous media, the resulting numerical strategies are applied to the two high-resolution 3D Computed Micro-Tomography (CMT) images showed in Fig. 2.11. The domain (a) is a sample of virgin Calcarb [87], a carbon fiber preforms

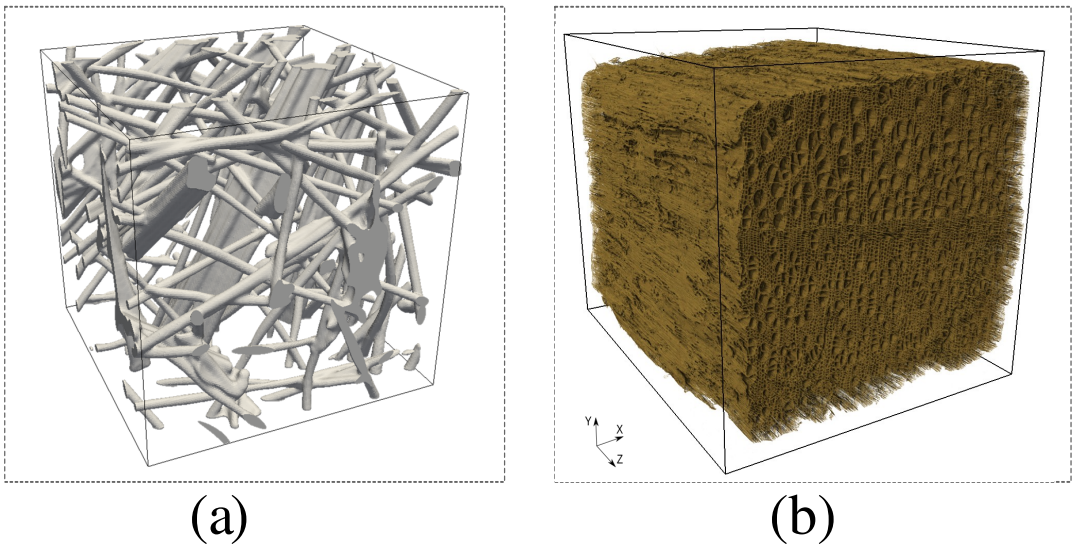


FIGURE 2.11 – High-resolution 3D tomography images considering for the determination of the effective properties. The Calcarb domain (a) is analyzed in Chapters 5, 6, and 7. The hard-wood match domain (b) is considered in Chapter 8.

used as skeleton in heat-shield materials [68, 69, 88]. The domain (b) is a section of a hard-wood

match. The permeability tensor of domain (a) is determined in Chapter 5. Written with respect to the principal axes, the tensor is as follows

$$\underline{\underline{K}} = \begin{bmatrix} 1.74\ 10^{-10} & 0 & 0 \\ 0 & 1.49\ 10^{-10} & 0 \\ 0 & 0 & 1.11\ 10^{-10} \end{bmatrix} m^2 \tag{2.48}$$

A relative difference around 42 % is found with respect to the prediction obtained by Borner et al, 2017 [9]. This difference is attributed to the different working hypotheses: while Chapter 5 determines the full tensor, the work of Borner et al, 2017 [9], assumes the permeability tensor to be initially aligned with the principal axes and characterized by equal in-plane components. The slip correction tensor of domain (a) is determined in Chapter 6. Written with respect to the principal axes, the tensor is as follows

$$\underline{\underline{\beta}} = \begin{bmatrix} 971.5 & 0 & 0 \\ 0 & 948.1 & 0 \\ 0 & 0 & 901.4 \end{bmatrix} Pa \tag{2.49}$$

A relative difference around 8 % is found with respect to the prediction obtained by Borner et al, 2017 [9], where the same assumptions made for the permeability tensor hold for the slip correction tensor. The volumetric heat transfer coefficient of domain (a) is determined in Chapter 7 under the same conditions defined experimentally by Liu et al., 2022 [89]. The coefficient is found to be $h_v = 1.6\ 10^8\ Wm^{-3}K^{-1}$, while the value found in the experimental analysis is $h_v = 10^9\ Wm^{-3}K^{-1}$. The two values differ by an order of magnitude. Several reasons may lead to this difference: the Calcarb dataset considered for the numerical simulation is too small and not representative; the numerical value assigned to the effective conductivity tensor is not considering for the dispersion and tortuosity effects; the value of $h_v$ is so high that a local thermal equilibrium is achieved between the two phases, making its experimental estimation rather complex. The thermoelastic-pyrolysis mechanical deformation of a cross section in the $xy$ plane of domain (b) is characterized in Chapter 8. The resulting numerical deformation is compared with the deformation undergone experimentally by the same slice after a complete pyrolysis. This comparison is showed in Fig. 2.12. Due to the isotropic assumption, the original square shape is preserved. Despite this difference in the final shapes, the numerical model is able to predict the value of the final surface area with a relative error of 4.1%.

The determination of the effective properties is not the only result achieved. Different physical analysis and observations are carried out in the second part of the manuscript.
Chapter 5 addresses the issue of defining a physical limit to the validity of the flow creeping regime hypothesis. This limit is usually measured in terms of the Reynolds number, a dimensionless number that characterizes the relative importance of inertial and viscous forces within a fluid

$$Re = \frac{\rho_g |\langle \boldsymbol{v}_g \rangle| l}{\mu_g} \tag{2.50}$$

For $Re \ll 1$, viscous forces dominate and the flow is said to be in the creeping regime [90, 91]. This criterion is too generic and it depends on the chosen value for the characteristic length. This choice is

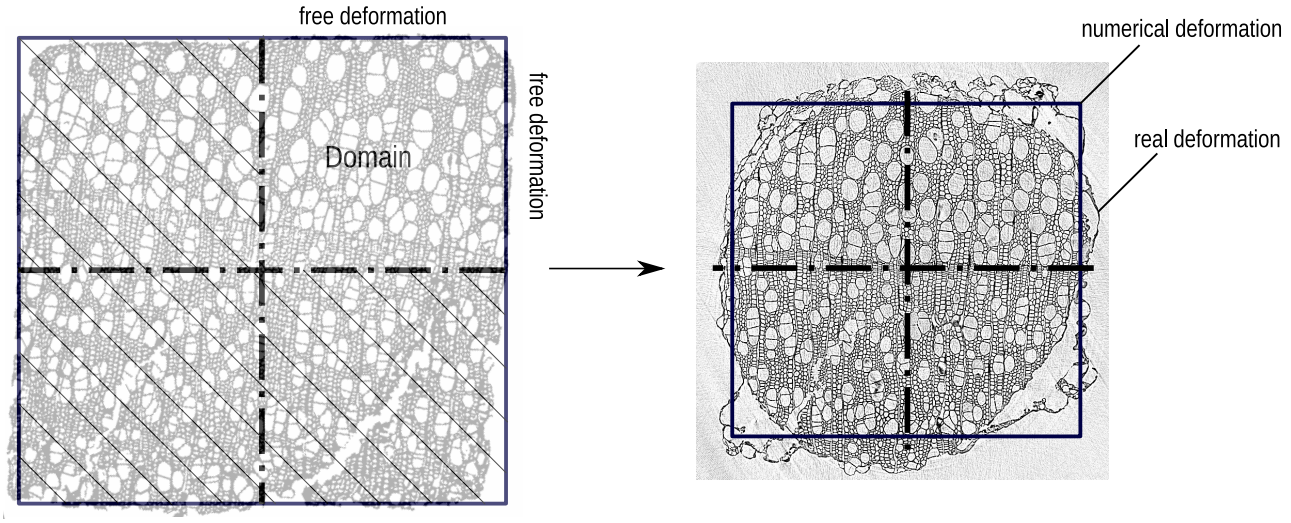


FIGURE 2.12 – Pyro-mechanical deformation of a 2D slice of domain (b) in the $xy$ plane. The resulting numerical deformation is compared with the actual deformation undergone experimentally by the same cross section after a complete pyrolysis.

not trivial as porous micro-structures are very diverse and better characterized by different lengths. For this reason, Chapter 5 defines a new criterion for delimiting the creeping regime based on the vorticity field, $\boldsymbol{\omega}$, which describes the tendency of a flow to rotate

$$\boldsymbol{\omega} = \partial_{\boldsymbol{x}} \times \boldsymbol{v} \tag{2.51}$$

For an incompressible flow, the velocity gradients at the boundaries generates the vorticity, which then diffuses over the entire domain. Due to the linear behaviour of the velocity, the vorticity increases proportional to the magnitude of the velocity in the creeping regime. However, as soon as the creeping regime falls, non-linearities in the velocity field change this simple trend. The criterion consists of keeping under observation the dimensionless vorticity, defines as

$$\boldsymbol{\omega}^* = \boldsymbol{\omega} \frac{\ell}{\langle v \rangle} \tag{2.52}$$

whose mean value remains constant in the creeping regime. One of the main advantages of this method is the fact that it is possible to identify in the domain the area where the vorticity presents its maximum values, that is, where non-linearity effects affect more the flow. This criterion is applied to characterize the high-resolution 3D Computed Micro-Tomography (CMT) of Calcarb showed in Fig. 2.11. The area influencing the behaviour of the flow inside the whole domain is reported in Fig. 2.13. This area is characterized by a characteristic length $l_{cl} \sim 80\ \mu m$. Thus, the physical limit of the creeping regime for the Calcarb dataset is found to be

$$Re_{cl} < 0.5 \longrightarrow \text{creeping regime}$$

Chapter 6 emphasizes the importance of considering the slip regime in the framework of TPS design. This aspect is highlighted in Fig. 2.14, where the entry trajectories of the Stardust [92] and Mars

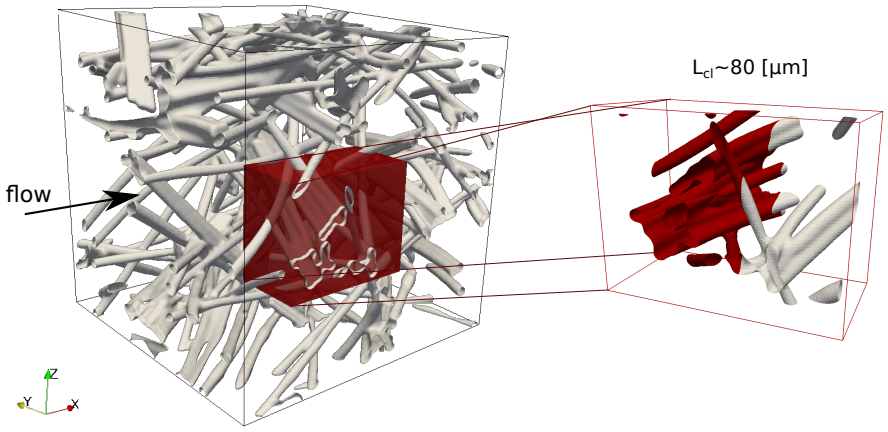


FIGURE 2.13 – Calcarb dataset characterized in Chapter 5. The red box highlights a small area influencing the behaviour of the flow inside the whole domain.

Science Laboratory [93] (MSL) missions are considered. It is possible to observe how, during these entry trajectories, different rarefaction regimes are crossed by the flow dynamics in the porous medium. Within the material, the temperature of the gas mixture decreases to values around 273 $K$, while the pressure can be considered constant. The two highlighted areas (blue for Stardust and red for MSL) give an indication of the rarefaction regimes crossed by the flow dynamics within the TPS. The figure shows that, for both missions, the continuum ($Kn < 0.01$) regime is partially crossed by the material when the heating conditions reach their peak. A larger part of the trajectories is covered by the slip regime ($0.01 < Kn < 0.1$). From Fig. 2.14, it is possible to conclude that the set of slip and continuum regimes is able to fully cover the part of the entry trajectories characterized by ablation effects.
Chapter 7 proposes a new definition of the volumetric heat transfer term coefficient able to generically account for anisotropic effects

$$h_v = \langle \boldsymbol{v}_g \rangle^T \cdot \underline{\underline{h}}_v \cdot \langle \boldsymbol{v}_g \rangle \ \frac{1}{||\boldsymbol{v}_g||^2} \tag{2.53}$$

where a volumetric heat transfer tensor, $\underline{\underline{h}}_v$, is introduced. When $x$, $y$, and $z$ correspond to the principal axes, $\underline{\underline{h}}_v$ reduces to a diagonal tensor

$$\underline{\underline{h}}_v = \begin{bmatrix} h_{v,x} & 0 & 0 \\ 0 & h_{v,y} & 0 \\ 0 & 0 & h_{v,z} \end{bmatrix} \tag{2.54}$$

where $h_{v,x}$, $h_{v,y}$, and $h_{v,z}$ are the volumetric heat transfer coefficients when the velocity is aligned with the $x$, $y$, and $z$ directions respectively. This definition is applied to characterize the anisotropic effects for a periodic square cell-centered array with porosity $\epsilon = 0.5$. Results are showed in Fig. 2.15, where for different Peclet numbers, the averaged velocity vector is made rotating in the $xy$ plane. $\theta$ defines the angle between the average velocity vector and the x-axis. In this case, Eq. (2.53) reduces to

$$h_v = cos^2(\theta) \ \ h_{v,x} + sin^2(\theta) \ \ h_{v,y} \tag{2.55}$$

Results show that the volumetric heat transfer tensor is able to capture the shape of the anisotropic behaviour, but not exactly its amplitude, which seems to depend on the Peclet number. For $Pe =$

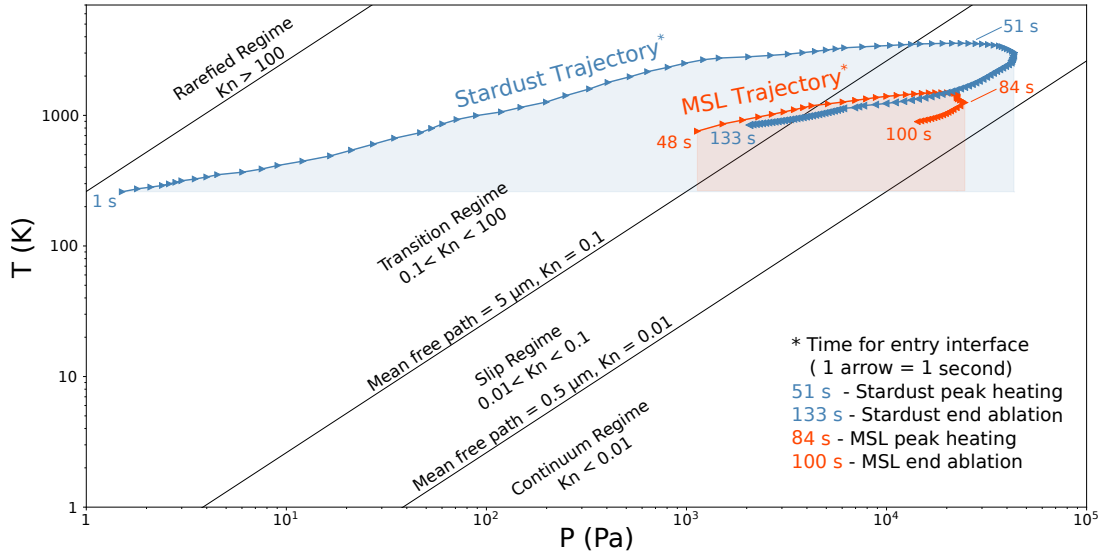


FIGURE 2.14 – Rarefied flow regimes encountered along the Stardust and MSL entry trajectories within the porous medium. Wall temperature-pressure values are taken at the stagnation point along the entry trajectories.

66.7, the correlation perfectly captures the anisotropic effects. In the figure, a linear variation of the coefficient as a function of $\theta$ is also represented. It can be seen that the tensorial formulation of the property leads to a good capturing of the anisotropy effects.
Chapter 8 derives a physical *pyrolysis-shrinkage* function to account for the pyrolysis contribution on the displacement field. The derivation of this function is based on the idea of writing the contribution of pyrolysis to the deformation field in the same form as the thermal one, as both contributions lead to volumetric deformations. The pyrolysis-shrinkage function is defined as

$$\xi = \frac{1}{3}\frac{V_0 - V_{\text{end}}}{V_0} \tag{2.56}$$

The value of $\xi$ has to be defined from experimental observations.

## 2.7 Conclusions and Perspectives

### 2.7.1 Achievements

Various technologies and engineering applications are centered on porous materials. In this work, attention is oriented towards the subset of reactive porous materials interacting with high-temperature flows, a theme of great relevance particularly for the biomass, space, and fire-safety communities. The objective of this PhD project was to contribute to the development of a generic theoretical and numerical framework to assess and model mass, momentum, and heat exchanges between an elastic and reactive solid structure interacting with a high temperature flow. The study consisted of two interre-

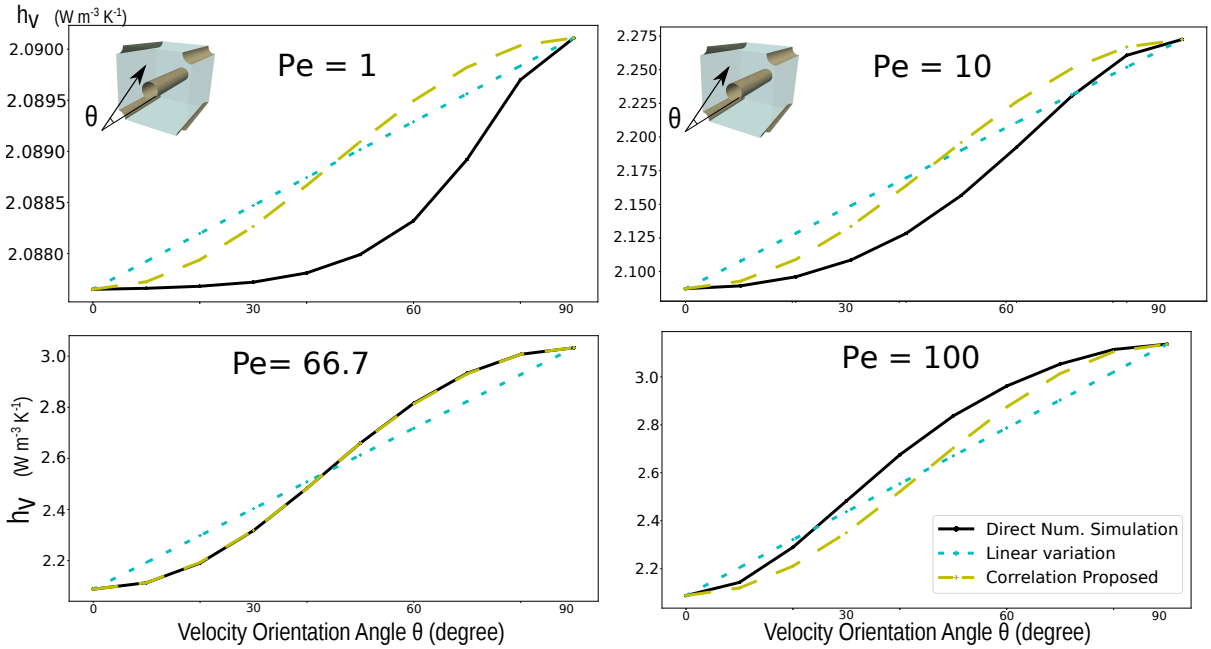


FIGURE 2.15 – Estimation of the anisotropy effects for the 2D periodic array of 5-cylinders case. A constant porosity $\epsilon = 0.5$ and different Peclet numbers are considered. The volumetric heat transfer tensor captures the shape of the anisotropic behaviour, but not its amplitude.

lated parts relying on a multi-scale approach: (1) multi-physical numerical simulations are performed on a macroscopic scale to investigate the impact of some physical effects in the numerical description; (2) direct numerical simulations are carried out at the microscopic scale on digitalized images to define numerical strategies for the evaluation of the effective properties.

The first part of the work aimed investigating, at the continuum scale, the effects on the numerical results of the local thermal equilibrium assumption and the decoupled material-external flow description. The analysis focused on two specific applications: the design of a TPS for space vehicle and the description of fire propagation. For the case of ablative materials under typical entry conditions, results show that under chemical equilibrium, the local thermal equilibrium model is able to correctly predict the evolution of the design parameters within the material. However, under chemical non-equilibrium, the local thermal equilibrium assumption loses its accuracy in capturing the species distribution within the material. For the second application, the burning of a wood log was considered. Results show that the numerical simulation of fire propagation requires capturing the coupling between wood pyrolysis and combustion of different gaseous species. The assumption of a decoupled material-external flow description is strong as the two regions highly influence one another: the evolution of the flame and its temperature are affected by the concentration of the gaseous species produced in the material, and at the same time, due to the flame and temperature rise, the pyrolysis process accelerates and the concentrations of species change according to the speed of the reactions.

The second part of the work focused on defining numerical strategies based on Pore-Scale Numerical Simulation (PS-NS) to accurately predict the effective properties. The importance of this analysis lies

in the fact that the accuracy of macroscopic models depends on the precision with which the effective properties are determined, and the literature does not provide a complete numerical methodology. To this end, a in-depth analysis was conducted to define numerical strategies. The term numerical strategy refers to the definition of the numerical domain and the set of boundary conditions, the selection of governing equations and the specification of the numerical operation to determine a specific effective property. As effective properties, the permeability tensor, slip correction tensor, volumetric heat transfer coefficient, Young modulus, Poisson's ratio, and the thermal expansion and pyrolysis correction terms were considered. The numerical strategies were defined on simple test-cases, validated with literature results, and applied to the characterization of two high-resolution 3D Computed Micro-Tomography (CMT) images, the Calcarb and the white pine dataset.

### 2.7.2 Perspectives

This work is a contribution to the on-going effort of three communities to better describe the interactions between pyrolysing materials and high-temperature flows. Ordered according to the topics covered in the six articles, the main perspectives are now presented.

Chapter 3 addresses the analysis of the entry process into planetary atmospheres. The work highlights a particular lack of reliable chemical mechanisms. With a view to more realistic modeling, greater efforts must be placed on the development of non-equilibrium chemistry models.

Chapter 4 proposes the analysis of a wood log combustion by implementing and employing a coupled material-external flow code. Despite the advanced nature of the simulation, different physical aspects have been neglected. The solid phase is considered rigid, radiation is not taken into account, combustion is modeled with a simplified laminar finite rate model, and the pyrolysis mechanism is described with a basic multi-component single reactions model.

Chapter 5 investigates the direct proportionality between the flow rate and the pressure gradient of creeping and continuum flows. Chapter 6 extends the study to $0.1 < Kn < 0.01 <$ to account for rarefied effects in the slip regime. The extension to high Reynolds numbers is missing to complete the analysis, i.e., to investigate how the proportionality between flow rate and pressure gradient changes due to inertial effects.

Chapter 7 focuses on the evaluation of the volumetric heat transfer coefficient by making two main assumptions. Incompressible flows are assumed, that is the thermodynamics is not considered and constant variables are assumed in the domain. This is a strong assumption with respect to the applications of interest, where temperatures may reach thousands of degrees and compressible flows must be considered. The second assumption concerns the effective thermal conductivity tensor. This property is defined only in terms of molecular diffusion, while the effects of dispersion and tortuosity are neglected in the study. The numerical determination of the thermal conductivity tensor requires the

definition of a new numerical strategy.

Chapter 8 extends the analysis to deformable solid phases. The study is based on the assumptions of small strain, linearized elastic solid material, and isotropic materials. These are very strong assumptions considering that the main application concerns wood deformation. The extension to orthotropic models and plasticity behaviours must now be considered.

# Part I

# Multi-Physical Simulations

# Chapitre 3

# Two-Temperature Ablative Material Response Model With Application to Stardust and MSL Atmospheric Entries

**Nomenclature**

*Latin Letters*

| | |
|---|---|
| $\mathcal{A}$ | Arrhenius law pre-exponential factor $[s^{-1}]$ |
| $A$ | generic element/species |
| $C_H$ | surface heat transfer coefficient $[kg\ m^{-2}\ s^{-1}]$ |
| $c_p$ | specific heat at constant pressure $[J\ kg^{-1}\ K^{-1}]$ |
| $d_p$ | mean pore diameter $[m]$ |
| $\mathcal{E}$ | Arrhenius law activation energy $[J\ mol^{-1}]$ |
| $e$ | specific internal energy $[J\ kg^{-1}]$ |
| $\boldsymbol{\mathcal{F}}$ | effective diffusion flux $[kg\ m^{-2}\ s^{-1}]$ |
| $h$ | specific absolute enthalpy $[J\ kg^{-1}]$ |
| $h_v$ | volumetric heat transfer coefficient $[W\ m^{-3}\ K^{-1}]$ |
| $\underline{\underline{k}}_{\text{eff}}$ | effective thermal conductivity tensor $[W\ m^{-1}\ K^{-1}]$ |
| $\underline{\underline{K}}$ | permeability tensor $[m^2]$ |
| $\mathcal{M}$ | molar mass $[kg\ mol^{-1}]$ |
| $m, n$ | Arrhenius law parameters |
| $N_g$ | number of gaseous species |
| $N_{p,i}$ | number of sub-phases in the solid phase $i$ |
| $N_s$ | number of solid phases |
| $\mathcal{P}_i, \mathcal{P}_{i,j}$ | solid phase $i$ and sub-phase $j$ of solid phase $i$ |
| $p$ | macro-scale pressure $[Pa]$ |
| $\boldsymbol{\mathcal{Q}}$ | effective diffusion heat flux $[J\ m^{-2}\ s^{-1}]$ |

## Nomenclature

| | |
|---|---|
| $R$ | specific perfect gas constant $[J\ mol^{-1}\ K^{-1}]$ |
| $t$ | time $[s]$ |
| $T$ | macro-scale temperature $[K]$ |
| $\boldsymbol{v}$ | macro-scale velocity $[m\ s^{-1}]$ |
| $\boldsymbol{x}$ | position vector $[m]$ |
| $y, z$ | species and element mass fraction |

*Greek Letters*

| | |
|---|---|
| $\underline{\underline{\beta}}$ | Klinkenberg correction tensor $[Pa]$ |
| $\Delta$ | relative difference |
| $\epsilon$ | volume fraction |
| $\mu$ | dynamic viscosity $[Pa\ s]$ |
| $\nu$ | stoichiometric coefficient |
| $\pi_k$ | pyrolysis mass production rate of element/species $k$ $[kg\ m^{-3}\ s^{-1}]$ |
| $\Pi$ | global mass production rate of the pyrolysis reactions $[kg\ m^{-3}\ s^{-1}]$ |
| $\rho$ | macro-scale density $[kg\ m^{-3}]$ |
| $\chi_{i,j}$ | advancement of the pyrolysis reaction of sub-phase $j$ within phase $i$ |

*Subscripts and Superscripts*

| | |
|---|---|
| 0 | initial time |
| $c, v$ | char and virgin |
| eff | effective |
| $g$ | gas |
| $i, j, k$ | indexes used in the sum operator |
| $s$ | solid |
| tot | total |
| $w$ | wall |

*Adimensional Groups*

| | |
|---|---|
| Pe | thermal Peclet number |

*Acronyms*

| | |
|---|---|
| LTE | Local Thermal Equilibrium |
| LTNE | Local Thermal Non-Equilibrium |
| MSL | Mars Science Laboratory |
| PATO | Porous material Analysis Toolbox based on OpenFoam |
| REV | Representative Elementary Volume |
| TACOT | Theoretical Ablative Composite for Open Testing |
| TPS | Thermal Protection System |

## Preamble

Authors: H. Scandelli; A. Ahmadi-Senichault; J. Lachaud;
Affiliations: Arts et Métiers Institute of Technology, Univ. Bordeaux, CNRS, Bordeaux INP, I2M, UMR 5295, F-33400 Talence, France;
Published: Yes, but for a different version of the work entitled "*Two-Temperature Ablative Material Response Model with Application to Low-Density Carbon Phenolic Ablators*". Current version to be submitted to *Aerospace Science and Technology*;
Journal: Conference proceedings;
Published: 2 June 2022;
Conference: This work has been presented at the 2nd International Conference on Flight Vehicles, Aerothermodynamics and Re-entry Missions & Engineering (FAR) - Heilbronn (Germany);

## Abstract

Ablative material response codes currently in use consider local thermal equilibrium between the solid phases and the pyrolysis gases. For typical entry conditions, this hypothesis may be justified by the fact that the thermal Peclet number within the pores is small, which is a necessary condition for thermal equilibrium in non-reactive materials. However, the validity of this analysis may fall under some circumstances. The thermal Peclet number may become large due to high pyrolysis gas velocities. Additional physical phenomena not accounted for in the Peclet analysis may become non-negligible, such as the change of enthalpy due to chemical reactions. The objective of this study is two-fold. First, a detailed two temperature material response model for porous reactive materials is presented. This model has been implemented and made available in the Porous material Analysis Toolbox based on OpenFOAM (PATO). Second, the model is applied to the Theoretical Ablative Composite for Open Testing (TACOT) in a wide range of conditions to assess the true range of validity of the thermal equilibrium hypothesis. Simulations are carried out on the Stardust and Mars Science Laboratory (MSL) atmospheric entries. The main design variables have been monitored and compared between the two models: temperature evolution and species concentration within the material, pyrolysis gas blowing rate, extension of the pyrolysis zone, and wall recession due to ablation. Results show that under chemical equilibrium conditions, no significant deviation in the monitored quantities are observed, while under chemical non-equilibrium conditions there is a large impact on the species concentration.

**Keywords**: Local Thermal Non-Equilibrium; Chemical Non-Equilibrium; Thermal Protection System; TACOT; Stardust and MSL missions.

## 3.1 Introduction

Extra-orbital missions often involve the analysis of entry processes into planetary atmospheres at hypersonic speeds. Under these conditions, a high enthalpy curved detached shock (bow shock) forms in front of the spacecraft and the kinetic energy is progressively dissipated into heat. Convection of this flow around the capsule and radiation progressively heat the material. The temperature at the surface of the material can increase to approximately 3000 $K$ for severe entry conditions. To ensure the integrity of the structure, a thermal protection system (TPS) is designed to absorb and dissipate the heat through phase changes, chemical reactions, and material removal. Charring ablative materials represent a traditional approach to thermal protection [68, 69]. A famous example is the new class of phenolic impregnated ablators (PICA [70], PICA-X, ASTERM [71]) that consists of a carbon fiber preform partially impregnated with phenolic resin, resulting in very light weight, good insulation, and high mechanical strength. When heated, the resin thermally decomposes and progressively carbonizes, losing mass and releasing pyrolysis gases. These gases percolate and diffuse towards the surface, reacting with each other (homogeneous reactions) and with the solid phases (heterogeneous reactions). Once at the surface, the gases are blown into the flow-field boundary layer, changing its composition. The blowing also induces a blockage of the convective heat flux impinging on the surface of the spacecraft, thus reducing the thermal load. In addition, the heat shield surface is ablated due to the occurrence of heterogeneous chemical reactions between the gas mixture and the surface (vaporization, sublimation, oxidation) [96].
Engineering design tools must be able to correctly predict the in-depth temperature experienced by the internal structure of the vehicle as well as the total recession of the material. As described above, an atmospheric entry involves a wide range of phenomena, which makes the development of these tools challenging. This leads to the introduction of assumptions into the design models in order to simplify the description. It is therefore important to check the accuracy of these assumptions in the assessment of the efficiency of the ablator, to avoid unnecessarily increasing the safety margin in the design process. In particular, two assumptions are considered: (1) Local Thermal Equilibrium (LTE) between the gas phase and the ablative material, meaning the gas temperature accommodates to the solid one within the pores. It follows that, from an energy point of view, only one governing equation is enough to model the ablative material. According to Puiroux et al. [97], this assumption can generically be considered true as long as the Peclet number for heat diffusion inside the pores is small ($Pe \ll 1$). In the case of entry flow conditions, the small pore size ($d_p < 100\ \mu m$) and the slow pyrolysis gas flow ($v_g \sim 1\ m/s$) ensure the condition to be true. However, the validity of this analysis may fall under some circumstances. The thermal Peclet number may become large due to high pyrolysis gas velocities, or additional physical phenomena not considered in the non-dimensional number may turn out to be non-negligible, such as strong change of enthalpy due to chemical reactions. Under these circumstances, a Local Thermal Non-Equilibrium (LTNE) model, i.e. two energy equations, would be necessary to accurately characterize the temperature of the gas. The importance of this aspect lies in the fact that the chemical reactions taking place in the mixture are strongly affected by the temperature of the gas. The use of LTE models, when inappropriate, may lead to an incorrect description of the gas phase.

(2) Chemical equilibrium is assumed in the gas mixture. Although this may be acceptable for the numerical description at the surface and in the boundary layer, it is strongly believed that the assumption decays for colder mixtures within the material. A first nonequilibrium mechanism has been proposed by April and Pike, 1971 [1], after matching numerical results with experimental ones. The mechanism features 11 species and 10 chemical reactions, strongly simplifying the reality. This may lead to unsatisfactory results, as already observed in the literature [98]. Due to the lack of well founded mechanism available in the literature, some authors used the reduced 22-species homogeneous finite-rate chemical mechanism derived from the combustion database of Blanquart [99], even thought its validation has not been proved in the context of ablative materials.
The objective of this study is two-fold. First, a detailed two temperature material response model for reactive porous materials is detailed. This model has been implemented and made available in the Porous material Analysis Toolbox based on OpenFOAM (PATO). Its numerical description is presented in Section 3.2. Secondly, in Section 3.3, the model is applied to the Theoretical Ablative Composite for Open Testing (TACOT) in a wide range of conditions to assess the true range of validity of the thermal equilibrium hypothesis. Simulations are carried out on the Stardust and Mars Science Laboratory (MSL) atmospheric entries with both chemical equilibrium and non-equilibrium conditions. Finally, conclusions are drawn in Section 3.4.

## 3.2 Numerical Model

The material response code, PATO, has been implemented and validated over the last decade [73–75]. In what follows, a short review of its main assumptions and governing equations is presented. We invite the reader to refer to the cited articles for more details.

### 3.2.1 Main Assumption

The model provides the numerical description of the interaction between a multi-phase reactive material ($N_s$ solid phases) with a multi-species reactive gas mixture ($N_g$ gaseous elements/species). Any liquid phase present in the ablative material (such as water) is modelled as a solid static phase. The numerical description is carried out at the macro-scale. The governing equations are derived from upscaling theories [15,16,100], relying on the existence of a Representative Elementary Volume (REV) of the domain and on the assumption of scales separation. The specific choice of the upscaling theory is not critical, as all approaches lead to equivalent results, provided the same physical hypotheses and level of mathematical approximations [17]. As the entire section is aimed at the macro-scale, unmarked notations are employed to address to intrinsic phase variables [75].

### 3.2.2 Pyrolysis

$N_s$ solid phases compose the material. For example, in TACOT the main components are the carbon fiber preform and the phenolic resin, which are modeled as two phases. Each solid phase, $\mathcal{P}_i$,

may decompose following multiple pyrolysis kinetics. We deal with this aspect by splitting each phase $i$ into $N_{p,i}$ sub-phases. A generic sub-phase $\mathcal{P}_{i,j}$ undergoes a determined kinetic mechanism which results in the production of species, or element, $A_k$ according to the stoichiometric coefficients $\nu_{i,j,k}$

$$\mathcal{P}_{i,j} \longrightarrow \sum_{k=1}^{N_g} \nu_{i,j,k} A_k \tag{3.1}$$

The Arrhenius model is adopted to model the pyrolysis reactions. This leads to the definition of the advancement of the pyrolysis reaction $\chi_{i,j}$ of sub-phase $j$ within phase $i$ as follows

$$\partial_t \chi_{i,j} = (1-\chi_{i,j})^{m_{i,j}} T_s^{n_{i,j}} \mathcal{A}_{i,j}\ exp\Big(-\frac{\mathcal{E}_{i,j}}{R\,T_s}\Big) \tag{3.2}$$

where $m$ and $n$ are the Arrhenius law parameters, $\mathcal{A}$ is the Arrhenius law pre-exponential factor, $\mathcal{E}$ represents the Arrhenius law activation energy, $R$ stands for the perfect gas constant, and $T_s$ indicates the temperature of the solid. By summing the productions of the $N_s$ solid phases it is possible to derive the total production rate $\pi$ of species/element $k$

$$\pi_k = \sum_{i=1}^{N_s} \sum_{j=1}^{N_{p,i}} \nu_{i,j,k}\ \epsilon_{i,0}\ \rho_{i,0}\ y_{i,j}\ \partial_t \chi_{i,j} \tag{3.3}$$

where $\epsilon_{i,0}$, $\rho_{i,0}$, and $y_{i,j}$, are respectively the initial (at t=0) volume fraction of phase $i$, intrinsic density of phase $i$, and mass fraction of sub-phase $j$ within phase $i$. The overall pyrolysis-gas production rate $\Pi$ is evaluated by summing over the elements and species in the mixture

$$\Pi = \sum_{k=1}^{N_g} \pi_k \tag{3.4}$$

### 3.2.3 Mass Conservation

Each solid phase, each species/element, and the gas mixture are characterized by a mass conservation equation. No heterogeneous reactions are considered.
For a generic solid phases $i$, the equation reads

$$\partial_t(\epsilon_i \rho_i) = -\pi_i \tag{3.5}$$

where $t$ is the time and the subscript 0 stands for the initial time ($t = 0$).
Depending on the chemical model used in the gas phase, elements or species are considered (elements for equilibrium or species for finite-rate chemistry). In case of chemical equilibrium the conservation equation for a generic element with mass fraction $z_k$ reads

$$\partial_t(\epsilon_g \rho_g z_k) + \partial_{\boldsymbol{x}} \cdot (\epsilon_g \rho_g z_k \boldsymbol{v_g}) + \partial_{\boldsymbol{x}} \cdot \boldsymbol{\mathcal{F}}_k = \pi_k \tag{3.6}$$

In case of finite rate chemistry, the conservation equation for a generic species with mass fraction $y_i$ reads

$$\partial_t(\epsilon_g \rho_g y_i) + \partial_{\boldsymbol{x}} \cdot (\epsilon_g \rho_g y_i \boldsymbol{v_g}) + \partial_{\boldsymbol{x}} \cdot \boldsymbol{\mathcal{F}}_i = \pi_i \tag{3.7}$$

where $\mathcal{M}_g$ is the molar mass of the gas mixture and $\boldsymbol{\mathcal{F}}_i$ and $\boldsymbol{\mathcal{F}}_k$ [75] are the effective multicomponent diffusion mass fluxes of the i-th species and k-th element. Mutation++ [84, 101], is used as a third party library to compute all thermodynamics and transport properties.
For the gas mixture, the mass conservation accounts for the pyrolysis production rate $\Pi$

$$\partial_t(\epsilon_g\rho_g) + \partial_{\boldsymbol{x}} \cdot (\epsilon_g\rho_g\boldsymbol{v_g}) = -\sum_{i=1}^{N_s} \partial_t(\epsilon_i\rho_i) = \Pi \tag{3.8}$$

### 3.2.4 Momentum Conservation

The average gas velocity is obtained from the resolution of Darcy's law [102]

$$\boldsymbol{v_g} = -\frac{1}{\epsilon_g}\Big[\frac{1}{\mu_g}\underline{\underline{K}}\Big(1 + \frac{1}{p_g}\underline{\underline{\beta}}\Big)\Big] \cdot \partial_{\boldsymbol{x}} p_g \tag{3.9}$$

where $p_g$ is the gas pressure, $\underline{\underline{K}}$ is the permeability tensor, and $\underline{\underline{\beta}}$ the Klinkenberg correction introduced to account for slip effects (at the pore scale) when the Knudsen number is not very small. This expression for the gas velocity vector can be substituted back into the gas mass conservation law, Eq.(3.8). Assuming a mixture of perfect gases, the following equation in pressure is found

$$\partial_t\Big(\frac{\epsilon_g\mathcal{M}_g}{RT_g}p_g\Big) - \partial_{\boldsymbol{x}} \cdot \Big[\frac{\epsilon_g\mathcal{M}_g}{RT_g}\frac{1}{\mu_g}\underline{\underline{K}}\Big(1 + \frac{1}{p_g}\underline{\underline{\beta}}\Big) \cdot \partial_{\boldsymbol{x}} p_g\Big] = \Pi + \Omega_h \tag{3.10}$$

where $\mu_g$ is the dynamic viscosity of the gas mixture.

### 3.2.5 Energy Conservation

Under the assumption of LTE, the temperature of the gas mixture accommodates to the one of the solid: $T_s = T_g = T$. A single conservation equation is then considered [75]

$$\partial_t(\rho_{\text{tot}}e_{\text{tot}}) + \partial_{\boldsymbol{x}} \cdot (\epsilon_g\rho_g h_g\boldsymbol{v}_g) = \partial_{\boldsymbol{x}} \cdot \sum_{k=1}^{N_g} \boldsymbol{\mathcal{Q}}_k + \partial_{\boldsymbol{x}} \cdot \Big(\underline{\underline{k}}_{\text{eff}} \cdot \partial_{\boldsymbol{x}} T\Big) \tag{3.11}$$

where the subscript tot stands for total, $e$, $h$, and $T$ denote respectively the internal energy, the absolute enthalpy, and the temperature, $\boldsymbol{\mathcal{Q}}_k$ is the heat transport by effective diffusion of the species, and $\underline{\underline{k}}_{\text{eff}}$ represents the effective thermal conductivity tensor. The terms on the left hand-side of the equation are the ones of accumulation and advection. While, on the right hand-side there are the terms of diffusion of the pyrolysis gases and the conduction flux. The conduction flux is described by Fourier's law where the effective conductivity tensor accounts for conduction in the gas and solid phases and radiative heat transfer within the pores [74, 82].
Eq. (3.11) can be further developed by expressing the total storage internal energy ($\rho_{\text{tot}}$ $e_{\text{tot}}$) as the sum of the energy of its phases

$$\rho_{\text{tot}}e_{\text{tot}} = \epsilon_g\rho_g e_g + \sum_{i=1}^{N_s} \epsilon_i\rho_i h_i \tag{3.12}$$

By substituting this term back in Eq. (3.11) and by performing the time derivatives, the energy conservation equation takes its final form

$$\sum_{i=1}^{N_s} \epsilon_i \rho_i c_{p,i} \partial_t T + \epsilon_g \rho_g c_{p,g} \partial_t T = \partial_{\boldsymbol{x}} \cdot \Big( \underline{\underline{k}}_{\text{eff}} \cdot \partial_{\boldsymbol{x}} T \Big) - \sum_{i=1}^{N_s} h_i \partial_t (\epsilon_i \rho_i) - \sum_{j=1}^{N_g} h_j \partial_t (\epsilon_g \rho_g y_j) + \partial_t (\epsilon_g p_g) + \\ - \partial_{\boldsymbol{x}} \cdot (\epsilon_g \rho_g h_g \boldsymbol{v}_g) + \partial_{\boldsymbol{x}} \cdot \sum_{k=1}^{N_g} \boldsymbol{\mathcal{Q}}_k \tag{3.13}$$

where $c_p$ is the specific heat. All the accumulation terms are gathered on the left hand-side of the equation. Whereas, on the right hand-side it is possible to find (in order) the terms related to conduction, pyrolysis, pressure, advection and species diffusion.
Under the assumption of LTNE, two energy conservation equations are needed to describe the solid and gas phases. The two equations are

$$\sum_{i=1}^{N_s} \epsilon_i \rho_i c_{p,i} \partial_t T_s + \sum_{i=1}^{N_s} h_i \partial_t (\epsilon_i \rho_i) = \partial_{\boldsymbol{x}} \cdot \Big( \underline{\underline{k}}_{\text{eff},s} \cdot \partial_{\boldsymbol{x}} T_s \Big) + h_v \Big( T_g - T_s \Big) \tag{3.14}$$

and

$$\epsilon_g \rho_g c_{p,g} \partial_t T_g + \sum_{j=1}^{N_g} h_j \partial_t (\epsilon_g \rho_g y_j) - \partial_t (\epsilon_g p_g) = - \partial_{\boldsymbol{x}} \cdot \Big( \epsilon_g \rho_g \boldsymbol{v}_g h_g \Big) + \partial_{\boldsymbol{x}} \cdot \Big( \underline{\underline{k}}_{\text{eff},g} \cdot \partial_{\boldsymbol{x}} T_g \Big) + \\ + \partial_{\boldsymbol{x}} \cdot \sum_{k=1}^{N_g} \boldsymbol{\mathcal{Q}}_k + h_v \Big( T_s - T_g \Big) \tag{3.15}$$

where $h_v$ is the volumetric heat transfer coefficient that identifies the heat exchanged by the two phases. It should be mentioned, if summing the two LTNE equations (Eq. (3.14) and Eq. (3.15)), the LTE equation (Eq. (3.13) is obtained.

## 3.3 Application of the Model to the Ablation Cases

In this section, the numerical model is applied in order to assess the validity of the thermal equilibrium hypothesis for atmospheric entry applications. Two different ablation cases are considered: Stardust and MSL missions. A subsection is dedicated to each of them. The same ablative material, TACOT, is considered for all cases. This theoretical material is characterized by a composition and properties that are comparable to NASA's Phenolic Impregnated Carbon Ablator. In volume, TACOT is made of 10% of carbon fibers (phase-1) and 10% of phenolic resin (phase-2), hence $N_s = 2$. It is 80% porous (phase-0: gas). During the thermal degradation process, the carbon fibers phase does not decompose, while the phenolic resin undergoes several parallel pyrolysis mechanisms, as showed in Table 3.1. 1D Simulations have been carried out on uniform meshes. The thickness of the geometry is specified in each subsection. A convective thermal boundary condition involving the resolution of the mass and energy balances at the surface [73] is enforced to the surface with the external environment.

| j | Pyrolyis of phenolic matrix | Peak (K) | $\mathcal{A}_{2,j}$ $(s^{-1})$ | $\mathcal{E}_{2,j}$ $(J/mol)$ | $m_{2,j}$ | $n_{2,j}$ |
|---|---|---|---|---|---|---|
| 1 | $\mathcal{P}_{2,1} \longrightarrow H_2O$ | 373 | $8.56 \cdot 10^3$ | $7.12 \cdot 10^4$ | 3 | 0 |
| 2 | $\mathcal{P}_{2,2} \longrightarrow 0.69H_2O + 0.01C_6H_6 + 0.01C_7H_8 + 0.23C_6H_6O$ | 773 | $8.56 \cdot 10^3$ | $7.12 \cdot 10^4$ | 3 | 0 |
| 3 | $\mathcal{P}_{2,3} \longrightarrow 0.09CO_2 + 0.33CO + 0.58CH_4$ | 873 | $4.98 \cdot 10^8$ | $1.70 \cdot 10^5$ | 3 | 0 |
| 4 | $\mathcal{P}_{2,4} \longrightarrow H_2$ | 1073 | $4.98 \cdot 10^8$ | $1.70 \cdot 10^5$ | 3 | 0 |

TABLE 3.1 – Pyrolysis balance equations and kinetic parameters for the phenolic matrix in TACOT.

A 600-cells mesh has been adopted following a mesh convergence analysis.
For each case, both the LTE (Eq. (3.13)) and the LTNE (Eqs. (3.14) and (3.15)) models are applied. Results are then compared and commented. The comparison is made in terms of temperature evolution and species concentration (non-equilibrium) within the material, pyrolysis gas blowing rate at the surface, wall recession due to pyrolysis ablation, and identification of the pyrolysis zone. The latter is defined as the intermediate region between two thresholds in terms of the density: virgin 98% and char 2%, defined as $\rho_v(98\%) = \rho_c + 0.98(\rho_v - \rho_c)$ and $\rho_c(2\%) = \rho_c + 0.02(\rho_v - \rho_c)$. The relative difference, $\Delta$ between the results is defined as follows

$$\Delta = \frac{\rho_v(98\%)_{1T} - \rho_v(98\%)_{2T}}{\rho_v(98\%)_{1T}} \; 100 \tag{3.16}$$

where the quantity $\rho_v(98\%)$ is taken as example.
In order to apply the LTNE model, it is necessary to quantify the volumetric heat transfer coefficient between the gas phase and the TACOT material. Its value has been set equal to $h_v = 10^9 \; Wm^{-3}K^{-1}$, after experimental characterization [89].

For the chemical non-equilibrium analysis, a modified April mechanism [1] has been considered for the composition of the gas mixture. This mechanism is reported in Table 3.2.

| | Reaction Formula | $\mathcal{A}$ $(s^{-1})$ | $\mathcal{E}$ $(J/mol)$ |
|---|---|---|---|
| 1 | $CH_4 \longrightarrow 0.5 \; H_2 + 0.5 \; C_2H_6$ | 7.6 $10^{14}$ | 397480 |
| 2 | $C_2H_6 \longrightarrow H_2 + C_2H_4$ | 3.1 $10^{14}$ | 292880 |
| 3 | $C_2H_4 \longrightarrow C_2H_2 + H_2$ | 2.6 $10^8$ | 167360 |
| 4 | $C_2H_2 \longrightarrow 2C + H_2$ | 2.1 $10^{10}$ | 167805 |
| 5 | $C + 2H_2 \longrightarrow CH_4$ | 2.0 $10^9$ | 71128 |
| 6 | $C_6H_5OH + H_2 \longrightarrow H_2O + C_6H_6$ | 2.0 $10^{13}$ | 188280 |
| 7 | $C_6H_6 \longrightarrow 3 \; C_2H_2$ | 1.4 $10^9$ | 246440 |
| 8 | $C + H_2O \longrightarrow CO + H_2$ | 1.2 $10^{12}$ | 343088 |
| 9 | $CO + H_2O \longrightarrow H_2 + CO_2$ | 1.0 $10^{10}$ | 125520 |
| 10 | $C + CO \longrightarrow 2 \; CO$ | 1.0 $10^6$ | 209200 |
| 11 | $2 \; CO \longrightarrow C + CO$ | 1.0 $10^{-9}$ | 255224 |

TABLE 3.2 – Modified April mechanism [1] considered for the chemical non-equilibrium analysis.

| t (s) | $p_w$ (Pa) | $C_H$ $(kg/m^2/s)$ | $h_e$ $(J/kg)$ |
|---|---|---|---|
| 0 | 1.5 | 0.00005 | 77926960 |
| 1 | 1.8 | 0.00006 | 77984280 |
| 2 | 2.1 | 0.00007 | 78040736 |
| 3 | 2.4 | 0.00008 | 78095240 |
| 4 | 2.6 | 0.00009 | 78146168 |
| .. | .. | .. | .. |
| 50 | 19142.319 | 0.17378 | 61280148 |
| 51 | 21350.19075 | 0.18082 | 59093460 |
| 52 | 23558.0625 | 0.18786 | 56748968 |
| .. | .. | .. | .. |
| 131 | 2144.746275 | 0.01705 | 95178 |
| 132 | 2067.8406 | 0.01644 | 89990 |
| 133 | 2067.8406 | 0.01582 | 84957 |

TABLE 3.3 – Stardust case. Partial summary of the environment properties. Input data are the wall pressure and boundary layer edge enthalpy, $p_w, h_e$ and the surface heat transfer coefficient $C_H$.

### 3.3.1 Stardust Ablation Case

The Stardust mission was a 390-kilogram robotic space probe launched by NASA on 7 February 1999. Its primary mission was to collect dust samples from the coma of the comet Wild 2, as well as cosmic dust samples, and return these to Earth for analysis. It was the first sample-return mission of its kind. The primary mission was successfully completed on 15 January 2006, when the sample space probe returned to Earth.
The TPS is modeled as a 1D material composed of three layers: 5.8 cm of TACOT material, 0.14 cm of adhesive film (HT-424), and 1.27 cm of aluminium 2024 [103]. An overview of the input data for the convective boundary condition is given in Table 3.3. Standard air is considered for the initial gas composition of the material and for the element composition at the boundary.

#### 3.3.1.1 Chemical Equilibrium

Results of the thermocouple and temperature difference are showed in Fig. 3.1 Without any abrupt change of condition, the gas temperature tends to be closer to that of the solid. Referring to the figure on the right, it can be seen that at most, the difference between the two predictions is about 25 K. Considering that the temperatures are about 3000 K, the 25 K difference (less than 1%) can be considered negligible. In fact, in the figure on the left, the temperature curves of the gas and the solid are superimposed at each position. This aspect is also reflected in the comparison of other quantities of interest. This is represented in Fig. 3.2, where the maximum relative difference, $\Delta = 0.2\%$ is related to the prediction of the location of the virgin front.

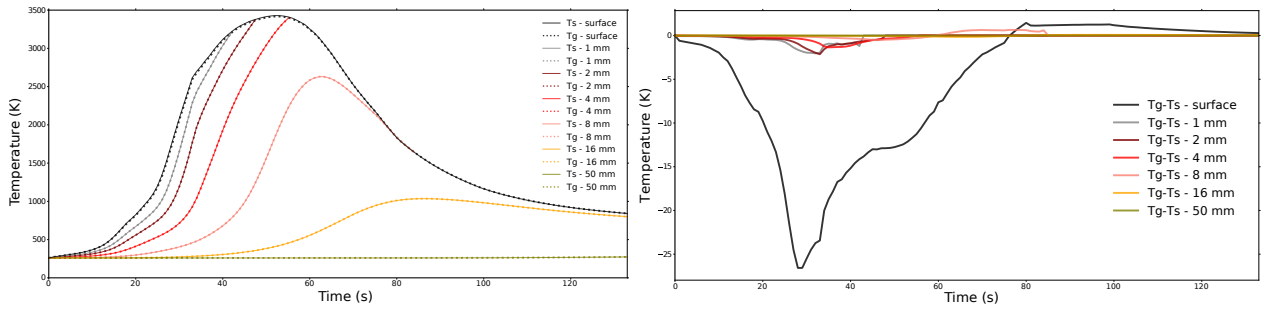


FIGURE 3.1 – Stardust case. Thermocouple data are reported on the left figure and temperature difference on the right one.

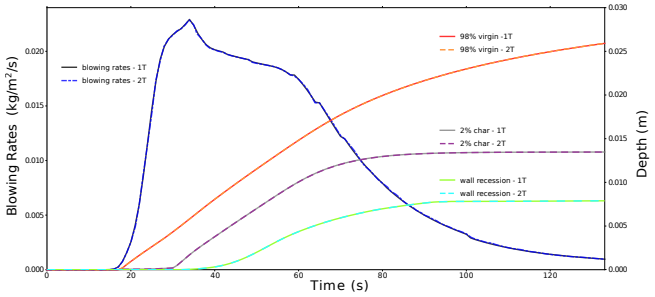


FIGURE 3.2 – Stardust case. Blowing rates, pyrolysis zone, and wall recession.

### 3.3.1.2 Chemical Non-Equilibrium

The species distribution within the material at time $t = 40\ s$ is reported in Fig. 3.3 It can be observed that the use of LTE or LTNE strongly influences the species distribution. In particular, $CO$, $H_2$, $CH_4$, and $CO_2$ are the species that undergo a higher difference in the predictions. The difference concerns both the evolution of the mass fractions in the material and at the interface with the external environment. It follows that, depending on the model, the boundary layer will be characterized by a different composition, hence different properties.

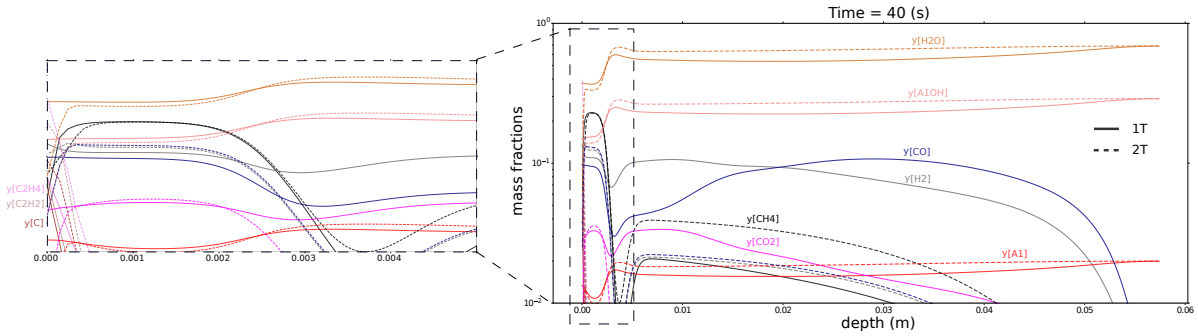


FIGURE 3.3 – Stardust case. Species distribution within the material at time $t = 40\ s$. At the left: a zoom of the mass fractions near the surface with the external environment.

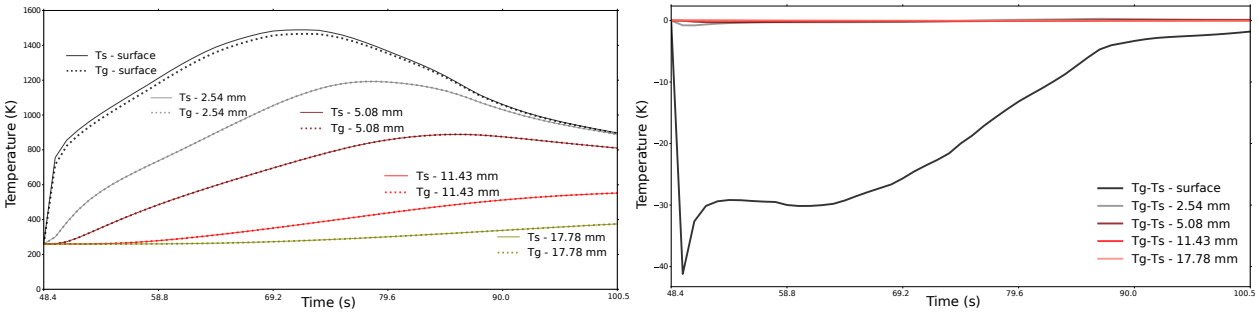


FIGURE 3.4 – MSL case. Thermocouple data are reported on the left figure and temperature difference on the right one.

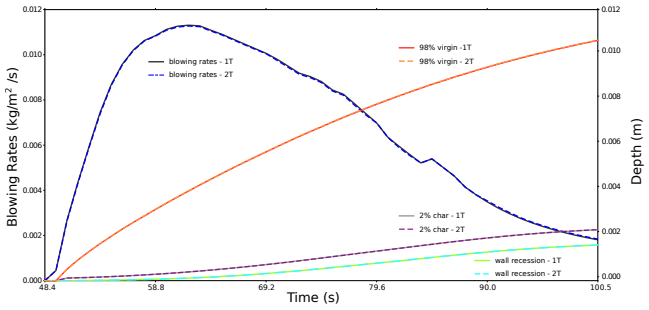


FIGURE 3.5 – MSL case. Blowing rates, pyrolysis zone, and wall recession.

### 3.3.2 MSL Ablation Case

The Mars Science Laboratory mission was a robotic space probe mission to Mars launched by NASA on November 26, 2011. It successfully landed Curiosity, a Mars rover, in Gale Crater on August 6, 2012. The overall objectives include investigating Mars' habitability, studying its climate and geology, and collecting data for a human mission to Mars.
The depth of the ablative material is of 4.385 *cm* [93]. The Mars atmosphere is considered for the initial gas composition of the material and for the composition of the elements in the boundary layer. The input data for the convective boundary layer are taken from the study by Meurisse et al., 2018 [93], where 11 discrete times along the MSL trajectory are considered: 48.4, 59.1, 64.4, 69.6, 71.5, 73.9, 76.2, 80.5, 84.4, 87.5 and 100.5 *s*. A linear variation of the conditions is assumed in the intermediate intervals.

#### 3.3.2.1 Chemical Equilibrium

The thermocouple and temperature difference results are showed in Fig. 3.4. A difference of 40 *K* is reached at the beginning of the simulation between the two temperatures due to the initial sharp change of condition. After the first few seconds in which the value remains constant, the difference gradually decreases to 3 *K* at 100.5 *s*. Nevertheless, as can be seen in Fig. 3.5, this small difference in temperature does not lead to any discrepancy on any other quantity of interest. The maximum

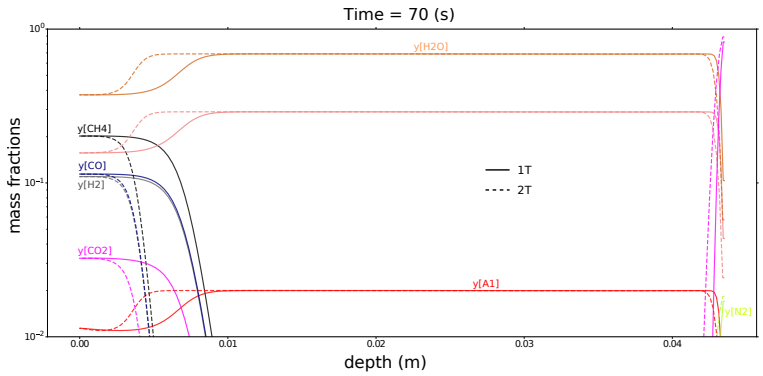


FIGURE 3.6 – Stardust case. Species distribution within the material at time $t = 21\ s$.

relative error is still provided by the prediction of the virgin front location with a value of 0.2%.

#### 3.3.2.2 Chemical Non-Equilibrium

The species distribution within the material at time $t = 70\ s$ is reported in Fig. 3.6. The figures shows again a clear difference between the two models. However, due to the lower temperatures reached, the difference is less marked than in the Stardust case. The species difference concerns only the internal part of the material, and not the interface. The composition of the boundary layer between the two models remains unaltered.

## 3.4 Conclusions and Perspectives

This study investigates the validity of the local thermal equilibrium assumption for ablative material responses. To this end, a two-temperature model has been implemented and integrated in the Porous material Analysis Toolbox based on OpenFOAM (PATO). This toolbox has been then used to simulate the pyrolysis of the Theoretical Ablative Composite for Open Testing (TACOT) in a wide range of conditions to assess the true range of validity of the thermal equilibrium hypothesis. 1D simulations are performed on the Stardust and Mars Science Laboratory atmospheric entry missions. Both Local Thermal Equilibrium (LTE) and Local Thermal Non-Equilibrium (LTNE) energy models have been adopted. The comparison between the two models has been carried out by monitoring the temperature evolution and species concentration (non-equilibrium) inside the material, the pyrolysis gas blowing rate, the pyrolysis zone, and the wall recession due to ablation. Results show that the gas temperature does not perfectly match that of the solid at the surface, especially when a sudden change in conditions occurs. Nevertheless, the temperature difference does not lead to a significant deviation in the monitored quantities (the maximum relative difference in the results has been found to be about $\Delta = 1.4\%$) under chemical equilibrium assumption. The relative difference values are possible sources of uncertainty to include in the design analysis. The same conclusion does not hold for the case of chemical non-equilibrium. In this case, especially in the Stardust case where higher temperatures are reached, the species distribution prediction is strongly influenced by the use of LTE or LTNE models.

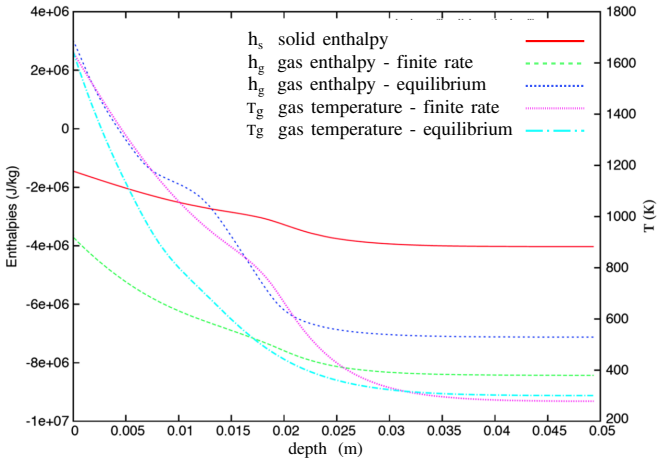


FIGURE 3.7 – Test case #1. Comparison of the temperature and enthalpy profiles.

In particular, the difference concerns both the evolution of the mass fractions of the species in the material and at the interface with the external environment. It follows that, depending on the model, the boundary layer will be characterized by a different composition, hence different properties.

Results obtained in this study must be considered with caution. As the main purpose of the work is to estimate possible differences resulting from the use of LTE or LTNE models, no effort has been directed towards the description of chemical mechanisms. The April mechanism has been employed, despite knowing its inaccuracy. In the perspective of a more realistic modelling, greater efforts must be placed on the description of the chemical mechanisms and in particular on the estimation of the enthalpy variations of individual reactions. An acknowledgement of this problem can be seen in Fig. 3.7, where the pyrolysis gas enthalpies profiles within the material, at equilibrium and finite rate, are reported for the ablative test case #1. It can be observed how the two are significantly different, thus underlining a fundamental problem in the treatment of the pyrolysis mechanism.

## 3.5 Acknowledgments

The research of H.S. was sponsored by a PhD grant awarded by Arts et Métiers Institute of Technology.

# Chapitre 4

# Simulation of Wood Combustion in PATO Using a Detailed Pyrolysis Model Coupled to fireFoam

**Nomenclature**

*Latin Letters*

| | |
|---|---|
| $\mathcal{A}$ | Arrhenius law pre-exponential factor $[s^{-1}]$ |
| $a_1, .., a_7$ | Janaf coefficients |
| $A$ | generic species |
| $c_p$ | specific heat at constant pressure $[J\ kg^{-1}\ K^{-1}]$ |
| $C_1, C_2$ | Sutherland coefficients |
| $C_{B1}, C_{B2}$ | Boussinesq approximation coefficients |
| $D$ | mass diffusivity $[m^2\ s^{-1}]$ |
| $\mathcal{E}$ | Arrhenius law activation energy $[J\ mol^{-1}]$ |
| $\boldsymbol{\mathcal{F}}$ | effective diffusion flux $[kg\ m^{-2}\ s^{-1}]$ |
| $f$ | puffing frequency $[Hz]$ |
| $\boldsymbol{g}$ | gravitational field $[m\ s^{-2}]$ |
| $h$ | specific absolute enthalpy $[J\ kg^{-1}]$ |
| $\underline{\underline{I}}$ | identity tensor |
| $\underline{\underline{K}}$ | permeability tensor $[m^2]$ |
| $\underline{\underline{k}}$ | thermal conductivity tensor $[W\ m^{-1}\ K^{-1}]$ |
| $k_{fw}, k_{bw}$ | forward and backward chemical rate constants |
| $k_{sgs}$ | sub-grid scale turbulent kinetic energy $[J]$ |
| $l, L$ | microscopic and macroscopic characteristic lengths $[m]$ |
| $\mathcal{M}$ | molar mass $[kg\ mol^{-1}]$ |
| $m, n$ | Arrhenius law parameters |
| $\boldsymbol{n}$ | surface normal |

## Nomenclature

| | |
|---|---|
| $N_g$ | number of gaseous species |
| $N_{p,i}$ | number of sub-phases in the solid phase $i$ |
| $N_s$ | number of solid phases |
| $N_t$ | number of reactants and products in a chemical reaction |
| $\mathcal{P}_i, \mathcal{P}_{i,j}$ | solid phase $i$ and sub-phase $j$ of solid phase $i$ |
| $p$ | macro-scale pressure $[Pa]$ |
| $\boldsymbol{\mathcal{Q}}$ | effective diffusion heat flux $[J\ m^{-2}\ s^{-1}]$ |
| $Q_{\text{comb}}$ | heat generated by combustion $[J]$ |
| $\boldsymbol{q}_r$ | thermal radiation flux $[J\ m^{-1}\ s^{-1}]$ |
| $R$ | specific perfect gas constant $[J\ mol^{-1}\ K^{-1}]$ |
| $\underline{\underline{S}}_{sgs}$ | sub-grid strain rate tensor $[s^{-1}]$ |
| $\mathcal{T}$ | time period $[s]$ |
| t | time $[s]$ |
| $T$ | macro-scale temperature $[K]$ |
| $\boldsymbol{v}$ | macro-scale velocity $[m\ s^{-1}]$ |
| $\boldsymbol{x}$ | position vector $[m]$ |
| $y$ | species mass fraction |

*Greek Letters*

| | |
|---|---|
| $\alpha$ | thermal diffusivity $[m^2\ s^{-1}]$ |
| $\Delta$ | local filter cutoff width |
| $\epsilon$ | volume fraction |
| $\mu$ | dynamic viscosity $[Pa\ s]$ |
| $\nu$ | stoichiometric coefficient |
| $\pi_k$ | pyrolysis mass production rate of element/species $k$ $[kg\ m^{-3}\ s^{-1}]$ |
| $\Pi$ | global mass production rate of the pyrolysis reactions $[kg\ m^{-3}\ s^{-1}]$ |
| $\rho$ | macro-scale density $[kg\ m^{-3}]$ |
| $\underline{\underline{\tau}}_{sgs}$ | sub-grid scale stress tensor $[J\ kg\ m^{-3}]$ |
| $\tau$ | total advancement of the pyrolysis reactions |
| $\Phi$ | generic variable |
| $\chi_{i,j}$ | advancement of the pyrolysis reaction of sub-phase $j$ within phase $i$ |
| $\omega$ | chemical reaction rate $k$ $[kg\ m^{-3}\ s^{-1}]$ |

*Subscripts and Superscripts*

| | |
|---|---|
| 0 | initial time |
| bw | backward |
| comb | combustion |
| eff | effective |
| $f$ | external flow |
| fw | forward |

## Nomenclature

| | |
|---|---|
| $g$ | gas |
| $i, j, k, z$ | indexes used in the sum operator |
| $m$ | modified |
| $pl$ | power law |
| ref | reference |
| $s$ | solid |
| $sgs$ | sub-grid scale |
| sim | simulation |
| $w$ | wood |

*Notation*

| | |
|---|---|
| $\overline{\Phi}$ | filtered variable |
| $\tilde{\Phi}$ | filtered density-weighted variable |

*Acronyms*

| | |
|---|---|
| $LES$ | Large Eddy Simulation |
| $LTE$ | Local Thermal Equilibrium |
| $PATO$ | Porous material Analysis Toolbox based on OpenFoam |
| $REV$ | Representative Elementary Volume |

## Preamble

Authors: H. Scandelli; A. Ahmadi-Senichault; F. Richard* ; J. Lachaud;
Affiliations: Arts et Métiers Institute of Technology, Univ. Bordeaux, CNRS, Bordeaux INP, I2M, UMR 5295, F-33400 Talence, France; * Institut Pprime (UPR 3346 CNRS), Université de Poitiers, Futuroscope Chasseneuil Cedex, France;
Published: No;
Journal: Applied Sciences;
Published: 10 November 2021;
DOI: https://doi.org/10.3390/app112210570;
Conference: This work has been presented at the 30e journées du GDR Feux, 02/03 December 2021 - Paris (France);

## Abstract

The numerical simulation of fire propagation requires capturing the coupling between wood pyrolysis, which leads to the production of various gaseous species, and the combustion of these species in the flame, which produces the energy that sustains the pyrolysis process. Experimental and numerical works of the fire community are targeted towards improving the description of the pyrolysis process to better predict the rate of production and the chemical nature of the pyrolysis gases. We know that wood pyrolysis leads to the production of a large variety of chemical species: water, methane, propane, carbon monoxide and dioxide, phenol, cresol, hydrogen, etc. With the idea of being able to capitalize on such developments to study more accurately the physics of fire propagation, we have developed a numerical framework that couples a detailed three-dimensional pyrolysis model and fireFoam. In this article, we illustrate the capability of the simulation tool by treating the combustion of a wood log. Wood is considered to be composed of 3 phases (cellulose, hemicellulose and lignin), each undergoing parallel degradation processes leading to the production of methane and hydrogen. We chose to simplify the gas mixture for this first proof of concept of the coupling of a multi-species pyrolysis process and a flame. In the flame, we consider two separate finite-rate combustion reactions for methane and hydrogen. The flame evolves during the simulation according to the concentration of the two gaseous species produced from the material. It appears clearly that introducing different pyrolysis species impacts the temperature and behavior of the flame.

## 4.1 Introduction

Charring materials (timber and composite materials) are widely used in many civil [59] and aeronautical [104] applications. On the one hand this leads to a sustainable development with lower energy requirements and less pollution, but on the other hand, this may lead to fire hazards. These materials have a flammable nature, and this makes necessary the prediction of a fire potential with the consequent loss of stiffness, strength, and resistance of a structure [61, 62]. In the recent few decades, different studies approached the topic and aimed to characterize the performance of charred materials under combustion. Fire retardancy [63], flammability properties [64], and gaseous emissions [65] are just a few examples of the main properties that have been studied. The main strength of this fire community lies in its ability to describe how a fire behaves for a given material, including the description of ignition, fire growing, propagation and extinction processes [66]. Different numerical simulation programs have been developed for such purposes. One of the most successful is fireFoam [105], an opensource code to simulate and visualize the fire behaviour in a defined geometry. Different application cases can be found in the literature [106–108].

In a numerical simulation, modeling the flame is not enough. A description of the charred material degradation process in the absence of oxygen (the pyrolysis), as well as the coupling between material and environment, are fundamental aspects that need to be captured. Pyrolysis leads to the production of a large variety of chemical species: water, methane, propane, carbon monoxide and dioxide, phenol, cresol, hydrogen, etc. The production of these species and their concentration is strongly affected by the imposed conditions [51, 52]. This would not affect only the material, but even the combustion

process. The gaseous species, once produced, will percolate in the material and eventually reach the external environment. Many of these species are fuels, therefore the correct prediction of their formation could change the outcome of the simulation. Different pyrolysis models have been developed during the years, each characterized by a different level of accuracy in the description of the chemical reactions. The simplest one is the single reaction mechanism [54] in which only a single decomposition reaction is considered. A next step is done with the multi-component single reaction model [55] where the description becomes sensible to the feed-stock. With an increase in complexity, there is the competitive model [56] that introduces competitive reactions to predict different product distributions depending on the conversion conditions, such as heating rate and pressure. Finally, there are the competitive multi-component models [57, 58] which represent efficiently the dependence on the feed-stock as well as the temperature effect on the yields.
Pyrolysis is not the only process to model in charring materials. Mass, momentum, and energy of the material need to be conserved, and the transport of gaseous species also need to be taken also into account. A generic combustion problem with a charring material is schematized in Fig. 4.1. The

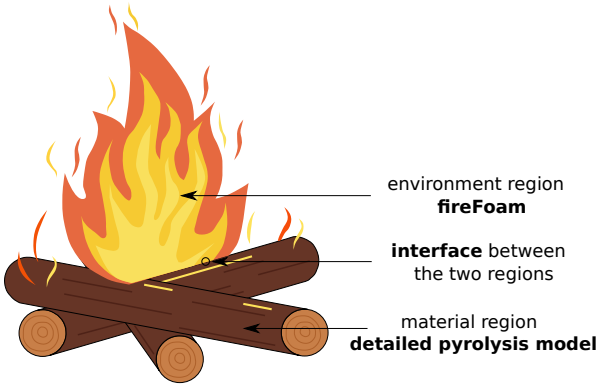


FIGURE 4.1 – A generic combustion problem. Two different regions are present: the environment, where combustion happens, and the material, characterized by pyrolysis.

problem may be split in two regions: the environment, where combustion happens, and the material, characterized by a thermal degradation process, the pyrolysis. Two different models are required for the numerical resolution. We chose to couple fireFoam with a detailed pyrolysis model. The latter enters in the type-3 models classification proposed by Lachaud et al., 2011 [72], and it has already been applied to different applications, like ablative heat-shield design and pyrolysis of lignocellulosic biomass [73–75].
The main objective of this paper is to propose for the first time a numerical framework that couples a detailed three-dimensional pyrolysis model and fireFoam. The numerical framework with the description of the two numerical models is given in the next sections: Section 4.2 presents the detailed pyrolysis model and Section 4.3 presents the combustion process. The coupling conditions between the two models are given in Section 4.4. The capabilities of the solver are showed in Section 4.5, where two different applications are considered. The first one aims to show how the introduction of different pyrolysis species impacts the temperature and the behavior of the flame. The second application is a 2D simulation of a wood log combustion. Here, we chose to simplify the gas mixture for this first

proof of concept of coupling of a multi-species pyrolysis process and a flame. Results show a perfect coupling between the two models and highlight the impact of the species, whose concentration change in time, on the fire behaviour. Finally, conclusions are drawn in Section 4.6.

## 4.2 Numerical Model: Material Region

The model to describe the material region is presented in this section. It consists of a generic pyrolysis model that allows the description of the interaction between several solid phases and a gas phase [75]. A summary of the governing equations of the solid phases, gas and species are presented in the following subsections.

### 4.2.1 Main Assumptions

The model considers the interaction between a multi-phase reactive material ($N_s$ solid phases) with a multi-species reactive gas mixture ($N_g$ gaseous elements/species). No liquid phase is modeled. Any liquid present in the material (water) is modeled as a solid phase. The description is done at the macroscopic scale, where the governing equations can be derived from upscaling theories. Their derivation relies on the existence of a representative elementary volume (REV) of the domain and on the assumption of scales separation, as illustrated in Fig. 4.2. As the entire section is aimed at the

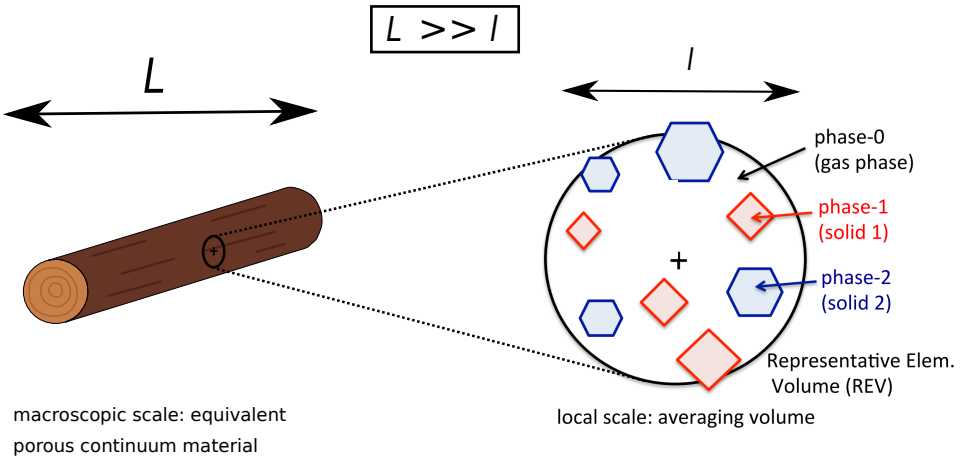


FIGURE 4.2 – Illustration of the problem: interaction between a multi-phase reactive material with a multi-species reactive gas mixture. The model characterizes this problem at the macroscopic scale under the assumption of scale separation ($L >> l$).

macro-scale, unmarked notations are employed to address to intrinsic phase variables [75].

### 4.2.2 Pyrolysis

The material is assumed to be composed of $N_s$ solid phases. For example, in the wood-cell walls the main components are cellulose, hemicellulose, and lignin, which are modeled as three phases. Each solid phase $\mathcal{P}_i$ may decompose following several pyrolysis kinetics in the absence of oxygen. For this reason, each phase $i$ is split into $N_{p,i}$ sub-phases to model the different degradation mechanisms. A generic decomposition of a sub-phase $j$ (from solid phase $i$) leads to the production of species $A_k$ according to the stoichiometric coefficients $\nu_{i,j,k}$ as follows

$$\mathcal{P}_{i,j} \longrightarrow \sum_{k=1}^{N_g} \nu_{i,j,k} A_k \tag{4.1}$$

where $N_g$ is the total number of the gaseous species accounted for in the gas mixture. Pyrolysis reactions are modeled by Arrhenius laws. In this way, the advancement of the pyrolysis reaction $\chi_{i,j}$ of sub-phase $j$ within phase $i$ can be defined as

$$\partial_t \chi_{i,j} = (1-\chi_{i,j})^{m_{i,j}} T_s^{n_{i,j}} \mathcal{A}_{i,j} exp\Big(-\frac{\mathcal{E}_{i,j}}{RT_s}\Big) \tag{4.2}$$

where $R$ is the perfect gas constant, $T_s$ the temperature of the solid phases, $\mathcal{A}$ the Arrhenius law pre-exponential factor, $\mathcal{E}$ the Arrhenius law activation energy, and $m$ and $n$ the Arrhenius law parameters. The total advancement in the pyrolysis process, $\tau$, is evaluated as follows

$$\tau = \sum_{i=1}^{N_s} \sum_{j=1}^{N_{p,i}} \frac{\epsilon_{i,0}\rho_{i,0}y_{i,j}}{\sum_{i=1}^{N_s}\sum_{j=1}^{N_{p,i}} \epsilon_{i,0}\rho_{i,0}y_{i,j}} (1-\chi_{i,j}) \tag{4.3}$$

where $\epsilon_i$, $\rho_i$, and $y_{i,j}$ denote respectively the volume fraction of phase $i$, the density of phase $i$, and the mass fraction of sub-phase $j$ within phase $i$. The subscript 0 indicates the initial time ($t = 0$).
The total production rate of species $\pi_k$ is given by

$$\pi_k = \sum_{i=1}^{N_s} \sum_{j=1}^{N_{p,i}} \nu_{i,j,k} \epsilon_{i,0}\rho_{i,0}y_{i,j}\partial_t \chi_{i,j} \tag{4.4}$$

By summing all the contributions in the gas mixture, it is possible to obtain the overall pyrolysis-gas production rate

$$\Pi = \sum_{k=1}^{N_g} \pi_k \tag{4.5}$$

### 4.2.3 Mass Conservation

We assume no heterogeneous reactions between the gaseous species and the solid phase. The only production terms come from the pyrolysis.
All the solid phases, the species, and the gas mixture should be taken into account. Each of them is characterized by a different mass conservation equation. For the solid phases, the equation reads

$$\partial_t(\epsilon_i \rho_i) = -\pi_i \tag{4.6}$$

For a generic specie with mass fraction $y_i$, the conservation equation is

$$\partial_t(\epsilon_g \rho_g y_i) + \partial_{\boldsymbol{x}} \cdot (\epsilon_g \rho_g y_i \boldsymbol{v_g}) + \partial_{\boldsymbol{x}} \cdot \boldsymbol{\mathcal{F}}_i = \pi_i \tag{4.7}$$

where $\boldsymbol{\mathcal{F}}_i$ models the effective diffusion flux. For the gas phase, the mass conservation needs to take into account the pyrolysis production rate. The term is added on the right hand-side

$$\partial_t(\epsilon_g \rho_g) + \partial_{\boldsymbol{x}} \cdot (\epsilon_g \rho_g \boldsymbol{v_g}) = -\sum_{i=1}^{N_s} \partial_t(\epsilon_i \rho_i) = \Pi \tag{4.8}$$

where $\boldsymbol{v_g}$ is the macro-scaled gas velocity.

### 4.2.4 Momentum Conservation

The macro-scale gas velocity is obtained from Darcy's law

$$\boldsymbol{v}_g = -\frac{1}{\epsilon_g \mu_g} \underline{\underline{K}} \cdot \partial_{\boldsymbol{x}} p_g \tag{4.9}$$

where $\underline{\underline{K}}$ is the permeability tensor, $p_g$ the gas pressure, and $\mu_g$ the dynamic viscosity of the mixture. This expression for the velocity can be substituted back into the gas mass conservation law, Eq.(4.8). By assuming the gas obeys the perfect gas, the overall equation becomes

$$\partial_t\Big(\frac{\epsilon_g \mathcal{M}_g}{RT_g} p_g\Big) - \partial_{\boldsymbol{x}} \cdot \Big(\frac{p_g \mathcal{M}_g}{RT_g} \frac{1}{\mu_g} \underline{\underline{K}} \cdot \partial_{\boldsymbol{x}} p_g\Big) = \Pi \tag{4.10}$$

where $\mathcal{M}_g$ is the molar mass of the gas mixture. This equation in pressure is directly solved instead of handling the mass conservation law (Eq.(4.8)), the momentum equation (Eq.(4.9)), and the perfect gas law.

### 4.2.5 Energy Conservation

The Local Thermal Equilibrium (LTE) condition is assumed between the phases: $T_s = T_g = T$. A single energy conservation is then necessary

$$\sum_{i=1}^{N_s}[(\epsilon_i \rho_i c_{p,i})\partial_t T] + \epsilon_g \rho_g c_{p,g} \partial_t T = \partial_{\boldsymbol{x}} \cdot (\underline{\underline{k}}_{\text{eff}} \cdot \partial_{\boldsymbol{x}} T) - \sum_{i=1}^{N_s} h_i \partial_t(\epsilon_i \rho_i) - \sum_{j=1}^{N_g} h_j \partial_t(\epsilon_g \rho_g y_j) + \partial_t(\epsilon_g \rho_g) +$$
$$-\partial_{\boldsymbol{x}} \cdot (\epsilon_g \rho_g h_g \boldsymbol{v}_g) + \partial_{\boldsymbol{x}} \cdot \sum_{k=1}^{N_g} \boldsymbol{\mathcal{Q}}_k \tag{4.11}$$

where $c_p$ is the heat capacity at constant pressure, $\underline{\underline{k}}_{\text{eff}}$ is the effective thermal conductivity tensor, $h$ is the specific absolute enthalpy, and $\boldsymbol{\mathcal{Q}}_k$ is the heat transport by effective diffusion of the species.

## 4.3 Numerical Model: Environment Region

The model to describe the environment region is now presented. The governing equations are derived from the Navier-Stokes equations after applying the LES filtering process and using the Favre mean variables [109]. By considering a generic $\Phi$ variable, the following notations are introduced: $\overline{\Phi}$ the filtered variable over a time period $\mathcal{T}$

$$\overline{\Phi} = \frac{1}{\mathcal{T}} \int_{\mathcal{T}} \Phi(t) dt \tag{4.12}$$

and the filtered density-weighted variable $\tilde{\Phi}$

$$\tilde{\Phi} = \frac{\overline{\rho\Phi}}{\Phi} \tag{4.13}$$

### 4.3.1 Continuity Equation

The continuity equation reads

$$\partial_t \overline{\rho}_f + \partial_{\boldsymbol{x}} \cdot (\overline{\rho}_f \tilde{\boldsymbol{v}}_f) = 0 \tag{4.14}$$

where the subscript $f$ refers to the external flow.

### 4.3.2 Momentum Conservation

By considering Newtonian fluids the equation takes the following form

$$\partial_t \overline{\rho}_f \tilde{\boldsymbol{v}}_f + \partial_{\boldsymbol{x}} \cdot (\overline{\rho}_f \tilde{\boldsymbol{v}}_f \tilde{\boldsymbol{v}}_f) = -\partial_{\boldsymbol{x}} \overline{p_m} - (\boldsymbol{g} \cdot \boldsymbol{x}) \partial_{\boldsymbol{x}} \overline{\rho}_f + \partial_{\boldsymbol{x}} \cdot \left[ \mu_{eff,f} (\partial_{\boldsymbol{x}} \tilde{\boldsymbol{v}}_f + (\partial_{\boldsymbol{x}} \tilde{\boldsymbol{v}}_f)^T - \frac{2}{3} (\partial_{\boldsymbol{x}} \cdot \tilde{\boldsymbol{v}}_f) \underline{\underline{I}}) \right] \tag{4.15}$$

where $\boldsymbol{g}$ stands for the gravitational field, $\underline{\underline{I}}$ represents the identity tensor, and $\overline{p_m}$ is the modified pressure, introduced to improve the effectiveness of the numerical solution [110]. It is defined from the thermodynamic pressure as $\overline{p_m} = \overline{p}_f - \overline{\rho}_f \, \boldsymbol{g} \cdot \boldsymbol{x}$. The isotropic part of the sub-grid scale stress tensor is neglected since in this work small Mach number are considered [111].

### 4.3.3 Energy Conservation

The equation is solved in terms of the enthalpy $\tilde{h}$

$$\partial_t (\overline{\rho}_f \tilde{h}_f) + \partial_{\boldsymbol{x}} \cdot (\overline{\rho}_f \tilde{\boldsymbol{v}}_f \tilde{h}_f) = \frac{D\overline{p}_f}{Dt} + \partial_{\boldsymbol{x}} \cdot (\overline{\rho}_f \, \alpha_{eff,f} \, \partial_{\boldsymbol{x}} \tilde{h}_f) + \overline{Q}_{\text{comb}} - \partial_{\boldsymbol{x}} \cdot \overline{\boldsymbol{q}}_r \tag{4.16}$$

where $\alpha_{eff,f}$ is the effective thermal diffusivity, defined as the sum of the flow mixture thermal diffusivity $\alpha_f$ with the sub-grid scale thermal diffusivity $\alpha_{sgs}$. $Q_{\text{comb}}$ is the heat generated by combustion and $\boldsymbol{q}_r$ the thermal radiation flux.

### 4.3.4 Species Transport Equations

The gas is a mixture of different species. In order to determine its composition, a transport equation for each specie is needed

$$\partial_t(\overline{\rho}_f\tilde{y_k}) + \partial_{\boldsymbol{x}} \cdot (\overline{\rho}_f \tilde{\boldsymbol{v}}_f \tilde{y_k}) = \partial_{\boldsymbol{x}} \cdot (\overline{\rho}_f D_{\text{eff},f} \partial_{\boldsymbol{x}} \tilde{y_k}) + \overline{\omega_i} \tag{4.17}$$

where $D_{\text{eff},f}$ is the effective mass diffusivity, defined as the sum of the flow diffusion coefficient $D_f$ with the sub-grid scale mass diffusivity $D_{sgs}$. $\omega_k$ is the rate of reaction of the species $k$.

### 4.3.5 Ideal Gas

The flow mixture is assumed ideal. The following equations of state are considered

$$\overline{\rho}_f = \frac{\overline{p}_f \mathcal{M}_f}{R\tilde{T}_f}, \qquad \mathcal{M}_f = \Big[\sum_{k=1}^{N_g} \frac{\tilde{y_k}}{\mathcal{M}_k}\Big]^{-1} \tag{4.18}$$

$$\tilde{h}_f = \sum_{k=1}^{N_g} \tilde{y_k} h_k(\tilde{T}), \qquad h_{s,k}(\tilde{T}) = h_k^{\text{ref}} + \int_{\tilde{T}^{\text{ref}}}^{\tilde{T}} c_{p,k} dT \tag{4.19}$$

where the Janaf model is used to evaluate the specific heat at constant pressure

$$c_{p,f}(\tilde{T}) = R\Big[\frac{a_1}{\tilde{T}^2} + \frac{a_2}{\tilde{T}} + a_3 + a_4\tilde{T} + a_5\tilde{T}^2 + a_6\tilde{T}^3 + a_7\tilde{T}^4\Big] \tag{4.20}$$

where $a_1, .., a_7$ are the Janaf coefficients given as input.
The dynamic viscosity $\mu_f$ is calculated by the Sutherland viscosity law

$$\mu_f = \frac{C_1 \tilde{T}_f^{3/2}}{\tilde{T}_f + C_2} \tag{4.21}$$

where $C_1$ and $C_2$ are the Sutherland coefficients [112].
The thermal conductivity is determined from the modified Eucken approximation [113]. The thermal diffusivity, $\alpha_f$, is given by

$$\alpha_f = \frac{k_f}{\overline{\rho}_f c_{p,f}}, \qquad c_{p,f} = \sum_{k=1}^{N_g} \tilde{y_k} c_{p,k}(\tilde{T}) \tag{4.22}$$

### 4.3.6 Combustion Model

Combustion is a high-temperature exothermic chemical reaction between a fuel and an oxidant (oxygen in this case). It is modeled with a laminar finite rate model. The effect of turbulent fluctuations is ignored and the reaction rates are determined by Arrhenius kinetic expressions. This model is then

generally inaccurate for turbulent flames and exact for laminar ones.
The chemical reaction $z$ can be written as

$$\sum_{k=1}^{N_t} \nu_{kz}^{fw} A_k^{fw} \rightleftharpoons \sum_{k=1}^{N_t} \nu_{kz}^{bw} A_k^{bw} \tag{4.23}$$

where the superscripts $fw$ and $bw$ distinguish between the forward and backward hand-sides and $N_t$ is the number of reactants and products in the chemical reaction. The overall reaction rate of this chemical reaction is

$$\omega_z = k_z^{fw} \prod_k [A^{fw}]_k^{\nu^{fw}} - k_z^{bw} \prod_k [A^{bw}]_k^{\nu^{bw}} \tag{4.24}$$

whereas the reaction rate of the specie is

$$\omega_{k,z} = \frac{d[A_k^{bw}]}{dt} = \sum_z \omega_z (\nu_{k,z}^{fw} - \nu_{k,z}^{bw}) \tag{4.25}$$

The forward and backward reaction rate constant $k^{fw}$ and $k^{bw}$ are needed in order to evaluate the reaction rates. Their calculation is done again by the Arrhenius law.
Finally, the heat generated by the reaction is

$$\overline{Q}_{comb,z} = \delta h_z \, \overline{\omega_z} \tag{4.26}$$

where $\delta h_z$ is enthalpy variation in reaction $z$.

### 4.3.7 Turbulence Model

Turbulence is modeled through the Large Eddy Simulation (LES) method. The one-equation eddy viscosity model has been used to model the sub-grid scale stress tensor. The following conservation equation for the turbulent kinetic energy is solved

$$\partial_t(\overline{\rho_f k_{sgs}}) + \partial_{\boldsymbol{x}} \cdot (\overline{\rho}_f \tilde{\boldsymbol{v}}_f k_{sgs}) = \partial_{\boldsymbol{x}} \cdot (\mu_{eff,f} \partial_{\boldsymbol{x}} k_{sgs}) - \overline{\rho}_f \underline{\underline{\tau}}_{sgs} : \tilde{\underline{\underline{S}}}_{sgs} - C_{B,1} \, \overline{\rho} \, \frac{k_{sgs}^{1.5}}{\Delta} \tag{4.27}$$

where $\Delta$ is the local filter cutoff width, calculated by taking the cubic root of the grid cell volume, $\underline{\underline{S}}_{sgs}$ and $\underline{\underline{\tau}}_{sgs}$ are the sub-grid strain rate and stress tensors, $C_{B,1}$ is a constant which value is usually set equal to 1.048 [114]. The Boussinesq approximation is considered to model the sub-grid scale stress tensor and dynamic viscosity

$$\underline{\underline{\tau}}_{sgs} = -2\mu_{sgs} \frac{1}{2} [\partial_{\boldsymbol{x}} \tilde{\boldsymbol{v}}_f + (\partial_{\boldsymbol{x}} \tilde{\boldsymbol{v}}_f)^T] + \frac{2}{3} \overline{\rho}_f k_{sgs} \underline{\underline{I}} \tag{4.28}$$

$$\mu_{sgs} = \rho \, C_{B,2} \Delta k_{sgs}^{0.5} \tag{4.29}$$

where the constant $C_{B,2}$ is usually set equal to 0.094 [114] and $k_{sgs}$ is the sub-grid scale turbulent kinetic energy.

### 4.3.8 Radiation Model

In this work no radiation model has been considered. The model is kept as simple as possible in order to prove the feasibility of the numerical tool. Moreover, for the simulations considered, the fire is so small that the radiation contribution may be negligible.

## 4.4 Numerical Model: Interface

The coupling between the two regions is schematized in Fig. 4.3. As it can be seen, at the interface

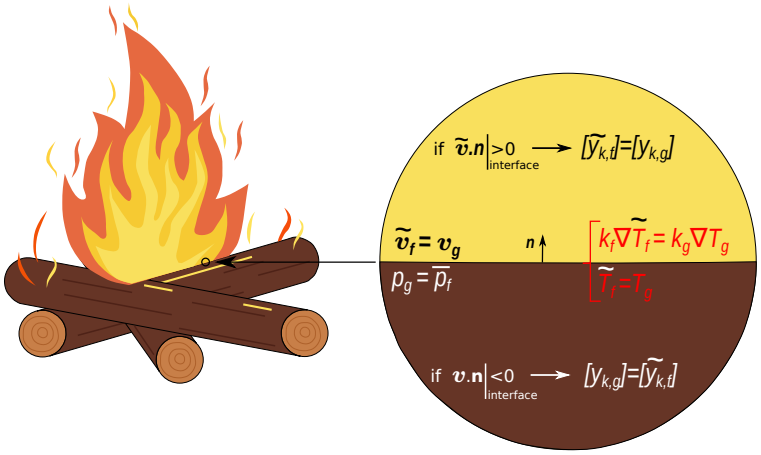


FIGURE 4.3 – Illustration of the numerical boundary conditions for the coupling between the two regions. Conditions for the velocity, temperature, pressure, and species concentration need to be imposed.

the flow updates its velocity with the one of the gas, whereas for the pressure, it is the other way around. From the thermal point of view, the coupling is done by imposing the equality of the temperatures and the normal heat fluxes at the interface. Finally, for the species concentrations, the coupling depends on the flux direction. If the flux is coming from the flow to the porous material, then the concentration of the species inside the porous domain are taken equal to the ones in the flow. In the opposite case, it is the concentration of the species in the flow which are taken equal to the ones of the gas in the porous material.

## 4.5 Results

Two test cases have been considered to illustrate the capability of the simulation tool. All the details are presented in the next subsections.

| | $\mathcal{A}$ $(s^{-1})$ | $\mathcal{E}$ $(J\ mol^{-1})$ |
|---|---|---|
| $\mathbf{CH_4}$ | 5.2 e16 | 14906 |
| $\mathbf{H_2}$ | 4.74 e12 | 10064 |

TABLE 4.1 – Kinetics parameters of the two combustion reactions. $CH_4$ indicates the combustion of the methane, whereas $H_2$ the combustion of the hydrogen.

### 4.5.1 Hydrogen vs Methane Flames

The first case considers the combustion of two gaseous species in the same domain. Two separate finite-rate combustion reactions have been considered

$$CH_4 + 2O_2 \rightarrow CO_2 + 2H_2O \tag{4.30}$$

$$2H_2 + O_2 \rightarrow 2H_2O \tag{4.31}$$

The first reaction describe the combustion reaction for methane, $CH_4$, where $O_2$, $CO_2$, and $H_2O$ indicate respectively the oxygen, carbon dioxide, and the water. The second reaction is the combustion of hydrogen, $H_2$. The kinetics of the two reactions has been modeled with an Arrhenius type formulation. The relative input parameters are showed in Table 4.1. The test case is schematized in Fig. 4.4.

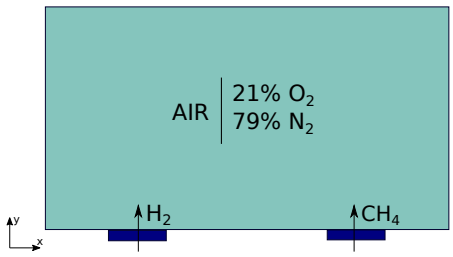


FIGURE 4.4 – Illustration of the test case: methane and hydrogen are introduced, at initial time, at high temperature inside a domain of air. The combustion reactions for both species are implemented.

The domain corresponds entirely to the environment region. Air is considered as fluid. Air is initially composed of 21% of $O_2$ and 79% of $N_2$. At time $t = 0$, methane and hydrogen are injected in the domain at two different positions at temperature $500K$. This temperature is high enough to trigger the two combustion reactions. Two flames propagate in the domain as showed in Fig. 4.5.

Different time intervals are considered. For each of them the flames are coloured based on the temperature. The two flames are different. The one on the left, that is the one due to the hydrogen combustion, is smaller and generates more energy than the one due to the combustion of methane. This is just a confirmation of what is known from the theory [115]. The hydrogen mixture burns faster than the one of methane and reaches higher temperatures (2500 K against 2100 K).
This simple case proves the importance of introducing different pyrolysis species in the overall problem. The flame, and so the overall simulation, strongly depends on the species taken into account.

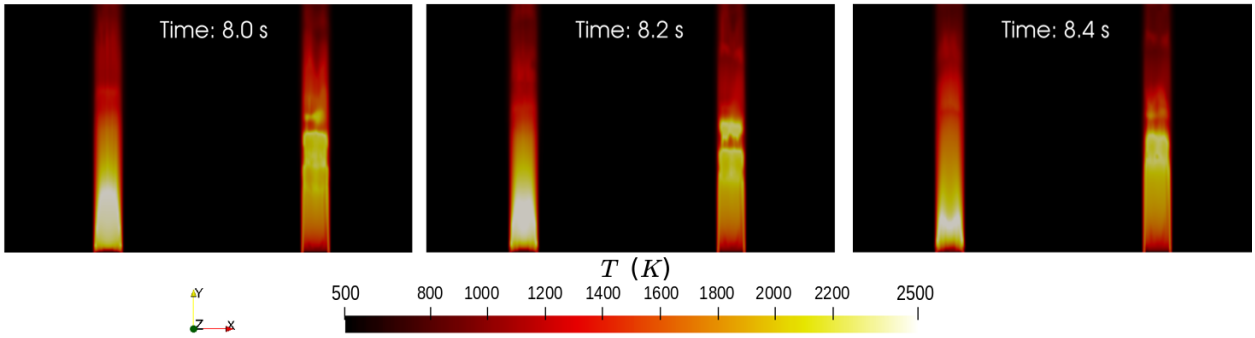


FIGURE 4.5 – Temperature description in the domain. Three different time steps are considered. The figures show on the left the flame generated by the hydrogen combustion and on the right the one generated by the methane combustion. The two flames are different from each other. They differ both in terms of temperature and in terms of size.

### 4.5.2 Wood Log Combustion

The second case aims to simulate the combustion of a wood log. The computational domain is schematized in Fig. 4.6.

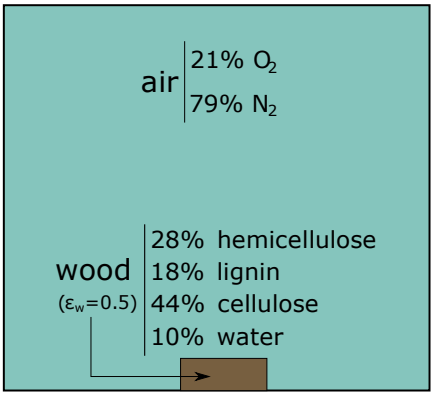


FIGURE 4.6 – Numerical domain for the simulation of the burning of a wood log. A generic hardwood composition has been considered for the log. Air, with simplified composition, has been taken as flow.

A wood log with a porosity $\epsilon_w = 0.5$ is placed at the bottom of the domain. It is modeled as being composed of 4 phases: hemicellulose, lignin, cellulose, and water. The phases composition reflects a generic hardwood. Air, with the same composition as in the previous case, is surrounding it. At time $t = 0$ the bottom part of the log is heated up by a Dirichlet condition at $800K$. Due to the heat, different pyrolysis reactions are triggered. A list of them with the considered kinetic parameters can be found in Table 4.2.

All the phases undergo different pyrolysis reactions, each characterized by different parameters. The species, once produced, percolate through the material and eventually reach the external environment. At time $t = 0.15\ s$, 2 sparks are simulated at the two sides of the log. These sparks have the purpose of

| j | Hemicellulose | $y_{1,j}$ | $\mathcal{A}_{1,j}(s^{-1})$ | $\mathcal{E}_{1,j}$ $(J\,mol^{-1})$ | $m_{1,j}$ | $n_{1,j}$ |
|---|---|---|---|---|---|---|
| 1 | $\mathcal{P}_{1,1} \longrightarrow 0.4H_2 + 0.4CO + 0.1CO_2 + 0.05CH_4 + 0.05N_2$ | 0.40 | 7.94e16 | 195000 | 1 | 0 |
| 2 | $\mathcal{P}_{1,2} \longrightarrow 0.4H_2 + 0.4CO + 0.1CO_2 + 0.05CH_4 + 0.05N_2$ | 0.30 | 1.26e7 | 106000 | 1 | 0 |
| | Cellulose | | | | | |
| 1 | $\mathcal{P}_{2,1} \longrightarrow 0.4H_2 + 0.4CO + 0.1CO_2 + 0.05CH_4 + 0.05N_2$ | 0.75 | 7.94e18 | 202650 | 1 | 0 |
| 2 | $\mathcal{P}_{2,2} \longrightarrow 0.4H_2 + 0.4CO + 0.1CO_2 + 0.05CH_4 + 0.05N_2$ | 0.16 | 1.26e7 | 245000 | 1 | 0 |
| | Lignin | | | | | |
| 1 | $\mathcal{P}_{3,1} \longrightarrow 0.4H_2 + 0.4CO + 0.1CO_2 + 0.05CH_4 + 0.05N_2$ | 0.66 | 6.0e7 | 120000 | 1 | 0 |
| | Water | | | | | |
| 1 | $\mathcal{P}_{4,1} \longrightarrow H_2O$ | 1 | 5.13e6 | 86000 | 1 | 0 |

TABLE 4.2 – Pyrolysis reactions and kinetic parameters. The four species (hemicellulose, cellulose, lignin, and water) undergo different degradation processes according to the chemical reactions listed in this table.

triggering the combustion. Methane and hydrogen start to burn and the fire evolves according to the concentration of the species in the air. Some snapshots of the first physical second of the simulation are collected in Fig. 4.7.

At around 30 $s$ of physical time, the wood log is completely pyrolysed. At around 50 $s$ of physical time, the fire is turned off due to the lack of fuel. Results in terms of $H_2$ and $CH_4$ concentration are showed in Fig. 4.8.

In the figure it can be appreciated how the concentrations of the gaseous species change in time and depend on the pyrolysis activity in the material region. The latter is captured by the parameter $\tau$ (Eq.(4.3)), that describes the advancement of the overall pyrolysis process. When $\tau = 1$, no chemical reaction has yet occurred. When $\tau = 0$ all the pyrolysis mechanisms have taken place and only char is left in the material. Some snapshots of the evolution of this parameter during the simulation are showed in Fig. 4.9.

Four different time steps have been captured, and each of them focuses on the material region. It can be appreciated how the log evolves from the initial state to the final one, where only char is left. At around 30 $s$ of physical time, all the pyrolysis reactions are completed and gas is no longer produced. Once the flame in the environment region has consumed all the fuels ($CH_4$ and $H_2$), the fire extinguishes.

A particular effect that is captured in this simulation is the so called "puffing phenomenon". It is an instability effect of the fire due to gravity, which results in a pulsation behaviour. These periodic fluctuations of the fire are repeated in time with a frequency $f$. In Fig. 4.7 the effect can be observed by looking the time laps $t = 0.5\,s$ and $t = 0.7\,s$. The two snapshots both represent the end of the respective pulsation and they are quite similar. We can deduce that for the numerical simulation, the frequency of the puffing effect is about $f_{\text{sim}} \approx 5\,Hz$. Different studies attempted to study this effect and to try to correlate it with physical dimensions [116–118]. A power law has been defined to fit the data

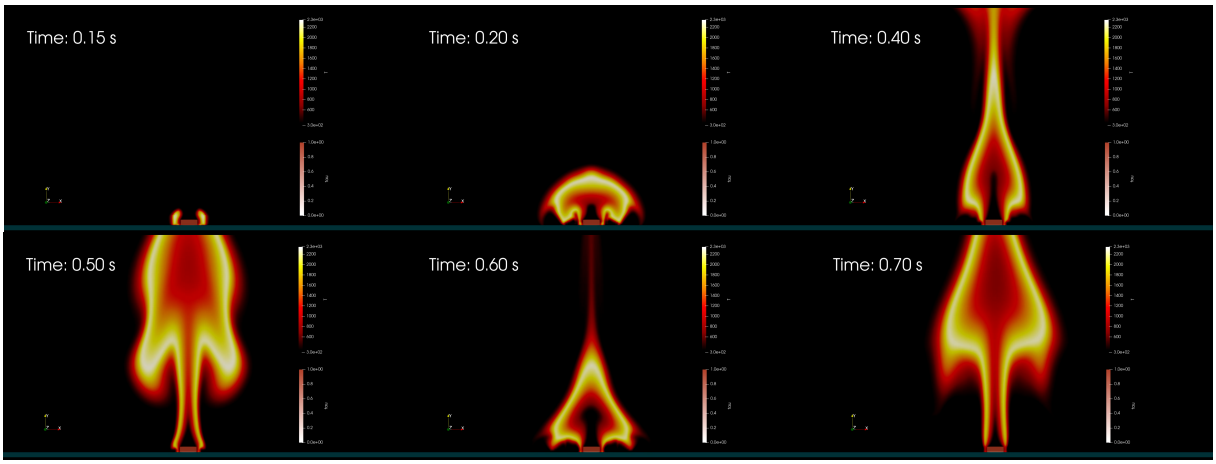


FIGURE 4.7 – Starting of the fire. Six different snapshots to represent the initial evolution of the fire. At time $t = 0.15\ s$ two sparks are generated on the side of the wood log to trigger the combustion. A fire is generated and start propagating in the domain. By comparing the time $t = 0.50\ s$ with the time $t = 0.70\ s$ it is possible to observe a periodic behaviour of the flame, the puffing effect.

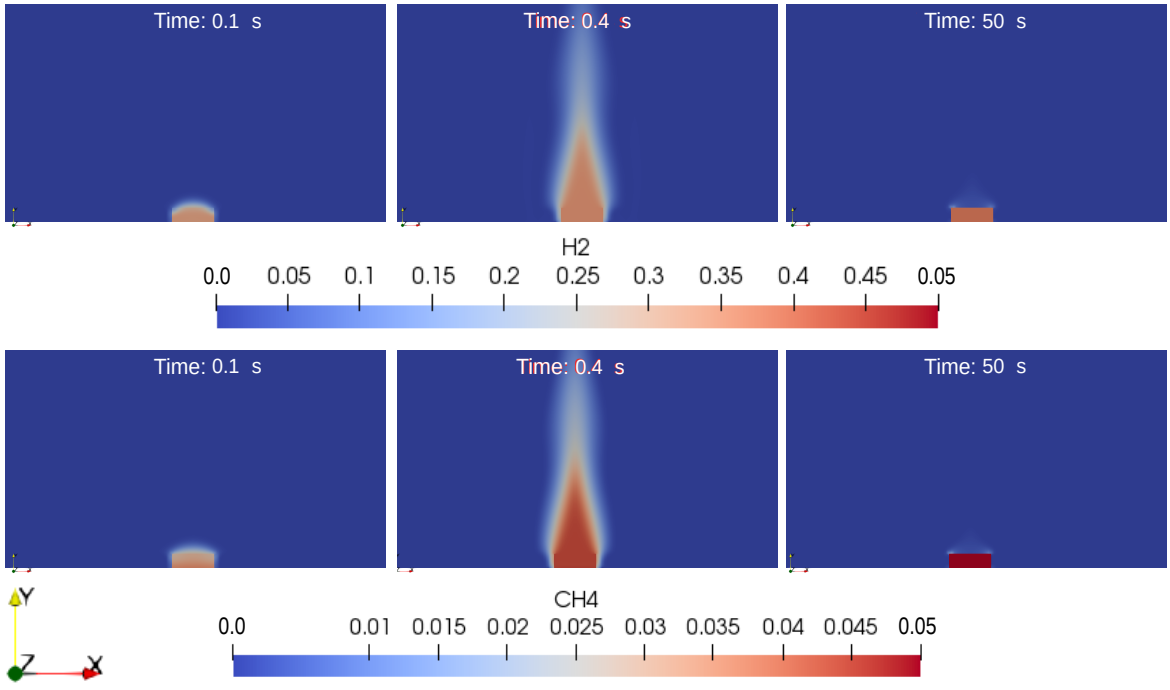


FIGURE 4.8 – Concentration of hydrogen and methane in the simulation. It can be observed how their concentration is time dependent. At time $t = 0.1\ s$ the concentration of the gases in the environment region is close to zero. With time, thanks to the advancement of pyrolysis, their concentration increases. For the two gases different values of concentration are reached. At time $t = 50\ s$ it can be see how the fire has consumed the two species and their concentration is again nearly zero.

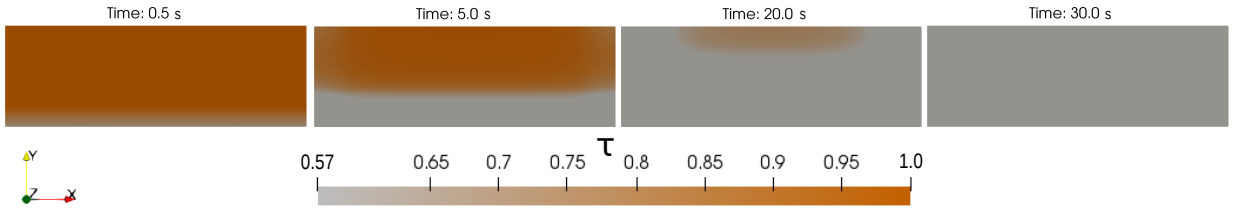


FIGURE 4.9 – Advancement of pyrolysis of the wood log during the simulation. When $\tau = 1$, no chemical reactions has still occurred. When $\tau = 0$ all the pyrolysis mechanisms have taken place and only char is left in the material. At time $t = 0.5\ s$ it can be seen how the pyrolysis process starts from the bottom of the material and at time $t = 30\ s$ how all the material has been pyrolysed.

$$f_{pl} = 1.5\frac{1}{\sqrt{L}} \tag{4.32}$$

where $L$ in this case is the burner diameter. By considering the diameter of the fire at the base as the measure of $L$, it is possible to find out that this correlation gives us $f_{pl} \approx 7\ Hz$. The two measures of the puffing frequency are approximately the same.

## 4.6 Conclusions

This study proposes a new numerical framework to investigate the combustion of pyrolysis materials. A detailed three-dimensional pyrolysis model is coupled with fireFoam, a numerical solver for combustion processes. The pyrolysis model captures the physics in the material region and describes the interaction between a multi-phase reactive material with a multi-species reactive gas mixture. The description is done at the macroscopic scale, where the governing equations are derived from upscaling theories. FireFoam is used to describe the environment region. Its governing equations are derived from the Navier-Stokes equations after applying the LES filtering process and using the Favre mean variables. The two models are coupled at the material-environment interface, where specific conditions for velocity, pressure, temperature, and species concentration are imposed. Two applications are considered to illustrate the capabilities of the tool. The first one considers the combustion of two different gaseous species with the implementation of two separate finite-rate combustion reactions. Results show how the two generated flames differ between each other in terms of temperature and reaction times. The behaviour of the flames is strongly influenced by the pyrolysis species considered in the model. The second case illustrates the combustion of a wood log. Results illustrate how gaseous species are produced with time through the pyrolysis of the wood log and how these species enter in the environmental region to start and sustain the flame. Thanks to the flame and to the temperature increase, the pyrolysis processes speed up and the species concentrations continuously change in time according to the rate of reactions. Once the wood is fully pyrolysed, the fire consumes all the fuels and extinguishes by itself. The puffing effect can be observed during the evolution of the simulation: the fire exhibits periodic fluctuations that follow each other with a numerical frequency that is approximately the same as the theoretical one.

The numerical framework that was developed during this study is available in the Porous material Analysis Toolbox based on OpenFoam (PATO) released Open Source by NASA (www.pato.ac).

# Part II

# Contribution to the Numerical Estimation of the Effective Properties

# Chapitre 5

# Computation of the Permeability Tensor of Non-Periodic Anisotropic Porous Media from 3D Images

**Nomenclature**

*Latin Letters*

| | |
|---|---|
| $c$ | artificial compressibility coefficient $[m^{1/2}s^{-1/2}]$ |
| $\underline{\underline{d}}$ | velocity deviation tensor $[m\ s^{-1}]$ |
| $\boldsymbol{e}$ | pressure deviation term $[Pa]$ |
| $\underline{\underline{I}}$ | identity tensor |
| $\underline{\underline{K}}$ | permeability tensor $[m^2]$ |
| $\boldsymbol{l}$ | size of the periodic domain |
| $\ell$ | reference length $[m]$ |
| $N$ | total number of values predicted by the strategies |
| $p$ | pore-scale pressure $[Pa]$ |
| $\boldsymbol{r}$ | position vector $[m]$ |
| $S$ | interface area $[m^2]$ |
| $\boldsymbol{v}$ | pore-scale velocity $[m\ s^{-1}]$ |
| $V$ | volume of the domain $[m^3]$ |
| $\boldsymbol{w}$ | pore-scale vorticity $[s^{-1}]$ |
| $\boldsymbol{x}$ | pore-scale coordinates $[m]$ |

*Greek Letters*

| | |
|---|---|
| $\delta$ | thickness of the lateral fluid layer $[m]$ |
| $\epsilon$ | porosity of the medium |
| $\theta$ | rotation angle |

## Nomenclature

| | |
|---|---|
| $\mu$ | dynamic viscosity $[Pa\ s]$ |
| $\rho$ | pore-scale density $[kg\ m^{-3}]$ |

*Symbols*

| | |
|---|---|
| $*$ | non-dimensional variable |
| $\langle\rangle$ | intrinsic average |
| $\langle\rangle^g$ | phase average |
| $\sim$ | deviation term |

*Subscripts and Superscripts*

| | |
|---|---|
| art | artificial |
| avg | average |
| cl | cluster |
| dg | diagonal |
| g | gas |
| s | solid |

*Adimensional Groups*

| | |
|---|---|
| Re | Reynolds number |

*Acronyms*

| | |
|---|---|
| CMT | Computed Micro-Tomography |
| PATO | Porous material Analysis Toolbox based on OpenFoam |
| REV | Representative Elementary Volume |

## Preamble

Authors: H. Scandelli; A. Ahmadi-Senichault; C. Levet; J. Lachaud;
Affiliations: Arts et Métiers Institute of Technology, Univ. Bordeaux, CNRS, Bordeaux INP, I2M, UMR 5295, F-33400 Talence, France;
Published: Yes;
Journal: Transport in Porous Media;
Published: 13 April 2022;
DOI: https://doi.org/10.1007/s11242-022-01766-8;
Conference: This work has been presented at the 12th Annual InterPore2020 Meeting, 31 August 2020 to 4 September 2020, online;

## Abstract

The direct proportionality between the flow rate and the pressure gradient of creeping flows was experimentally discovered by H. Darcy in the 19th century and theoretically justified a couple of decades ago using upscaling methods such as volume averaging or homogenisation. X-ray computed micro-tomography (CMT) and pore-scale numerical simulations are increasingly being used to estimate the permeability of porous media. However, the most general case of non-periodic anisotropic porous media still needs to be completely numerically defined. Pore-scale numerical methods can be split into two families. The first family is based on a direct resolution of the flow solving the Navier-Stokes equations under the assumption of creeping flow. The second one relies on the resolution of an indirect problem - such as the closure problem derived from the volume averaging theory. They are known to provide the same results in the case of periodic isotropic media or when dealing with representative element volumes (REV). To address the most general case of non-periodic anisotropic porous media, we have identified four possible numerical approaches for the first family and two for the second. We have compared and analyzed them on three-dimensional generated geometries of increasing complexity, based on sphere and cylinder arrangements. Only one, belonging to the first family, has been proved to remain rigorously correct in the most general case. This has been successfully applied to a high-resolution 3D CMT of Carcarb, a carbon fiber preform used in the thermal protection systems of space vehicles. The study concludes with a detailed analysis of the flow behaviour (streamlines and vorticity). A quantitative technique based on a vorticity criterion to determine the characteristic length of the material is proposed. Once the characterized length is known, the critical Reynolds number can be estimated and the physical limit of the creeping regime identified.

**Keywords**: Porous media; Permeability tensor; Pore-scale numerical simulations; Micro-CT image; Calcarb; Characteristic length scale

## 5.1 Introduction

At the pore scale, the flow of a Newtonian and incompressible fluid in a solid porous medium is described by the Navier-Stokes equations. Under the assumption of steady-state flow and negligible volume forces, these equations become

$$\begin{cases} \partial_{\boldsymbol{x}} \cdot \boldsymbol{v} = 0 \\ \partial_{\boldsymbol{x}} \cdot (\rho\, \boldsymbol{v} \otimes \boldsymbol{v}) - \partial_{\boldsymbol{x}} \cdot (\mu\, \partial_{\boldsymbol{x}} \boldsymbol{v}) = -\partial_{\boldsymbol{x}} p \\ BC: \quad \boldsymbol{v} = \boldsymbol{0} \quad at\ S_{gs} \end{cases} \tag{5.1}$$

where $\rho$ and $\mu$ denote the density and the dynamic viscosity of the fluid, $\boldsymbol{v}$ and $p$ the pore-scale velocity and pressure, and $S_{gs}$ the fluid-solid area interface. The above system of equations may be written in a non-dimensional form by introducing the dimensionless variables reported in Table 5.1. In order

| quantity | dimensionless variable |
|---|---|
| length | $\boldsymbol{r}^* = \boldsymbol{r}/\ell$ and $\partial_{\boldsymbol{x}^*} = \ell\partial_{\boldsymbol{x}}$ |
| velocity | $\boldsymbol{v}^* = \boldsymbol{v}/\langle\boldsymbol{v}\rangle$ |
| pressure | $p^* = p\ell/(\mu\langle\boldsymbol{v}\rangle)$ |

TABLE 5.1 – Non-dimensional variables for making Eq. (5.1) dimensionless.

to completely define them, three reference values need to be chosen. In porous media, the reference velocity is taken as the magnitude of the average velocity in the domain, $\langle\boldsymbol{v}\rangle$ [90]. For the reference length, $\ell$, the choice is not trivial as porous micro-structures are very diverse and better characterized by different lengths. The most widely adopted in the modern literature is the porous medium grain diameter [119]. Once the dimensionless variables have been introduced, Eq. (5.1) can be written as

$$\begin{cases} \partial_{\boldsymbol{x}^*} \cdot \boldsymbol{v}^* = 0 \\ Re\ \ \partial_{\boldsymbol{x}^*} \cdot (\boldsymbol{v}^* \otimes \boldsymbol{v}^*) - \partial^{*2}_{\boldsymbol{x}} \boldsymbol{v}^* = -\partial_{\boldsymbol{x}^*} p^* \\ BC: \ \ \boldsymbol{v}^* = \boldsymbol{0} \qquad at\ S_{gs} \end{cases} \tag{5.2}$$

where $Re$ is the Reynolds number defined as

$$Re = \frac{\rho\,\langle\boldsymbol{v}\rangle\,\ell}{\mu} \tag{5.3}$$

The Reynolds number characterizes the relative importance of inertial and viscous forces within a fluid. For $Re \ll 1$, viscous forces dominate and the flow is said to be in the creeping regime, also known as the Darcy regime. In this regime, a generalized form of Darcy's law finds its validity at the macroscopic scale and the system of Eq. (5.2) becomes [102]

$$\begin{cases} \partial_{\boldsymbol{x}} \cdot \langle\boldsymbol{v}\rangle = 0 \\ \langle\boldsymbol{v}\rangle = -\dfrac{1}{\mu}\,\underline{\underline{K}} \cdot \partial_{\boldsymbol{x}} \langle p\rangle^g \end{cases} \tag{5.4}$$

where $\langle p\rangle^g$ and $\langle\boldsymbol{v}\rangle$ are the macroscopic pressure and velocity (see Appendix A (Section 5.6)) and $\underline{\underline{K}}$ is the permeability tensor. However, when increasing the Reynolds number inertial forces are no longer negligible and Darcy's law loses its validity. Extensions to Darcy's law have been proposed to capture the physics of inertial [120–122], transition (unsteady laminar) [90], and turbulence regimes [119].

For most engineering applications related to transport processes in porous media, macroscopic models are used to evaluate the macroscopic pressure and velocity fields [75, 123–128]. In this way the physics of the problem are greatly simplified as showed in Fig. 5.1. Simplifications come from the introduction of macroscopic properties, such as the permeability tensor, that enclose information about the micro-scopic interactions between the flow and the material. The counterpart is a loss of information: the pore-scale approach provides the detailed velocity and pressure fields from the direct resolution of Eq. (5.1) whereas the macro-scale one only provides averaged (macroscopic) values of these two fields from the resolution of macroscopic models, such as the Darcy model presented in Eq. (5.4). One important

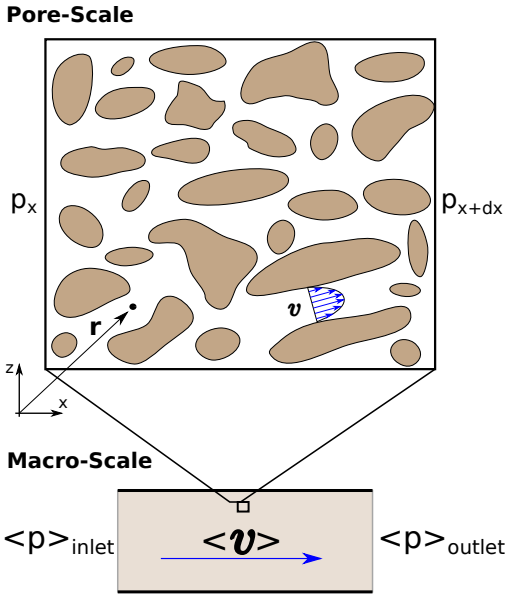


FIGURE 5.1 – Pore-scale and macro-scale descriptions of the transport problem in porous media.

advantage that emerges from the micro-scale studies is the possibility of visualizing the flow behaviour in digital images. The study of streamlines and pressure gradients throughout the domain brings very rich insight. This quantitative microscopic information can be used to better define the characteristic length $\ell$ as well as to introduce physical parameters as transition criterion, such as the maximum local vorticity. This quantity will be used in this article to derive a new criterion for the validity of Darcy's law.

The objective of this work is to establish and validate a numerical strategy to estimate the anisotropic permeability tensor. This tensor is an essential input to the macroscopic models. It can be determined in several ways. Obviously, experiments can be performed to infer the effective properties. To-date, this remains the most reliable and preferred way [18, 23, 129–131]. With the generalization of super-computers during the last two decades, on the one hand the developing of pore-network models and the possibility to perform lightweight simulations on common laptop, on the other hand numerical simulations have progressively gained popularity for the computation of effective properties [132–135]. They are particularly useful to study conditions not accessible in the laboratory [9]. Digitalized geometries of porous media can be obtained either by an idealized mathematical representation or by a reconstructed digital image. In the first case the pore structure is described from a statistical point of view [39] and then reconstructed with small primitive objects within a finite domain [30]. Finally, numerical simulations can be performed in order to obtain approximation of the effective properties [27–30, 136]. In the second case actual digital images are obtained, typically by X-ray CMT [137, 138], and simulations can be performed on the precise geometries. Porous ceramic [31, 34, 139], metal foams [35, 36], fibrous materials [9, 140], and rock samples [37, 38], are just some examples of the materials that have already been analyzed using this approach.

Regardless of the method used to produce the digital image, pore-scale numerical simulations need to be defined in terms of computational domains and boundary conditions. In this article, we denote as *strategy* a generic numerical setting in terms of the considered domain (sample) and the boundary conditions of a pore-scale simulation. It is a well-known fact [40, 41, 141] that the latter need to be chosen carefully as they strongly impact the results if the sample scale is not a representative element volume (REV). The strategies proposed in the literature are presented in Fig. 5.2 where computational domains are represented in two dimensions for an easier comprehension. Different comments on the strategies may be made:

- The strategies can be split into two families: strategies A [34, 142–144], B [40], C, and D1 [39, 40, 145, 146], which aim to determine the permeability tensor from Darcy's law where pressure and velocity terms are obtained by solving the Navier-Stokes equations with $Re \ll 1$ and then properly averaged; strategies D2 [40] and E [39, 40, 146] which aim to determine the tensor by solving the closure problem derived from upscaling techniques [102, 147];
- In strategies B, C, D1/2, and E, periodic boundary conditions are imposed on the pressure deviation (see Aappendix A (Section 5.6)) and on the velocity field [40];
- In strategies A, B, and C, the effective domain is enclosed between two buffer domains in order to avoid inlet/outlet boundary effects. The averaging of the flow properties is performed only inside the effective domain;
- In strategies B, D1, and D2, a layer of pure fluid of a thickness $\delta$ is added between the effective domain and the boundaries in order to enforce periodic boundary conditions. The thickness, $\delta$, should be large enough to make the domain periodic, but small enough to avoid any possible influence on the problem. To be noticed that for periodic domains $\delta$ could also be set equal to zero.
- In strategy E, the domain is made periodic by three symmetry operations (one for each axis); in strategy C, the domain is made symmetric on the direction orthogonal to the flow (in the figure, planes with normal vectors in the y and z directions).

The choice of the strategy to adopt depends on the studied porous medium. This aspect has been highlighted numerous times in the literature. Pickup et al, 1994 [141], investigated the impact of several flow models on the calculation of the permeability tensors for sedimentary structures. They demonstrated that periodic boundary conditions are reliable in the example problems considered and that in many cases the differences between the various methods were slight. However, periodic boundary conditions can be considered only for periodic media or when dealing with volumes large enough to be considered as REV. For the other cases, a non-periodic strategy needs to be defined. Manwart et al, 2002 [148], analyzed and compared the accuracy of two different numerical algorithms (one based on the lattice-Boltzmann method and the other on finite-difference techniques) for computing the permeability of three-dimensional porous media. They argued in favour of the finite difference code for different reasons. A relevant study on the estimation of the effects of the boundary conditions on the numerical simulations has been proposed by Guibert et al, 2016 [40]. They selected strategy A with fixed pressure boundary conditions as the most suitable one in the case of 2D periodic synthetic porous media. A further step in this analysis has been proposed by Gerke et al, 2019 [41], where they investigated possible strategies to capture the tensorial nature of the permeability tensor when dealing

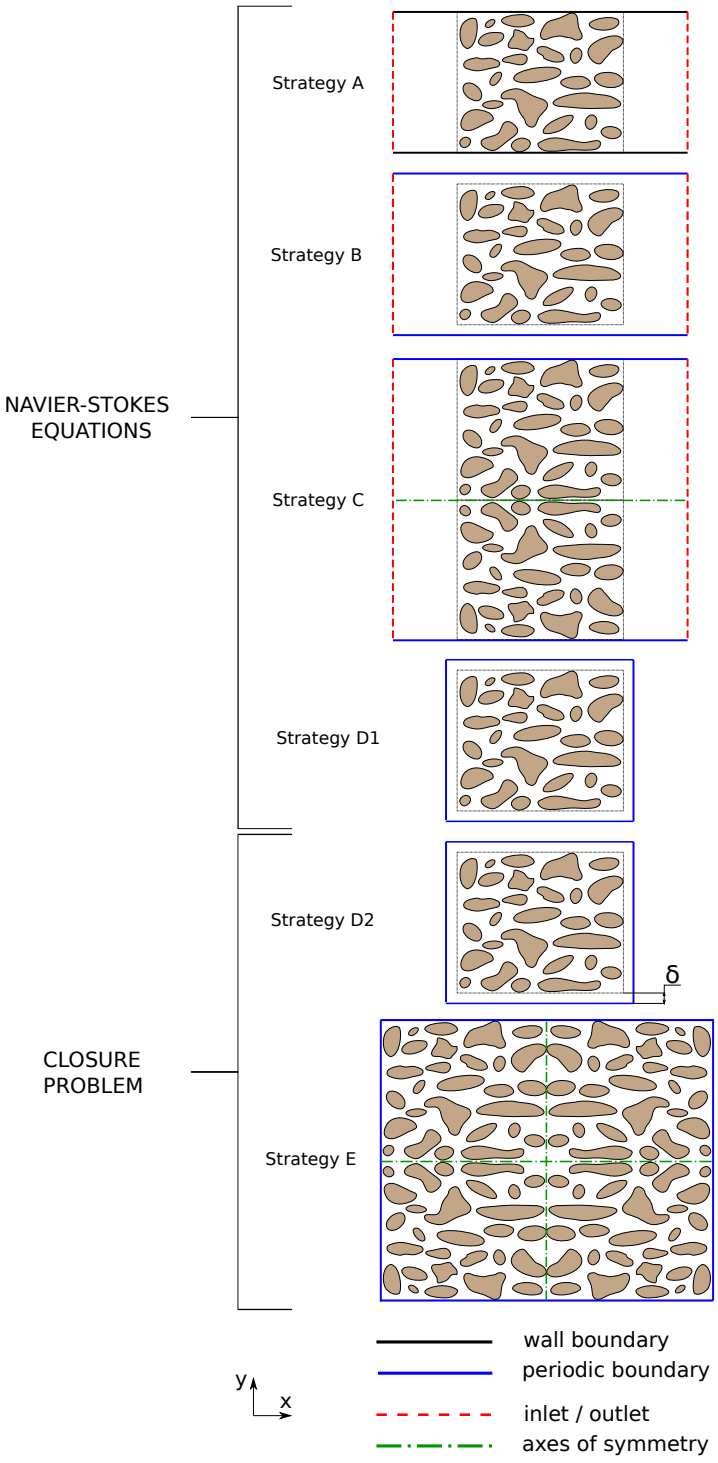


FIGURE 5.2 – 2D sketches of the computational domains of the six selected strategies between the most used in the literature.

with periodic stochastic reconstructions of porous media. They came to the conclusion that strategy D was the only way to obtain symmetric permeability tensor that preserved traversal fluxes.

The main objective of this work is to define for the first time a complete numerical procedure to estimate the permeability tensor of non-periodic anisotropic porous media when dealing with volumes not large enough to be considered as REV. A mathematical description of the two families of approaches presented in the introduction is given in Section 5.2. In Section 5.3, the six possible strategies are fully described and down-selected thanks to comparisons against well-known elementary test cases, such as beds of spheres and cylinders. Actually, only strategy A was found to provide correct predictions in the most general case of anisotropic non-periodic porous media. In Section 5.4, this strategy is applied to estimate the permeability tensor of a carbon fiber preform, called Calcarb, and compared with data from the literature. This section also introduces, verifies, and applies a microscopic criterion based on the vorticity to estimate the limit of validity of the creeping regime. We show that the study of the vorticity at the pore scale also helps to identify the proper characteristic length of the domain. Conclusions of the work are finally presented in Section 5.5.

## 5.2 Mathematical Description of the Two Families of Approaches

As introduced before, there are two families of approaches that can be used to estimate the permeability tensor.

The first family relies on direct simulations at the pore-scale using Eq. (5.1). Pressure gradients and velocity components are then averaged at the macroscopic scale and substituted into Darcy's law. The latter is conveniently decomposed into the following system

$$\begin{cases} \langle v\rangle_x = -\dfrac{1}{\mu}(K_{xx}\partial_{\boldsymbol{x}}\langle p\rangle_x^g + K_{xy}\partial_{\boldsymbol{x}}\langle p\rangle_y^g + K_{xz}\partial_{\boldsymbol{x}}\langle p\rangle_z^g) \\ \langle v\rangle_y = -\dfrac{1}{\mu}(K_{yx}\partial_{\boldsymbol{x}}\langle p\rangle_x^g + K_{yy}\partial_{\boldsymbol{x}}\langle p\rangle_y^g + K_{yz}\partial_{\boldsymbol{x}}\langle p\rangle_z^g) \\ \langle v\rangle_z = -\dfrac{1}{\mu}(K_{zx}\partial_{\boldsymbol{x}}\langle p\rangle_x^g + K_{zy}\partial_{\boldsymbol{x}}\langle p\rangle_y^g + K_{zz}\partial_{\boldsymbol{x}}\langle p\rangle_z^g) \end{cases} \tag{5.5}$$

Following the pore-scale simulations, the components of the macroscopic velocity, $\langle v\rangle_x, \langle v\rangle_y, \langle v\rangle_z$ are obtained as averaged values over the domain and the components of the pressure gradients across the material, $\partial_{\boldsymbol{x}}\langle p\rangle_x^g, \partial_{\boldsymbol{x}}\langle p\rangle_y^g, \partial_{\boldsymbol{x}}\langle p\rangle_z^g$, are obtained from the averaged pressure values over the boundaries and the domain sizes in the $x, y, z$ directions. The remaining unknowns of the system are the nine permeability components, namely $K_{xx}, K_{xy}, ..., K_{zz}$. Therefore, in order to have a closed system, it is necessary to perform a total of three simulations by considering three different flow directions. In this way a global system of nine equations can be defined such as showed in Eq. (5.6), where the exponents $1, 2, 3$ refer to the first, second, and third numerical simulations. For simplicity those simulations can be done such that the inlet flow is aligned with the x, y and finally z directions. Once $\underline{\underline{K}}$ is determined from this system, the symmetry conditions [149] on the extra-diagonal components need to be applied in order to enforce the equality of two components which may differ slightly from each other. To be

$$\begin{bmatrix} \langle v\rangle_x^1 \\ \langle v\rangle_y^1 \\ \langle v\rangle_z^1 \\ \langle v\rangle_x^2 \\ \langle v\rangle_y^2 \\ \langle v\rangle_z^2 \\ \langle v\rangle_x^3 \\ \langle v\rangle_y^3 \\ \langle v\rangle_z^3 \end{bmatrix} = -\frac{1}{\mu} \begin{bmatrix} \partial_{\boldsymbol{x}}\langle p\rangle_x^{g,1} & \partial_{\boldsymbol{x}}\langle p\rangle_y^{f,1} & \partial_{\boldsymbol{x}}\langle p\rangle_z^{g,1} & 0 & 0 & 0 & 0 & 0 & 0 \\ 0 & 0 & 0 & \partial_{\boldsymbol{x}}\langle p\rangle_x^{g,1} & \partial_{\boldsymbol{x}}\langle p\rangle_y^{f,1} & \partial_{\boldsymbol{x}}\langle p\rangle_z^{f,1} & 0 & 0 & 0 \\ 0 & 0 & 0 & 0 & 0 & 0 & \partial_{\boldsymbol{x}}\langle p\rangle_x^{g,1} & \partial_{\boldsymbol{x}}\langle p\rangle_y^{g,1} & \partial_{\boldsymbol{x}}\langle p\rangle_z^{g,1} \\ \partial_{\boldsymbol{x}}\langle p\rangle_x^{g,2} & \partial_{\boldsymbol{x}}\langle p\rangle_y^{g,2} & \partial_{\boldsymbol{x}}\langle p\rangle_z^{g,2} & 0 & 0 & 0 & 0 & 0 & 0 \\ 0 & 0 & 0 & \partial_{\boldsymbol{x}}\langle p\rangle_x^{g,2} & \partial_{\boldsymbol{x}}\langle p\rangle_y^{g,2} & \partial_{\boldsymbol{x}}\langle p\rangle_z^{g,2} & 0 & 0 & 0 \\ 0 & 0 & 0 & 0 & 0 & 0 & \partial_{\boldsymbol{x}}\langle p\rangle_x^{g,2} & \partial_{\boldsymbol{x}}\langle p\rangle_y^{g,2} & \partial_{\boldsymbol{x}}\langle p\rangle_z^{g,2} \\ \partial_{\boldsymbol{x}}\langle p\rangle_x^{g,3} & \partial_{\boldsymbol{x}}\langle p\rangle_y^{g,3} & \partial_{\boldsymbol{x}}\langle p\rangle_z^{g,3} & 0 & 0 & 0 & 0 & 0 & 0 \\ 0 & 0 & 0 & \partial_{\boldsymbol{x}}\langle p\rangle_x^{g,3} & \partial_{\boldsymbol{x}}\langle p\rangle_y^{g,3} & \partial_{\boldsymbol{x}}\langle p\rangle_z^{g,3} & 0 & 0 & 0 \\ 0 & 0 & 0 & 0 & 0 & 0 & \partial_{\boldsymbol{x}}\langle p\rangle_x^{g,3} & \partial_{\boldsymbol{x}}\langle p\rangle_y^{g,3} & \partial_{\boldsymbol{x}}\langle p\rangle_z^{g,3} \end{bmatrix} \begin{bmatrix} K_{xx} \\ K_{xy} \\ K_{xz} \\ K_{yx} \\ K_{yy} \\ K_{yz} \\ K_{zx} \\ K_{zy} \\ K_{zz} \end{bmatrix} \tag{5.6}$$

noted that even if the real unknowns of the tensor are six, three simulations are required to fully compute them. In order to solve Eq. (5.6), the matrix of the pressure gradients should be invertible, that is, its determinant should be different from zero. In the creeping regime, an equivalent condition for that is

$$\left(\langle \boldsymbol{v}\rangle^1 \times \langle \boldsymbol{v}\rangle^2\right) \cdot \langle \boldsymbol{v}\rangle^3 \neq 0 \tag{5.7}$$

The second family of strategies is based on upscaling theories to evaluate the permeability. As long as the same physical hypotheses are used, results coming from the different techniques are the same [17,150]. In this work we have chosen to adopt the volume averaging theory. The method leads to the definition of the following closure problem [102,147]

$$\begin{cases} \partial_{\boldsymbol{x}}\boldsymbol{e} - \partial^2_{\boldsymbol{x}}\underline{\underline{d}} = \underline{\underline{I}} & in\ V \\ \partial_{\boldsymbol{x}} \cdot \underline{\underline{d}} = 0 & in\ V \\ BC1 : \underline{\underline{d}} = 0 & at\ S_{gs} \\ BC2 : \underline{\underline{d}}(\boldsymbol{r}+\boldsymbol{l}) = \underline{\underline{d}}(\boldsymbol{r}),\ \ \boldsymbol{e}(\boldsymbol{r}+\boldsymbol{l}) = \boldsymbol{e}(\boldsymbol{r}) & \end{cases} \tag{5.8}$$

where $\boldsymbol{e}$ is the pressure deviation term (see Appendix A (Section 5.6)) and $\underline{\underline{d}}$ the velocity deviation tensor. $BC2$ enforces periodic boundary conditions for the two deviation components, being $\boldsymbol{l}$ the size of the periodic domain. The permeability tensor is a function of the velocity deviation tensor as follows

$$\underline{\underline{K}} = -\,\epsilon\,\frac{1}{V}\int_V \underline{\underline{d}}\; dV \tag{5.9}$$

where $\epsilon$ is the porosity of the medium and $V$ the volume of the domain.

In this work, both volume averaging upscaling and direct simulations at the pore-scale are addressed using OpenFoam [151] for the simulations and Paraview [152] for the post-processing. Navier-Stokes equations are solved with SIMPLE [153,154], a steady-state solver for incompressible flow. The closure problem (Eq. (5.8)) is solved with KclosureSolver (more information in Appendix B (Section 5.7)), a solver that we have implemented and that is released in the Open Source in the Porous material Analysis Toolbox based on OpenFOAM (PATO) [73,155].

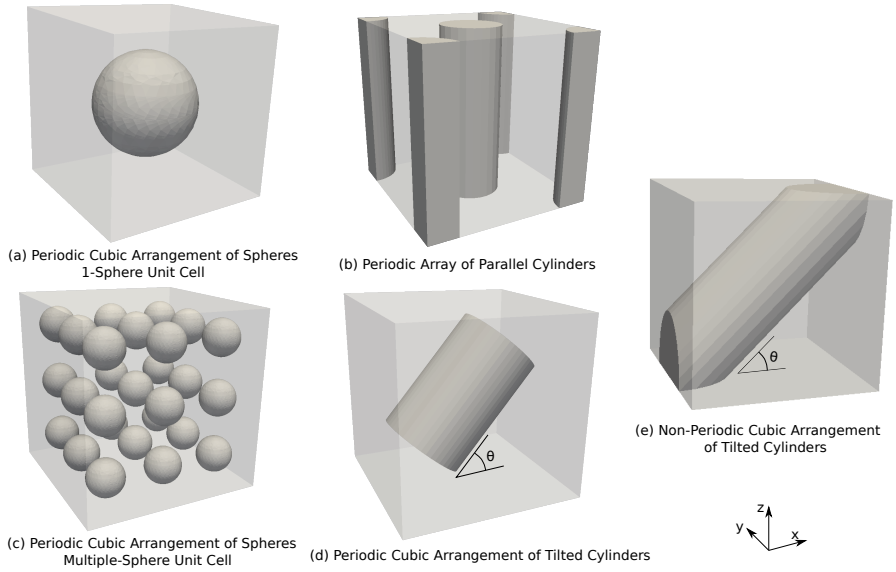


FIGURE 5.3 – Six basic test cases with increasing complexity used to apply, compare, and select the most suitable strategy.

## 5.3 Down-Selection of the numerical strategy

We have implemented the six different strategies showed in Fig. 5.2 with the objective of verifying their validity on simple test cases to select the most suitable one. The simple test cases considered are showed in Fig. 5.3 and presented in the following sections. Reference values are available in the literature for configurations (a), (b) and (c) [7,8]. We have chosen simple domains with increasing complexity thus allowing us to progressively discard inaccurate strategies. Strategies needed to be defined in terms of boundary conditions for pressure and velocity. Different combinations may be considered. Therefore, to be as thorough as possible seven sub-strategies have been defined in order to take all combinations into account. They are summarized in Table 5.2.

In the following sections, strategies are compared between each other and to reference solutions. For such purpose, the following relative error is defined

$$\text{relative error} = \frac{1}{N}\sum_{n}^{N}\frac{K_{\text{ref},n} - K_n}{K_{\text{ref},n}}\,100 \tag{5.10}$$

where $K_n$ is a generic permeability value resulted from the simulation and N is the total number of values predicted by the strategies. As generic indication, strategies will be discarded when their relative error is higher than 25%.

| / | | *fixedValue* | | *periodic* | | *slip* | | *no-slip* | | *zero gradient* | | *linear gradient* | |
|---|---|---|---|---|---|---|---|---|---|---|---|---|---|
| | | $\boldsymbol{v}$ | $p$ | $\boldsymbol{v}$ or $\underline{\underline{d}}$ | $p$ or $\boldsymbol{e}$ | $\boldsymbol{v}$ | $p$ | $\boldsymbol{v}$ | $p$ | $\boldsymbol{v}$ | $p$ | $\boldsymbol{v}$ | $p$ |
| **S A1** | *inlet* | | | | | | | | | | | | |
| | *outlet* | | | | | | | | | | | | |
| | *buffer wall* | | | | | | | | | | | | |
| | *effective wall* | | | | | | | | | | | | |
| **S A2** | *inlet* | | | | | | | | | | | | |
| | *outlet* | | | | | | | | | | | | |
| | *buffer wall* | | | | | | | | | | | | |
| | *effective wall* | | | | | | | | | | | | |
| **S A3** | inlet | | | | | | | | | | | | |
| | outlet | | | | | | | | | | | | |
| | *buffer wall* | | | | | | | | | | | | |
| | *effective wall* | | | | | | | | | | | | |
| **S A4** | inlet | | | | | | | | | | | | |
| | outlet | | | | | | | | | | | | |
| | *buffer wall* | | | | | | | | | | | | |
| | *effective wall* | | | | | | | | | | | | |
| **S A5** | inlet | | | | | | | | | | | | |
| | outlet | | | | | | | | | | | | |
| | *buffer wall* | | | | | | | | | | | | |
| | *effective wall* | | | | | | | | | | | | |
| **S A6** | inlet | | | | | | | | | | | | |
| | outlet | | | | | | | | | | | | |
| | *buffer wall* | | | | | | | | | | | | |
| | *effective wall* | | | | | | | | | | | | |
| **S A7** | inlet | | | | | | | | | | | | |
| | outlet | | | | | | | | | | | | |
| | *buffer wall* | | | | | | | | | | | | |
| | *effective wall* | | | | | | | | | | | | |
| **S B** | inlet | | | | | | | | | | | | |
| | outlet | | | | | | | | | | | | |
| | *buffer wall* | | | | | | | | | | | | |
| | *effective wall* | | | | | | | | | | | | |
| **S C** | inlet | | | | | | | | | | | | |
| | outlet | | | | | | | | | | | | |
| | *effective wall* | | | | | | | | | | | | |
| **S D1** | inlet | | | | | | | | | | | | |
| | outlet | | | | | | | | | | | | |
| | *effective wall* | | | | | | | | | | | | |
| **S D2** | inlet | | | | | | | | | | | | |
| | outlet | | | | | | | | | | | | |
| | *effective wall* | | | | | | | | | | | | |
| **S E** | inlet | | | | | | | | | | | | |
| | outlet | | | | | | | | | | | | |
| | *effective wall* | | | | | | | | | | | | |

TABLE 5.2 – List of all the strategies considered determining the permeability. Velocity and pressure settings are indicated respectively in blue and red. For the pressure, *zero gradient* means that the pressure gradient normal to the wall is set to zero. For the velocity, the *slip condition* preserves the velocity tangential to the wall and sets to zero the normal component.

### 5.3.1 Periodic Cubic Arrangement of Spheres: 1-Sphere Unit Cell

The unit cell of this domain consists of a solid sphere and a cubic fluid zone (Fig. 5.3a) thus leading to an isotropic porous medium for which the permeability tensor reduces to a diagonal tensor with equal components (K = $K_{xx} = K_{yy} = K_{zz}$). Four cases are considered, each one characterized by a different sphere radius, hence a different porosity.
The permeabilities computed with strategies A (including the 7 sub-strategies), B, D1, and D2 are plotted in Fig. 5.4. Strategies C and E are not necessary here as the domain is already symmetric.

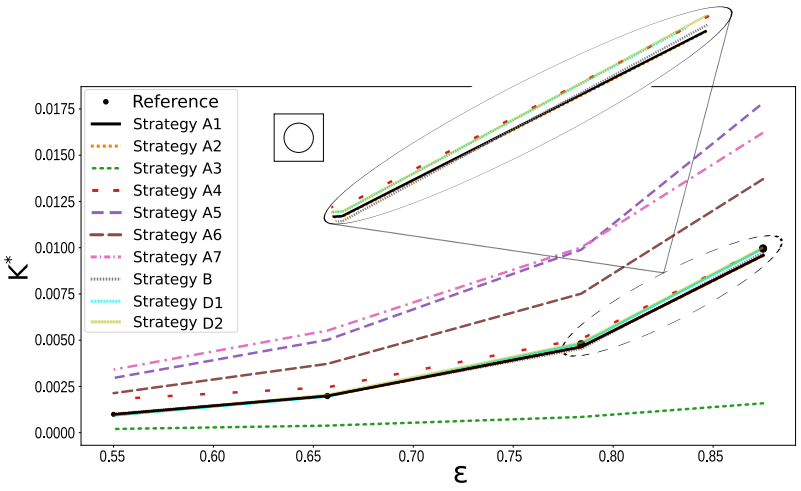


FIGURE 5.4 – Dimensionless permeability estimations for the periodic cubic arrangement of spheres obtained by applying the different strategies defined in Table 5.1, compared to the reference values [7,8]. One-sphere unit cell has been considered with increasing radius, thus with different porosity values. Permeability values have been made non-dimensional by the square of the unit cube dimension.

Permeability values are conveniently made dimensionless with the square of the unit cube dimension. Mesh refinement has been selected after a convergence analysis (see Appendix C (Section 5.8)). Several observations can be made:

- Since the domain is symmetric, strategies B, D1, and D2 have been set with $\delta = 0$. Moreover, always because of the symmetry of the domain, strategies C and E are identical to B and D2 respectively;
- The relative error between the reference and strategy D1 and D2 is less than 1%;
- Results from strategies A1 and A2 differ by less than 0.01%. The only difference between them is that strategy A2 displays a longer convergence time (doubled). For this reason strategy A2 is discarded in what follows;
- Boundary conditions defined for strategies A3, A5, and A7 are not able to provide accurate predictions in terms of permeability (relative error higher than 25%). They are then discarded;

### 5.3.2 Periodic Array of Parallel Cylinders With a Face-Centered Square Arrangement

The unit cell of this periodic orthotropic structure is presented in Fig. 5.3b. In this case the permeability tensor is characterized by two different values, $K_{xx} = K_{yy}$ and $K_{zz}$, whereas all the extra-diagonal components are equal to zero. Ten different cases are defined, each characterized by a different value of porosity. The permeability components are estimated using strategies A1, A4, A6, B, D1, and D2. After being made dimensionless by the square of unit cube dimension, they are compared with the reference values in Fig. 5.5. The domain is symmetric, so strategies C and E are not considered

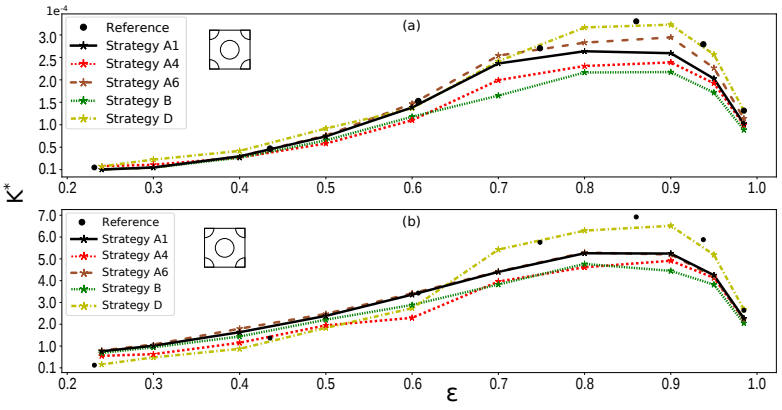


FIGURE 5.5 – Dimensionless permeability estimation for the array of parallel cylinders with face-centered square arrangement as a function of the domain porosity: a) Kxx=Kyy, b) Kzz.

and $\delta = 0$ for strategies B, D1 and D2. Strategies D1 and D2 lead again to a similar description of the problem. Their results differ by 0.1% and that is why we decided to group them under the generic name of Strategy D. Results from strategy D are very accurate, the relative error with the reference is always lower than 5%. Due to its boundary conditions and in particular to the forcing of the periodicity in one direction only, strategy B is not able to accurately capture the orthotropic tensor (relative error around 30%). For this reason it has been discarded.

### 5.3.3 Periodic Cubic Arrangement of Spheres: Multiple-Sphere Unit Cell

This arrangement of spheres is produced by cloning several times the single-sphere unit cell along each direction. Theoretically, the permeability of the domain is the same regardless of the number of single-spheres considered. However, due to the effects of the boundary conditions the estimated permeability values differ as it has been observed above. Indeed, by increasing the domain size, hence the number of spheres, the effect of the boundaries should reduce and the difference between the true and the estimated permeability should tend to zero.
The porosity of each unit is constant and equal to $\epsilon = 0.875$, closer to the porosities expected for the applications we are targeting. Different cases are analyzed, each defined by a different number of unit cells along each direction. In order to make a reasonable comparison, the mesh discretization of a single cell is kept the same regardless of the total number of cells. This makes the size of the mesh to

exponentially increase every time a unit cell added and we have stopped after 6 unit cells per direction because of the computational cost. Strategies A1, A4, A6, and D (with $\delta = 0$) are used to estimate the permeability. Once made dimensionless with the square of the unit cube dimension, the results are plotted in Fig. 5.6. Strategies C and E are not considered since the domain is symmetric. Different

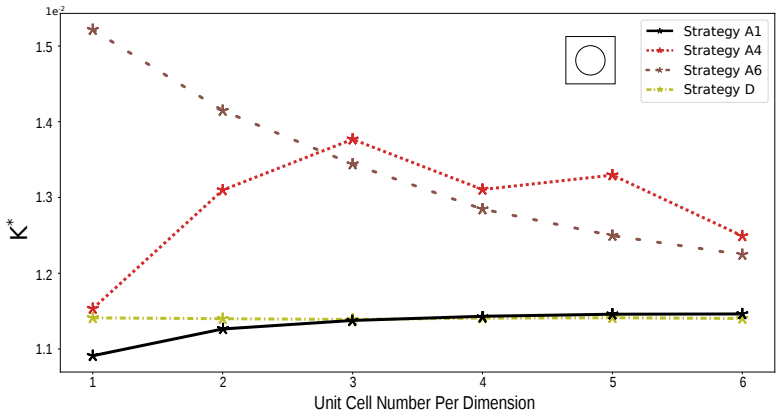


FIGURE 5.6 – Dimensionless permeability estimations for the periodic cubic arrangement of spheres as a function of the number of spheres inside one unit cell.

observations on the results can be made:

- Strategy D provides constant results with increasing unit-cell numbers, as expected;
- As expected, strategies A1, A4, and A6 have the tendency to converge to the results of strategy D, with relative errors given in Table 5.3;

| | **1-Cell** | **2-Cells** | **3-Cells** | **4-Cells** | **5-Cells** | **6-Cells** |
|---|---|---|---|---|---|---|
| **STRATEGY A1** | 4.8 % | 1.3 % | 0.22 % | 0.31 % | 0.45 % | 0.48 % |
| **STRATEGY A4** | 1.17 % | 16.3 % | 22.8 % | 16.4 % | 18.0 % | 10.4 % |
| **STRATEGY A6** | 36.5 % | 26.5 % | 19.6 % | 13.9 % | 10.4 % | 8.1 % |

TABLE 5.3 – Relative errors between strategies A with respect to strategy D for the periodic cubic arrangement of spheres by increasing the number of unit cells. By increasing the number of unit cells the relative errors for the different strategies decrease.

- Strategy A4 has a non-monotonous converging rate. A possible explanation is that this boundary condition forces the flow to be aligned to the inlet-outlet axis leading to a wrong velocity field, thus wrong results [39]. By increasing the unit cells in the domain the effects of the boundaries start to affect less the field and the estimated permeability converges to the correct value. This strategy has been discarded.
- Strategy A1 has the fastest convergence. This strategy is the one that less affects the simulations and hence the results.

### 5.3.4 Periodic Cubic Arrangement of Tilted Cylinders

The unit cell of the periodic porous medium, Fig. 5.3d, consists of a solid cylinder placed in the middle of the unit cube. It is progressively tilted along the y axes until a full rotation of 90 degrees. It is the simplest periodic test case capable of providing extra-diagonal terms in the permeability tensor. Indeed, the latter is characterized by the three diagonal terms plus the extra-diagonal $K_{xz} = K_{zx}$ components.
Ten different cases are defined, each characterized by a different rotation angle $\theta$. The dimensionless tensors inferred from strategies A1 and A6 have been plotted and compared in Fig. 5.7. Results from the closure problem (strategy D with $\delta = 0$) are considered here as reference results. Different

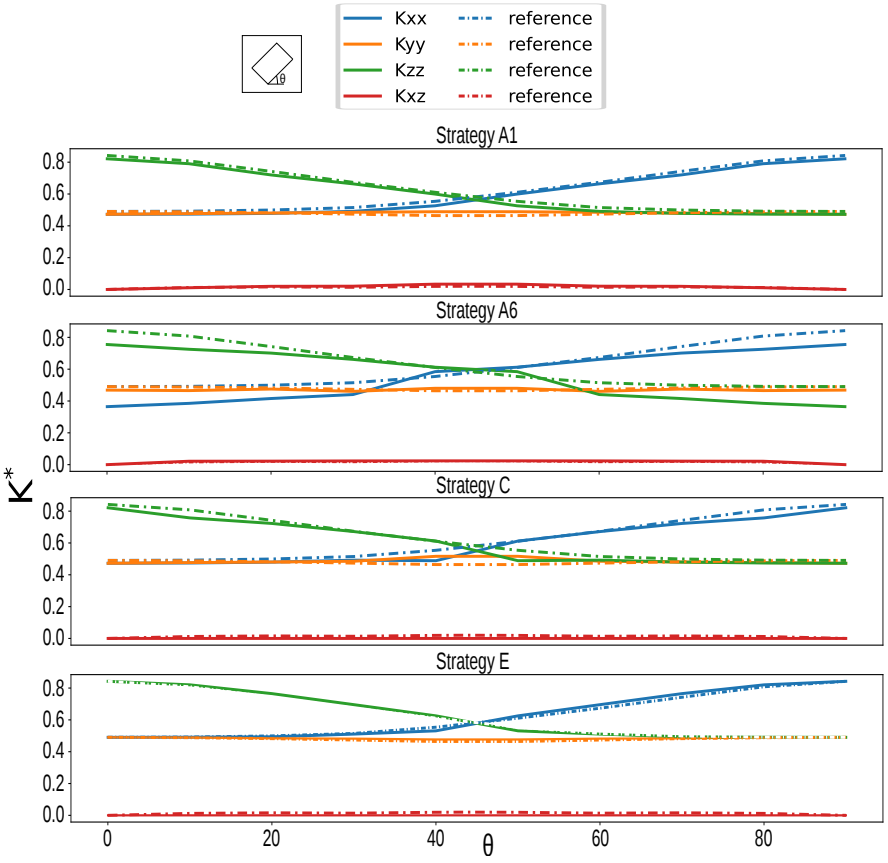


FIGURE 5.7 – Dimensionless permeability estimation of the periodic cubic arrangement of tilted cylinders as a function of the orientation angle ($\theta$) for the unit cell of Fig. 5.3d estimated by different strategies and compared with results of strategy D.

observations can be made:

- All the strategies correctly predict (error below 10%) the constant values of the $K_{yy}$ component during the rotations;
- Strategy A1 predicts diagonal components with a maximum error of 5% and extra-diagonal terms within 10% of error. The error has been observed to remain almost constant for all the

rotation angles.

- Strategy A6 correctly predicts the extra-diagonal term (error less than 1%) but not the diagonal ones (higher relative errors with respect of A1). The symmetric condition for the velocity field on the lateral boundaries strongly reduces the anisotropy features inside the domain;
- Strategies C and E lead to a good prediction of the three diagonal components (especially strategy E), but they completely cancel the non-diagonal term: by construction both of them annihilate the transverse flow and kill any anisotropy features inside the domain. So, the use of symmetry operations allow us to use the periodic boundary conditions but at the price of losing the ability to predict extra-diagonal components. For this reason these two strategies have been discarded.

### 5.3.5 Non-Periodic Cubic Arrangement of Tilted Cylinders

The last basic test case consists of a non-periodic cubic arrangement of tilted solid cylinders, Fig. 5.3e. The case is similar to the previous one, with the only difference that now the domain is non-periodic for most of the values of $\theta$, thus, it has been possible to check the strategies on a non-periodic domain in order to be relevant for fibrous media.
As in the previous case, ten different values of the rotation angle are considered and dimensionless permeability results are plotted and compared in Fig. 5.8. Strategies A1 and A6 are considered and results are verified by strategy D with $\delta = 0$ only for those angles that make the domain periodic: $\theta = 0°, 45°$, and $90°$. The generic strategy D with $\delta \neq 0$ is found to be unsuitable in this study. When having small domains (as in this article) the value of $\delta$ to make it periodic becomes too big with respect to the domain size to avoid any influence on the results. This strategy has to be discarded for non-periodic media. Again, strategy A1 leads to a prediction with less than 5% of error in the three periodic cases, while the other two lead to errors above 40%.

Thanks to these six cases it has been possible to compare the different strategies. Strategy A1 has been proved to be the only suitable one for generic non-periodic porous materials. It is the only one to predict with a good accuracy both diagonal and extra-diagonal terms of the permeability tensor. The boundary conditions used in this strategy are the ones that less affect the numerical simulations.

## 5.4 Selected Strategy Applied to an Anistropic Non-Periodic Medium

Now that strategy A1 has been selected to estimate the permeability tensor, let's apply it to a real case. The geometry considered is a sample of virgin Calcarb, illustrated in Fig. 5.9. Carbon fiber preforms, such as Calcarb [87], are used as skeleton in heat-shield materials [68, 69, 88] with average porosities higher than 85 %. Its micro-structure is generally characterized by fibers preferentially aligned at about $\pm$ 15 degrees with one of the planes and this gives transverse isotropic properties to the material. The digital representation of its micro-structure has been acquired at the Advanced Light Source at Lawrence Berkeley National Laboratory and more details can be found in Borner

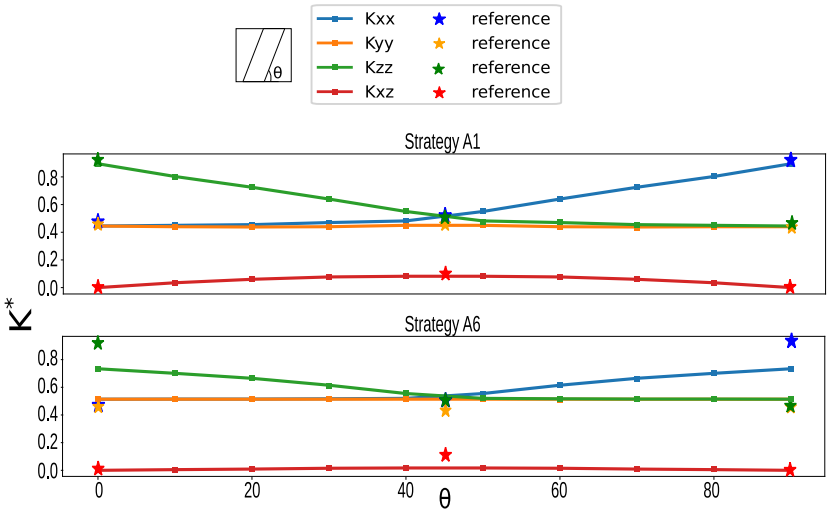


FIGURE 5.8 – Dimensionless permeability estimation of the non-periodic cubic arrangement of tilted cylinders as a function of the orientation angle ($\theta$) for the unit cell of Fig. 5.3e estimated by strategies A1 and A6, while strategy D is used as reference only for the three periodic cases $\theta = 0°, 45°$, and $90°$.

et al, 2017 [9]. The resulting dataset (Fig. 5.9) has a resolution of 200 X 200 X 200 voxels, with a voxel size of 2.6 $\mu m$. Moreover, the dataset has been characterized in terms of volume fraction as a function of the pore-size in the through-thickness direction, computed using a granulometry method in Geodict. Fig. 5.10 shows the results of this analysis and in particular the average pore-size in the through-thickness direction for the domain can be estimated to be equal to $\ell_{\text{avg}} = 135\ \mu m$. We can conclude that the Calcarb dataset analyzed in this paper (Fig. 5.9) is too small to be a REV of the material: the size of 520 $\mu m$ leads to an average of 4 pores for each direction, not enough to guarantee the domain to be representative.

### 5.4.1 Mesh Convergence Analysis

The mesh has been created with the OpenFoam utility *snappyHexMesh*. This tool can be considered as a mesh sculptor since it requires an already existing base mesh (usually created with the *blockMesh* utility) to chisel it into the desired mesh. The quality of the resultant mesh strongly depends on the tuning of different parameters. For the purpose of this simulation, the parameters are tuned in order to produce a good quality mesh (small values of skewness and non-orthogonality, and aspect ratio close to one) and to define a mesh as homogeneous as possible. Once the parameter configuration process is over, a convergence analysis is required in order to check that the defined mesh does not influence the results. In order to do that, the behaviour of a physical quantity should be monitored by repeating pore-scale numerical simulations with increasingly fine meshes. The pressure difference between the inlet and the outlet is considered as an appropriate criterion to study the convergence, since this quantity is strictly related to the permeability estimation. At this stage these cases will be distinguished by the value of the input velocity and Re values will not be given. A further analysis will

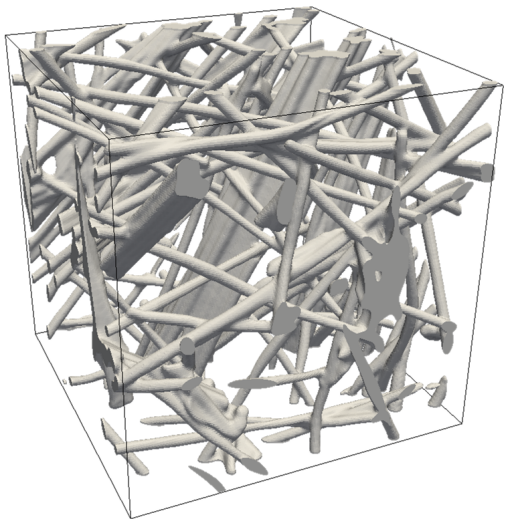

FIGURE 5.9 – Volume rendering of the CMT of Calcarb.

allow the proper choice of the characteristic length for the definition of the Reynolds number. Three different inlet velocity values (corresponding to three different Reynolds numbers) are considered in order to include in the mesh analysis both the creeping and the inertial regimes. Indeed, to detect the limit of validity of Darcy's law we need a good mesh in both regimes. The mesh convergence study has been made with pressure residuals lower than $10^{-6}$ and velocity residuals lower than $10^{-8}$. The results of this study are showed in Figs. 5.11 and 5.12. In figure 5.11 it is possible to observe how the monitored quantity converges by refining the mesh. Moreover, for small velocities, cases a) and b), a creeping flow regime is expected thus, the pressure difference results are similar and just scaled between the two different velocities due to the linearity of the Stokes problem. However, as the velocity increases, case c), the appearance of inertial effect leads to different pressure difference relationships, thus scaling the value is no longer sufficient (see detailed investigation for numerous inlet velocities in the Section 5.4.2). Simulations a) and b) capture the creeping regime; simulations c) captures the inertial regime. The mesh convergence analysis is then performed for both regimes. Figure 5.12 shows the behaviour of the numerical error between two consecutive simulations

$$\text{error} = \frac{\Delta\langle p\rangle^g_{n+1} - \Delta\langle p\rangle^g_n}{\Delta\langle p\rangle^g_{n+1}} \tag{5.11}$$

where the index $n+1$ indicates the numerical simulation with more mesh refinement. In the figure the green lines have first order slopes. The numerical methods is then first order with respect to the discretization. The errors decay until they stabilize around $10^{-3}$ and $10^{-4}$ when the grid-size reaches the image resolution (2.6 $\mu m$). Based on this observation we have decided to select the 25 million cells-mesh to proceed with the computation of the permeability tensor. Some details of the meshed geometry are showed in Fig. 5.13

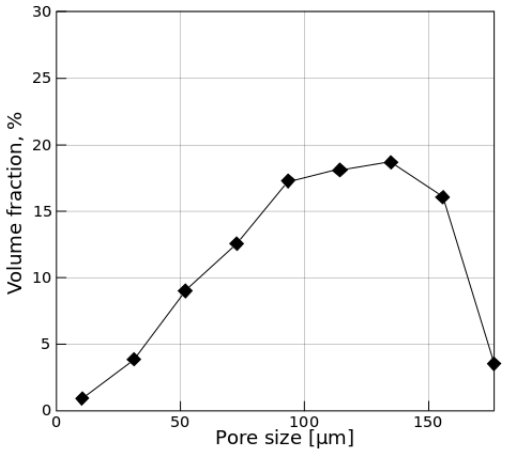


FIGURE 5.10 – Granulometry analysis done in Geodict [9]. The average pore-size in the through-thickness direction for the domain can be estimated to be equal to $\ell_{\text{avg}} = 135\ \mu m$.

### 5.4.2 Permeability Tensor

The objectives of this section are two-fold: compute the permeability tensor of the Calcarb sample and investigate the validity of Darcy's law corresponding to the creeping regime at the pore-scale. The strategy has been applied for different values of the inlet velocity. A chosen from the analysis detailed in Sections 5.2 and 5.3. The computed permeability components are presented in Fig. 5.14. It is possible to notice that when the inlet velocities are higher than $0.1\ m/s$, the components of the permeability start to decrease. This is due to the appearance of non-linearity effects. As said in Section 5.1, in order to take those effects into account at the macroscopic scale, the Forchheimer correction should be considered. However, for velocities lower than $0.1\ m/s$, the flow is in the creeping regime and the predicted tensor is constant and equal to

$$\underline{\underline{K}} = \begin{bmatrix} 1.56\ 10^{-10} & 1.39\ 10^{-11} & 1.02\ 10^{-11} \\ 1.39\ 10^{-11} & 1.63\ 10^{-10} & -5.4\ 10^{-12} \\ 1.02\ 10^{-11} & -5.4\ 10^{-12} & 1.15\ 10^{-10} \end{bmatrix} m^2 \tag{5.12}$$

where the average of the extra-diagonal terms ($\frac{K_{xy}+K_{yx}}{2}$, $\frac{K_{xz}+K_{zx}}{2}$, and $\frac{K_{zy}+K_{yz}}{2}$) have been considered to force tensor symmetry. The obtained permeability tensor characterizes just the domain considered and not the whole material and this makes really difficult to check the results. However, this domain has already been studied by Borner et al, 2017 [9], by using a different approach [1] and by making several simplifications, reducing the tensor to just two scalars: in-plane and through-thickness components. In order to compare results of Eq. (5.12) a diagonalization procedure is required in order to write the tensor aligned to the principal axes of rotation

$$\underline{\underline{K}}_{dg} = \begin{bmatrix} 1.74\ 10^{-10} & 0 & 0 \\ 0 & 1.49\ 10^{-10} & 0 \\ 0 & 0 & 1.11\ 10^{-10} \end{bmatrix} m^2 \tag{5.13}$$

1. The computation of the permeability is based on Monte Carlo simulations.

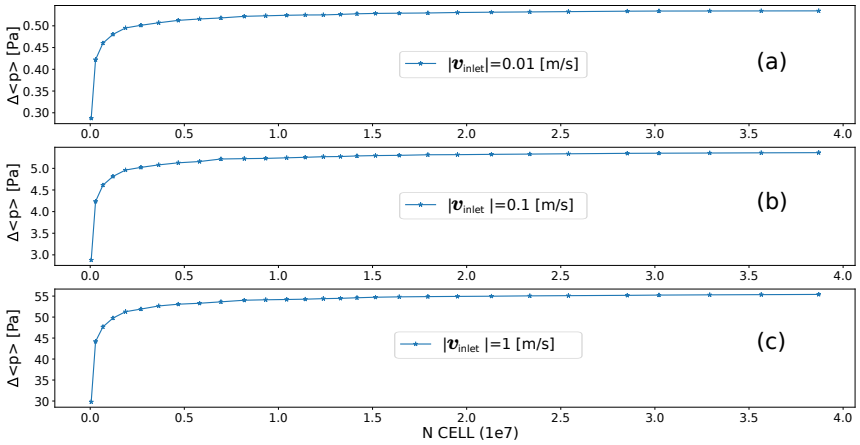


FIGURE 5.11 – Mesh convergence analysis of the digitalized Calcarb domain Fig. 5.9 characterized by three different inlet velocity values. The pressure difference between the inlet and the outlet is studied as the number of cells within the domain increases. Due to a different scaling in the pressure difference, cases a) and b) correspond to the creeping regime, whereas case c) to the inertial one.

and results have a relative difference around 42% with respect to the prediction obtained by Borner et al, 2017 [9].

### 5.4.3 Characteristic Length of the Domain

As seen before, the relative importance between inertial and viscous forces within a fluid is characterized by the Reynolds number (Eq. (5.3)). Once defined, this parameter allows the determination of the flow regime hence which equations must be considered for its resolution. The problem is that a characteristic length $\ell$ needs to be defined and this choice is not trivial [119]. Both macroscopic and microscopic information can be considered for its determination and in this article we propose a new method based on the latter. This new technique is based on the vorticity vector, which is defined as

$$\boldsymbol{\omega} = \partial_{\boldsymbol{x}} \times \boldsymbol{v} \tag{5.14}$$

It describes the tendency of a flow to rotate. For an incompressible flow this field is governed by the following equation [2]

$$\frac{D\boldsymbol{\omega}}{Dt} = (\boldsymbol{\omega} \cdot \partial_{\boldsymbol{x}})\boldsymbol{v} + \frac{\mu}{\rho}\partial^2_{\boldsymbol{x}}\boldsymbol{\omega} \tag{5.15}$$

Vorticity is therefore generated close to boundaries where velocity gradients contribute to the stretching/tilting term (the first source term at the second-hand side). Once generated, the vorticity diffuses into the entire domain due to the diffusion term. Due to the linear behaviour of the velocity, the vorticity increases proportional to the magnitude of the velocity in the creeping regime since the source term remains the same. However, as soon as the creeping regime falls, non-linearities in the velocity field change this simple trend. So, a simple way to check the validity of the creeping regime is to keep

2. The vorticity equation has been derived by taking the curl of the transient momentum equation.

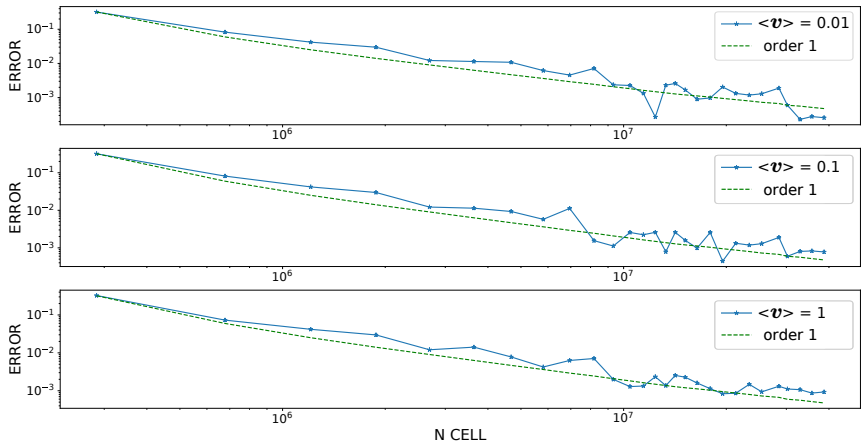


FIGURE 5.12 – Relative error convergence analysis of the digitalized Calcarb domain Fig. 5.9 characterized by three different inlet velocity values. Cases a) and b) correspond to the creeping regime, whereas case c) to the inertial one. Lines with first order slopes have been plotted to show the convergence order of the numerical method.

under observation the mean value of the vorticity over the whole domain. To investigate the loss of proportionality of the velocity (linear dependence on velocity) which exists in the creeping regime, it is possible to consider the dimensionless vorticity, defined as

$$\boldsymbol{\omega}^* = \boldsymbol{\omega} \frac{\ell}{\langle v \rangle} \tag{5.16}$$

whose mean value remains constant in the creeping regime.
In order to illustrate this concept, let's apply it to the 1-sphere unit cell case showed in Fig. 5.3a with a high porosity value ($\epsilon = 0.875$) to simulate the case of flow around a sphere. This is a well-known case and according to a Reynolds number computed with respect to the diameter of the sphere, the limit for the creeping regime is usually set between 0.1 and 0.5 according to different authors [156–158]. As done in Section 5.4 for the Calcarb geometry, let's first evaluate the permeability value of the high porosity 1-sphere porous medium for different Reynolds numbers. Then, based on those values, a limit for the creeping regime can be indirectly estimated by plotting the evolution of the estimated permeability or of the drag. A change in the slope indicates the appearance of inertial effect [156–158]. The limit can be inferred by directly evaluating for each simulation the mean vorticity value in the domain. This technique has the additional advantage of requiring fewer simulations. Results are showed in Table 5.4, where the diameter of the sphere has been considered as the characteristic length of the domain for the Reynolds numbers. As it is possible to see, both the permeability and vorticity start to change for $Re = 0.1$, but a significant variation can be really appreciated after $Re = 1$. So, depending on the precision desired, the creeping regime limit could be set at different Reynolds. One of the main advantages of this method is the fact that it is possible to identify in the domain the area where the vorticity presents its maximum values, that is, where non-linearity effects affect more the flow. In other words, it points to the area of the domain that is first subject to a transition to a different flow behaviour. This area could be considered as the physics-based characteristic length of the domain. In

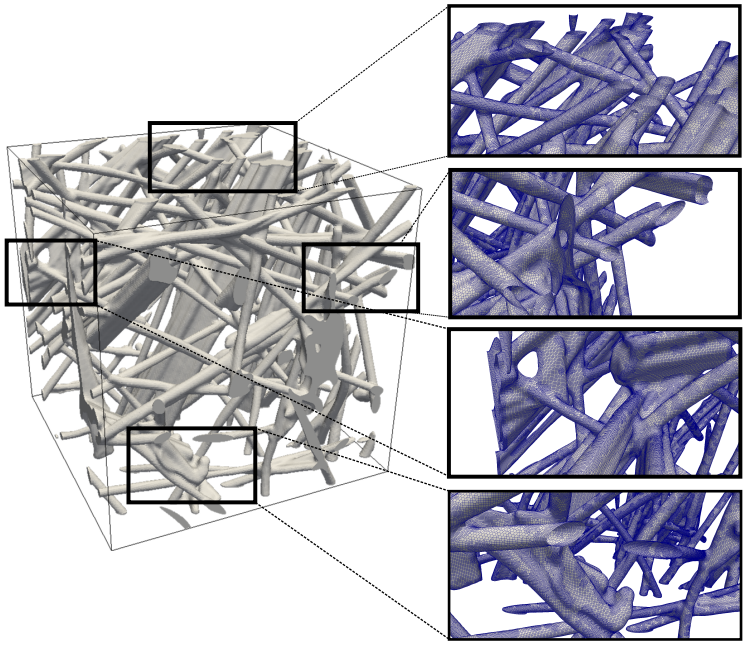

FIGURE 5.13 – Some details of the meshed geometry. The final mesh accounts about 25 million cells.

| $Re$ | 0.001 | 0.01 | 0.1 | 0.5 | 1 | 10 | 100 |
|---|---|---|---|---|---|---|---|
| $K^*$ | 0.09911 | 0.09911 | 0.09912 | 0.09918 | 0.09939 | 0.11471 | 0.17641 |
| $\Delta K^*$ | / | 0.00 % | 0.010 % | 0.071 % | 0.283 % | 15.74 % | 77.99 % |
| $\lvert\boldsymbol{w}^*\rvert$ | 3.985e+06 | 3.985e+06 | 3.985e+06 | 3.984e+06 | 3.982e+06 | 3.801e+06 | 3.2116e+06 |
| $\Delta\lvert\boldsymbol{w}^*\rvert$ | / | 0.00 % | 0.003 % | 0.025 % | 0.070 % | 4.63 % | 19.42 % |

TABLE 5.4 – Results for the high porosity 1-sphere porous medium case (Fig. 5.3a) with different Reynolds number in terms of permeability and mean vorticity over the domain. The $\Delta$ values refer to the quantity difference with respect to the lowest inlet Reynolds case.

this case of the high porosity 1-sphere porous medium, the vorticity technique identifies the sphere area, leading to a characteristic length equal to the sphere diameter, as expected.

Let's now apply the same method to the Calcarb geometry. Results are showed in Table 5.5. The average pore-size length presented in Section 5.4, $\ell_{\text{avg}} = 135\ \mu m$, has been considered as the characteristic length for the computed Reynolds number denoted $Re_{\text{avg}}$. In the table $\Delta$ is taken as the difference of the quantity between a given simulation and the lowest Reynolds case. Based on the $\Delta$ values it is possible to set the limit for the creeping regime as $Re_{\text{avg}}$ between 1 and 5, depending on the acceptable tolerance. As previously done, the vorticity can be now used to locate the portions of the domain where non-linearities effects are dominant. By progressively increasing the velocity in the domain it is possible to observe that the dimensionless vorticity field assumes its maximum values mainly inside a specific area in the domain [3]. This area is showed in Fig. 5.15 where on the right it is

3. For the moment the method is based on a qualitative analysis of the vorticity field. More analysis with different geometries should be performed to make the analysis more rigorous.

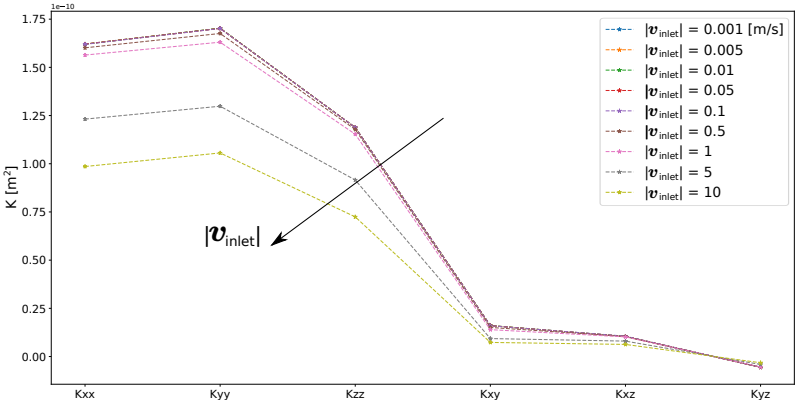


FIGURE 5.14 – Permeability components of the digitalized Calcarb domain by varying the inlet velocity.

| $Re_{\text{avg}}$ | 0.01 | 0.05 | 0.1 | 0.5 | 1 | 5 | 10 | 50 | 100 |
|---|---|---|---|---|---|---|---|---|---|
| $\Delta K^*$ | / | 0.00 | 0.005 % | 0.008 % | 0.1 % | 1.2 % | 3.52 % | 24.0 % | 47.1 % |
| $\Delta\lvert\boldsymbol{w}\rvert^*$ | / | 0.00 | 0.005 % | 0.009 % | 0.11 % | 0.65 % | 0.97 % | 3.93 % | 7.51 % |

TABLE 5.5 – Permeability and mean vorticity variation for the Calcarb geometry as function of different inlet magnitude velocities. The $\Delta$ values refer to the quantity difference with respect to the lowest inlet Reynolds case.

enlarged and the first obstacle found in the upwind direction is highlighted in red: a cluster of fibers with diameter $\ell_{cl} \sim 80\ \mu m$.

A verification on the vorticity analysis is given by a direct observation of the flow behaviour. By referring to the left of Fig. 5.15, let's assume a flow is coming along the x direction. About halfway through the domain, the flow faces the big cluster of fibers highlighted in red in Fig. 5.15. When velocities are small enough, the flow overtakes the cluster without any particular problem and therefore continues towards the outlet; with the increase of velocities, a part of the flow close to the right boundary ($Y = 0$) starts to move towards the center of the domain. This behaviour becomes more and more marked with increasing Reynolds as showed in Fig. 5.16; when $Re_{\text{avg}} \sim 10$, two counter-rotating vortices are formed in the area downstream of the cluster. So, the flow close to the right boundary, first overtakes the cluster, then feeds the vortices, and finally spreads towards the center of the domain; by further increasing Reynolds, the high-vorticity flow from the back of the cluster spreads the non-linearity effects all over the domain and this leads to the formation of different vortices. Therefore, the area downstream of the cluster is found to trigger the transition to inertial regime for the whole domain. This cluster of fibers is the same found through the vorticity field analysis, with a diameter of $\ell_{cl} \sim 80\ \mu m$. By recalling the average pore-size length $\ell_{\text{avg}} = 135\ \mu m$ presented in Section 5.4, it can be easily noticed that the red box is characterized by a cluster size that is nearly half of the pore domain average.

This analysis allows taking into account the real arrangement of the fibres inside the domain, however, it is limited to a specific case and with a different sample all the procedure should be repeated.

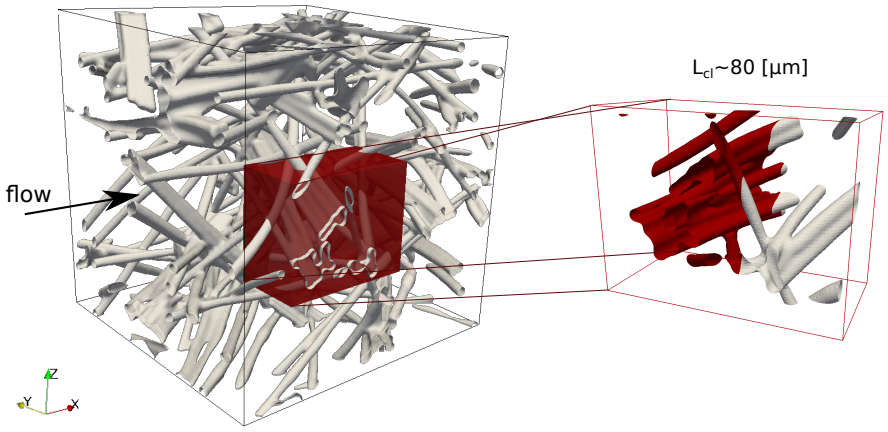


FIGURE 5.15 – Calcarb dataset characterized in this article, with a red box to highlight a small area that influences the behaviour of the flow inside the whole domain.

The Reynolds number can be defined by using $\ell_{cl}$ and thus the limits of the creeping regime [90, 91] expressed as

$$Re_{cl} < 0.5 \longrightarrow \text{creeping regime}$$

It should be remarked that this technique investigates the limit of the creeping regime, that is the weak inertial regime [90] where flows are no longer fully viscous but still steady. Thanks to it, we are able to provide a physical limit to the applicability of this study in the estimation of the permeability tensor. Future analysis and developing on this technique are however necessary.

## 5.5 Conclusions

In this work, a numerical strategy has been defined in order to characterize the dynamic interaction between a flow and a generic anistoropic non-periodic porous material. Specific attention was paid to the definition of the computational domain and the boundary conditions by defining different strategies and comparing their results on simple test cases. Both periodic and non-periodic geometries were considered in order to be as generic as possible. The selected strategy is based on the direct resolution of the Navier-Stokes equations under the assumption of creeping flow in order to estimate the physical quantities that appear in Darcy's law and leave the permeability tensor as the only unknown. In order to close the system and obtain all the components of the tensor three pore-scale numerical simulations need to be considered. Pore-scale simulations in the real geometry bring numerous information such as pressure gradients and velocity fields. All this information has been used in this article to introduce a criterion for delimiting the creeping regime with the onset of the inertial regime. This criterion is based on the vorticity field and it has been verified and applied to the high porosity 1-sphere porous medium and to the Calcarb dataset. As showed in the results, the limit strongly depends on the error tolerance chosen to be acceptable. The analysis of vorticity was also adopted to define a physics-based characteristic length in the domain which has been used to define the Reynolds number and its value corresponding to the onset of the inertial regime. This criterion can be used to train deep learning

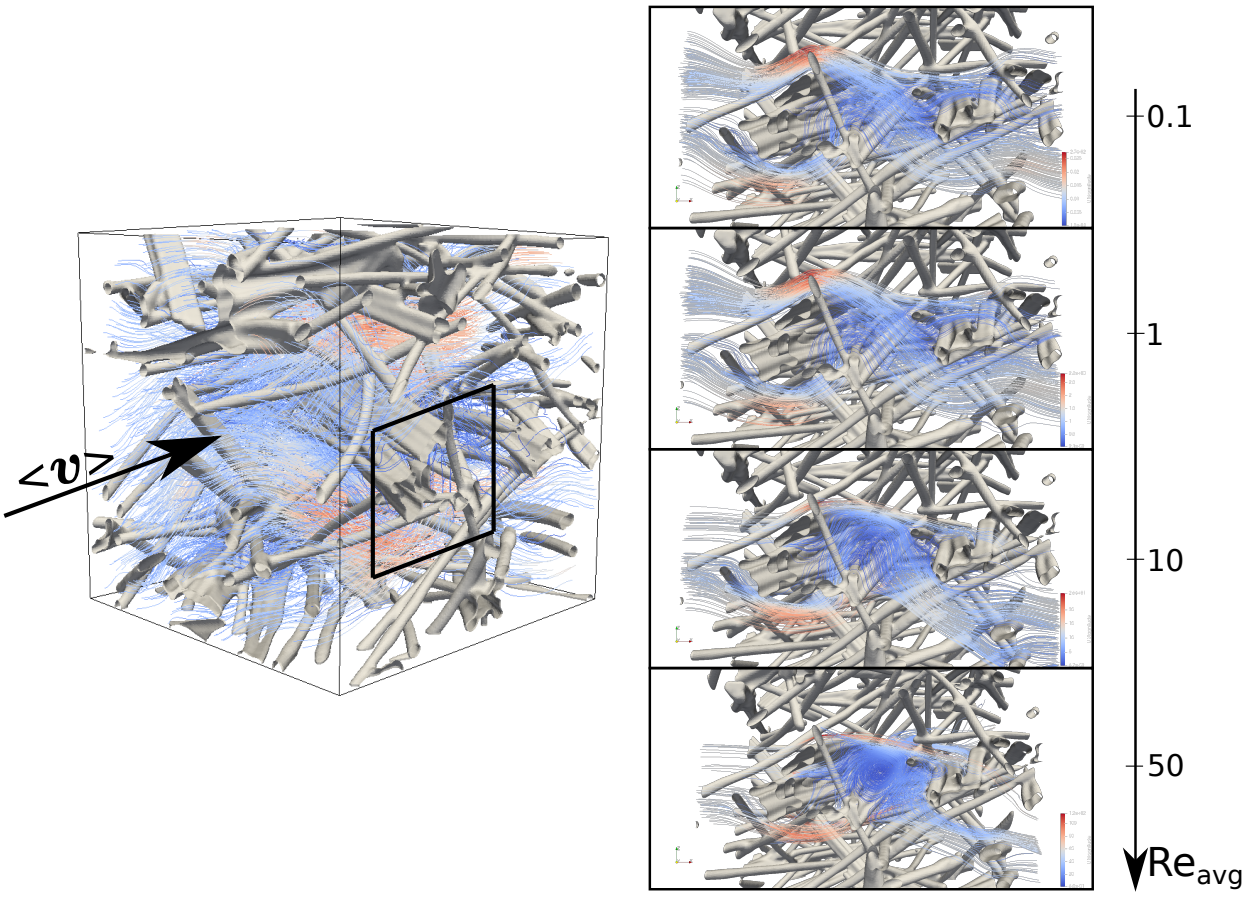


FIGURE 5.16 – Streamlines visualization in the domain and zoom on the characteristic area of the domain with flow behaviour at different Reynolds number. Streamlines are colored based on the velocity magnitude.

techniques in the process of automatic identification of the physics-based characteristic length in a generic domain. The numerical framework that has been developed during this study is available in the Porous material Analysis Toolbox based on OpenFoam (PATO) released Open Source by NASA (www.pato.ac).

## Conflict of interest

The authors declare that they have no conflict of interest.

## 5.6 Appendix A. Remarks on the Volume Averaging Method

This appendix has the only purpose to introduce the concepts of the volume averaging method used in this article. Further details can be found in the literature [15].
The volume averaging is a technique used to derive continuum-macroscopic equations for multiphase systems. In this way the complexity of a porous medium is replaced with an equivalent porous-continuum model in which each point is characterized by the properties of a representative elementary volume (REV) centered on it. Within this REV variables can be averaged. Two different definitions of averages have been adopted: the phase average which in this article has been used for the pressure term

$$\langle p \rangle^g = \frac{1}{V_f} \int_{V_f} p \, dV \tag{5.17}$$

and the intrinsic average, used for the velocity field

$$\langle \boldsymbol{v} \rangle = \frac{1}{V_{\text{REV}}} \int_{V_f} \boldsymbol{v} \, dV \tag{5.18}$$

Inside the REV each variable can be decomposed using Gray's decomposition [159]) as the sum of its average plus a deviation contribution. For the pressure field this decomposition is as follows

$$p = \langle p \rangle^g + \tilde{p} \tag{5.19}$$

## 5.7 Appendix B. KclosureSolver

KclosureSolver is a solver implemented in PATO to solve the closure problem Eq. (5.8). By following the work of Anguy and Bernanrd, (1994) [160], transients terms have been added to the system to improve its stability. The desired solution is taken at the steady-state. An artificial compressibility, $c$, and an artificial viscosity coefficient, $\mu_{\text{art}}$, are also introduced. The modified transient problem is as follows

$$\begin{cases} \partial_t \underline{\underline{d}} + \partial_{\boldsymbol{x}} \boldsymbol{e} - \partial^2_{\boldsymbol{x}} (\mu_{\text{art}} \underline{\underline{d}}) = \underline{\underline{I}} & in \ V \\ \partial_t \boldsymbol{e} + c^2 \partial_{\boldsymbol{x}} \cdot \underline{\underline{d}} = 0 & in \ V \\ BC1 : \underline{\underline{d}} = 0 & at \ S_{gs} \\ BC2 : \underline{\underline{d}}(\boldsymbol{r} + l_i) = \underline{\underline{d}}(\boldsymbol{r}), \ \ \boldsymbol{e}(\boldsymbol{r} + l_i) = \boldsymbol{e}(\boldsymbol{r}) & i = 1, 2, 3 \end{cases} \tag{5.20}$$

The two equations are solved sequentially. Each equation can be iterated in a loop. The time integration is carried out through an implicit scheme.

## 5.8 Appendix C. Mesh Convergence Test Cases

In section 3, numerical simulations on six test cases are presented. The mesh refinement has been selected after a convergence analysis. By considering the 1-sphere unit cell with porosity $\epsilon = 0.55$, results of the convergence study with strategy A1 are presented in Table 5.6. The error% is evaluated

| **N Cells** | 2414 | 11795 | 34099 | 74352 | 138911 | 233039 | 362489 | 533190 |
|---|---|---|---|---|---|---|---|---|
| **Error %** | 2.72 | 1.37 | 1.02 | 0.66 | 0.56 | 0.01 | 0.01 | / |
| $V_{ratio}$ | 5.431 e-4 | 6.8 e-5 | 2.0 e-5 | 8.5e-6 | 4.3 e-6 | 2.5 e-6 | 1.6 e-6 | 1.1 e-6 |

TABLE 5.6 – Mesh Convergence analysis with strategy A1 for the 1-sphere unit cell case defined in Section 3 with constant porosity $\epsilon = 0.55$. The error% is evaluated with respect to the result of the finer mesh. $V_{ratio}$ is the ratio between the volume of the biggest finite-volume cell in the domain and the domain itself.

taking into account the permeability estimation of two consecutive simulations as follows

$$\text{error}\% = 100\ \frac{|K_{\text{Finer\_Mesh}} - K_{\text{Coarser\_Mesh}}|}{K_{\text{Finer\_Mesh}}} \tag{5.21}$$

The quantity $V_{\text{ratio}}$ is the ratio between the volume of the biggest cell in the domain and the domain itself. From the results in the table we can see that the convergence of the mesh is immediately achieved since the error is always decreasing by increasing the refinement. This trend, however, should stop when the tolerances of the simulation are reached. That is what happens in the table for the most refined meshes. The resolution of the mesh with 233039-cells can be then selected for the analysis in section 3.

# Chapitre 6

# Multiscale modeling of flow in porous thermal protection systems from the continuum to the slip regime

**Nomenclature**

*Latin Letters*

| | |
|---|---|
| $d$ | gas kinetic diameter $[m]$ |
| $d_p$ | mean pore diameter $[m]$ |
| $\underline{\underline{K}}$ | corrected permeability tensor $[m^2]$ |
| $\underline{\underline{K}}_0$ | permeability tensor in the limit of continuum flow $[m^2]$ |
| $k_b$ | Boltzmann constant $m^2\ kg\ s^{-2}\ K^{-1}]$ |
| $\boldsymbol{n}$ | surface normal |
| $p$ | pore-scale pressure $[Pa]$ |
| $Q_N$ | flow rate $[kg\ s^{-1}]$ |
| $r$ | radius of the cylinder $[m]$ |
| $S$ | interface area $[m^2]$ |
| $T$ | micro-scale temperature $[K]$ |
| $\boldsymbol{v}$ | pore-scale velocity $[m\ s^{-1}]$ |
| $V$ | volume of the domain $[m^3]$ |
| $\boldsymbol{x}$ | pore-scale coordinates $[m]$ |

*Greek Letters*

| | |
|---|---|
| $\alpha_s$ | generic function of $\sigma_v$ |
| $\underline{\underline{\beta}}$ | slip correction tensor $[Pa]$ |

## Nomenclature

| | |
|---|---|
| $\lambda$ | mean free path $[m]$ |
| $\mu$ | dynamic viscosity $[Pa\ s]$ |
| $\rho$ | pore-scale density $[kg\ m^{-3}]$ |
| $\sigma_p$ | first order velocity slip coefficient |
| $\sigma_v$ | tangential momentum accommodation coefficient |

*Symbols*

| | |
|---|---|
| $*$ | non-dimensional variable |
| $\sim$ | deviation term |
| $\langle\rangle$ | intrinsic average |
| $\langle\rangle^g$ | phase average |

*Subscripts and Superscripts*

| | |
|---|---|
| g | gas |
| s | solid |
| sl | slip |
| w | wall |

*Adimensional Groups*

| | |
|---|---|
| Kn | Knudsen number |

*Acronyms*

| | |
|---|---|
| CFD | Computational Fluid Dynamics |
| CMT | Computed Micro-Tomography |
| DSMC | Direct Simulation Monte Carlo |
| MSL | Mars Science Laboratory |
| PICA | Phenolic Impregnated Carbon Ablator |
| PS-NS | Pore-Scale Numerical Simulations |
| TPS | Thermal Protection System |

## Preamble

Authors: H. Scandelli; A. Ahmadi-Senichault; J. Lachaud;
Affiliations: Arts et Métiers Institute of Technology, Univ. Bordeaux, CNRS, Bordeaux INP, I2M, UMR 5295, F-33400 Talence, France;
Published: No;
Conference: No;

## Abstract

By analysing the pressure and temperature profiles during atmospheric entry of the Stardust and MSL space missions, it can be observed that a large and important (peak heating) portion of the entry trajectory occurs when the gas dynamic within the porous medium is in the continuum and slip regimes. An extension of CFD methods to account for rarefied slip gas effects would allow a large computational gain over the use of DSMC methods. To this end, the corrected permeability tensor must be characterized. However, the most general case of non-periodic anisotropic porous media still needs to be completely numerically defined. In this article we propose a pore-scale numerical technique to estimate the effective tensor when addressing the most most general case of non-periodic anisotropic porous media. The Navier-Stokes equations are used in combination with a partial slip boundary condition on the fluid-solid interface. Results are averaged and substituted in the macroscopic Darcy-Klinkenberg model, leaving the effective tensor as the only unknown. Verification by comparison with direct simulation Monte Carlo (DSMC) is performed on a square array of cylinders. The CFD confirms its ability to infer the full effective tensor and it leads to a gain in simulation time. The method is applied to the analysis of a 3D X-ray computed micro-tomography (CMT) of Calcarb, a porous carbon fiber material used in the thermal protection systems of space vehicles. Results are compared with literature data derived from DSMC methods and a relative difference of around 8% is found.

**Keywords**: Porous media; Permeability tensor; Slip Regime; Pore-scale numerical simulations; Micro-CT image; Calcarb.

## 6.1 Introduction

During hypersonic entry into a planetary atmosphere, a space vehicle is subjected to high aerothermodynamic heating from the surrounding free-stream plasma. The spacecraft surface can reach a temperature of about 3000 $K$ for severe entry conditions. Thermal Protection System (TPS) are adopted to dissipate the heat and protect the integrity of the structure. For very high entry speeds, ablators are the current option as TPS materials. They are designed to absorb and dissipate heat through phase changes, chemical reactions, and material removal. An example of this class of TPS material is the Phenolic Impregnated Carbon Ablator (PICA) [70], a carbon fiber preform partially impregnated with phenolic resin, resulting in very light weight, good insulators, and high mechanical strength. This material was used for the Stardust [92] and Mars Science Laboratory [93] (MSL) missions. During the entry trajectories of these missions, different rarefaction regimes were crossed by the flow dynamics within the porous medium. The different regimes are classified in terms of the Knudsen number. In porous media, the Knudsen number is defined as the ratio of the mean free path $\lambda$ to the

mean pore diameter $d_p$

$$Kn = \frac{\lambda}{d_p} \tag{6.1}$$

For PICA-like materials, the mean pore diameter of the carbon preform can be considered to be around $d_p = 50\ \mu m$ [9]. The mean free path of the gas mixture is given by the kinetic theory

$$\lambda = \frac{k_b T_g}{\sqrt{(2)}\pi d^2 p_g} \tag{6.2}$$

where $k_b$ is the Boltzmann constant, $T$ and $p$ are the micro-scale temperature and pressure of the gas, and $d$ indicates the kinetic diameter of the gas. We can consider the gas mixture inside the material to be composed by pyrolysis gases. Estimating the kinetic diameter results to be a complex task for two main reasons. First, the composition of the mixture is a function of local temperature and pressure; second, the value of the kinetic diameter depends on the gas pair being considered. We decide to take the lowest value in the mixture as it relates to the first molecules entering the slip regime. For pyrolysis gases, this value corresponds to hydrogen molecules colliding with each other: $d = 289\ 10^{-12} m$ [161]. Given the wall temperature-pressure values at the stagnation point along the entry trajectories, the flow dynamics of the MSL and Stardust missions are showed in Fig. 6.1. Within the material, the temperature of the gas decreases to values around 273 $K$, while the pressure

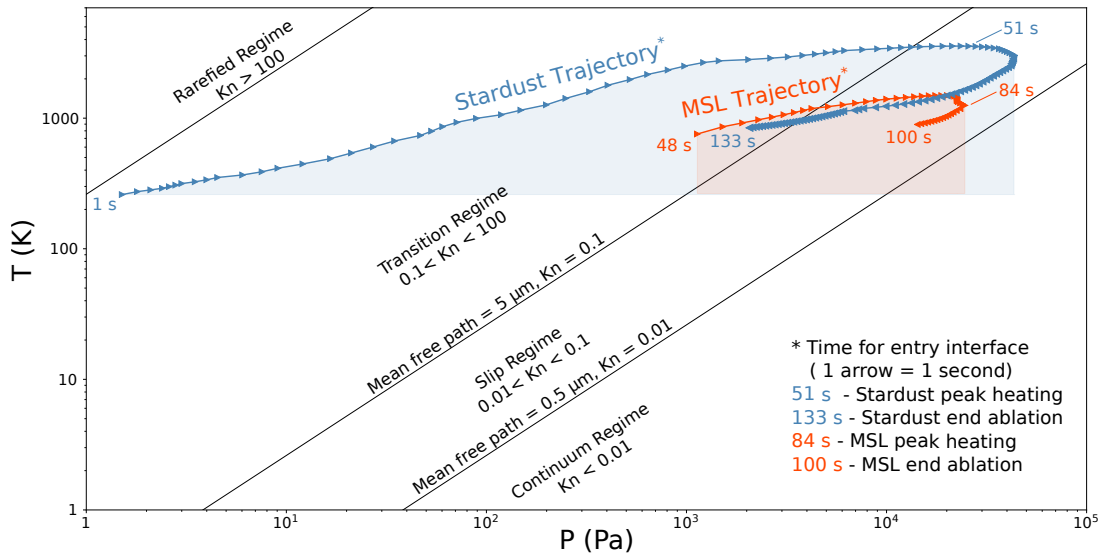


FIGURE 6.1 – Rarefied flow regimes encountered along the Stardust and MSL entry trajectories within a porous medium of mean pore diameter 50 $\mu m$ [9]. Wall temperature-pressure values are taken at the stagnation point along the entry trajectories.

can be considered constant. The two highlighted areas (blue for Stardust and red for MSL) give an indication of the rarefaction regimes crossed by the flow dynamics within the TPS. A change of regime implies that the mass transport at the pore scale has to be solved using different mathematical models (Boltzmann equation [162], Burnett equation [163], Navier-Stokes equations). The figure shows that,

for both missions, the continuum ($Kn < 0.01$) regime is partially crossed when the heating conditions reach their peak. A larger part of the trajectories, especially when ablation effects are significant, is covered by the slip regime ($0.01 < Kn < 0.1$). In this regime, the continuum assumption is still valid within the fluid bulk, but non-equilibrium effects dominate near the solid walls. CFD methods can still be used with allowance for discontinuities in velocity and temperature at solid boundaries [164]. The importance of this extension is twofold. Firstly, numerical methods for solving the Boltzmann equation are time consuming when reducing the Knudsen number [165]; secondly, CFD methods would thus be able to describe a large and important portion of the Stardust and MSL mission trajectories (Fig.6.1). In order to understand how this extension occurs, the micro-scale and macro-scale descriptions of the problem must be introduced.
The generic problem of interest is schematized in Fig. 6.2. At the micro-scale, under the assumption of

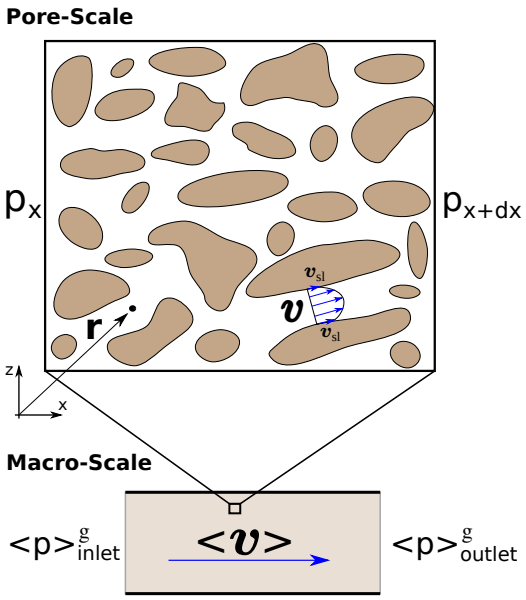


FIGURE 6.2 – Pore-scale and macro-scale descriptions of the generic transport problem in porous media considered in this article. At the microscopic scale the Navier-Stokes equations with slip velocity condition at the fluid-solid interface (Eq. 6.3) are considered. At the macroscopic scale, the system of Eq. 6.7 is solved.

a Newtonian, isothermal, creeping, steady-state, and incompressible fluid, a rigid solid porous medium, and negligible volume forces, the pore-scale governing equations reduce to

$$\begin{cases} \partial_{\boldsymbol{x}} \cdot \boldsymbol{v}_g = 0 \\ \partial_{\boldsymbol{x}} \cdot (\mu_g \, \partial_{\boldsymbol{x}} \boldsymbol{v}_g) = \partial_{\boldsymbol{x}} p_g \\ \text{for} \quad Kn < 0.01 : \quad BC \quad \boldsymbol{v}_g = \boldsymbol{v}_w \qquad at \; S_{gs} \\ \text{for} \quad Kn < 0.1 : \quad BC \quad \boldsymbol{v}_g = \boldsymbol{v}_{sl} \qquad at \; S_{gs} \end{cases} \tag{6.3}$$

where $\mu_g$ denotes the dynamic viscosity of the fluid, $\boldsymbol{v}_g$ and $p_g$ are the pore-scale velocity and pressure, and $S_{gs}$ represents the gas-solid area interface. At the boundaries, the velocity accommodates to the

one of the wall, $\boldsymbol{v}_w$, in the continuum regime and to the slip velocity, $\boldsymbol{v}_{sl}$, in the slip regime. In this article, the first-order Maxwell model [10] is used to express the slip condition

$$\boldsymbol{v}_{sl} = \boldsymbol{v}_w + \sigma_p \lambda \Big(\partial_{\boldsymbol{n}} \boldsymbol{v}_{sl}\Big)_w + \frac{3}{4}\frac{\mu_g}{\rho_g T_g}\Big(\partial_{\boldsymbol{n}} T_g\Big)_w \tag{6.4}$$

where $\sigma_p$ is the first order velocity slip coefficient, $\lambda$ represents the mean free path, $w$ stands for wall, $\boldsymbol{n}$ is the normal vector to the wall, $\rho_g$ is the micro-scale density of the gas. As isothermal condition are assumed, the term with the temperature contribution is neglected. The dimensionless form of this expression is [165]

$$\boldsymbol{v}^*_{sl} = \boldsymbol{v}^*_w + \sigma_p \; Kn \; \Big(\partial_{\boldsymbol{n}^*} \boldsymbol{v}^*_{sl}\Big)_w \tag{6.5}$$

where the role of the Knudsen number is highlighted. In the continuum regime, $Kn << 1$ thus the discontinuous term can be neglected and the non-slip boundary condition applied. As reviewed by Zhang et al., 2012 [10], different models have been developed to express the slip condition, however, as long as small Knudsen number are considered ($Kn < 0.1$), the models differ by negligible amounts [10]. The velocity slip coefficient, $\sigma_p$, unitary in Maxwell's model [166], is empirically defined as

$$\sigma_p = \alpha_s \frac{2 - \sigma_v}{\sigma_v} \tag{6.6}$$

where $\sigma_v$ is the tangential momentum accommodation coefficient and $\alpha_s$ represents a generic function of $\sigma_v$. The tangential momentum accommodation coefficient coefficient indicates the fraction of the molecules reflected diffusively from the walls. For $\sigma_v = 0$, the molecules reflect specularly; for $\sigma_v = 1$ the molecules reflect diffusively. The tangential momentum accommodation coefficient depends on the surface roughness, the gas temperature and pressure. Many studies have investigated this coefficient, proposing different methods of determination. These are reviewed, discussed, and compared in the work of Zhang et al., 2012 [10], where the authors, in Fig. 6.3, compared the non-dimensional flow rate $Q_N$ as a function of the Knudsen number $Kn$ predicted for various slip models. As showed, small

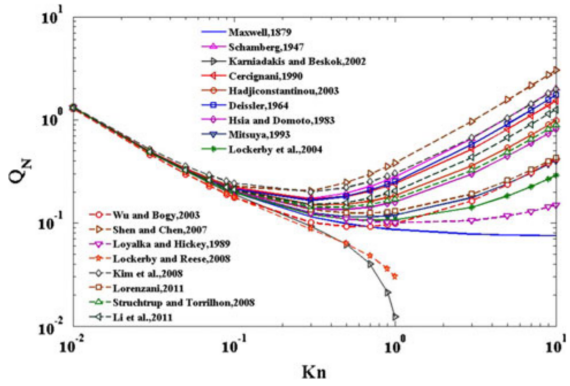


FIGURE 6.3 – Comparison of the non-dimensional flow rate $Q_N$ as a function of the Knudsen number Kn for various slip models. Reference to the work of Zhang et al., 2012 [10].

discrepancies characterize the models when $Kn < 0.1$. Thus, any model can be then selected for the

purpose of this work. For simplicity, the unitary Maxwell model is adopted in this work.
At the macro-scale, under the same assumptions, the system of Eq. 6.3 becomes

$$\begin{cases} \partial_{\boldsymbol{x}} \cdot \langle \boldsymbol{v}_g \rangle = 0 \\ \langle \boldsymbol{v}_g \rangle = -\dfrac{1}{\mu_g} \underline{\underline{K}} \cdot \partial_{\boldsymbol{x}} \langle p_g \rangle^g \end{cases} \tag{6.7}$$

where $\langle p \rangle^g$ and $\langle \boldsymbol{v}_g \rangle$ are the macroscopic average pressure and velocity fields [1], and $\underline{\underline{K}}$ is the corrected permeability tensor. The latter is expressed via the Klinkenberg model [167–169]

$$\underline{\underline{K}} = \underline{\underline{K}}_0 \Big( 1 + \frac{\underline{\underline{\beta}}}{\langle p_g \rangle^g} \Big) \tag{6.8}$$

where $\underline{\underline{K}}_0$ is the permeability tensor in the limit of continuum flow and $\underline{\underline{\beta}}$ the slip correction tensor. While $\underline{\underline{K}}_0$ depends on the microstructure of the material only, $\underline{\underline{\beta}}$ is also a function of the temperature and gas composition.
Now that the microscopic and macroscopic models have been introduced, it is easy to see that extending the use of CFD models to the slip regime requires the knowledge of the corrected permeability tensor. When dealing with TPS materials, the knowledge of this effective property is not immediate. In fact, the microscopic structure appears to be anisotropic and non-periodic. A few studies on the subject can be found in the literature. The DSMC technique proves to be the primary method used to determine the targeted effective properties of porous materials under rarefied flow conditions. White et al., 2016 [170], investigated numerically rarefied effects using micro-CT scans of ablative material samples and validated the method by comparison with experimental results. Both the virgin and pyrolysed states have been considered and, as expected, the pyrolysed material samples were found to be more permeable due to their higher porosity values. The article concludes on the importance of choosing a representative gas when performing permeability studies that include rarefied gases. A similar study has been performed by Borner et al., 2017 [9], where they computed the permeabilities of four X-ray microtomographies of carbon fiber materials submitted to high temperature gases. Results were in good agreement with experimental data published in the literature. The study shows that the corrected permeability is strongly dependant on the porosity of the material and on the pore size distribution. Kalarakis et al., 2012 [171], investigated with both DSMC and a modified Lattice Boltzmann method the behaviour of the corrected permeability in a two-dimensional reconstructed porous medium for Knudsen numbers varying in the range $0.1 - 10$. They noticed a good accuracy of the modified LBM predictions, which makes the method quite attractive to compute the permeability owing to the considerable saving in computational time and memory requirements compared to the DSMC method. For more examples concerning the use of the DSMC in determining the correct permeability tensor, we invite the reader to consult the following articles [12, 172–174], where different materials and applications are considered: catalytic converters and fuel cells [172], shale gas [173], and TPS materials [12, 174]. CFD techniques are also adopted to investigate the variation of the effective phenomena due to rarefied effects. Hosseini and Tafreshi, 2010 [175], studied the effect of slip flow on the permeability of 3-D virtual geometries of fibrous materials that reproduce the microstructure of a

1. See Appendix A (Section 6.6).

nano-fiber material. With the use of Stokes equation and partial slip boundary conditions, they inferred the permeability in one direction and found a good agreement with empirical correlations of the literature. Krakowska et al, 2019 [176], determined the corrected permeability tensor, still assumed as a spherical tensor, on computed X-ray tomography images of rock samples. They combined the results fluid flow simulations with laboratory measurement to investigated the impact of the accommodation coefficient on the volumetric flow rate and on the permeability. A similar study has been made by Madejski et al., 2019 [177], who studied a 3D X-ray tomography of tight rock samples. They observed that the corrected permeability can be up to 1.68 times greater considering the slip phenomenon. Nojoomizadeh et al., 2018 [178], worked with nano-fluids and they observed the influence of the velocity and temperature jumps conditions for Knudsen varying from 0.001 to 0.1 and were able to observe that an increase in the slip coefficient, thus of the Knudsen number, leads to an increase of the temperature jump at the wall.
The main objective of this work is to determine the corrected permeability tensor using PS-NS, a subject of great importance for the space community. For the first time, a complete numerical procedure is defined to estimate the slip correction tensor of non-periodic anisotropic porous media. The article is structured as follows. The numerical method for the estimation of the effective properties is described in Section 6.2. In Section 6.3 the numerical method is verified by comparison to literature data for a square array of cylinders. In Section 6.4, the effective properties of the material of the study, a carbon fiber preform called Calcarb, are derived for Knudsen varying from 0.001 to 0.1. Conclusions are drawn in Section 6.5.

## 6.2 Numerical Method

This section introduces the numerical method to evaluate the effective transport properties from the continuum to the slip regime. PS-NS on generic non-periodic anisotropic porous media are considered. The numerical procedure to determine the permeability tensor ($\underline{\underline{K}}_0$) for non-periodic anisotropic porous media, has been introduced by Scandelli et al., 2021 [11]. In this study, the authors define a particular set of boundary conditions, schematized in Fig. 6.4, in order to estimate the desired tensor. This estimation is done directly from Darcy's law [179], which is conveniently decomposed into the following system

$$\begin{cases} \langle \boldsymbol{v}_{g,x} \rangle = -\dfrac{1}{\mu_g}\Big(K_{0,xx}\nabla\langle p_{g,x}\rangle + K_{0,xy}\nabla\langle p_{g,y}\rangle + K_{0,xz}\nabla\langle p_{g,z}\rangle\Big) \\ \langle \boldsymbol{v}_{g,y} \rangle = -\dfrac{1}{\mu_g}\Big(K_{0,yx}\nabla\langle p_{g,x}\rangle + K_{0,yy}\nabla\langle p_{g,y}\rangle + K_{0,yz}\nabla\langle p_{g,z}\rangle\Big) \\ \langle \boldsymbol{v}_{g,z} \rangle = -\dfrac{1}{\mu_g}\Big(K_{0,zx}\nabla\langle p_{g,x}\rangle + K_{0,zy}\nabla\langle p_{g,y}\rangle + K_{0,zz}\nabla\langle p_{g,z}\rangle\Big) \end{cases} \tag{6.9}$$

The average macroscopic velocity components $\langle \boldsymbol{v}_{g,x} \rangle$, $\langle \boldsymbol{v}_{g,y} \rangle$, $\langle \boldsymbol{v}_{g,z} \rangle$ and pressure fields $\nabla\langle p_{g,x}\rangle$, $\nabla\langle p_{g,y}\rangle$, $\nabla\langle p_{g,z}\rangle$ are derived from the results of PS-NS. The remaining unknowns of the system are the nine permeability components, namely $K_{0,xx}, K_{0,xy}, ..., K_{0,zz}$. To close the system, a total of three simulations has to be performed by considering three different flow directions. For simplicity, the inlet flow

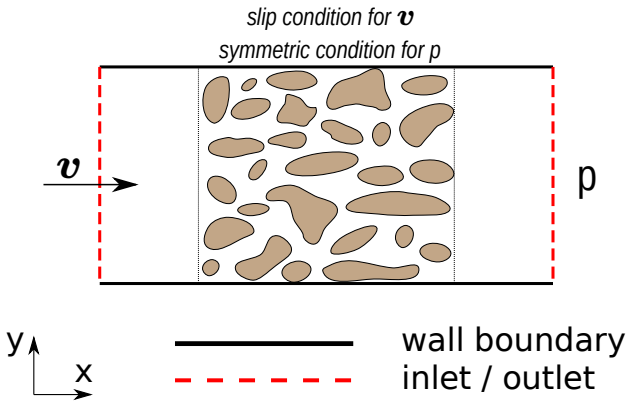


FIGURE 6.4 – Representation of a generic numerical domain to estimate the permeability tensor for non-periodic anisotropic media. The full numerical procedure is presented in [11].

can be aligned with the x, y and z directions in the different simulations. A global system of nine equations can be defined such as showed in Eq. (6.10), where the exponents $1, 2, 3$ refer to the first,

$$\begin{bmatrix} \langle \boldsymbol{v}^1_{g,x} \rangle \\ \langle \boldsymbol{v}^1_{g,y} \rangle \\ \langle \boldsymbol{v}^1_{g,z} \rangle \\ \langle \boldsymbol{v}^2_{g,x} \rangle \\ \langle \boldsymbol{v}^2_{g,y} \rangle \\ \langle \boldsymbol{v}^2_{g,z} \rangle \\ \langle \boldsymbol{v}^3_{g,x} \rangle \\ \langle \boldsymbol{v}^3_{g,y} \rangle \\ \langle \boldsymbol{v}^3_{g,z} \rangle \end{bmatrix} = -\frac{1}{\mu_g} \begin{bmatrix} \nabla\langle p^1_{g,x} \rangle & \nabla\langle p^1_{g,y} \rangle & \nabla\langle p^1_{g,z} \rangle & 0 & 0 & 0 & 0 & 0 & 0 \\ 0 & 0 & 0 & \nabla\langle p^1_{g,x} \rangle & \nabla\langle p^1_{g,y} \rangle & \nabla\langle p^1_{g,z} \rangle & 0 & 0 & 0 \\ 0 & 0 & 0 & 0 & 0 & 0 & \nabla\langle p^1_{g,x} \rangle & \nabla\langle p^1_{g,y} \rangle & \nabla\langle p^1_{g,z} \rangle \\ \nabla\langle p_{g,x} \rangle^2 & \nabla\langle p_{g,y} \rangle^2 & \nabla\langle p_{g,z} \rangle^2 & 0 & 0 & 0 & 0 & 0 & 0 \\ 0 & 0 & 0 & \nabla\langle p_{g,x} \rangle^2 & \nabla\langle p_{g,y} \rangle^2 & \nabla\langle p_{g,z} \rangle^2 & 0 & 0 & 0 \\ 0 & 0 & 0 & 0 & 0 & 0 & \nabla\langle p_{g,x} \rangle^2 & \nabla\langle p_{g,y} \rangle^2 & \nabla\langle p_{g,z} \rangle^2 \\ \nabla\langle p_{g,x} \rangle^3 & \nabla\langle p_{g,y} \rangle^3 & \nabla\langle p_{g,z} \rangle^3 & 0 & 0 & 0 & 0 & 0 & 0 \\ 0 & 0 & 0 & \nabla\langle p_{g,x} \rangle^3 & \nabla\langle p_{g,y} \rangle^3 & \nabla\langle p_{g,z} \rangle^3 & 0 & 0 & 0 \\ 0 & 0 & 0 & 0 & 0 & 0 & \nabla\langle p_{g,x} \rangle^3 & \nabla\langle p_{g,y} \rangle^3 & \nabla\langle p_{g,z} \rangle^3 \end{bmatrix} \begin{bmatrix} K_{0,xx} \\ K_{0,xy} \\ K_{0,xz} \\ K_{0,yx} \\ K_{0,yy} \\ K_{0,yz} \\ K_{0,zx} \\ K_{0,zy} \\ K_{0,zz} \end{bmatrix} \tag{6.10}$$

second, and third numerical simulations.
The same numerical procedure can be repeated to retrieve the slip correction tensor. In Eqs. 6.9 and 6.10, the corrected permeability tensor $\underline{\underline{K}}$ is considered instead of $\underline{\underline{K}}_0$. Once $\underline{\underline{K}}_0$ and $\underline{\underline{K}}$ are known, the slip tensor $\underline{\underline{\beta}}$ can be retrieved directly from Eq. (6.8).

## 6.3 Corrected Permeability of Square Arrays of Cylinders

We study in this section a flow through a square array of cylinders. The purpose is to validate our numerical method to compute the corrected permeability tensor. This problem has already been investigated experimentally, numerically and theoretically by several authors [9,12,13,180]. Moreover, to extend the reference database in the slip regime, DSMC simulations have been conducted with the OpenFoam DSMC solver [181]. The infinite array of parallel cylinders is modeled as a two dimensional problem and two cylinders in the direction of the flow are considered, as chosen by Stern et al., 2015 [12], and by Borner et al., 2017 [9]. The computational domain is schematized in Fig. 6.5. To comply with the references, the radius of the cylinders is taken as characteristic length. The only

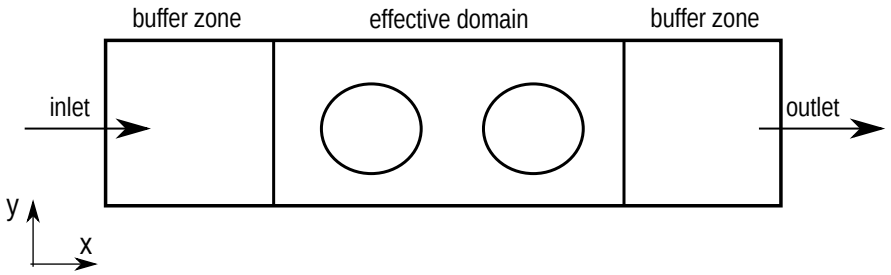


FIGURE 6.5 – Flow through a square array of cylinders. The array is modeled as a two dimensional problem and two cylinders (as considered in the references [9, 12]) are considered in the direction of the flow.

difference between this work and the one in the references is on the choice of the boundary conditions. In the literature, periodic boundary conditions are considered in the direction of the flow, whereas in this work we consider the numerical configuration showed in Fig. 6.4: imposed velocity field at the inlet and pressure at the outlet, with the addition of two buffer zones to limit the effects of these boundary conditions in the effective domain. The reason is that we want to validate the method even for generic non-periodic materials. Different porosities are considered by increasing its value, $\epsilon$, from 0.69 to 0.95. The porosity is changed by modifying the cylinder diameter. Argon is used as the carrier gas. Eight different values of the mean free path hence of the Knudsen number are studied. All rarefaction regimes are covered by at least one value, with the exception of the slip regime that is characterized by five different values. For this isotropic case, the corrected permeability reduces to a spherical tensor with only one component, $K$.
Results are showed in Fig. 6.6, where permeability values are made non-dimensional using the cylinder radius. Two plots compose the figure. In plot (a), a range of Knudsen numbers from 0.001 to 1 is considered. As expected, it can be observed that permeability increases with both porosity and Knudsen number. In particular, for $Kn < 0.01$, the effective property remains constant and equal to the material permeability in the limit of the continuum regime. For higher Knudsen numbers, the rarefied effects change its value as represented in the figure. Given a porosity value and the Knudsen number, the difference between the corrected permeability and the material permeability is directly linked to the slip correction tensor via Eq. (6.8). The reference database is composed by results from our DSMC, from the study of Borner et al., 2017 [9], and from the one of Shou et al., 2011 [13], where the following analytical solution is derived

$$K/r^2 = \frac{-0.5\ ln(1-\epsilon) + 0.25 - \epsilon - 0.25(1-\epsilon)^2 + 2Kn\ (-0.5\ ln(1-\epsilon) - 0.25 + 0.25(1-\epsilon)^2)}{4\ (1-\epsilon)(1+2Kn)} \tag{6.11}$$

to expresses the non-dimensional permeability as a function of the porosity and the Knudsen number for a flow perpendicular to a 1D fibrous medium. This equation was derived using a unit cell method from Stokes equation with a first-order slip boundary condition, thus limiting its validity to $Kn < 0.1$. DSMC results, both from this work and from Borner et al., 2017 [9], are taken as reference as valid also for high Knudsen values. The following average relative error in terms of K can be defined at a

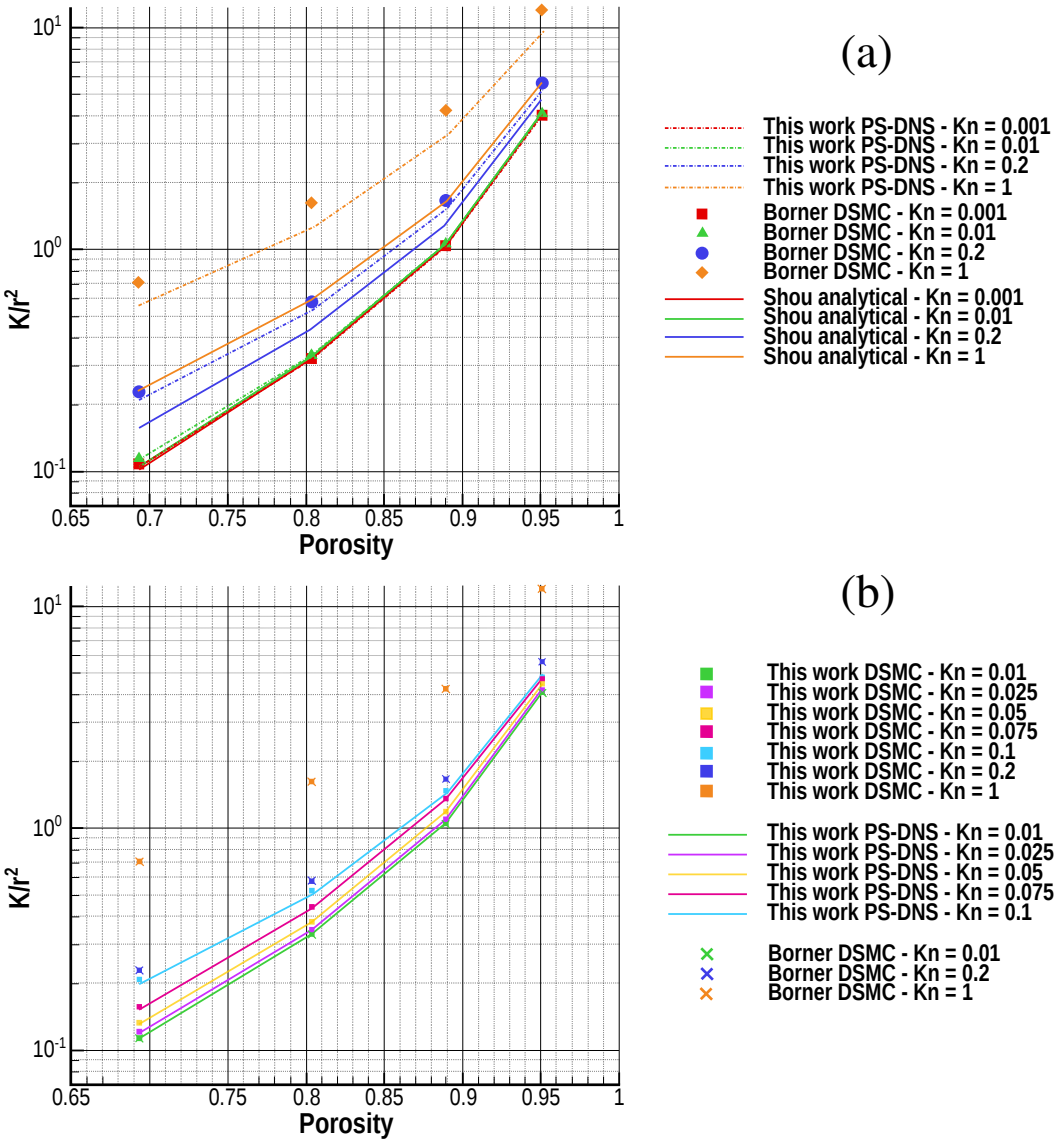


FIGURE 6.6 – Adimensional permeability behaviour for the flow through a square array of cylinders. Different porosity values and Knudsen numbers are considered. In plot (a), a range of Knudsen numbers from 0.001 to 1 is showed; in plot (b) a range of Knudsen numbers from 0.01 to 0.1 is highlighted. The reference database is composed by results from our DSMC, from the study of Borner et al., 2017 [9], and from the one of Shou et al., 2011 [13].

| **Kn = 0.001** | **Kn = 0.01** | **Kn = 0.2** | **Kn = 1** |
|---|---|---|---|
| 0.5% | 0.9% | 26.3% | 39.8% |

TABLE 6.1 – Relative average errors in terms of $K$ of our CFD results with the reference database.

| **Kn = 0.01** | **Kn = 0.025** | **Kn = 0.05** | **Kn = 0.075** | **Kn = 0.1** |
|---|---|---|---|---|
| 0.9% | 1.7% | 3.0% | 4.5% | 6.1% |

TABLE 6.2 – Relative average errors in terms of $K$ of our CFD results with the reference database, with emphasis on the slip regime.

fixed Knudsen number

$$\text{error } (\%) = \sum_{i=1}^{N} \frac{K_{i,ref} - K_{i,PS-NS}}{K_{i,ref}} \, 100 \tag{6.12}$$

where $i$ is the index to take into account the $N$ porosity values, the subscript $ref$ and $PS-NS$ refer respectively to the reference and our work. Errors are presented in Table 6.1. A good agreement is observed for small Knudsen numbers, that is when the flow is in the continuum regime and permeability values are nearly constants. The partial slip boundary condition (Eq. (6.4)) is a correct approximation when rarefied effects are not important. For Knudsen number $Kn = 0.2$ and higher, our results diverge form the reference ones. This is also expected: for this range of Knudsen number the flow is beyond the slip regime and Eq. 6.3. The comparison for the slip regime is done in plot (b) of Fig. 6.6, where a more specific range of Knudsen numbers from 0.01 to 0.1 is considered. Errors are presented in Table 6.2. Results lead to the desired validation: the partial slip boundary condition (Eq. (6.4)) allows the extension of the PS-NS method up to the slip regime.

## 6.4 Permeability of Calcarb

In this section, the PS-NS method is applied to the 3D X-ray computed-tomography segmented image of Calcarb showed in Fig. 6.7. Calcarb [87] is a carbon fiber preforms used as skeleton in heat-shield materials [68, 69, 88] with average porosities higher than 85 %. Its micro-structure is generally characterized by fibers preferentially aligned at about $\pm$ 15 degrees with one of the planes and this gives transverse isotropic properties to the material. The digital representation of its micro-structure has been acquired at the Advanced Light Source at Lawrence Berkeley National Laboratory and more details can be found in Borner et al, 2017 [9]. The resulting dataset (Fig. 6.7) has a resolution of 200 X 200 X 200 voxels, with a voxel size of 2.6 $\mu m$. This particular dataset has already been analyzed in the literature. Scandelli et al., 2022 [11], have determined its permeability tensor using PS-NS in the continuum regime; Borner et al, 2017 [9], have analyzed its permeability in rarefied conditions ($Kn < 0.1$).

The discretization of the domain is performed with the OpenFoam utility *snappyHexMesh*. For the purpose of this simulation, a good-quality (small values of skewness and non-orthogonality, and aspect

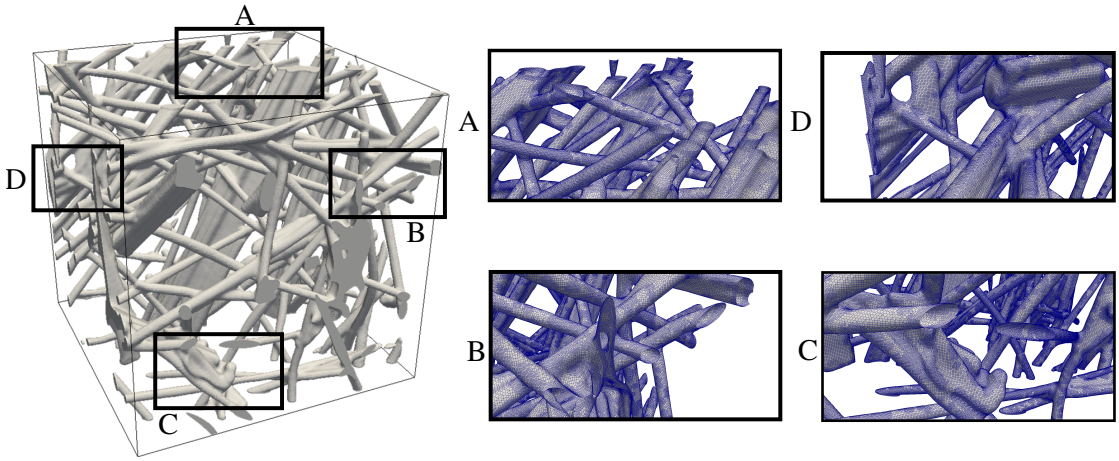


FIGURE 6.7 – On the left-hand side, volume rendering of the CMT of Calcarb. The dataset has a resolution of 200 X 200 X 200 voxels, with a voxel size of 2.6 $\mu m$; on the right-hand side, some details of the meshed geometry. The mesh accounts about 25 million cells.

ratio close to one) and homogeneous (as much as possible) mesh is targeted. A convergence analysis is conducted by monitoring the pressure difference between the inlet and the outlet of the domain by repeating pore-scale numerical simulations with increasingly fine meshes. The same conclusions as in the analysis of Scandelli et al., 2022 [11], are drawn: a 25 million cells-mesh is considered to proceed with the computation of the effective properties. Some details of the meshed geometry are given in Fig. 6.7. The permeability tensor is first computed in the limit of the continuum regime by considering the numerical method described in Section 6.2. A Knudsen number $Kn = 0.00001$ has been adopted. The resultant tensor, written with respect to the principal axes of rotation, is equal to

$$\underline{\underline{K}}_0 = \begin{bmatrix} 1.74\ 10^{-10} & 0 & 0 \\ 0 & 1.49\ 10^{-10} & 0 \\ 0 & 0 & 1.11\ 10^{-10} \end{bmatrix} m^2 \tag{6.13}$$

that is the same result found in Scandelli et al., 2022 [11]. With the aim of adopting representative conditions to the entry trajectories of space missions (Fig. 6.1), pyrolysis gases are considered at a constant temperature of $1000K$ and for pressure values to vary the Knudsen number in the continuity and flow regimes: $Kn = 0.0001$, $Kn = 0.001$, $Kn = 0.01$, $Kn = 0.025$, $Kn = 0.050$, $Kn = 0.075$, $Kn = 0.1$. For each value, the corrected permeability tensor ($\underline{\underline{K}}$) has been evaluated and written with respect to the principal axes of rotation. The behaviour of the three components of the tensor as functions of the Knudsen number is showed in Fig. 6.8. As expected, the three components increase in magnitude as the Knudsen number increases. The highest Knudsen number considered in the analysis is $Kn = 0.1$, since, as found in Section 6.3, this is the upper limit of validation of the partial slip model (Eq. (6.4)). Extrapolated results from Borner et al., 2017 [9], are also showed. A similar behaviour is observed with the Knudsen number, although they result to be shifted to higher permeability values. This is due to a different prediction of $\underline{\underline{K}}_0$: as outlined in Scandelli et al., 2022 [11], the adopted numerical procedure leads to an underestimation with respect to Borner et al., 2017 [9], of the effective

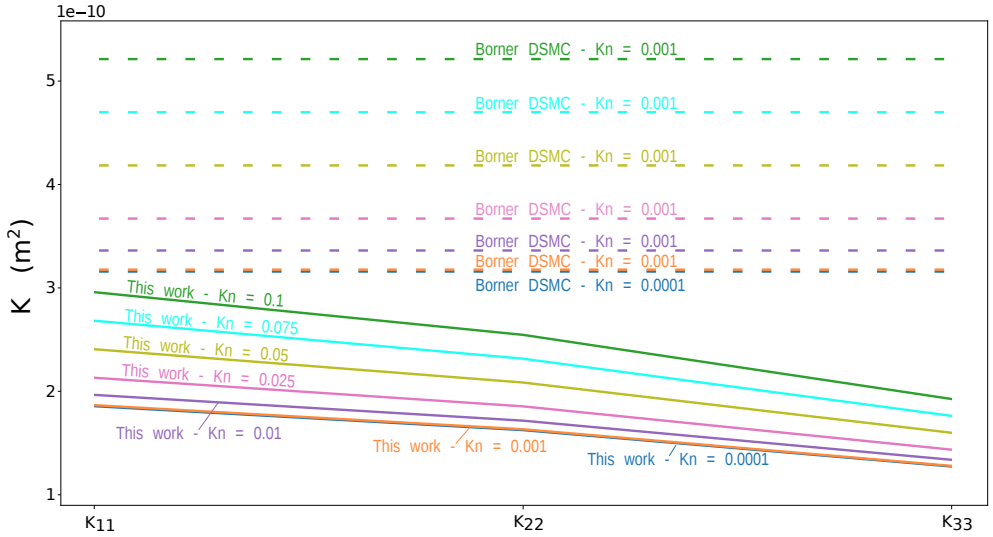


FIGURE 6.8 – Corrected permeability tensor components as function of the Knudsen number. $Kn = 0.0001$, $Kn = 0.001$, $Kn = 0.01$, $Kn = 0.025$, $Kn = 0.050$, $Kn = 0.075$, $Kn = 0.1$ are considered. It is possible to observe how rarefied effects lead to an increase of the three components. Extrapolated results from Borner et al., 2017 [9], are also showed.

property by a factor of 42%.
The knowledge of $\underline{\underline{K}}$ and $\underline{\underline{K}}_0$ allows the determination of the effective slip correction tensor (from Eq. (6.8)). The average of the different values is taken. The tensor, written with respect to the principal axes, is as follows

$$\underline{\underline{\beta}} = \begin{bmatrix} 971.5 & 0 & 0 \\ 0 & 948.1 & 0 \\ 0 & 0 & 901.4 \end{bmatrix} Pa \tag{6.14}$$

results have a relative difference around 8% with respect to the value predicted by Borner et al., 2017 [9].

## 6.5 Conclusions

In this work, a pore-scale numerical simulation is defined to characterize the dynamic interaction between a flow and a generic anistoropic non-periodic porous material when considering the effects of rarefied flow gas. In particular, the numerical method allows the determination of the corrected permeability tensor. This allows CFD methods to be extended to the slip regime and, as a result, a large computational gain over the use of DSMC methods. The numerical method is first presented and then verified by comparison to literature data for a square array of cylinders. Results are in good agreement with the reference database obtained from direct simulations with Monte Carlo methods, provided that the continuum or slip regime is considered. At this point, the method is applied to the characterization of a carbon fiber preform material called Calcarb. With the aim of adopting

representative conditions to the entry trajectories of space missions, the corrected permeability tensor has been computed for different values of the Knudsen number: $Kn = 0.0001$, $Kn = 0.001$, $Kn = 0.01$, $Kn = 0.025$, $Kn = 0.075$, $Kn = 0.1$. Based on the results, the slip correction tensor is evaluated. Results are in good agreement with literature data derived from DSMC methods. As future work, the analysis needs to be extended for non-isothermal flow conditions with the purpose to investigate possible variations of the effective thermal properties (effective conductivity tensor and heat transfer coefficient) in the slip regime. In this case, a temperature jump condition needs to be enforced to account for the thermal accomodation at the gas-solid boundary.

## 6.6 Appendix A. Remarks on the Volume Averaging Method

This appendix introduces the concepts of the volume averaging method are introduced. Further details can be found in the work of Whitaker, 2013 [15].
The volume averaging is a technique used to derive continuum-macroscopic equations for multiphase systems. In this way the complexity of a porous medium is replaced with an equivalent porous-continuum model in which each point is characterized by the properties of a representative elementary volume (REV) centered on it. Within this REV variables can be averaged. Two different definitions of averages have been adopted: the phase average which in this article has been used for the pressure term

$$\langle p \rangle^g = \frac{1}{V_g} \int_{V_g} p \, dV \tag{6.15}$$

and the intrinsic average, used for the velocity field

$$\langle \boldsymbol{v} \rangle = \frac{1}{V} \int_{V_g} \boldsymbol{v} \, dV \tag{6.16}$$

Inside the REV each variable can be decomposed using Gray's decomposition [159]) as the sum of its average plus a deviation contribution. For the pressure field this decomposition is as follows

$$p = \langle p \rangle^g + \tilde{p} \tag{6.17}$$

# Chapitre 7

# Volumetric Heat Transfer Coefficient: Numerical Evaluation and Introductory Analysis to Anisotropic Effects

## Nomenclature

*Latin Letters*

| | |
|---|---|
| $\boldsymbol{b}$ | first mapping variable for the temperature deviation $[m]$ |
| $c_p$ | specific heat at constant pressure $[J\ kg^{-1}\ K^{-1}]$ |
| $c_f$ | coefficients in the Nu-Pe correlation |
| $\underline{\underline{h_v}}$ | volumetric heat transfer tensor $[W\ m^{-3}\ K^{-1}]$ |
| $h_v$ | volumetric heat transfer coefficient $[W\ m^{-3}\ K^{-1}]$ |
| $\underline{\underline{I}}$ | identity tensor |
| $I$ | thermal inertia $[J\ m^{-2}\ K^{-1}\ s^{-1/2}]$ |
| $\boldsymbol{j}$ | transport coefficient vector $[W\ m^{-1}\ K^{-1}]$ |
| $\underline{\underline{K}}$ | permeability tensor $[m^2]$ |
| $\underline{\underline{k}}_{\text{eff}}$ | effective thermal conductivity tensor $[W\ m^{-1}\ K^{-1}]$ |
| $k$ | thermal conductivity coefficient $[W\ m^{-1}\ K^{-1}]$ |
| $\boldsymbol{l}$ | size of the periodic domain |
| $L$ | reference length $[m]$ |
| $\boldsymbol{n}$ | surface normal |
| $N$ | total number of values predicted by the strategies |
| $p$ | pore-scale pressure $[Pa]$ |
| $\boldsymbol{r}$ | position vector $[m]$ |
| $s$ | second mapping variable for the temperature deviation |
| $S$ | surface interface $[m^2]$ |
| $T$ | pore-scale temperature $[K]$ |

## Nomenclature

| | |
|---|---|
| $\boldsymbol{v}$ | pore-scale velocity $[m\ s^{-1}]$ |
| $V$ | volume of the domain $[m^3]$ |
| $\boldsymbol{x}$ | pore-scale coordinates $[m]$ |

*Greek Letters*

| | |
|---|---|
| $\alpha$ | angle between the averaged velocity direction and the x-axis |
| $\boldsymbol{\delta}$ | Dirac distribution function |
| $\delta$ | thickness of the buffer zone $[m]$ |
| $\epsilon$ | porosity of the medium |
| $\theta$ | angle of velocity orientation |
| $\mu$ | dynamic viscosity $[Pa\ s]$ |
| $\xi$ | arbitrary function |
| $\rho$ | pore-scale density $[kg\ m^{-3}]$ |
| $\psi$ | generic field |

*Subscripts and Superscripts*

| | |
|---|---|
| 0 | change of variable |
| cnt | center |
| g | gas |
| in | inlet |
| long | longitudinal |
| n | generic value |
| out | outlet |
| ref | reference |
| s | solid |
| transv | transversal |

*Special Symbols*

| | |
|---|---|
| $*$ | non-dimensional variable |
| $\sim$ | deviation term |
| $\langle\ \rangle$ | phase average |
| $\langle\ \rangle^f$ | intrinsic average |

*Adimensional Groups*

| | |
|---|---|
| Bi | Biot number |
| Nu | Nusselt number |
| Pe | thermal Peclet number |
| Pr | Prandtl number |
| Re | Reynolds number |

## Nomenclature

*Acronyms*

| | |
|---|---|
| CMT | Computed Micro-Tomography |
| LTE | Local Thermal Equilibrium |
| LTNE | Local Thermal Non-Equilibrium |
| REV | Representative Elementary Volume |

## Preamble

Authors: H. Scandelli; A. Ahmadi-Senichault; S. Liu; J. Lachaud;
Affiliations: Arts et Métiers Institute of Technology, Univ. Bordeaux, CNRS, Bordeaux INP, I2M, UMR 5295, F-33400 Talence, France;
Published: No;
Conference: This work has been presented at the 13th Annual InterPore2021 Meeting, 31 May 2021 to 3 June 2021, online;

## Abstract

In porous media, the direct proportionality between the heat flux and the fluid-solid temperature difference is driven by the heat transfer coefficient. This effective property, originally introduced in a heuristic way, has been theoretically justified a couple of decades ago using upscaling methods such as volume averaging and homogenization. Many parameters affect its value, mainly the Reynolds and Prandtl numbers, the porosity and the micro-structure of the material, and the velocity direction. The objective of this work is to define a new formulation of the heat transfer coefficient able to generically account for anisotropic effects. To this end, it is first necessary to define a numerical strategy for its determination. Two families of methods have been developed. (1) When dealing with periodic materials or with Representative Elementary Volume (REV), the effective property can be obtained by solving the associated closure problem derived from upscaling methods. (2) From microscopic numerical simulations, the heat transfer coefficient can be evaluated directly from its definition: the ratio between the heat flux at the solid-fluid interface and the difference of the averaged temperatures of the two phases. Family (2) can be applied to any type of geometry, but must be supplemented by the definition of appropriate boundary conditions. Deduced from the literature, or defined in this work, different set of boundary conditions have been tested on simple geometry cases. Only one set, defined in this work, proved to be able to correctly predict the heat transfer coefficient for small Peclet numbers. The latter has been applied to the characterization of a 3D computed microtomography (CMT) of Calcarb and

good agreement are found with experimental results. Finally, anisotropic effects are investigated. It will be showed that a tensorial form of the heat exchange between the two phases is able to perfectly accounts for anisotropic effects under certain conditions.

**Keywords**: Porous media; Volumetric Heat Transfer Coefficient; Closure Problem; Pore-scale numerical simulations; Boundary conditions; Calcarb CMT; Anisotropic Effects

## 7.1 Introduction

The subject of porous materials submitted to high temperatures is of great relevance for a wide range of engineering applications: design of ablative heat shields of space vehicles [74, 182, 183], prediction of fire propagation in a closed environment [59, 60], thermal conversion of biomass into biofuel [52, 184], thermal insulation [185], cracking of hot gases passing through a porous material [186, 187], and many others. The numerical description of these applications is, however, a very complex topic. It can be faced either at the pore-scale or at the macro-scale. The former approach implies to simultaneously deal with heat and mass transfer phenomena and complex pore geometries; the latter simplifies the description by averaging the local variations and focusing on the macroscopic behavior, which is often sufficient to analyze a system. Both approaches are now presented.
At the pore scale, the flow of a Newtonian, incompressible, steady-state, and isotropic fluid in a rigid porous medium is described by the Navier-Stokes equations coupled with the energy conservation equation for non-isothermal problems. Under the assumptions of negligible volume forces, constant properties, and solid phase at a fixed temperature $T_s$ [1], these equations become

$$\begin{cases} \partial_{\boldsymbol{x}} \cdot \boldsymbol{v}_g = 0 \\ \rho_g \ \partial_{\boldsymbol{x}} \cdot (\boldsymbol{v}_g \otimes \boldsymbol{v}_g) - \mu_g \partial^2_{\boldsymbol{x}} \boldsymbol{v}_g = -\partial_{\boldsymbol{x}} p_g \\ \rho_g \, c_p \ \boldsymbol{v}_g \cdot \partial_{\boldsymbol{x}} T_g = k \partial^2_{\boldsymbol{x}} T_g \\ BC1: \ \ \boldsymbol{v}_g = 0 \qquad at \ S_{gs} \\ BC2: \ \ T_g = T_s \qquad at \ S_{gs} \end{cases} \tag{7.1}$$

where $\boldsymbol{v}_g$, $p_g$, and $T_g$ represent the velocity, pressure, and temperature, while $\rho_g$, $c_p$, and $k$ denote the density, specific heat at constant pressure, and thermal conductivity of the gas. $S_{gs}$ is the area of the gas-solid interface.
These equations can be written in a non-dimensional form by introducing the dimensionless variables reported in Table 7.1. References values for the velocity, pressure, and temperature are commonly taken as the field averages in the domain [2]. The mean porous medium grain diameter can be chosen as reference value for the length [188], $L$. The non-dimensional form of the governing equations is given

1. See Appendix A (Section 7.7).
2. See Appendix B (Section 7.8).

| quantity | dimensionless variable |
|---|---|
| temperature | $T_g^* = T_g/\langle T_g\rangle$ |
| pressure | $p_g^* = p_g L/(\mu_g\|\langle \boldsymbol{v}_g\rangle\|)$ |
| velocity | $\boldsymbol{v}_g^* = \boldsymbol{v}_g/\|\langle \boldsymbol{v}_g\rangle\|$ |
| length | $\boldsymbol{r}^* = \boldsymbol{r}/L$ and $\partial_{\boldsymbol{x}^*} = L\partial_{\boldsymbol{x}}$ |

TABLE 7.1 – Non-dimensional variables to introduce in order to obtain the non-dimensional form of the Eq.(7.1).

by

$$\begin{cases} \partial_{\boldsymbol{x}^*}\cdot \boldsymbol{v}_g^* = 0 \\ Re\ \partial_{\boldsymbol{x}^*}\cdot(\boldsymbol{v}_g^*\otimes\boldsymbol{v}_g^*) - \partial^2_{\boldsymbol{x}^*}\boldsymbol{v}_g^* = -\partial_{\boldsymbol{x}^*}p_g^* \\ \rho_g^*\boldsymbol{v}_{\boldsymbol{g}}^*\cdot\partial_{\boldsymbol{x}^*}T_g^* = \dfrac{1}{Pe}\partial_{\boldsymbol{x}^*}\cdot(\partial_{\boldsymbol{x}^*}T_g^*) \\ BC1: \ \boldsymbol{v}_g^* = \boldsymbol{0} \qquad\qquad at\ S_{gs} \\ BC2: \ T_g^* = T_s/\langle T_g\rangle \qquad at\ S_{gs} \end{cases} \tag{7.2}$$

Two dimensionless groups arise from this analysis. The Reynolds $Re$ and the thermal Peclet $Pe$ numbers, defined as follows

$$Re = \frac{\rho_g\,|\langle \boldsymbol{v}_g\rangle|\,L}{\mu_g} \tag{7.3}$$

$$Pe = \frac{\rho_g\,c_p\,|\langle \boldsymbol{v}_g\rangle|L}{k} \tag{7.4}$$

The Reynolds number characterizes the relative importance of inertial and viscous forces within a fluid. In this study we suppose $Re \ll 1$, that is, the flow is in the creeping regime where non-linear effects are negligible. The thermal Peclet number is the ratio of the rates of the processes of advection $\left(\dfrac{|\langle \boldsymbol{v}_g\rangle|}{L}\right)$ and thermal diffusion $\left(\dfrac{k}{\rho_g\,c_p\,L^2}\right)$. No assumption is made on this number.
The thermal problem is assumed to be in Local Thermal Non-Equilibrium (LTNE). At the macroscopic scale, the averaged governing equations [179, 189] can be written as

$$\begin{cases} \partial_{\boldsymbol{x}}\cdot\langle \boldsymbol{v}_g\rangle = 0 \\ \langle \boldsymbol{v}_g\rangle = -\dfrac{1}{\mu_g}\,\underline{\underline{K}}\cdot\partial_{\boldsymbol{x}}\langle p_g\rangle \\ \rho_g\,c_p\langle \boldsymbol{v}_g\rangle\cdot\partial_{\boldsymbol{x}}\langle T_g\rangle = \partial_{\boldsymbol{x}}\cdot\underline{\underline{k}}_{\text{eff}}\cdot\partial_{\boldsymbol{x}}\langle T_g\rangle + h_v(T_s - \langle T_g\rangle) \\ BC1: \ \langle \boldsymbol{v}_g\rangle = \boldsymbol{0} \qquad at\ S_{gs} \\ BC2: \ \langle T_g\rangle = T_s \qquad at\ S_{gs} \end{cases} \tag{7.5}$$

where $\underline{\underline{K}}$ is the permeability tensor, $\underline{\underline{k}}_{\text{eff}}$ the effective conductivity tensor of the fluid phase, and $h_v$ the volumetric heat transfer coefficient. This dual description of the problem can be observed in Fig.7.1. The average macroscopic results arising from solving the direct pore-scale problem (Eq. (7.1)) and from solving the averaged macroscopic problem (Eq. (7.5)) are equivalent, provided that the Representative Elementary Volume (REV) [190] is carefully chosen and the macroscopic properties

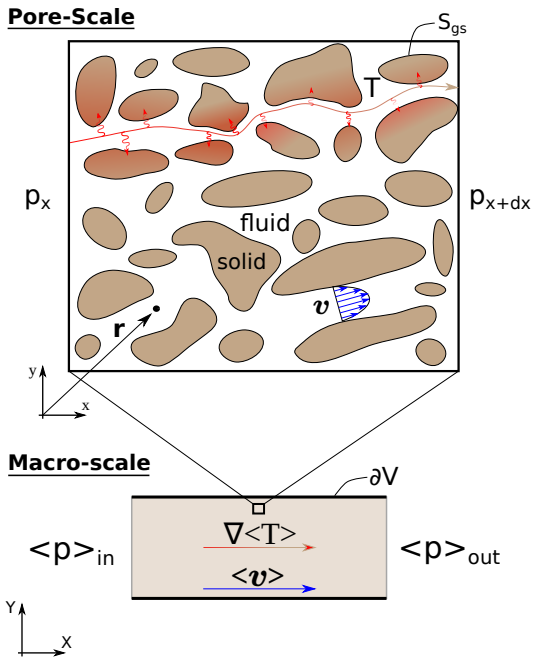


FIGURE 7.1 – Pore-scale and macro-scale representations of the heat-transport problem in porous media.

are correctly derived. In particular, for this problem, three properties need to be determined: $\underline{\underline{K}}$, $\underline{\underline{k}}_{\text{eff}}$, and $h_v$. The macroscopic energy equation in the system of Eq.(7.5) has originally been introduced in a heuristic way by Vortmeyer et al, 1974 [189] and since then it has been widely used and improved in the literature [191, 192]. This equation can be also derived from a theoretical basis. From the volume averaging theory [193], the following equation can be obtained

$$\rho_g\, c_p \langle \boldsymbol{v}_g \rangle \cdot \partial_{\boldsymbol{x}} \langle T_g \rangle + \rho_g\, c_p \partial_{\boldsymbol{x}} \cdot \langle \tilde{\boldsymbol{v}}_g \tilde{T}_g \rangle = \partial_{\boldsymbol{x}} \cdot \left[ \epsilon k\ \partial_{\boldsymbol{x}} \langle T_g \rangle + \frac{1}{V} \int_{S_{gs}} k T_g \boldsymbol{n}_{gs} dS \right] + \frac{1}{V} \int_{S_{gs}} k \partial_{\boldsymbol{x}} T_g \cdot \boldsymbol{n}_{gs} dS \quad (7.6)$$

Where $\epsilon$ identifies the porosity of the medium and $\boldsymbol{n}_{gs}$ the normal at the interface from the fluid phase to the solid one. By comparing the two macroscopic descriptions, which are equivalent as long as the correct effective properties are considered, the following relationships can be inferred

$$\underline{\underline{k}}_{\text{eff}} \cdot \langle T_g \rangle = \underbrace{\epsilon k\ \partial_{\boldsymbol{x}} \langle T_g \rangle}_{\text{thermal diffusion}} + \underbrace{\frac{1}{V} \int_{S_{gs}} k T_g \boldsymbol{n}_{gs} dS}_{\text{Tortuosity}} - \underbrace{\rho_g\, c_p \partial_{\boldsymbol{x}} \cdot \langle \tilde{\boldsymbol{v}}_g \tilde{T}_g \rangle}_{\text{Dispersion}} \quad (7.7)$$

$$h_v = \frac{\frac{1}{V} \int_{S_{gs}} k \partial_{\boldsymbol{x}} T_g \cdot \boldsymbol{n}_{gs} dS}{T_s - \langle T_g \rangle} \quad (7.8)$$

Three different terms contribute to the effective conductivity tensor: the thermal molecular diffusion, the tortuosity, and the dispersion. Due to the complexity in their determination, the tortuosity and dispersion terms are often neglected (which is correct if $Pe < 1$ [193]) or obtained with correlations [192].

The energy conservation of the system can be otherwise characterized by Local Thermal Equilibrium (LTE) models, which assume the fluid and solid temperatures to rapidly reach an equilibrium temperature value: $\langle T_g \rangle = \langle T_s \rangle = \langle T \rangle$. The LTE assumption simplifies the modeling but its validity is strongly affected by several parameters, like the thermal diffusion properties of the phases and the geometrical characteristics of the material [194–197]. Quintard and Whitaker, 1993 [198] identifies several physical situations in which the local thermal equilibrium fails. These include processes in which the convective transport is important, transient processes when short time are considered, and transient diffusion processes in which the solid and fluid phases are characterized by different values of thermal conductivity (the greatest departure from local equilibrium is observed for $k_s/k_g = 100$). The analysis of the validity of LTE models was further developed by Dorea and De Lemos, 2010 [199], who simulated an impinging jet on a flat plate covered with a layer of a porous material and showed how the two models led to different results when varying the microstructure. In particular, they observed that the differences between the two models were more pronounced for higher values of porosity, permeability, and the ratio between the solid and the flow phases thermal conductivities; similar results were observed by [200] for metal foams and by [201] for geothermal systems. Quintard, 1997 [193], argued that as the temperature difference between the two phases cannot be easily estimated, assessing the validity of the local thermal equilibrium hypothesis is not a simple task. He suggested that the use of a LTNE model is a possible solution to the problem. This solution has been increasingly used over the years and further developments have been proposed by Saito and Lemos, 2010 [202] to deal with turbulent flows, by Gao et al., 2017 [203] to study flow with phase changes, by Jiang and Ren, 2001 [204] to analyze forced convection, and by Wang et al., 2019 [205] to deal with unsteady heat transfer.
The use of the LTNE model given in the system of Eq. (7.5) necessitates the knowledge of the effective properties. In this work, the permeability and the effective conductivity tensors are assumed to be known, while the volumetric heat transfer coefficient needs to be evaluated. Three families of methods have been identified from the literature: the *Closure Method*, which can be applied for Representative Elementary Volumes (REV) or periodic media and consists in solving a closure problem [193]; the *Integral Method*, which can be adopted for any volume of a generic porous media, even those that are not periodic or non-representative. This method consists in performing direct numerical simulations of the coupled heat and mass transfer problem (Eq. (7.1)) and then using Eq. (7.8) to derive the heat transfer coefficient; the *Trivial Method*, introduced by Cimmino et al, 2017 [206], where the interface heat flux is defined from a simplified version of the macroscopic heuristic model

$$h_v = \frac{(\rho_g c_p)\, \epsilon\, \partial_t \langle T_g \rangle}{\langle T_s \rangle - \langle T_g \rangle} \tag{7.9}$$

This third method is strongly dependant on the LTNE model considered and the values chosen for the permeability and effective conductivity tensors. As the latter are not evaluated directly in this work, this third method will not be further analyzed.

The heat transfer coefficient is a function of different parameters in the problem, such as Reynolds and Prandtl numbers [193, 207], porosity [192, 208], geometry of the problem [209], and the velocity direction [210], to cite some of them. This last dependency characterizes only anisotropic media and

Nakayama et al., 2002 [210], proposed a correlation to account for this effect

$$Nu = c_{f1} cos^2(\alpha) + c_{f2} sin^2(\alpha) + c_{f3}^{0.3} Re^{0.6} Pr^{1/3} \tag{7.10}$$

where $Pr$ and $Nu$ are respectively the Prandtl and Nusselt numbers, two non-dimensional groups defined as follows

$$Pr = \frac{\mu_g c_p}{k} \tag{7.11}$$

$$Nu = \frac{h_v \, l}{k} \tag{7.12}$$

and $\alpha$ is the angle between the averaged velocity direction and the x-axis. It can be seen that when the Reynolds and Prandtl numbers are constant, the Nusselt number may vary due the variation of $\alpha$. However, this correlation is not generic. The coefficients $c_{f1}$, $c_{f2}$, and $c_{f3}$ are functions of the geometry and of the Reynolds and Prandtl numbers. Their values can highly change every time a new problem is tackled. The objective of this article is to define a new formulation of the heat transfer coefficient that generically accounts for anisotropy effects without the need of any correlation. To this end, it is first necessary to define a numerical strategy for its determination. The mathematical description of the closure and integral methods is presented in Section 7.2. The methods need to be implemented, completed with appropriate set of boundary conditions, and validated. This is done in Section 7.3, where simple geometry cases are considered. Section 7.4 investigates the anisotropic effects and proposes a new formulation to characterize the heat exchange between the two phases. In Section 7.5, the volumetric heat transfer coefficient of a carbon fiber preform, named Calcarb, is estimated and compared with experimental results. Conclusions are finally drawn in Section 7.6.

## 7.2 Mathematical Description of the Two Families of Approaches

This section presents the mathematical description of the two families of numerical methods used in this work to estimate the volumetric heat transfer coefficient.

### 7.2.1 The Closure Method

The closure method can be applied to periodic unit cells or to sufficiently large volume domains to take into account all the characteristics of the pore structure (REV). For the case of a solid phase at constant temperature, the related closure problem has never been derived. This is proposed in what follows through the volume average theory.
The starting point is the thermal governing equations at the pore-scale, which can be averaged as

$$\left\langle \rho_g \, c_p \, \boldsymbol{v}_g \cdot \partial_{\boldsymbol{x}} T_g \right\rangle = \left\langle \partial_{\boldsymbol{x}} \cdot (k \partial_{\boldsymbol{x}} T_g) \right\rangle \tag{7.13}$$

The two terms can be developed by making extensive use of the divergence and scalar product properties, and of the averaging theorems [211]

$$\langle \partial_{\boldsymbol{x}} \psi_g \rangle = \partial_{\boldsymbol{x}} \langle \psi_g \rangle + \frac{1}{V} \int_{S_{gs}} \psi_g \, \boldsymbol{n}_{gs} dS \tag{7.14}$$

$$\langle \partial_{\boldsymbol{x}} \cdot \boldsymbol{\psi_g} \rangle = \partial_{\boldsymbol{x}} \cdot \langle \boldsymbol{\psi_g} \rangle + \frac{1}{V} \int_{S_{gs}} \boldsymbol{n}_{gs} \cdot \boldsymbol{\psi_g} \, dS \tag{7.15}$$

where $\psi_g$ is a generic field. The averaged thermal equation takes the following form

$$\rho_g \, c_p \, \langle \boldsymbol{v}_g \rangle \cdot \partial_{\boldsymbol{x}} \langle T_g \rangle + \rho_g \, c_p \, \langle \tilde{\boldsymbol{v}_g} \cdot \partial_{\boldsymbol{x}} \tilde{T}_g \rangle = \partial_{\boldsymbol{x}} \cdot \Big[ k(\epsilon \partial_{\boldsymbol{x}} \langle T_g \rangle + \frac{1}{V} \int_{S_{gs}} \tilde{T}_g \boldsymbol{n}_{gs} dS) \Big] + \frac{1}{V} \int_{S_{gs}} k \partial_{\boldsymbol{x}} \tilde{T}_g \cdot \boldsymbol{n}_{gs} dS \tag{7.16}$$

A boundary value problem for the spatial deviation temperature $\tilde{T}_g$ must be developed to obtain a closed form of the thermal equation. For such purpose, Eq. (7.16) is first divided by $\epsilon$ and then subtracted to the pore-scale thermal equation (Eq.(7.1)). The following system is obtained

$$\begin{cases} \rho_g \, c_p \, \tilde{\boldsymbol{v}_g} \cdot \partial_{\boldsymbol{x}} \langle T_g \rangle + \rho_g \, c_p \, \boldsymbol{v}_g \cdot \partial_{\boldsymbol{x}} \tilde{T} = \partial_{\boldsymbol{x}} \cdot (k \partial_{\boldsymbol{x}} \tilde{T}_g) + \\ \qquad\qquad -\epsilon^{-1} \partial_{\boldsymbol{x}} \cdot \Big( k \frac{1}{V} \int_{S_{gs}} \tilde{T}_g \boldsymbol{n}_{gs} dS \Big) - \epsilon^{-1} k \frac{1}{V} \int_{S_{gs}} \partial_{\boldsymbol{x}} \tilde{T}_g \cdot \boldsymbol{n}_{gs} \, dS, \quad in \;\; V_g \\ BC: \;\; \tilde{T}_g = T_s - \langle T_g \rangle \quad at \; S_{gs} \end{cases} \tag{7.17}$$

The system is characterized by two independent variables $T_g$ and $\tilde{T}_g$. Since the problem is linear, it is possible to express a generic linear dependence of the deviation variable ($\tilde{T}_g$) on the source terms of Eq.(7.17): $\partial_{\boldsymbol{x}} \langle T_g \rangle$ and $(\langle T_g \rangle - T_s)$. In addition, due to the scale separation assumption, a quasi-steady relationship [3] can be introduced. Based on these observations, the following generic relation can be assumed

$$\tilde{T}_g = \boldsymbol{b} \cdot \partial_{\boldsymbol{x}} \langle T_g \rangle - s(\langle T_g \rangle - T_s) + \xi \tag{7.18}$$

where $\xi$ is an arbitrary function, and $\boldsymbol{b}$ and $s$ are the mapping variables. The contribution of the arbitrary function to the temperature deviation field has been proved [193, 198] to be negligible with respect to the contribution of the mapping variables. Hence, $\xi$ can be neglected from the equation. Eq. (7.18) is substituted into Eq.(7.16), which becomes

$$\rho_g \, c_p \, \langle \boldsymbol{v}_g \rangle \cdot \partial_{\boldsymbol{x}} \langle T_g \rangle + \rho_g \, c_p \Big\langle \tilde{\boldsymbol{v}_g} \cdot \partial_{\boldsymbol{x}} \big[ \boldsymbol{b} \cdot \partial_{\boldsymbol{x}} \langle T_g \rangle - s(\langle T_g \rangle - T_s) \big] \Big\rangle = \partial_{\boldsymbol{x}} \cdot \Big[ k(\epsilon \partial_{\boldsymbol{x}} \langle T_g \rangle + \frac{1}{V} \int_{S_{gs}} \big[ \boldsymbol{b} \cdot \partial_{\boldsymbol{x}} \langle T_g \rangle$$

$$- s(\langle T_g \rangle - T_s) \big] \boldsymbol{n}_{gs} dS) \Big] + \frac{1}{V} \int_{S_{gs}} k \partial_{\boldsymbol{x}} \big[ \boldsymbol{b} \cdot \partial_{\boldsymbol{x}} \langle T_g \rangle - s(\langle T_g \rangle - T_s) \big] \cdot \boldsymbol{n}_{gs} dS \tag{7.19}$$

The equation can be written in a more compact form

$$\rho_g \, c_p \, \langle \boldsymbol{v}_g \rangle \cdot \partial_{\boldsymbol{x}} \langle T_g \rangle - \boldsymbol{j}_{gs} \cdot \partial_{\boldsymbol{x}} \langle T_g \rangle = \partial_{\boldsymbol{x}} \cdot (\underline{\underline{k}}_{\text{eff}} \cdot \partial_{\boldsymbol{x}} \langle T_g \rangle) - h_v (\langle T_g \rangle - T_s) \tag{7.20}$$

by introducing the transport coefficient vector $\boldsymbol{j}_{gs}$, the conductivity tensor $\underline{\underline{k}}_{\text{eff}}$, and the heat transfer coefficient $h_v$, defined as follows

$$\underline{\underline{k}}_{\text{eff}} = k(\epsilon \underline{\underline{I}} + \langle \boldsymbol{n}_{gs} \boldsymbol{b} \boldsymbol{\delta}_{gs} \rangle) - \rho_g \, c_p \, \langle \tilde{\boldsymbol{v}} \boldsymbol{b} \rangle \tag{7.21}$$

3. The quasi-steady relationship implies the averaged field to be time-dependant, while the deviation field is stationary.

$$\boldsymbol{j}_{gs} = \langle \boldsymbol{n}_{gs} \cdot k\partial_{\boldsymbol{x}} \boldsymbol{b} \boldsymbol{\delta}_{gs} \rangle - k\langle \boldsymbol{n}_{gs} s \boldsymbol{\delta}_{gs} \rangle + \rho_g \, c_p \, \langle \tilde{\boldsymbol{v}} s \rangle \tag{7.22}$$

$$h_v = \langle \boldsymbol{n}_{gs} \cdot k\partial_{\boldsymbol{x}} s \boldsymbol{\delta}_{gs} \rangle \tag{7.23}$$

where $\underline{\underline{I}}$ is the identity tensor and $\boldsymbol{\delta}_{gs}$ the Dirac distribution associated with the interface $S_{gs}$.
The goal of developing a boundary value problem for the spatial deviation temperature $\tilde{T}_g$ is converged into finding a set of boundary value problems for the mapping variables $\boldsymbol{b}$ and $s$. Thanks to the introduction of the arbitrary function $\xi$ in the generic relation for $\tilde{T}_g$ (Eq.(7.18)), even if negligible, the closure problems can be specified in any way. In particular, an expression similar to the system of Eq.(7.17) is looked for. For the purpose of this work, only the closure problem for the mapping variable $s$ is presented. The latter, by assuming the domain to be periodic, is defined as follows

$$\begin{cases} \rho_g \, c_p \, \boldsymbol{v}_g \cdot \partial_{\boldsymbol{x}} s = k\partial^2_{\boldsymbol{x}} s - \epsilon^{-1} h_v \, , & in \;\; V_g \\ BC: \quad s = 1 \, , & at \quad S_{gs} \\ s(\boldsymbol{r} + \boldsymbol{l}) = s(\boldsymbol{r}) \\ \langle s \rangle = 0 \end{cases} \tag{7.24}$$

where $\boldsymbol{l}$ represents the size of the periodic domain and in the first equation of the system it is possible to observe the presence, as a source term, of the integral term of the mapping variable ($h_v$). In order to solve the closure problem, the following change of variable has to be introduced

$$s = h_v s^0 - 1 \tag{7.25}$$

The closure problem for $s^0$ is found to be

$$\begin{cases} \rho_g \, c_p \, \boldsymbol{v}_g \cdot \partial_{\boldsymbol{x}} s^0 = k\partial^2_{\boldsymbol{x}} s^0 - \epsilon^{-1} \, , & in \;\; V_g \\ BC: \quad s^0 = 0 \, , & at \quad S_{gs} \\ s^0(\boldsymbol{r} + \boldsymbol{l}) = s^0(\boldsymbol{r}) \end{cases} \tag{7.26}$$

where the volumetric exchange coefficient is given by

$$h_v = -\frac{1}{\langle s^0 \rangle} \tag{7.27}$$

An in-house solver, hvClosureSolver, has been developed to solve the closure problem for $s^0$ (Eq. (7.26)). To improve its stability (especially at high Peclet numbers) a transient term has been added in the equation. The time integration is carried out through an implicit scheme. Once the solver converges, the volumetric heat transfer coefficient is evaluated via Eq. (7.27).

### 7.2.2 The Integral Method

The integral method can be applied to any type of geometry. The numerical approach relies on direct numerical simulations on the pore-scale structure and computation of the heat transfer coefficient

using Eq. (7.8). For the numerical implementation, the momentum and energy equations have been decoupled as the flow is assumed to be incompressible. This allows the velocity field to be obtained first and used as input to the energy equation. In particular, the *simpleFoam* [153,154] solver has been adopted to solve the momentum equation, and a dedicated solver has been implemented to solve the heat transfer problem. Once the temperature field was obtained, the $h_v$ coefficient has been evaluated from the temperature field distribution within the thermal boundary layer (Eq. (7.8)).

## 7.3 Selection of the Numerical Strategy

The numerical methods need to be defined in terms of computational domains and boundary conditions. In this work, we denote as *strategy* a generic numerical setting in terms of the considered domain (sample) and the boundary conditions of a pore-scale simulation. While for the closure method only a possible computational domain and set of boundary conditions can be considered, different strategies can be applied for the integral method. All the strategies explored in this section are schematized in Fig. 7.2 Strategies A, C, D, and E were found in the literature, whereas strategies B, F, G, and H have been defined in this work. Some comments on the strategies can be made:

- Strategy A is based on the closure method derived in Section 7.2;
- Strategies B, C, D, E, F, G, and H are based on the integral method;
- For strategies A and B periodic boundary conditions are considered. The flow is driven by pressure and thermal gradients. When media are not periodic, a layer of fluid $\delta$ is added outside the effective domain in order to adopt periodic boundary conditions;
- Strategy C has been defined in this work to imitate Strategy B without the use of periodic boundary conditions;
- For the integral method, Strategies D [35, 209, 212, 213], E [207, 208, 214–216], and H [36] have been defined in the literature;
- Strategy E aims to obtain a periodic profile for the velocity field and a similar profile for the temperature field by repeating the simulations several times. Each time the dimensionless temperature at the output is used to set the inlet profile for the next simulation, until convergence of the results;
- Strategies F and G have been defined in this work to obtain a non-uniform inlet temperature profile.

Once implemented, the strategies have been applied and compared to the four cases showed in Fig. 7.3. The geometries are the following: (a) periodic square array of cylinders with 1-sphere unit cell; (b) periodic square array of cylinders with 100-unit cells; (c) periodic cell-centered array of cylinders with 1-unit cells; (d) periodic cell-centered array of cylinders with 100-unit cells. All the cases are two-dimensional and for all of them two different porosity values have been considered: $\epsilon = 0.38$ and $\epsilon = 0.92$. Uniform meshes have been generated with surface refinements close to the solid cylinders. A mesh convergence analysis has been performed for the different cases by monitoring the convective heat transfer coefficient. Different Peclet values have been considered in a range from 0.1 to 1000.

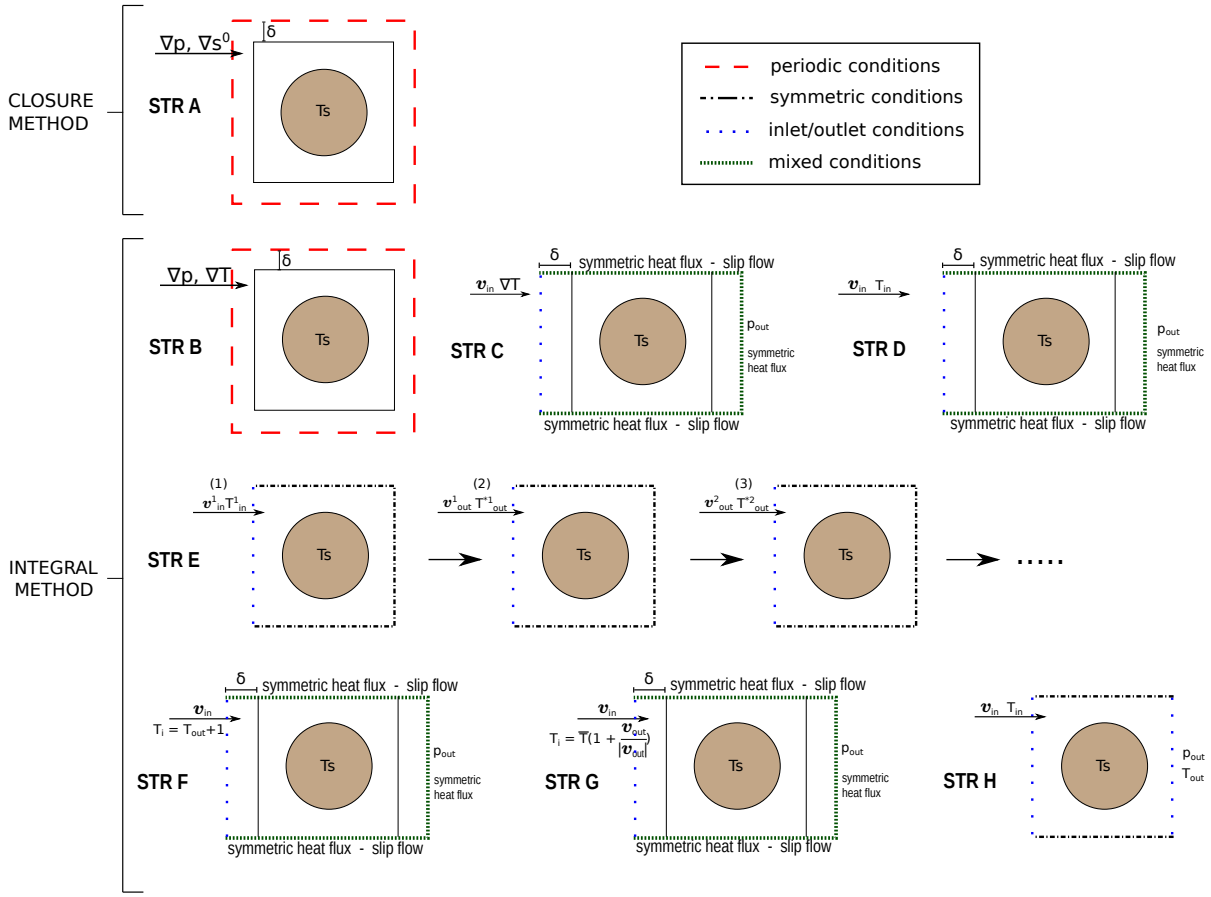


FIGURE 7.2 – 2D sketches of the numerical strategies explored in this work. Strategy A makes use of the closure method. Strategies B, C, D, E, F, G, and H are based on the integral method.

Strategies are compared between themselves by defining the following relative error

$$\text{relative error} = \frac{1}{N}\sum_{n}^{N}\frac{Nu_{ref,n} - Nu_n}{Nu_{ref,n}}\,100 \tag{7.28}$$

where $Nu_n$ is a generic Nusselt value resulted from the simulation, $Nu_{\text{ref}}$ is the reference strategy, and N is the total number of values predicted by the strategies.
Results are showed in terms of the Nusselt number, where the dimension of the unit cell, $L$, is considered as the characteristic length. Results for the case (a) with $\epsilon = 0.38$ are showed in Fig. 7.4. All the strategies have been applied and the following observations can be made:

— Strategies A and B have been applied with $\delta = 0$ since the domain is periodic. Their results are perfectly overlapped, expect for high Peclet number ($Pe > 100$) where values start to deviate slightly (1% of relative difference). The reason is due to the thickness of the thermal boundary layer which reduces as the Peclet number increases. So, at high Peclet numbers, a refinement of the mesh closer to the surfaces is needed to correctly capture the physics in the thermal boundary layers. In what follows, results from strategy A will be considered as the reference

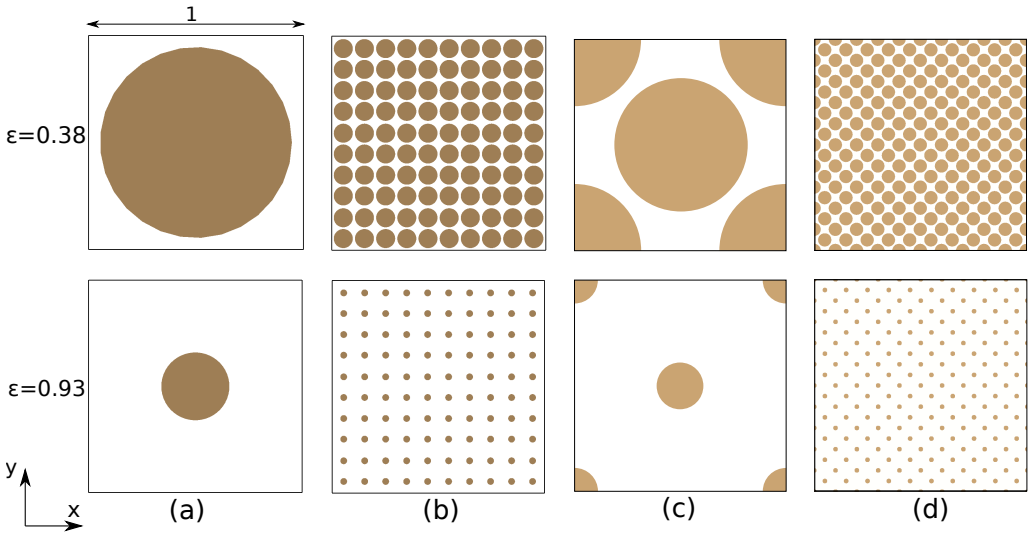


FIGURE 7.3 – The strategies defined in Fig. 7.2 have been applied to these cases in order to define the most suitable one in case on generic porous media.

case for the comparison between strategies;

— Strategies D, E, F, G, and H lead to completely wrong predictions, both at small and high Peclet values. In particular, it can be observed that Strategy E completely misses the trend of the Nusselt variation, by predicting a constant value up to $Pe = 60$. Same can be said for Strategies D, F, G, and H, which underestimate the results for the entire range of Peclet numbers. These strategies, are immediately discarded;

— Strategy C gives exact solutions for $Pe < 1$. The relative errors increase up to 5% for $Pe < 10$, and up to 30% for $Pe \sim 100$. Since many practical applications are characterized by small Peclet numbers and the analysis at high Peclet values is mostly theoretical, Strategy C is further investigated;

— Results from strategy C depend on the size of the buffer zone. This can be directly observed in Table 7.2, where for a constant $Pe = 1$, the Nusselt values are showed to be a function of

| $\delta/L$ | 0.0 | 0.1 | 0.25 | 0.5 | 1.0 | 1.5 | 2.0 | 5.0 |
|---|---|---|---|---|---|---|---|---|
| $Nu$ | 51.78 | 43.90 | 42.34 | 41.90 | 41.88 | 41.86 | 41.85 | 41.85 |

TABLE 7.2 – Analysis on the influence of the size of the buffer zone for strategy C. A constant $Pe = 1$ has been considered. The thickness should be at least the half of the domain size to avoid any inlet boundary effects.

the buffer size ($\delta$). In this case, the value of $\delta$ should be at least the half of the domain size to avoid any inlet boundary effects. Same conclusion has been found for the analysis at different Peclet numbers.

Results for cases (a) with $\epsilon = 0.93$, (b), (c), and (d) are given in Fig. 7.5. Strategies A, B, and C are applied. The same generic observations as above apply: Strategies A and B give overlapped results,

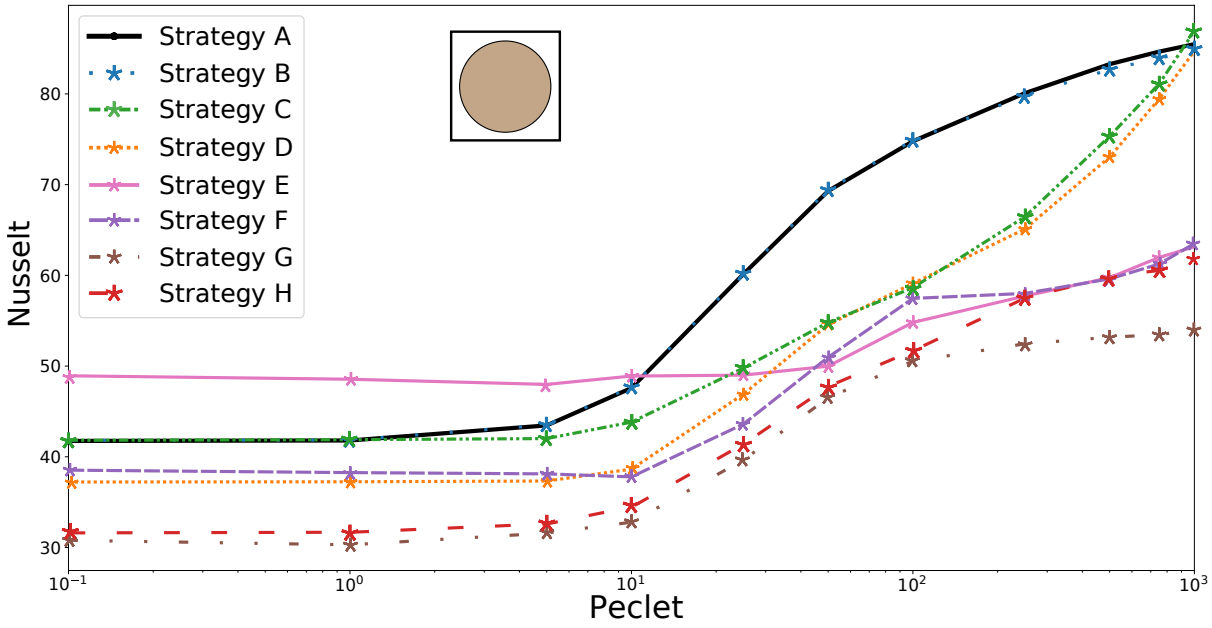


FIGURE 7.4 – Nusselt vs Peclet numbers for the test case (a) (Fig. 7.3) with porosity $\epsilon = 0.38$. Strategies A, B, C, D, E, F, G, and H are adopted. Strategies A and B give the same predictions. Strategies D, E, F, G, and H lead to completely wrong results and are discarded. Strategy C gives good predictions (relative error lower than 5% for $Pe < 10$).

while Strategy C leads to correct results only for small Peclet number. In the figure, it can be observed how the effects of the boundary conditions decrease as the domains become bigger. For all cases, results of Strategy C are accurate up to $Pe \sim 10$. However, for case (d), that is when the domain is bigger, this range extends to higher values of the Peclet number.
To conclude, Strategies A and B can be applied on representative or periodic domains. For non-periodic and non-representative volumes, Strategy C is the only alternative. For non-periodic and representative domains, Strategies A and B can be applied by adding a buffer layer, $\delta > 0$. To characterize the effects of this buffer zone on the numerical solution, case (a) (Fig. 7.3) is considered and Strategy B applied. The change of the heat exchange coefficient with the increase of the thickness of the buffer layer, $\delta$, is reported in Table 7.3. $\delta$ has been made increasing progressively to 0.5%, 1%, 2%, and 3% of the size of the unit cube domain. It can be seen that already with a 1% of increase, results start to diverge from the reference solution ($\delta = 0$) with a maximum of 6.37% of error. The thickness of the buffer zone should be selected according to the targetted Peclet number.

## 7.4 Anisotropic Effects

In this section we investigate the anisotropy effects on the heat transfer coefficient. For such purpose, we consider a periodic square cell-centered array. The unit cube geometry is showed in

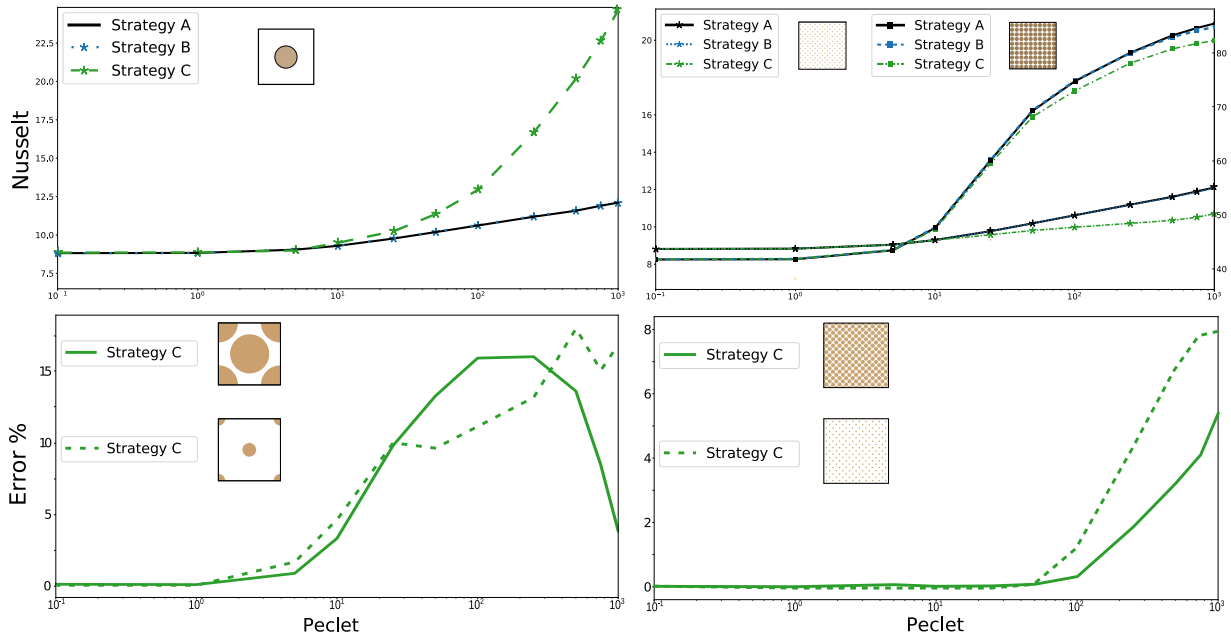


FIGURE 7.5 – Nusselt vs Peclet numbers for the cases (a) with $\epsilon = 0.93$, (b), (c), and (d) (Fig. 7.3). Strategies A, B, and C are applied. Strategies A and B give the same predictions. Strategy C correctly predicts the volumetric heat transfer coefficient for small Peclet numbers.

Fig. 7.6. We want to investigate if the volumetric heat transfer coefficient is affected by the anisotropy of the geometry. Different simulations have been then performed with a constant and small Reynolds number $Re \ll 1$. What varies are the porosity, the Peclet values, and the velocity direction. The averaged velocity vector has been always kept inside the xy plane. Different rotations ($\theta$) with respect to the x-axis are performed on the averaged velocity: when $\theta = 0$, the velocity is aligned in the x-direction; when $\theta = \pi/4$, the velocity is aligned in the y-direction. Strategy B has been adopted and the velocity direction is changed by acting on the applied pressure gradient. Results are given in Fig. 7.7. where it can be observed that $h_v$ is a function of $\theta$. This dependency becomes very marked at high Peclet numbers and low porosity values. The heat transfer coefficient can change up to 50% of its $\theta = 0$ - value. Up to our knowledge, the only correlation that tries to capture this dependency is the one proposed by Nakayama et al., 2002 [210]

$$Nu = c_{f1} cos^2(\alpha) + c_{f2} sin^2(\alpha) + c_{f3}^{0.3} Re^{0.6} Pr^{1/3} \tag{7.29}$$

The coefficients $(c_{f1}, c_{f2}, c_{f3})$ result to be highly dependent on the geometry and on the Peclet number. A new formulation of the heat transfer coefficient is needed to capture the anisotropy effects

$$h_v = \langle \boldsymbol{v}_g \rangle^T \cdot \underline{\underline{h}}_v \cdot \langle \boldsymbol{v}_g \rangle \ \frac{1}{||\boldsymbol{v}_g||^2} \tag{7.30}$$

| | $\delta = 0.005L$ | $\delta = 0.01L$ | $\delta = 0.02L$ | $\delta = 0.03L$ |
|---|---|---|---|---|
| Pe = 0.1 | 0.09 % | 0.23 % | 0.69 % | 0.93 % |
| Pe = 1 | 0.12 % | 0.29 % | 0.79 % | 1.01 % |
| Pe = 10 | 0.65 % | 2.48 % | 4.45 % | 5.99 % |
| Pe = 100 | 2.76 % | 4.80 % | 8.58 % | 11.07 % |
| Pe = 1000 | 3.49 % | 6.37 % | 11.00 % | 13.26 % |

TABLE 7.3 – Analysis on the effects of the thickness of the buffer zone, $\delta$, for strategy A and B. $\delta$ has been made increasing progressively to the 0.5%, 1%, 2%, and 3% of the size of the unit cube domain. Different Peclet numbers have been considered. Results indicate the relative error with respect to the $\delta = 0$ case.

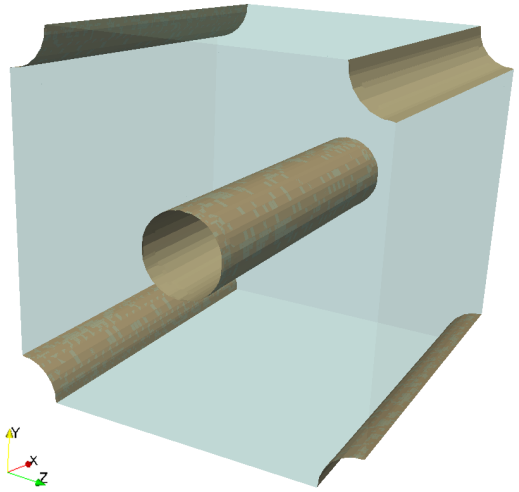


FIGURE 7.6 – Periodic array of 5-cylinders. Geometry considered for the investigation on the anisotropy effects.

where a volumetric heat transfer tensor, $\underline{\underline{h}}_v$, is introduced. When x, y, and z correspond to the principal axes, $\underline{\underline{h}}_v$ reduces to a diagonal tensor

$$\underline{\underline{h}}_v = \begin{bmatrix} h_{v,x} & 0 & 0 \\ 0 & h_{v,y} & 0 \\ 0 & 0 & h_{v,z} \end{bmatrix} \tag{7.31}$$

where $h_{v,x}$, $h_{v,y}$, and $h_{v,z}$ are the volumetric heat transfer coefficients when the velocity is aligned with the x, y, and z directions respectively. In the previous simulations, Fig. 7.7, the anisotropic effects have been investigated in the xy plane. In this case, Eq. (7.30) reduces to

$$h_v = cos^2(\theta)\ \ h_{v,x} + sin^2(\theta)\ \ h_{v,y} \tag{7.32}$$

Fig. 7.8 shows the predictions of the correlation given by Eq.(7.32) for the case with porosity $\epsilon = 0.5$ at different Peclet numbers. The volumetric heat transfer tensor is able to capture the shape of the

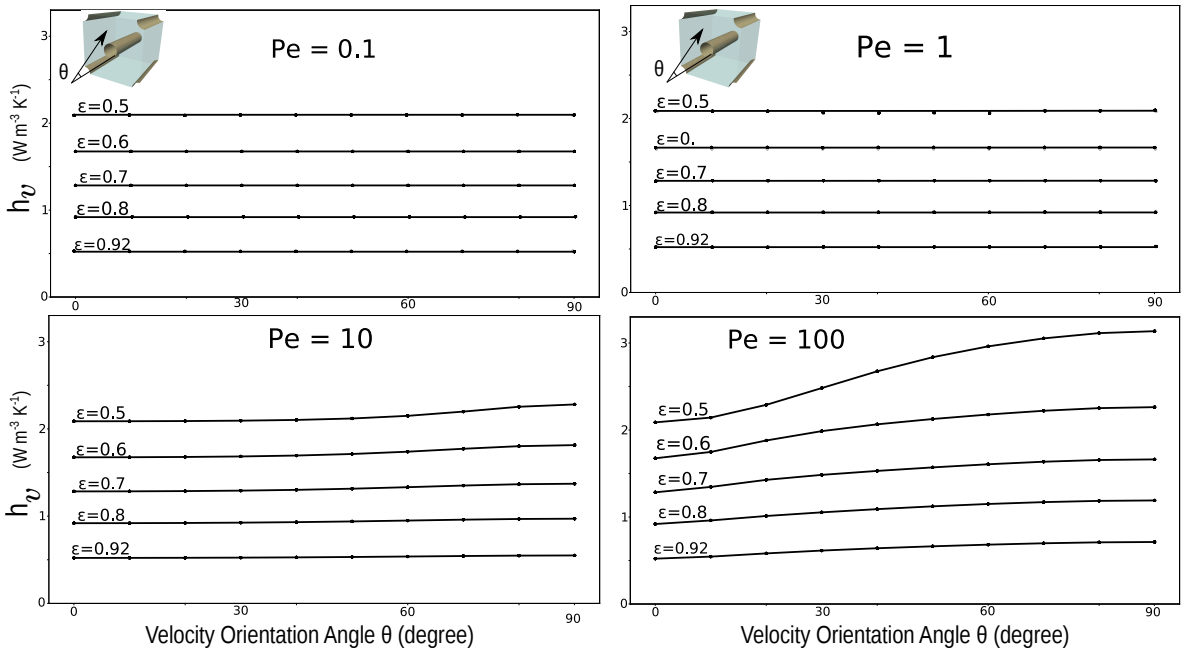


FIGURE 7.7 – Volumetric heat transfer coefficient as a function of the averaged velocity direction direction for the periodic array with 5-cylinders geometry (Fig. 7.6). Strategy B has been applied. Different porosities and Peclet numbers have been investigated.

anisotropic behaviour, but not exactly its amplitude, which seems to depend on the Peclet number. For $Pe = 66.7$, the correlation perfectly captures the anisotropic effects. In the figure, a linear variation of the coefficient as a function of $\theta$ is also represented. It can be seen that the tensorial formulation of the property leads to a good capturing of the anisotropy effects. Further analysis are needed. In particular, a theoretical derivation of the formulation needs to be developed.

## 7.5 Application to Calcarb

This section aims to evaluate the volumetric heat transfer coefficient of the digital sample of virgin Calcarb illustrated in Fig. 7.9. Calcarb is a carbon fiber preforms material with an average porosity of more than 85%. The digital representation in Fig. 7.9 has been acquired at the Advanced Light Source at Lawrence Berkeley National Laboratory and more details can be found in Borner et al, 2017 [9]). This domain has already been analyzed in the literature [9, 89, 188] in terms of permeability tensor, slip correction tensor, and volumetric heat transfer coefficient. As already observed [188], this domain is not representative of Calcarb and Strategies A and B can not be applied. Therefore, strategy C is considered and results are compared with those obtained by Liu et al., 2022 [89].
The same conditions as in the experimental study are adopted: a flow of nitrogen with an inlet velocity $|\boldsymbol{v}_{in}| = 0.5\, ms^{-1}$ is considered; a temperature difference of about $\Delta T \sim 50\, K$ is applied between the inlet flow and the material at the initial time step. The problem results in Reynolds and Peclet num-

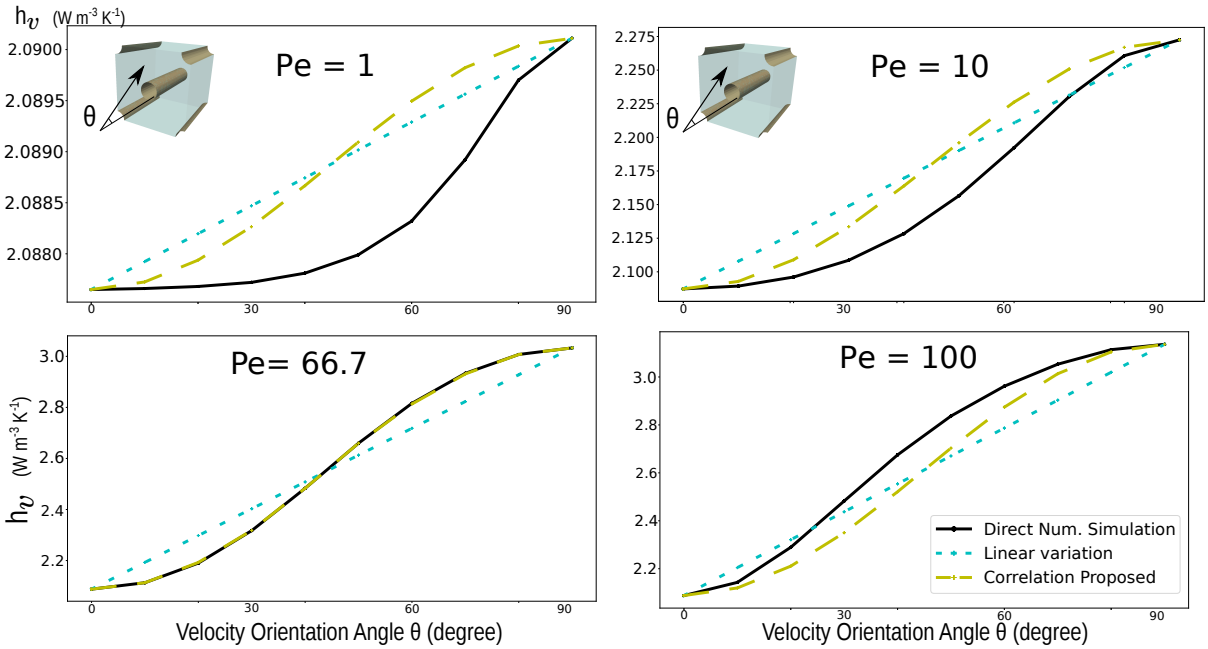


FIGURE 7.8 – Estimation of the anisotropy effects for the 2D periodic array of 5-cylinders case. A constant porosity $\epsilon = 0.5$ and different Peclet numbers are considered. The volumetric heat transfer tensor is able capture the shape of the anisotropic behaviour, but not exactly its amplitude, which seems to depend on the Peclet value. For $Pe = 66.7$, the correlation perfectly captures the anisotropic effects.

bers close to unity [4]. As small values of velocity and small variations in pressure and temperature flow are observed experimentally, the assumption of incompressibility and the the hypothesis of constant properties can be considered valid.

A mesh convergence of the domain is performed. Results are showed in Fig. 7.10. Both the convergence of the Nusselt number and the relative error are showed. The latter is evaluated between two consecutive simulations as follows

$$error = \frac{Nu_{n+1} - Nu_n}{Nu_{n+1}} \tag{7.33}$$

where the index $n+1$ indicates the numerical simulation with more mesh refinement. The numerical methods result to be first-order with respect to the space discretization, as indicate by the first-order slope line. Based on these results, a mesh of about 23 million cells has been considered (a similar conclusion to that found by Scandelli et al., 2021 [188], for the momentum problem). Some details of the mesh are showed in Fig. 7.9.

Results of the temperature field distribution are reported in Fig. 7.11. The temperature of the fluid phase reaches a condition of thermal equilibrium with the solid phase almost at the entrance of the domain. Under these conditions, LTNE models are not necessary. The numerical volumetric heat

4. For the characteristic length of the domain, the average pore-size in the through-thickness direction of the domain is considered [9]: $L = 135\ \mu_g m$

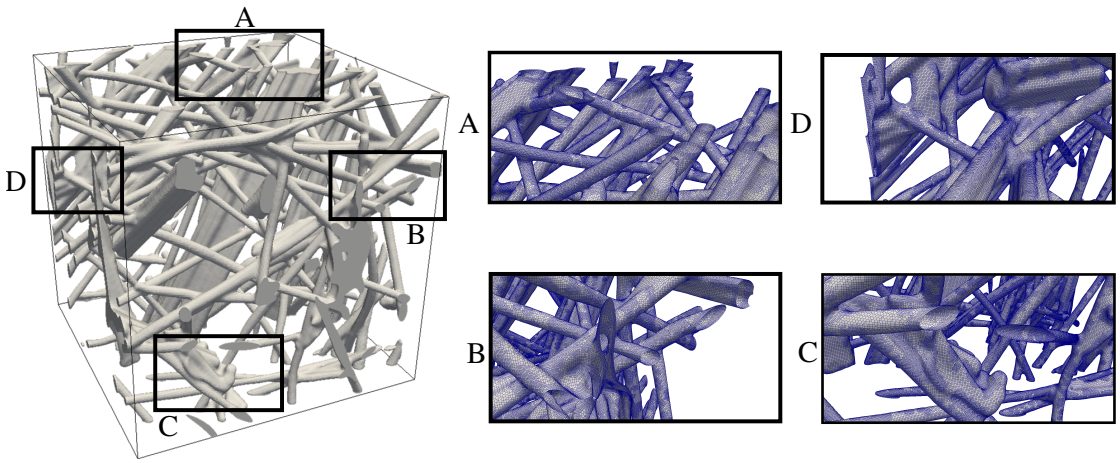


FIGURE 7.9 – On the left-hand side, volume rendering of the CMT of Calcarb. The dataset has a resolution of 200 X 200 X 200 voxels, with a voxel size of 2.6 $\mu_g m$; on the right-hand side, some details of the meshed geometry. The mesh accounts about 23 million cells.

transfer coefficient is found to be $h_v = 1.6e8\, Wm^{-3}K^{-1}$. The value found by experimental analysis is $h_v = 1e9\, Wm^{-3}K^{-1}$. The two values differ by an order of magnitude. Several reasons may lead to this difference: first, the Calcarb dataset considered for the numerical simulation is too small and not representative; second, dispersion and tortuosity effects have been neglected in the effective conductivity; third, the value of $h_v$ is so high that a local thermal equilibrium is achieved between the two phases. This makes its accurate estimation rather complex, especially from an experimental point of view.

## 7.6 Conclusions

This work aims to define a new formulation of the heat transfer coefficient able to generically account for anisotropic effects. First, however, it was first necessary to define a numerical method for its determination. Both integral and closure methods were considered. Specific attention was paid to the definition of the computational domain and the boundary conditions, defining different strategies and comparing their results on simple test cases. Results showed that only strategies that adopt periodic boundary conditions were able to provide correct predictions of the heat transfer coefficient for any Peclet number. However, the applicability of these strategies is limited to periodic or representative domains. For generic non-representative geometries, only one strategy was found to provide correct predictions of the coefficient, but only for small Peclet numbers ($Pe < 10$). This strategy was applied to the characterization of the heat transfer coefficient of a digital sample of virgin Calcarb and results are in agreement with experimental observations. Finally, the analysis of anisotropic effects on the volumetric heat transfer coefficient was conducted. It was observed that a tensorial formulation of the heat exchange between the two phases were able to capture the shape of the anisotropic behaviour, but not its amplitude, which seemed to depend on the Peclet number. THus, only at a precise Peclet

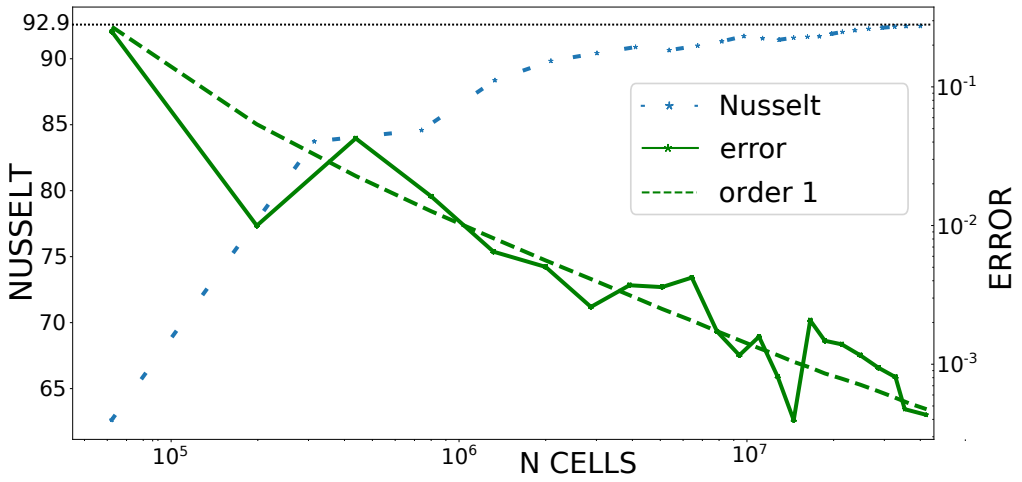


FIGURE 7.10 – Mesh convergence analysis performed on the Calcarb geometry (Fig. 7.9). A flow of Nitrogen with an inlet velocity $|\boldsymbol{v}_{in}| = 0.5\ ms^{-1}$ is considered. The pore-scale equations (Eq. (7.1)) are solved for different mesh sizes. Results show how the relative error between two consecutive simulations reduces with order 1.

number the tensorial formulation was able to perfectly capture the anisotropic effects. Further analysis are needed, in particular, a theoretical derivation of the formulation must be developed The numerical framework developed during this study will be made available in the Porous material Analysis Toolbox based on OpenFoam (PATO) released Open Source by NASA (www.pato.ac).

## 7.7 Appendix A. Physical Meaning of the Solid Phase at Fixed Temperature Ts

In this work we assume the solid phase to be at a constant temperature. To understand the meaning of this assumption, we first need to introduce two quantities. The first one is the Biot number, $Bi$, a dimensionless number related to the ratio of the heat transfer resistances inside and at the surface of a body

$$Bi = \frac{hL_s}{k_s} \tag{7.34}$$

where $h$ is the heat transfer coefficient. This non-dimensional quantity indicates whether the temperature field inside a body may vary significantly in space when a thermal gradient is applied at its surface. When $Bi \ll 1$, the temperature field inside the body remains homogeneous, that is, constant in space but not in time.
The second quantity is the thermal inertia $I$

$$I_s = \sqrt{k_s \rho_s c_{p,s}} \tag{7.35}$$

The higher this value, the slower the material reaches steady-state. By considering two phases only, when $I_s \gg I_g$, the thermal time scales of the phases are different by some orders of magnitude. The

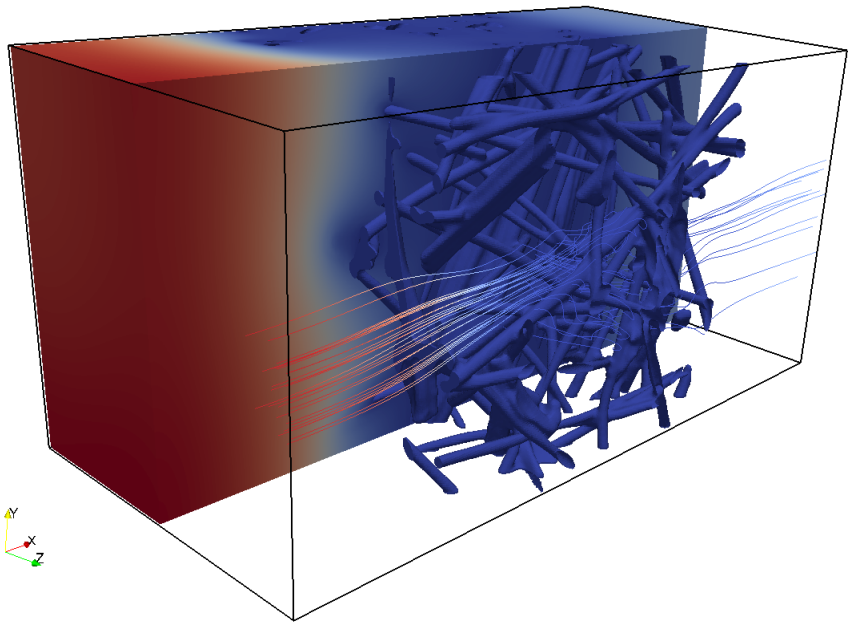

FIGURE 7.11 – Temperature field distribution inside the domain. Peclet and Reynolds numbers close to the unity. The flow and the solid phase are in local thermal equilibrium.

thermal transient effects of a gas phase is short compared to a solid phase, that can be considered to be in steady-state.
In conclusion, $Bi \ll 1$ implies a homogeneous temperature field and $I_s \gg I_g$ implies a constant temperature field of the solid phase within the time scale of the gas temperature evolution.

## 7.8 Appendix B. Remarks on the Volume Averaging Method

This appendix introduces the concepts of the volume averaging theory used in this article. Further details on the topic can be found in the literature [15].
The volume averaging is a technique used to derive continuum-macroscopic equations for multiphase systems. In this way the complexity of a porous medium is replaced with an equivalent porous-continuum model in which each point is characterized by the properties of a REV centered on it. Within the latter, variables can be averaged. Two different definitions of the average have been adopted: the phase average, used in this article for the pressure

$$\langle p_g \rangle^g = \frac{1}{V_g} \int_{V_g} p_g \, dV \tag{7.36}$$

and the intrinsic average, used for the velocity and temperature fields

$$\langle \boldsymbol{v}_g \rangle = \frac{1}{V} \int_{V_g} \boldsymbol{v}_g \, dV \tag{7.37}$$

$$\langle T_g \rangle = \frac{1}{V} \int_{V_g} T_g \, dV \tag{7.38}$$

| $L_{REV}$ | 25 | 50 | 100 | 150 | 200 | 250 | 300 | 350 | 400 |
|---|---|---|---|---|---|---|---|---|---|
| $\epsilon$ | 0.741 | 0.988 | 0.955 | 0.998 | 0.927 | 0.933 | 0.932 | 0.930 | 0.929 |
| $Nu$ | 0.316 | 0.887 | 0.588 | 0.914 | 0.63 | 0.579 | 0.584 | 0.669 | 0.631 |

TABLE 7.4 – REV analysis: porosity and Nusselt values by increasing the size of the cube volume placed at the center of the geometry. $L_c$ is expressed in $mm$.

being $V_g$ and $V$ the volumes of the fluid phase and of the representative element volume. Inside the REV each variable can be decomposed using Gray's decomposition [159] as the sum of its average and a deviation. For the pressure field this decomposition writes

$$p_g = \langle p_g \rangle^g + \tilde{p_g} \tag{7.39}$$

## 7.9 Appendix C. Numerical Methods on Non-Periodic Media

This appendix aims to numerically validate the upscaling process. To this end, the following procedure is followed: generate the geometry, find a REV, evaluate the $h_v$ coefficient of the REV, solve the thermal problem for the overall geometry with both the scale models, compare the temperature predictions.
A random packed sphere porous material has been generated with the software *PUMA* [217]. Details of the geometry are showed in Fig. 7.12. Spheres are allowed to overlap and the overall porosity has

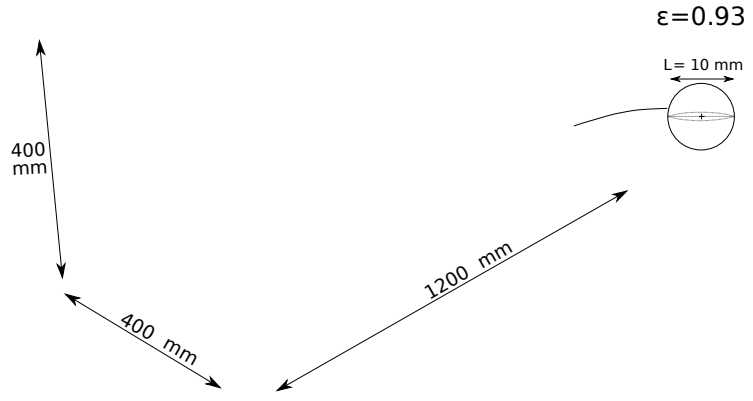


FIGURE 7.12 – Random packed sphere geometry.

been set to $\epsilon = 0.93$. The REV is looked for by considered a cube in the center of the geometry, with its dimension, ($L_{REV}$), gradually increased. At each value of $L_{REV}$, the pore-scale problem (Eq. (7.1)) has been solved. The following conditions have been considered: $k = 0.01\ Wm^{-1}K^{-1}$; $\mu_g = 10^{-5}\ Pa\,s$; $Pr = 10$; $L = 10\,mm$; $Re = 10^{-3}$. Strategy B has been applied. Both the porosity and the Nusselt number have been monitored during the simulations, as showed in Table 7.4. Following a trade-off between accuracy of the results and computational cost, the cube with dimensions $L_{REV} = 200\,mm$

| $x_{cnt}$ | 100 | 200 | 300 | 400 | 500 | 600 | 700 | 800 | 900 | 1000 | 1100 |
|---|---|---|---|---|---|---|---|---|---|---|---|
| $\epsilon$ | 0.938 | 0.926 | 0.926 | 0.937 | 0.933 | 0.927 | 0.928 | 0.928 | 0.927 | 0.934 | 0.935 |
| $Nu$ | 0.570 | 0.642 | 0.643 | 0.577 | 0.599 | 0.652 | 0.660 | 0.659 | 0.652 | 0.592 | 0.589 |

TABLE 7.5 – REV analysis: evolution of the porosity and Nusselt for the selected cube along the x axis of the geometry. $x_{cnt}$ is expressed in $mm$.

| $Pe$ | 0.1 | 1 | 5 | 10 | 25 | 50 | 100 | 250 |
|---|---|---|---|---|---|---|---|---|
| $Nu$ | 0.56 | 0.40 | 0.47 | 0.54 | 0.72 | 0.93 | 1.23 | 1.84 |

TABLE 7.6 – Nusselt vs Peclet characterization of the REV.

has been selected as REV of the geometry. For a further investigation of the REV, the cube has been displaced along the x-axis of the geometry to monitor the evolution of porosity and Nusselt. Results are showed in Table 7.5. The overall geometry is characterized by a porosity $\epsilon = 0.93$ and a Nusselt number $Nu = 0.631$. Based on the results of Table 7.4, both the porosities and the Nusselt numbers of the displaced cubes stay in a range $\pm 10\%$ with respect to the overall domain values.
The REV has been characterized in terms of the Nusselt number for different Peclet values. The Peclet number is changed by acting on the $c_p$ coefficient. Results of this characterization are showed in Table 7.6.
The thermal problem is then solved in the whole geometry with the pore-scale equations (Eq. 7.1). Some details of the mesh are given in Fig. 7.13. Eight simulations have been considered to vary the

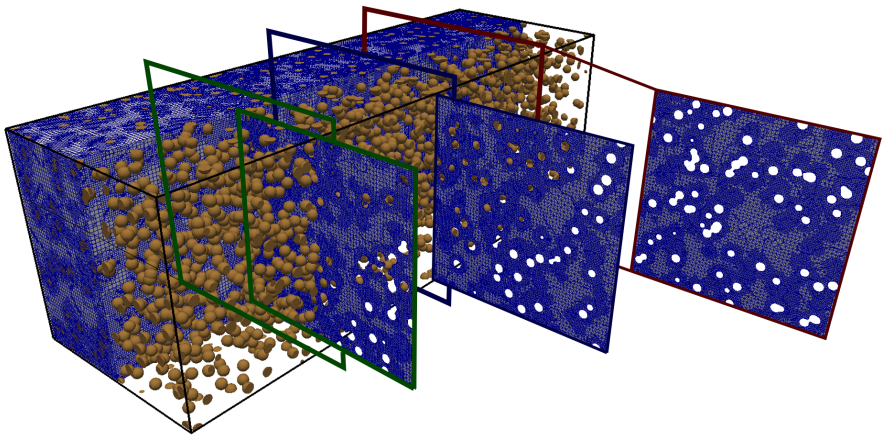

FIGURE 7.13 – Some details of the meshed geometry of Fig. 7.12.

Peclet number from 0.1 up to 1000. The same physical properties used for the REV analysis have been adopted. The same procedure is repeated for the equivalent continuum volume. The macroscopic model defined by the system of Eq. (7.5) has been used. The permeability tensor of the domain is computed by following the numerical strategy defined by Scandelli et al., 2021 [188]. The transverse and longitudinal components of the effective thermal conductivity tensor are evaluated with the correlation

proposed by Kuwahara et al., 1996 [214]

$$(k_{\text{eff,long}})/k_g = 2.1\frac{Pe}{(1-\epsilon)^{0.1}} \tag{7.40}$$

$$(k_{\text{eff,transv}})/k_g = 0.052\ (1-\epsilon)^{0.5}Pe \tag{7.41}$$

The volumetric heat transfer coefficients resulting from the REV analysis (Table 7.6) have been used. The temperature fields predicted by the two scales are finally compared. The comparison is done by averaging the fields in the $yz$ plane of the geometry and plotting th averages in the $x$-direction. Results are showed in Fig. 7.14. The pore-scale and macro-scale predictions match for the whole range of the

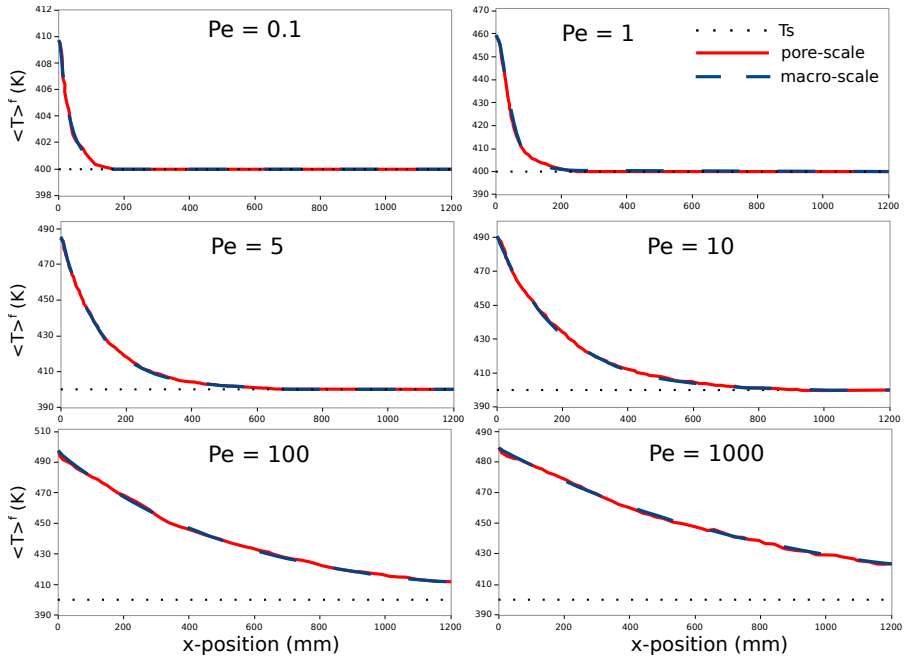


FIGURE 7.14 – Temperature fields comparison between the pore and macro-scale predictions. The fields are averaged in the $yz$ plane of the geometry and plotting along the $x$-direction. Different Peclet values are considered.

Peclet number, and this validates the upscaling process.

# Chapitre 8

# Multi-Scale Modeling of Wood Shrinkage During Pyrolysis

## Nomenclature

*Latin Letters*

| | |
|---|---|
| $\mathcal{C}$ | fourth-order stiffness tensor [$kg\ m^{-1}\ s^{-2}$] |
| $\boldsymbol{D}$ | pore-scale displacement field [$m$] |
| $E$ | Young modulus [$kg\ m^{-1}\ s^{-2}$] |
| $\boldsymbol{f}$ | generic body force [$m\ s^{-2}$] |
| $\underline{\underline{I}}$ | identity tensor |
| $l$ | length of the honeycomb wall [m] |
| $\boldsymbol{n}$ | surface normal |
| $\boldsymbol{T}$ | imposed traction force [kg $m^{-1}$ $s^{-2}$] |
| $t$ | time [$s$] |
| $T$ | pore-scale temperature [$K$] |
| $V$ | domain volume [$m^3$] |
| $w$ | thickness of the honeycomb wall [m] |
| $\boldsymbol{x}$ | pore-scale coordinates [$m$] |

*Greek Letters*

| | |
|---|---|
| $\underline{\underline{\alpha}}$ | thermal expansion tensor [$K^{-1}$] |
| $\alpha$ | thermal expansion coefficient [$K^{-1}$] |
| $\beta$ | coefficient of volume expansion [$K^{-1}$] |
| $\Gamma_0$ | boundary |
| $\Delta$ | relative difference |
| $\underline{\underline{\epsilon}}$ | pore-scale strain tensor |
| $\epsilon$ | material porosity |

## Nomenclature

| | |
|---|---|
| $\mu, \lambda$ | Lame's constant $[kg\ m^{-1}\ s^{-2}]$ |
| $\nu$ | Poisson ratio |
| $\underline{\underline{\xi}}$ | pyrolysis contribution tensor |
| $\xi$ | pyrolysis contribution coefficient |
| $\rho$ | pore-scale density $[kg\ m^{-3}]$ |
| $\underline{\underline{\sigma}}$ | pore-scale stress tensor $[kg\ m^{-1}\ s^{-2}]$ |
| $\tau$ | total advancement of the pyrolysis |
| $\psi$ | generic quantity |

*Subscripts and Superscripts*

| | |
|---|---|
| 0 | initial time |
| D | Dirichlet type boundary |
| eff | effective |
| N | Neumann type boundary |
| s | solid |

*Special Symbols*

| | |
|---|---|
| $\sim$ | imposed boundary condition |
| $tr()$ | trace operator |
| $\langle\ \rangle$ | intrinsic average |

*Acronyms*

| | |
|---|---|
| CMT | Computed Micro-Tomography |
| PATO | Porous material Analysis Toolbox based on OpenFoam |
| PS-NS | Pore-Scale Numerical Simulation |
| REV | Representative Elementary Volume |

## Preamble

Authors: H. Scandelli; A. Ahmadi-Senichault; W. Jomaa; F. lahouze; C. Foster*; F. Panerai*; J. Lachaud;
Affiliations: Arts et Métiers Institute of Technology, Univ. Bordeaux, CNRS, Bordeaux INP, I2M, UMR 5295, F-33400 Talence, France; * Department of Aerospace Engineering, University of Illinois at Urbana-Champaign, Urbana, IL 61801, USA;
Published: No;
Conference: No;

## Abstract

This paper deals with numerical homogenization in reactive porous media for the prediction of the effective thermo-elastic properties. While at the micro-scale these properties are usually known, a procedure for their derivation at the macro-scale is required. Experimental analysis, analytical results, pore-scale numerical simulations (PS-NS), are all possible alternatives for the same purpose. In this work, focus is put upon wood with an analysis through PS-NS. At first, the wood structure is simplified as a regular hexagonal honeycomb core. A solid mechanics model is adopted for its description. The numerical procedures to retrieve the effective thermoelastic properties are implemented and validated. Comparison with literature data is reported. The main contribution of this work is in the derivation of an additional term to account for the deformation due to pyrolysis. For this purpose, a *pyrolysis-shrinkage function* is defined. The numerical procedure to recover the effective pyrolysis contribution terms is presented and applied to the honeycomb structures. Results underline the importance of accounting for pyrolysis shrinkage in the solid mechanics model. Finally, a 2D computed micro-tomography (CMT) image of a wood sample is considered. The thermoelastic-pyrolysis solid mechanical problem is solved. The resulting numerical deformation shows to be qualitatively comparable with the actual deformation undergone by the sample following a complete pyrolysis process.

**Keywords**: Homogenization; Solid Mechanics Properties; Pyrolysis Shrinkage; micro-scale Numerical Simulations; Wood; Honeycomb Structure; Computed Micro-Tomography.

## 8.1 Introduction

Flows in rigid and deformable porous media are of great relevance to a wide range of engineering and environmental processes: reservoir engineering [218,219], groundwater flow [220], filtering devices [46], microfluidic sensors [47], catalytic converters [45], cracking of hot gases [185, 186], heat shield for atmospheric entry [221, 222], and many others. This breadth of topics has been the focus of many researchers for longer than a century. A first relevant contribution must be attributed to Darcy, 1856 [179], who derived the macroscopic governing equation of a creeping flow through a rigid skeleton from experimental observations. Over the years, several studies have contributed to the derivation and generalization of the macroscopic governing equations based on the microscopic scale problem, leading to established *Homogenization theories* [17]. In particular, the analysis has been extended to cover more general cases, such as inertial [120–122], transient [90, 223], and turbulent flows [119], flows of generalized Newtonian fluids [224], or flows in slip regime [225]. The extension to deformable porous media has proved to be more complicated [226], and remains an active research topic.
In this work we address a specific application of deformable and organic porous media: the deformation of wood under pyrolysis. Our main objective is to capture the full mechanical deformation of a cross-section of the virgin material as it is heated to high temperature. The cross-section is extracted from a two-dimensional (2D) slice of the digitalized computed micro-tomography (CMT) image showed in the left of Fig. 8.1. To fulfill the objective, the resulting numerical deformation is compared with the

equivalent cross-section extracted from the CMT image of the charred state showed in the right of Fig. 8.1. The two digital images are originated from a sample of *Pinus Strobus*, also known as white pinewood, resolved in a voxellized volume with 1.277 microns/pixel, able to capture the microstructure characteristics of the material. As a first approximation, its micro structure is modelled as a regular

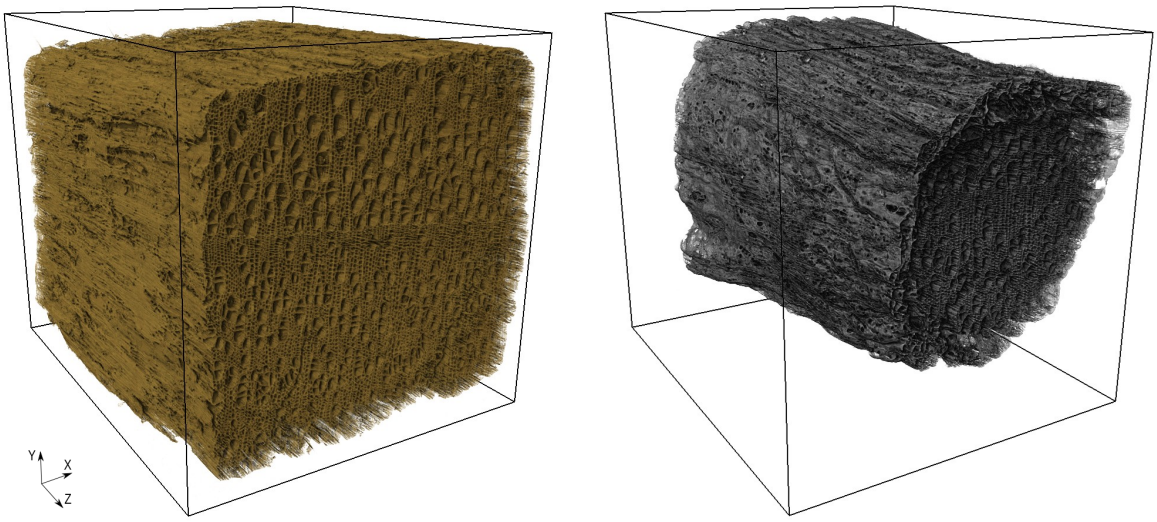


FIGURE 8.1 – Digitalized CMT sample of *Pinus Strobus*, also known as white pinewood. Resolution of 1.277 microns/pixel. The virgin state is showed on the left and the charred state on the right.

honeycomb structure in the transversal (xy) plane [227] elongated in the third (z) direction. In the transversal plane, the deformation at the micro-scale is described by the following governing equation and boundary conditions

$$\begin{cases} \partial_t(\rho_s\ \partial_t(\boldsymbol{D}_s)) = \partial_{\boldsymbol{x}} \cdot \underline{\underline{\sigma}} + \rho_s \boldsymbol{f} \\ BC1: \quad \boldsymbol{D}_s = \tilde{\boldsymbol{D}} \qquad\qquad at\ \Gamma_0^D \\ BC2: \quad \underline{\underline{\sigma}} \cdot \boldsymbol{n} = \tilde{\boldsymbol{T}} \qquad\qquad at\ \Gamma_0^N \end{cases} \tag{8.1}$$

where the quantities $\rho_s$, $\boldsymbol{D}_s$, $\underline{\underline{\sigma}}$, and $\boldsymbol{f}$ characterize the solid skeleton and denote the density, the displacement field, the stress tensor, and a generic body force, respectively; $t$ is the time and $\boldsymbol{n}$ the normal vector to the surface; $\tilde{\boldsymbol{D}}$ and $\tilde{\boldsymbol{T}}$ are the imposed solid displacement field and traction force on the Dirichlet boundary ($\Gamma_0^D$) and on the Neumann boundary ($\Gamma_0^N$). This governing equation is valid under the assumptions of infinitesimal strain ($\underline{\underline{\epsilon}}$) [86]

$$\underline{\underline{\epsilon}} = \frac{1}{2}(\partial_{\boldsymbol{x}} \boldsymbol{D}_s + \partial_{\boldsymbol{x}} \boldsymbol{D}_s^T) \tag{8.2}$$

and of linearized elastic solid material

$$\underline{\underline{\sigma}} = \mathbb{C} : \left(\underline{\underline{\epsilon}} - \underline{\underline{\alpha}}(T_s - T_0) - \underline{\underline{\xi}}(\tau_s - \tau_0)\right) \tag{8.3}$$

where $\mathbb{C}$ is the fourth order stiffness tensor [86], $\underline{\underline{\alpha}}$ and $\underline{\underline{\xi}}$ are the tensors of the thermal expansion coefficients ($\alpha$) and of the pyrolysis contribution terms ($\xi$), $T_s$ and $\tau_s$ are the solid temperature and the total advancement of the pyrolysis reactions, and the subscript 0 refers to the initial time. Eq (8.3)

is the constitutive law of the solid (or the generalized *Hooke's law*) with the addition of an extra term to account for the pyrolysis contribution in the overall structure deformation.
In the case of a regular honeycomb structure, the isotropic model can be adopted. The constitutive law (Eq. (8.3)) simplifies to

$$\underline{\underline{\sigma}} = 2\mu\underline{\underline{\epsilon}} + \lambda tr(\underline{\underline{\epsilon}})\underline{\underline{I}} - (2\mu + 3\lambda)\,\alpha\,(T_s - T_0)\underline{\underline{I}} - (2\mu + 3\lambda)\,\xi\,(\tau_s - \tau_0)\underline{\underline{I}} \tag{8.4}$$

where $tr()$ stands for the trace operator, $\underline{\underline{I}}$ indicates the identity tensor, and $\mu$ and $\lambda$ are the Lame's parameters. The latter are linked to the engineering constants (the Young modulus $E$ and the Poisson ratio $\nu$) by the following expressions

$$\lambda = \frac{E\nu}{(1+\nu)(1-2\nu)} \tag{8.5}$$

$$\mu = \frac{E}{2(1+\nu)} \tag{8.6}$$

We assume the pyrolysis contribution of Eq. (8.4) to vary linearly with the degradation of the solid, neglecting any possible cracking or fragmentation. This contribution is expressed through the *pyrolysis-shrinkage function*

$$\xi = \frac{1}{3}\frac{V - V_0}{V_0} \tag{8.7}$$

where $V$ is the volume of the solid. More information about its derivation are given in Appendix A (Section 8.7). We implemented this deformation model in the Porous material Analysis Toolbox based on OpenFoam (PATO) [75, 155]. PATO provides a full detailed description of the pyrolysis processes which we extended to include the thermoelastic-pyrolysis solid mechanical model presented in Eqs. (8.1) and (8.4). Experiments showed that wood may undergo a total volume loss up to 70% of its initial value [6, 52]. Only a few studies accounted for the contribution of pyrolysis deformation to model deformable porous media. Besides empirical correlations [228, 229], a first integration of a solid deformation equation inside a simple pyrolysis model has been proposed by Sreekanth et al., 2008 [230]. In their model, a deformation due to pyrolysis has been defined as an input parameter to calibrate with experimental results. A different technique to account for pyrolysis deformation has been proposed by Gentile et al., 2017 [79]. In their work, they defined a biomass pyrolysis model featuring mesh displacement of the boundary in order to capture the shrinkage effect. In this way, without solving any solid mechanics equation, the desired deformation effect has been obtained by setting the velocity of the boundary as a function of the mass loss due to pyrolysis.

With regard to the macro-scale aspect of the problem, there exists a wide range of models that can be taken into account [231]. They can be derived either in a semi-empirical way, where adaptive coefficients are fitted on the basis of experiments, or from homogenization approaches, which mainly depend on the assumptions made at the interface solid-flow. Iliev et al., 2007 [232], provided a complete description of the latter group, by classifying the models into three categories: (1) linear poroelasticity, characterized by infinitesimal strains in the solid and small displacement; (2) non-linear poroelasticity, where the displacements are decomposed into a rigid body motion and small extra displacements; (3)

non-linear Darcy, featuring a finite displacement for the interface. In this paper we do not address the full poroelasticity problem. Thus, the same solid mechanics governing equation defined for the micro-scale (Eq. (8.1)), is also used at the macro-scale [233], with two adjustments

$$\begin{cases} \partial_t(\rho_s\ \partial_t(\langle \boldsymbol{D}_s \rangle)) = \partial_{\boldsymbol{x}} \cdot \langle \underline{\underline{\sigma}} \rangle + \rho_s \boldsymbol{f} \\ BC1: \ \langle \boldsymbol{D}_s \rangle = \tilde{\boldsymbol{D}} \qquad at\ \Gamma_0^D \\ BC2: \ \langle \underline{\underline{\sigma}} \rangle \cdot \boldsymbol{n} = \tilde{\boldsymbol{T}} \qquad at\ \Gamma_0^N \end{cases} \tag{8.8}$$

First, the fields ($\langle \boldsymbol{D}_s \rangle$ and $\langle \underline{\underline{\sigma}} \rangle$) are averaged (intrinsic average) [15] over the domain ($V$). Second, the (effective) thermoelastic properties ($\mu^{\text{eff}}, \lambda^{\text{eff}}, E^{\text{eff}}, \nu^{\text{eff}}, \underline{\underline{\alpha}}^{\text{eff}}, \underline{\underline{\xi}}^{\text{eff}}$) have to be derived from homogenization procedures. Three different procedures can be followed for the derivation of the effective Young modulus and Poisson ratio. The first one is based upscaling theories. An example of this approach is the recent work by Arabnejad and Pasini, 2013 [4], where asymptotic homogenization is used to derive the macro-scale effective properties. The second approach is based on analytical homogenization. The work of Gibson and Ashby, 1982 [2], is one of the first studies where the full set of elastic properties of a honeycomb core with constant wall thickness was determined by the standard beam theory [234]. This technique is limited to high-porosity structures and only accounts for bending deformation. Follow up works have further investigated the analytical problem and derived with more generic solutions [235–238]. The third procedure is based on Pore-Scale Numerical Simulations (PS-NS). In this case, the effective properties are determined by using the strain energy homogenisation technique of periodic media [239]. This method has been already adopted by Catapano and Montemurro, 2014 [240], to determine the effective properties of a honeycomb structure. With regard to the derivation of the effective thermal expansion coefficient, one can use analytical and semi-empirical formulas [241–247]. Alternatively, PS-NS need to be considered. The works of Karch, 2014 [248], and Delucia et al., 2019 [249], provide a detailed description of the latter, by considering its application to a carbon fibre composite and a cork-based agglomerate, respectively. The main objective of this work is to present for the first time a detailed pyrolysis model (PATO [73,75]) that takes into account solid deformation (Eq. (8.1) and Eq. (8.4)), to define and validate the numerical procedures to retrieve the effective properties, and to apply the model to the numerical characterization of the solid deformation of a digital 2D TMC of wood. The article is structured as follows: the numerical procedures to determine the effective properties are detailed in Section 8.2. In Section 8.3, honeycomb structures with different porosity values are considered as simplified wood geometries. First, the thermoelastic effective properties are computed and compared with results from the literature. Then, the deformation process resulting from pyrolysis is presented. In Section 8.4, the full (thermoelastic-pyrolysis) solid mechanics problem is solved on a 2D slice of the virgin digital TMC image showed in the left of Fig. 8.1. The resulting numerical deformation is qualitatively compared with the actual deformation undergone by the same 2D slice following a complete pyrolysis process. Conclusions are drawn in Section 8.5.

## 8.2 Numerical Homogenization of the Thermoelastic-Pyrolysis Properties

This section presents the numerical techniques to derive the effective properties for the solid mechanics problem with PS-NS. The analysis is addressed to regular 2D honeycomb structures characterized

by different porosity values. The porosity ($\epsilon$) of a regular honeycomb structure can be expressed as

$$\epsilon = 1 - \frac{2}{\sqrt{(3)}} \frac{w}{l} \tag{8.9}$$

where $w$ and $l$ are respectively the thickness and the length of the cell wall. The case with porosity $\epsilon = 0.9$ is reported in Fig. 8.2. The figure shows the periodicity of the structure as well its Representative

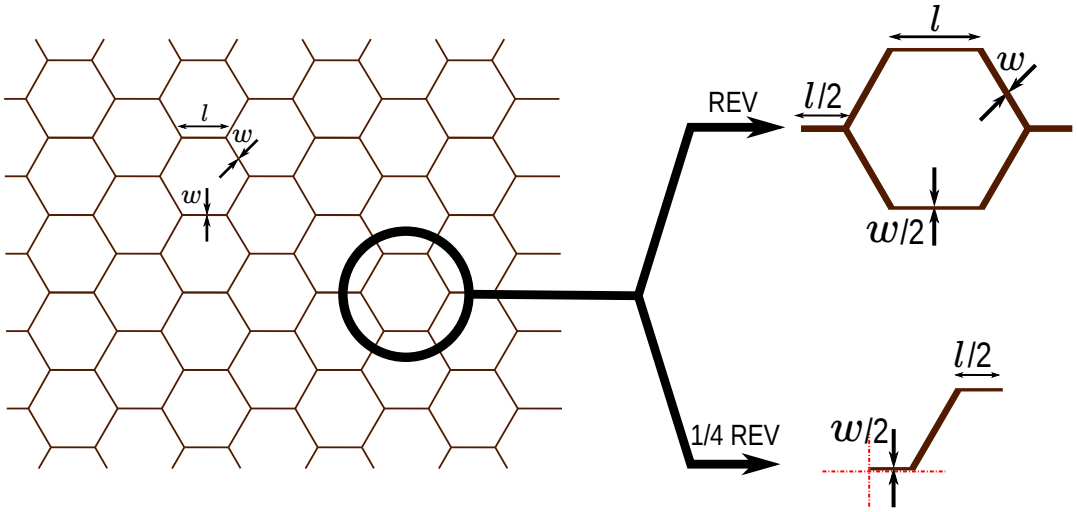


FIGURE 8.2 – A regular honeycomb structure. This periodic geometry is characterized by a REV with two planes of symmetry. This feature allows only one fourth of the representative unit cell to be taken into account during simulations.

Elementary Volume (REV). The latter features two planes of symmetry and this allow a further simplification of the structure: only one fourth of the representative unit cell can be considered if appropriate symmetric boundary conditions are applied. In what follows, the numerical procedures are described under the limitation of 2D, isotropic, and symmetric structures. Their generalization to the 3D orthotropic case can be found in Barbero, 2007 [239], and in Karch, 2014 [248].

### 8.2.1 Elastic Properties

Two PS-NS [239] are required to retrieve the effective Young modulus ($E$) and Poisson ratio ($\nu$). They are outlined in Fig. 8.3. The numerical domain is composed of two phases: the honeycomb structure and the elastic air. The latter is introduced as a "numerical artifact" [239] to apply the strain energy homogenisation technique. At the honeycomb-air interface, the continuity of the displacement and traction ($\underline{\underline{\sigma}} \cdot \boldsymbol{n}$) fields are provided [250]. On the external boundaries, a mixed condition is enforced: a fixed displacement condition for the normal component and a stress free condition for the tangential one. This forces the steady-state average strain tensor to have only one non-zero component: $\epsilon_{xx} = 1$ for simulation (1) and $\epsilon_{yy} = 1$ for simulation (2). Constant temperature conditions are considered.

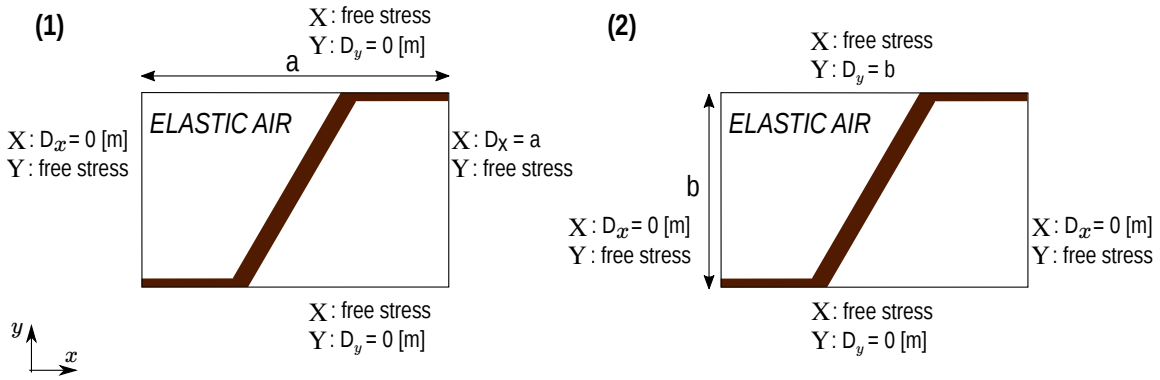


FIGURE 8.3 – The two PS-NS needed to retrieve the effective Young modulus and Poisson ratio are illustrated here. On the boundaries, a mixed condition has to be considered: a fixed displacement component for the normal component and a stress free condition for the tangential one. This combination of boundary conditions forces the average steady-state strain tensor to have only one non-zero component different from zero: $\epsilon_{xx} = 1$ for simulation (1) and $\epsilon_{yy} = 1$ for simulation (2).

Under the 2D plane strain assumption, Eq. (8.3), related to simulation (1), reduces to

$$\begin{bmatrix} \langle \sigma_{xx} \rangle \\ \langle \sigma_{yy} \rangle \\ \langle \sigma_{xy} \rangle \end{bmatrix} = \begin{bmatrix} \mathbb{C}_{11} & \mathbb{C}_{12} & \mathbb{C}_{13} \\ \mathbb{C}_{21} & \mathbb{C}_{22} & \mathbb{C}_{23} \\ \mathbb{C}_{31} & \mathbb{C}_{32} & \mathbb{C}_{33} \end{bmatrix} \begin{bmatrix} 1 \\ 0 \\ 0 \end{bmatrix} \tag{8.10}$$

It follows that $\mathbb{C}_{11} = \langle \sigma_{xx} \rangle$ and $\mathbb{C}_{21} = \langle \sigma_{yy} \rangle$. Due to the isotropic assumption, $\mathbb{C}_{31} = 0$. Similar expressions can be deduced for simulation (2) and for the second column of the stiffness tensor: $\mathbb{C}_{12} = \langle \sigma_{xx} \rangle$, $\mathbb{C}_{22} = \langle \sigma_{yy} \rangle$, and $\mathbb{C}_{32} = 0$. Due to the symmetry of the tensor, the results should lead to $\mathbb{C}_{12} = \mathbb{C}_{21}$. The knowledge of these terms is enough to evaluate the effective elastic properties in the isotropic plane [239]

$$\nu = \frac{\mathbb{C}_{12}}{\mathbb{C}_{12} + \mathbb{C}_{22}} \tag{8.11}$$

$$E = \frac{\mathbb{C}_{12}(1+\nu)(1-2\nu)}{\nu} \tag{8.12}$$

The Lame's coefficients can be derived from Eq. (8.5) and Eq. (8.6). The third column of the stiffness tensor can be filled without the need of a third simulation. Indeed, $\mathbb{C}_{31} = \mathbb{C}_{13} = \mathbb{C}_{32} = \mathbb{C}_{23} = 0$ and $\mathbb{C}_{33} = \dfrac{E}{1+\nu}$.

### 8.2.2 Thermal Expansion Tensor

Owing to the isotropy of the geometry, the effective thermal expansion tensor is characterized by only one coefficient, $\underline{\underline{\alpha}} = \alpha \underline{\underline{I}}$. We assume homogenized temperature for the honeycomb structure inside the REV, such that no radiation effects take place between adjacent walls. In addition, we consider infinitely fast thermal dynamics, so that the temperature of the domain accommodates instantaneously

to that imposed at the boundary. Only one PS-NS [248,249] is required and it is schematized in Fig. 8.4. The set of boundary conditions lead at the steady-state to an average strain tensor identically equal

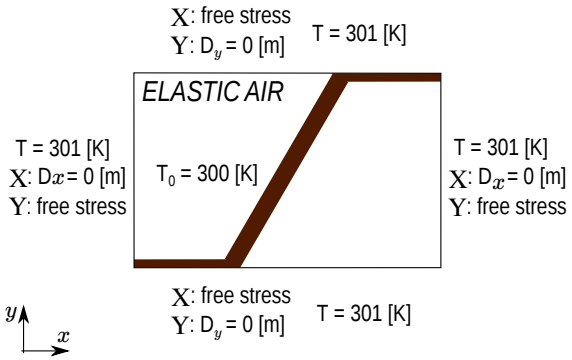


FIGURE 8.4 – One PS-NS is needed to retrieve the effective thermal expansion coefficient. The boundary conditions are chosen such that the steady-state average strain tensor is identically equal to zero, $\langle \underline{\underline{\epsilon}} \rangle = 0$. A uniform temperature load is applied.

to zero, $\langle \underline{\underline{\epsilon}} \rangle = 0$. A uniform temperature load is applied and no pyrolysis effects are considered. From Eq. (8.3), we can derive a direct expression for the thermal expansion tensor

$$\underline{\underline{\alpha}} = -\frac{1}{T - T_0} [\mathbb{C}]^{-1} \langle \underline{\underline{\sigma}} \rangle \tag{8.13}$$

This effective property results to be strictly related to the effective elastic properties.

### 8.2.3 Pyrolysis Tensor

We propose a first procedure to retrieve the effective pyrolysis tensor. The same considerations made in Section 8.2.2 for the thermal description are still valid.
Like for the thermal expansion tensor, the pyrolysis tensor is spherical and therefore characterized by only one component, $\xi$. For its prediction, one PS-NS is needed. The same boundary conditions for the displacement field reported in Fig. 8.4 have to be considered. The enforced temperature at the boundary is progressively increased, up to the complete pyrolysation of the solid phase. No thermal expansion effects are considered, $\alpha = 0$. From Eq. (8.3), we can derive the following equation

$$\underline{\underline{\xi}} = -\frac{1}{\tau_s - \tau_0} [\mathbb{C}]^{-1} \langle \underline{\underline{\sigma}} \rangle \tag{8.14}$$

Again, the equation highlights a direct dependence on the effective elastic properties.

## 8.3 Honeycomb Structures Homogenization

In this section, the deformation behaviour of the honeycomb structure (Fig. 8.2) is analyzed. The reduced (one fourth) symmetric representative elementary unit cell is considered. Porosity values ranging from 1 to 0 are considered (Eq. (8.9)). To this end, different geometries are defined with constant

| | $E\ [GPa]$ | $\nu$ | $\rho_s\ [kg/m^3]$ | $\alpha\ [1/K]$ | $\xi$ |
|---|---|---|---|---|---|
| **structure** | 70 | 0.33 | 600 | 1e-5 | 0.1667 |
| **elastic air** | 1e-3 | 0.00 | 1 | 0 | 0.0 |

TABLE 8.1 – micro-scale physical parameters considered for the two phases defined in the geometry: the honeycomb structure and the elastic air. The values are taken from the literature [2–6].

cell wall length $l = 1\ mm$ and varying wall thickness. The porosity value is given by Eq. (8.9). Literature data [2–6] are considered for the choice of the micro-scale physical properties of the two phases, summarized in Table 8.1, for the comparison, and for verification of the numerical procedure. The symmetric geometries are generated in openFoam, using the *blockMesh* and *snappyHexMesh* utilities [251]. Additional details on the mesh are given in Appendix B (Section 8.8).

### 8.3.1 Elastic Effective Properties

Results of the numerical homogenization are presented in Figs. 8.5 and 8.6. Fig. 8.5 illustrates the

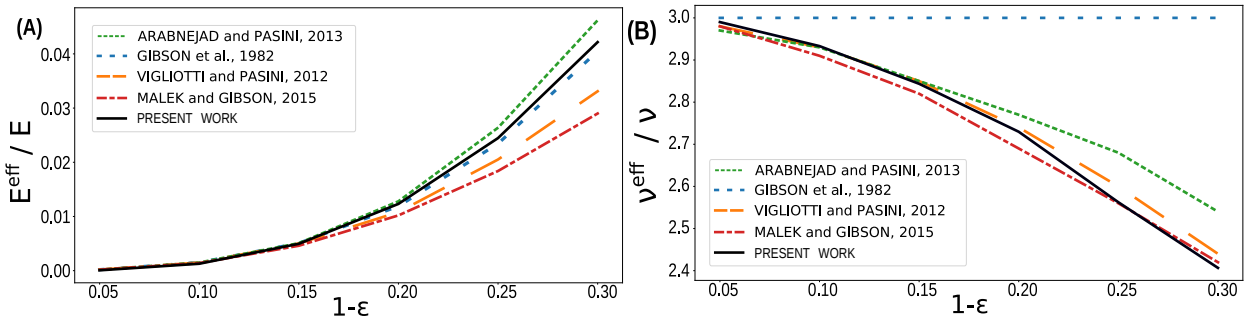


FIGURE 8.5 – Comparison of the effective elastic properties as a function of the solid fraction $(1 - \epsilon)$. High porosities ($\epsilon > 0.7$) cases are considered. On the left (A), the behaviour of the effective Young modulus, normalized with the micro-scale value, is reported; on the right (B), the behaviour of the effective Poisson ratio, normalized with the micro-scale value, is showed. Comparison data are taken from the literature [2–5].

behaviour of the two dimensionless effective elastic properties ($E^{\text{eff}}/E$ and $\nu^{\text{eff}}/\nu$) as porosity changes between 1 and 0.7. Results are compared with several works from the literature [2–5]. It should be remarked that, Gibson, 1982 [2], Vigliotti and Pasini, 2012 [3], and Malek and Gibson, 2015 [5], adopted analytical homogenization techniques, whose validity is limited to high porosity values. Arabnejad and Pasini, 2013 [4], instead used asymptotic homogenization theory to derive the macro-scale effective properties, subject therefore to no restrictions in terms of porosity. The figure highlights how, as the porosity decreases, the effective Young's modulus increases slightly while the Poisson's ratio decreases more markedly. These trends can be physically explained by the fact that as the porosity decreases, the solid part increases in volume, thus favouring greater structural rigidity in the porous medium. It is worth noting that our calculations are in good agreement with the literature. The only major

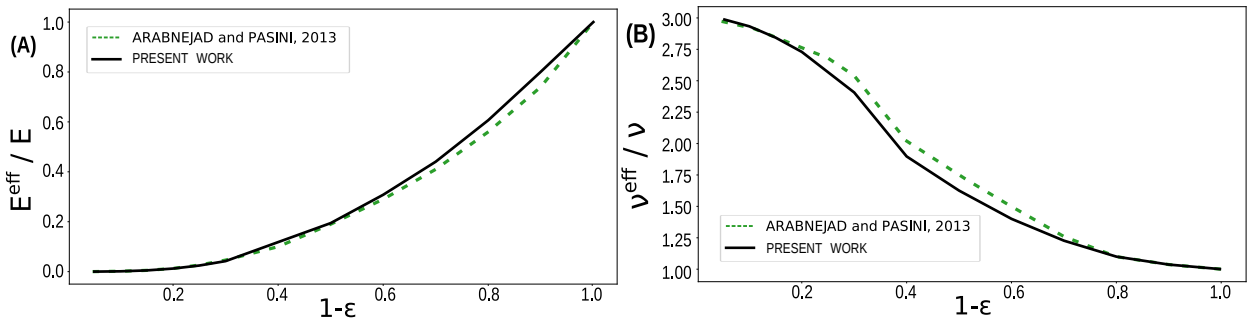


FIGURE 8.6 – Comparison of the effective elastic properties as a function of the solid fraction $(1-\epsilon)$. The whole porosity range is considered. On the left (A), the behaviour of the effective Young modulus, normalized with the micro-scale value, is reported; on the right (B), the behaviour of the effective Poisson ratio, normalized with the micro-scale value, is showed. Comparison data are taken from the literature [4].

discrepancy is noted with respect to the Poisson ratio predicted by Gibson et al., 1982 [2], where the axial and shear deformation of the cell wall were neglected, thus making the property independent of porosity.
Fig. 8.6 completes the description of the two effective elastic properties across the entire porosity range. Only fewer data [4] is available from the literature for this wide range of porosity. The figure completes the trends observed in Fig. 8.5 for the two effective properties, converging to an asymptotic equality between the homogeneous and micro-scale values in the limit in which the porosity tends to zero, $\epsilon \to 0$. Again, we can observe a good agreement between of our results with the work of Arabnejad and Pasini, 2013 [4].

### 8.3.2 Thermal Expansion Coefficient

Results from Section 8.3.1 allow the characterization of the full stiffness tensor for each geometry case. The thermoelastic simulations are now performed to evaluate the steady-state average stress tensor required in Eq. (8.13). Results indicate that for the entire porosity range, the effective thermal expansion coefficient is equal to that of the micro-scale structure. This is in agreement with the literature [2]. Indeed, the value of the thermal expansion coefficient should remain the same as long as regular honeycomb structures at uniform temperature are considered.

### 8.3.3 Pyrolysis Coefficient

For the homogenization of the pyrolysis contribution terms, we have considered the temperature values as a function of time given in Table 8.2. The pyrolysis model presented by Lachaud et al., 2017 [75], is adopted in this work. Results of the homogenization are reported in Table 8.3. It can be observed that, as the porosity increases, and thus as the solid volume decreases, the effective pyrolysis contribution term decreases. At a porosity of $\epsilon = 0.70$, the effective contribution accounts for only 1%

| **time** [s] | 0 | 10 | 20 | 30 | 40 | 50 |
|---|---|---|---|---|---|---|
| **temperature** [K] | 300 | 400 | 500 | 600 | 700 | 800 |

TABLE 8.2 – Increase of the temperature values in the domain as a function of time.

| $1-\epsilon$ | 0.05 | 0.10 | 0.15 | 0.20 | 0.25 | 0.30 | 0.40 | 0.50 | 0.60 | 0.70 | 0.80 | 0.90 | 1.00 |
|---|---|---|---|---|---|---|---|---|---|---|---|---|---|
| $\xi^{\text{eff}}/\xi$ | 0.00067 | 0.0017 | 0.0029 | 0.0042 | 0.0070 | 0.021 | 0.065 | 0.097 | 0.21 | 0.41 | 0.65 | 0.93 | 1.00 |

TABLE 8.3 – Effective pyrolysis contribution term as a function of the solid fraction $(1-\epsilon)$.

of its micro-scale value.
For a better understanding of the effects of pyrolysis on deformation, we have performed a simulation with mesh movement driven by the displacement field. The one fourth REV structure with porosity $\epsilon = 0.80$ has been considered. Its change of shape during the pyrolysis evolution can be appreciated in Fig. 8.7. The overall advancement of the pyrolysis reactions is described by $\tau_s$: when $\tau_s = 1$ the

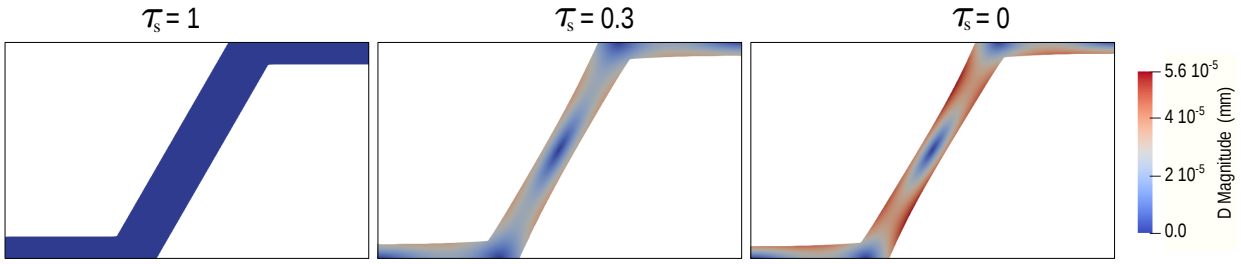


FIGURE 8.7 – Change of shape of the one fourth REV structure with porosity $\epsilon = 0.80$ due to pyrolysis effects. At the initial time step, $t = 0\ s$, the structure is fully virgin, $\tau_s = 1$. At the final time step, $t = 40\ s$, the structure is fully pyrolyzed, $\tau_s = 0$. The magnitude of the displacement field is showed.

structure is virgin, whereas $\tau_s = 0$ indicated a completely pyrolyzed structure. At the initial time step, $t = 0\ s$, the structure is fully virgin. As the simulation progresses, the temperature of the domain increases and triggers the pyrolysis reactions. The latter contribute to the stress tensor (Eq. (8.4)), thus to deformation. At the final time step, $t = 40\ s$, the structure is completely pyrolyzed, $\tau_s = 0$, and an overall shrinkage effect can be appreciated. The shape of the structure remains preserved, as a consequence of the set of boundary conditions applied on the displacement field (Fig 8.3).

## 8.4 Homogenization of Real Wood Structure

The homogenization techniques are now applied to a slice of the virgin wood sample reported on the left of Fig. 8.1 taken in the transversal plane (Fig. 8.8). As a first approximation, the domain is simplified in two independent regions (represented by the boxes in Fig. 8.8) featuring two different porosity values. This layering arises from the fact that the sample contains growth rings corresponding to wood produced in two different seasons. The figure shows also two cracks propagating from the

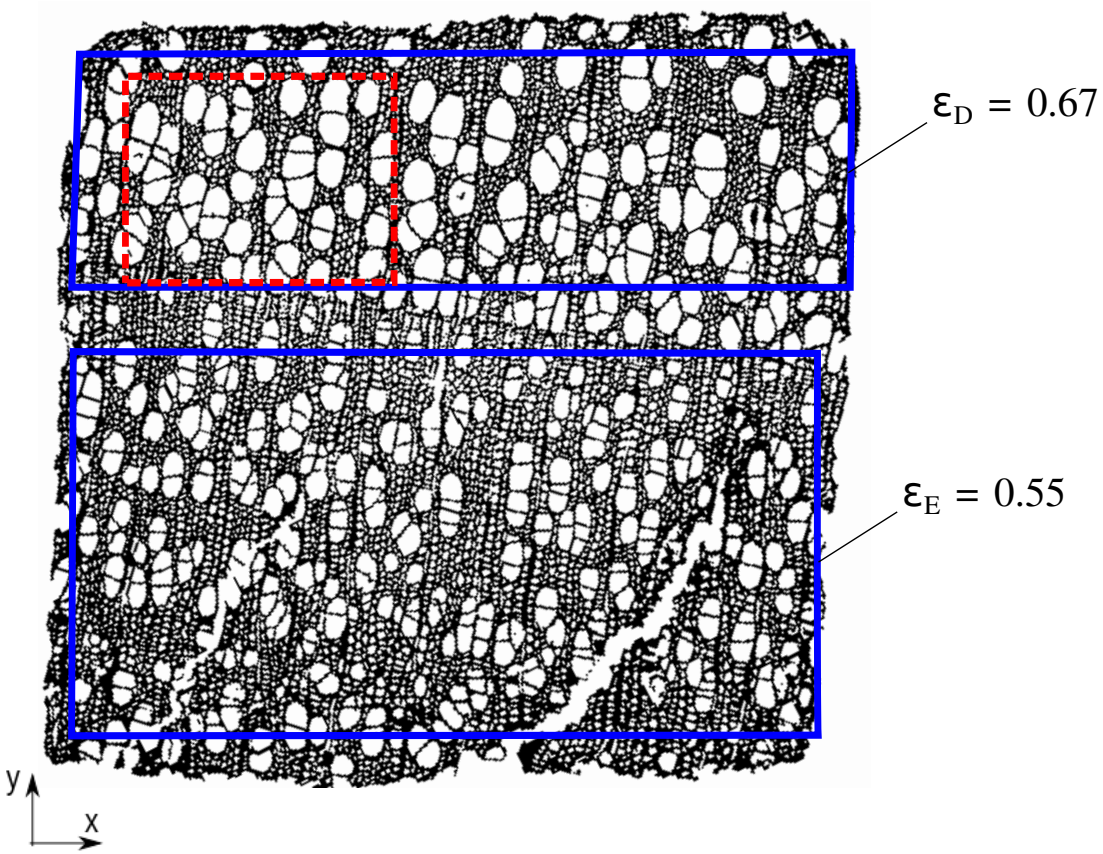


FIGURE 8.8 – Slice of the virgin wood sample (Fig. 8.1) in the transversal (xy) plane. The geometry shows two different regions featuring two different porosity values. In the red dashed domain, the two-step approach is tested. In the two blue continuous domains, the homogenization techniques are applied.

bottom part of the domain, which are neglected in the analysis by artificially sealing the void spaces. Each region (blue box) features a a bi-modal porosity distribution, with to prevalent pore scales of 3.82 and 14.2 microns characteristic scale, respectively. A two-step approach is defined to simplify the numerical characterization: in a first step, only the *small pores* are homogenized; the residual geometry is then treated in a second step. As a general rule, we denote as *small pores*, all the pores featuring an area lower than 10% of the maximum pore area in the domain. To verify the validity of this two-step approach, the red dashed square domain is considered. With reference to Fig. 8.9, the validation of the approach is done by comparing the results of the homogenization process applied to the full domain (A) with the results of the two-step approach: the domain (C) is homogenized and its results are used as the thermoelastic property values of the honeycomb phase (dark red zone) in the domain (B). The homogenized porosity of the domain (B) takes into account the porosity of the domain (C) as follows

$$\epsilon_B^{\text{eff}} = (1 - \epsilon_B)\epsilon_C + \epsilon_B \tag{8.15}$$

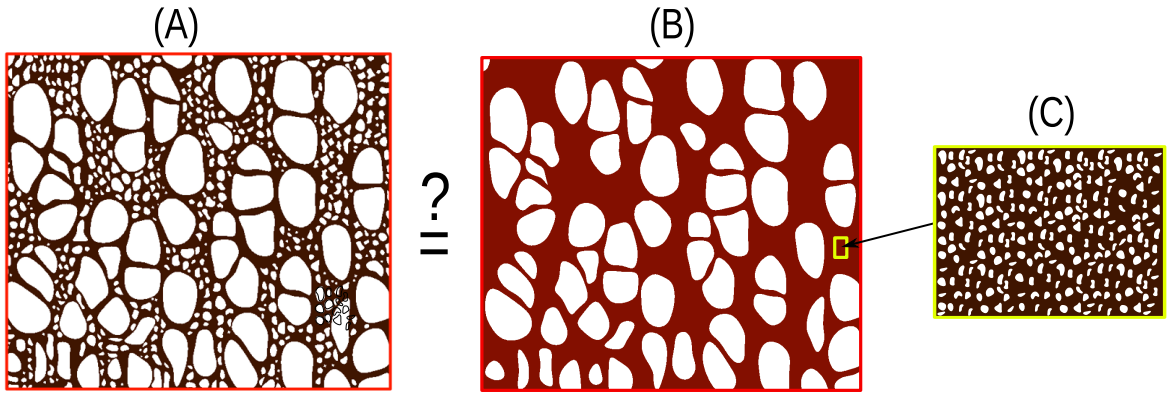


FIGURE 8.9 – Verification of the two-step approach on the domain in the red dashed square in Fig. 8.8. The homogenization results obtained from the domain (A) are compared with the ones obtained from domain (B), where a small pores are substituted from homogenization results obtained from domain (C).

| | $\epsilon$ | $E^{\text{eff}}/E$ | $\nu^{\text{eff}}/\nu$ | $\alpha^{\text{eff}}/\alpha$ | $\xi^{\text{eff}}/\xi$ |
|---|---|---|---|---|---|
| **domain (C)** | 0.36 | 0.1864 | 1.23 | 1.21 | 0.052 |
| **domain (B)** | 0.66 | 0.0424 | 1.69 | 1.17 | 0.36 |
| **domain (A)** | 0.65 | 0.0402 | 1.73 | 1.16 | 0.37 |
| $\Delta\%$ | 1.5 | 5.1 | 2.3 | 0.9 | 2.7 |

TABLE 8.4 – Results of the thermoelastic mechanic characterization of the domains showed in Fig. 8.9. Based on the relative difference between the predictions of domains (A) and (B), we can validate the two-step approach for the homogenization, knowing that this will lead to errors around $2-5\%$.

More details on the mesh used to characterize the domain (A) are given in Appendix B (Section 8.8). The homogenization is carried out with the numerical procedures described in Section 8.3. Results are showed in Table 8.4. To compare the results from domains (A) and (B), the following relative difference has been defined for any generic quantity $\psi$

$$\Delta\% = \frac{\psi_{\text{domain(A)}} - \psi_{\text{domain(B)}}}{\psi_{\text{domain(A)}}} \; 100 \tag{8.16}$$

The maximum difference is observed for the effective Young modulus, where the value goes up to 5%. We consider this error acceptable given the notable simplification that the technique brings to numerical description.

With the two-step approach being validated, we proceed to the characterization of the two blue continuous rectangles (Fig. 8.8), which are illustrated in Fig. 8.10 after the application of the first homogenization step. With reference to Fig. 8.8, the upper domain is denoted (D) and the lower one (E). More details on the mesh discretization of domain (D) are given in Appendix B (Section 8.8). Results of the second homogenization step for the two domains, with their differences, are reported in Table 8.5. The difference between the effective Young modulus of the two domains is up to 88.9%. As expected, the

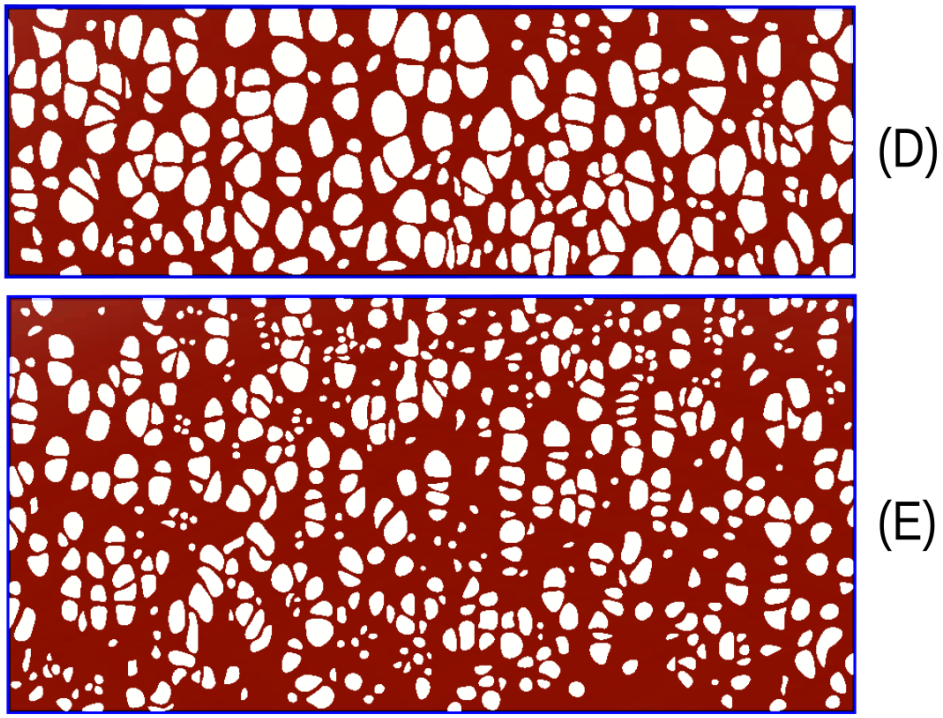


FIGURE 8.10 – Blue continuous domains of Fig. 8.8 after the first homogenization step. The *small pores* are homogenized and the results are taken as the thermoelastic properties of the matrix phase. With reference to Fig. 8.8, the upper domain is denoted (D) and the lower one (E).

two domains are characterized by different effective properties and they define two different structures.

To fulfill the objective of this work, the deformation of the virgin cross section (Fig.8.8) resulting form the thermoelastic-pyrolsysis solid mechanical problem is compared with the actual deformation undergone by the equivalent cross section extracted from the charred sample. The numerical analysis is simplified by considering homogeneous properties in the cross section: the effective properties are obtained from a mathematical average of the ones of domains (D) and (E) (Table8.5). Only one fourth of the slice is considered. The numerical domain, domain (F), and results are represented in Fig. 8.11. Symmetric conditions are imposed on the symmetric axes, and the domain is left free to deform on the

| | $\epsilon$ | $E^{\text{eff}}/E$ | $\nu^{\text{eff}}/\nu$ | $\alpha^{\text{eff}}/\alpha$ | $\xi^{\text{eff}}/\xi$ |
|---|---|---|---|---|---|
| **domain D** | 0.67 | 0.0471 | 1.90 | 1.20 | 0.38 |
| **domain E** | 0.55 | 0.0890 | 1.41 | 1.28 | 0.16 |
| $\Delta\%$ | 17.9 | 88.9 | 34.7 | 6.67 | 64.7 |

TABLE 8.5 – Results of the solid mechanics homogenization of domains D and E defined in Fig. 8.10. Their $\Delta\%$ values are also reported. Results indicate two different structures characterized by different effective parameters.

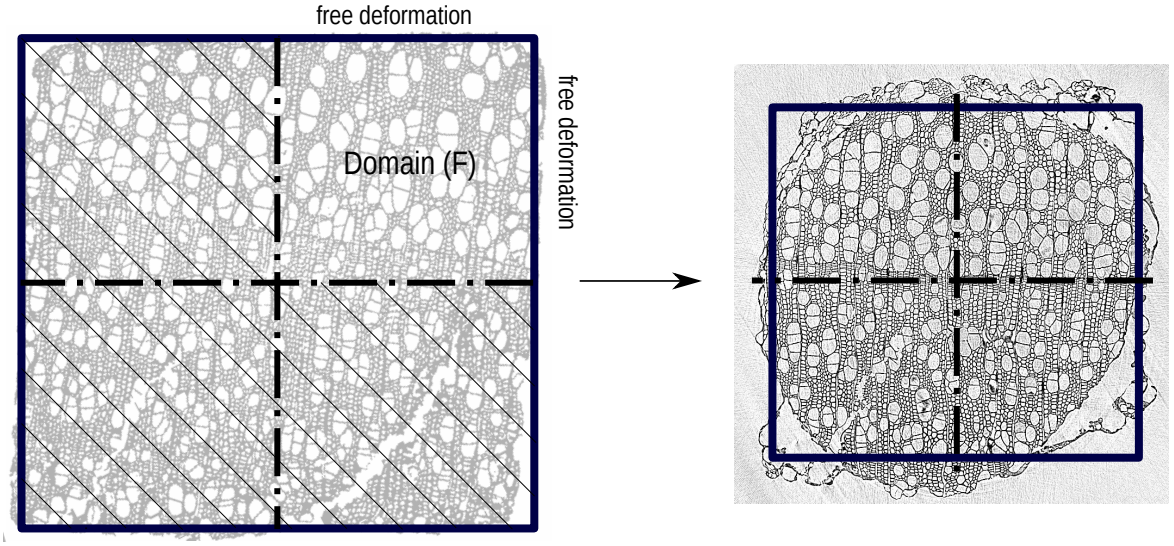


FIGURE 8.11 – One fourth of the slice of the virgin sample (Fig. 8.8) is considered. The Domain (F) is defined. Symmetric conditions are imposed on the symmetric axes, and the domain is left free to deform on the other boundaries. A uniform temperature load up to 800 $K$ is applied. The final domain is reconstructed by exploiting the axes of symmetry and overlapped to the actual deformation undergone by the equivalent cross section from the charred sample.

other boundaries. A uniform temperature load up to 800 $K$ is applied. Once the simulation converges, the entire domain is reconstructed by exploiting the axes of symmetry. The final domain is overlapped to the actual deformation undergone by the equivalent cross section from the charred sample. It can be observed that, due to the isotropic model, the deformation of Domain (F) results to be equal in the two directions. The original square shape is preserved. Despite the assumptions of isotropic and homogeneity of the domain, the model is able to predict the value of the final surface area with a relative error of 4.1 %.

## 8.5 Conclusions

In this work, the numerical homogenization process in reactive porous media has been investigated with micro-scale direct numerical simulations. The analysis focuses on a 2D computed microtomography image of a wood sample. At first, the geometry has been simplified as a honeycomb structure. The thermoelastic effective properties have been derived from numerical homogenization and compared with literature results. Wood has been then allowed to react and a *pyrolysis-shrinkage function* has been defined to account for the pyrolysis contribution on the displacement field. After having defined and applied the homogenization procedure for this new property, the effects of pyrolysis deformation are observed on the shrinkage of a honeycomb structure.
A slice of the wood sample has been then considered. As a first approximation, the domain is simplified in two independent regions featuring two different porosity values. A two-steps homogenization proce-

dure has been introduced in order to reduce the computational time for the numerical characterization. Once the two independent regions have been characterized in terms of their effective properties, the simplified domain is deformed and solved at both the macro and micro scales. A good agreement in the results is observed, underlying that, in the case of wood, a generic macroscopic description should account for the presence of the growth rings by dividing the domain into regions: the effective properties of each region must be determined at the microscopic level. Finally, the full (thermoelastic-pyrolysis) solid mechanics problem is solved on a 2D slice of the virgin digital TMC image. The main objective of the work is fulfilled by comparing the resulting numerical deformation to the actual deformation undergone by the same 2D slice following a complete pyrolysis process.

## 8.6 Acknowledgments

The research of H.S. was sponsored by a PhD grant awarded by Arts et Métiers Institute of Technology. We thank Anita Catapano and Marco Montemurro for their support and guidance.

## 8.7 Appendix A. The Pyrolysis-Shrinkage Function

The derivation of the pyrolysis-shrinkage function is based on the idea of writing the contribution of pyrolysis to the deformation field in the same form as the thermal one. The reason is that both contributions lead to volumetric deformations. In this analogy, the pyrolysis contribution term, $\xi$, should be defined in a similar way to the thermal expansion coefficient, $\alpha$.
The change of volume of the material due to thermal expansion is linked to the coefficient of volume expansion, $\beta$, defined as

$$\beta = \frac{1}{V}\Big(\frac{\partial V}{\partial T}\Big) \tag{8.17}$$

The linear thermal expansion coefficient is defined as the change of length of a material due to thermal expansion

$$\alpha = \frac{1}{L}\Big(\frac{\partial L}{\partial T}\Big) \tag{8.18}$$

For isotropic materials, when considering small variation of temperature and neglecting high order terms in volume expansion expression, the two coefficients $\alpha$ and $\beta$ are related as follows

$$\alpha = \frac{1}{3}\beta \tag{8.19}$$

A similar relationship can be found for the pyrolysis expansion term, $\xi$, by assuming small volume variations. In this case the parameter that leads to a variation of volume is $\tau$, the total advancement of the pyrolysis process. As a first order model, this term is supposed to be a linear function of $\tau$

$$\tau(t) = \frac{V(t) - V_{end}}{V_0 - V_{end}} \tag{8.20}$$

where $V_{end}$ is the final volume of the material. The variation of the material volume at a certain time step $t$

$$\Delta V = V(t) - V_0 \tag{8.21}$$

Eq. (8.20) can be substitute in Eq. (8.21) to express $V(t)$ and $V_0$ as a function of $\tau_s$. This leads to

$$\frac{\Delta V}{V_0} = \frac{V_0 - V_{end}}{V_0}\tau \tag{8.22}$$

The volume fraction term $\dfrac{V_0 - V_{end}}{V_0}$ has the same proportionality role as $\beta$ in Eq. (8.17). So, by taking reference to Eq.(8.19), the pyrolysis-shrinkage function has been defined as

$$\xi = \frac{1}{3}\frac{V_0 - V_{end}}{V_0} \tag{8.23}$$

The value of $\xi$ has to be defined from experimental observations.

## 8.8 Appendix B. Details on the Meshes

Further details on the meshing of the geometries are given in this appendix. For the homogenization of the honeycomb structures, in Section 8.3, mesh sizes of about 90000 cells have been considered for the different porosity values. This discretization results from a steady-state convergence analysis of the displacement field. The discretized geometry for the case of porosity $\epsilon = 0.80$ is reported in Fig. 8.12. On the right part of the figure, a corner of the geometry is zoomed to highlight the discretization of

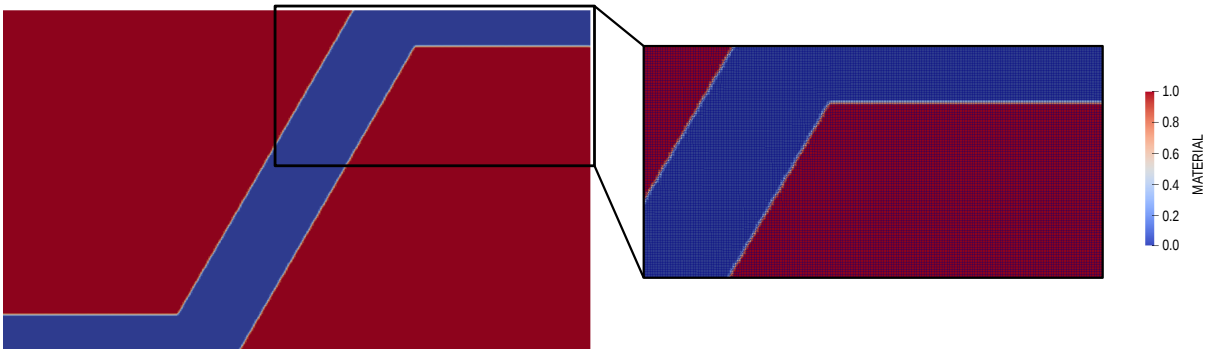


FIGURE 8.12 – Discretized geometry used for the homogenization of the honeycomb structure with porosity *epsilon* = 0.80. Approximately 90000 cells are considered. The *material* parameter allows the identification of the two different regions. *material*=0 denotes the honeycomb structure, whereas *material=1* indicates the elastic air.

the mesh. The *material* parameter allows the identification of the two different regions. *material*=0 denotes the honeycomb structure, whereas *material=1* indicates the elastic air.

For the homogenization of the red dashed square in Fig. 8.8, Section 8.4, a mesh size of about 180000 cells has been considered after a convergence study. The discretized geometry is showed in Fig. 8.13.

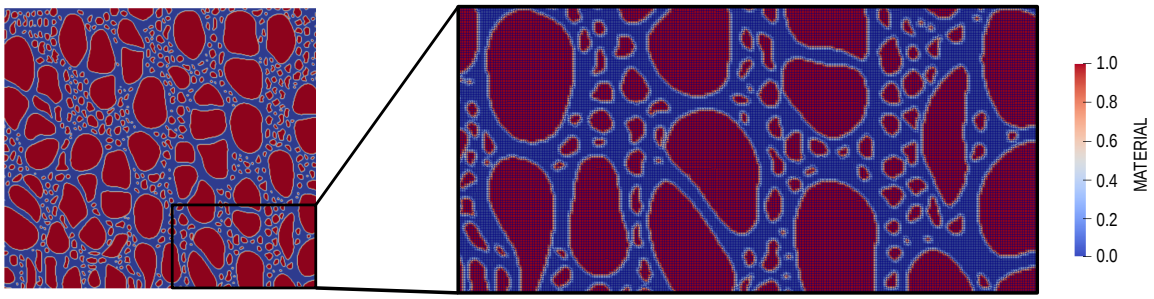


FIGURE 8.13 – Discretized geometry used for the domain (B) (8.9). Approximately 180000 cells are considered. In the right part of the figure, a corner of the geometry is zoomed in order to highlight the mesh discretization.

In the right part of the figure, a corner of the geometry is zoomed in order to highlight the mesh discretization. The *material* parameter allows the distinction between the two phases.

For the homogenization of the domain (D) in Fig. 8.10, Section 8.4, a mesh with approximately 320000 cells has been considered. This discretization is enough to guarantee the convergence of the simulation. The discretized geometry is showed in Fig. 8.13. In the right part of the figure, a corner of the

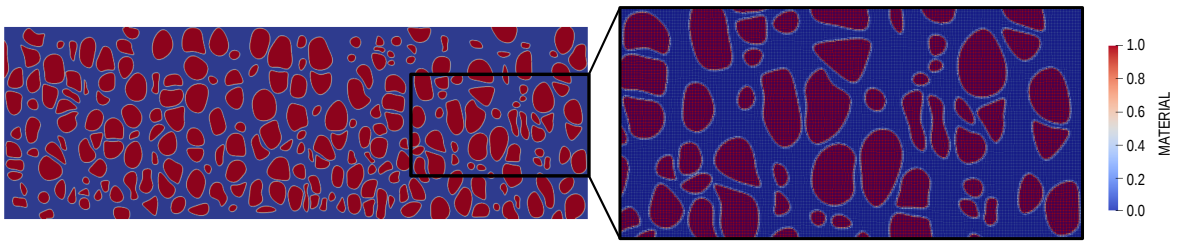


FIGURE 8.14 – Discretized geometry used for the domain (D) (8.10). Approximately 320000 cells are considered. In the right part of the figure, a corner of the geometry is zoomed in order to highlight the mesh discretization.

geometry is zoomed in order to highlight the mesh discretization. The *material* parameter allows the distinction between the two phases.

## 8.9 Appendix C. Validation of the Upscaling Method

The upscaling method is validated in this appendix by solving the domain (D) at both the micro-scale and macro-scale and comparing the results in terms of the average displacement fields. For the macro-scale, the homogeneous domain characterized by the effective properties of Table 8.5 is considered. The numerical domains and results are presented in Fig. 8.15. The same boundary conditions are applied to both domains: the domains are fixed on the left boundary and free to move elsewhere.

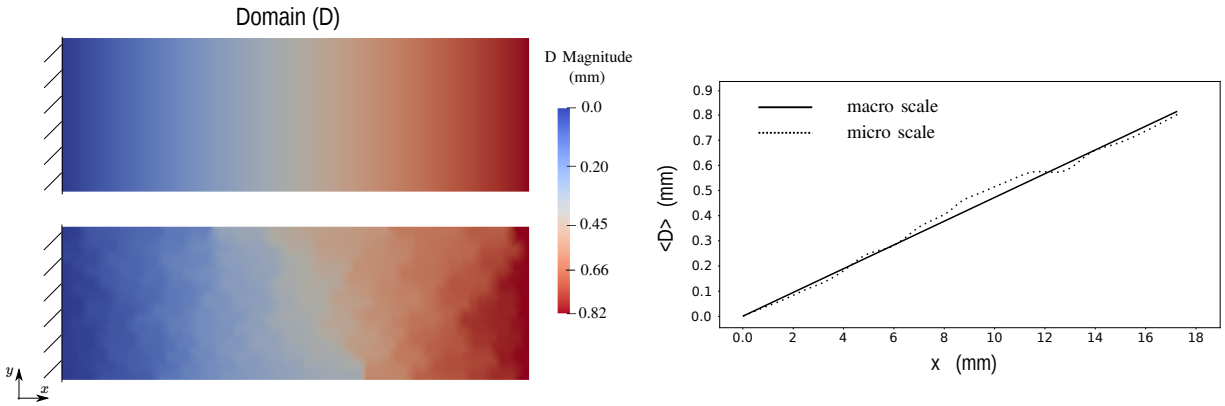


FIGURE 8.15 – Comparison of the displacement fields resulting from the pore and macro scale descriptions of the domain (D). The domain is fixed on the left boundary and free to move elsewhere. A uniform temperature load up to 800 $K$ is enforced. The resulting displacement fields are averaged in the y direction and are plotted as function of x on the right side of Fig. 8.15. A good agreement in the micro and macro scales is observed.

A uniform temperature load up to 800 $K$ is enforced. The resulting displacement fields are averaged in the y direction and are plotted as function of x on the right side of Fig. 8.15. A good agreement in the micro and macro scales is observed.

# Bibliographie


[1] G. C. April, R. W. Pike et E. G. Del Valle, "Modeling reacting gas flow in the char layer of an ablator," *AIAA Journal*, vol. 9, n°. 6, p. 1113–1119, 1971.

[2] L. J. Gibson, M. F. Ashby, G. Schajer et C. Robertson, "The mechanics of two-dimensional cellular materials," *Proceedings of the Royal Society of London. A. Mathematical and Physical Sciences*, vol. 382, n°. 1782, p. 25–42, 1982.

[3] A. Vigliotti et D. Pasini, "Linear multiscale analysis and finite element validation of stretching and bending dominated lattice materials," *Mechanics of Materials*, vol. 46, p. 57–68, 2012.

[4] S. Arabnejad et D. Pasini, "Mechanical properties of lattice materials via asymptotic homogenization and comparison with alternative homogenization methods," *International Journal of Mechanical Sciences*, vol. 77, p. 249–262, 2013.

[5] S. Malek et L. Gibson, "Effective elastic properties of periodic hexagonal honeycombs," *Mechanics of Materials*, vol. 91, p. 226–240, 2015.

[6] K. O. Davidsson et J. B. Pettersson, "Birch wood particle shrinkage during rapid pyrolysis," *Fuel*, vol. 81, n°. 3, p. 263–270, 2002.

[7] K. Chamsri et L. S. Bennethum, "Permeability of fluid flow through a periodic array of cylinders," *Applied Mathematical Modelling*, vol. 39, n°. 1, p. 244–254, 2015.

[8] R. Rocha et M. Cruz, "Calculation of the permeability and apparent permeability of three-dimensional porous media," *Transport in porous media*, vol. 83, n°. 2, p. 349–373, 2010.

[9] A. Borner, F. Panerai et N. Mansour, "High temperature permeability of fibrous materials using direct simulation monte carlo," *International Journal of Heat and Mass Transfer*, vol. 106, p. 1318–1326, 2017.

[10] W.-M. Zhang, G. Meng et X. Wei, "A review on slip models for gas microflows," *Microfluidics and nanofluidics*, vol. 13, n°. 6, p. 845–882, 2012.

[11] H. Scandelli, A. Ahmadi, C. Levet et J. Lachaud, "Computation of the permeability tensor of non-periodic anisotropic porous media from 3d images," *Transport in Porous Media*, 2022.

[12] E. C. Stern, "Microscale modeling of porous thermal protection system materials," Thèse de doctorat, University of Minnesota, 2015.

[13] D. Shou, J. Fan et F. Ding, "Hydraulic permeability of fibrous porous media," *International journal of heat and mass transfer*, vol. 54, n°. 17-18, p. 4009–4018, 2011.

[14] U. Hornung, *Homogenization and porous media*. Springer Science & Business Media, 1996, vol. 6.

[15] S. Whitaker, *The method of volume averaging*. Springer Science & Business Media, 2013, vol. 13.

[16] G. Dagan et S. P. Neuman, *Subsurface flow and transport*. International Hydrology Series, 1997.

[17] J. Cushman, L. Bennethum et B. Hu, "A primer on upscaling tools for porous media," *Advances in Water Resources*, vol. 25, n°. 8-12, p. 1043–1067, 2002.

[18] B. Antohe, J. Lage, D. Price et R. Weber, "Experimental determination of permeability and inertia coefficients of mechanically compressed aluminum porous matrices," *Journal of Fluids Engineering*, 1997.

[19] J. Paek, B. Kang, S. Kim et J. Hyun, "Effective thermal conductivity and permeability of aluminum foam materials," *International Journal of Thermophysics*, vol. 21, n°. 2, p. 453–464, 2000.

[20] V. Calmidi et R. Mahajan, "Forced convection in high porosity metal foams," *Journal of Heat Transfer*, vol. 122, n°. 3, p. 557–565, 2000.

[21] K. Boomsma et D. Poulikakos, "On the effective thermal conductivity of a three-dimensionally structured fluid-saturated metal foam," *International Journal of Heat and Mass Transfer*, vol. 44, n°. 4, p. 827–836, 2001.

[22] N. Gallego et J. Klett, "Carbon foams for thermal management," *Carbon*, vol. 41, n°. 7, p. 1461–1466, 2003.

[23] A. Straatman, N. Gallego, Q. Yu, L. Betchen et B. Thompson, "Forced convection heat transfer and hydraulic losses in graphitic foam," *Journal of heat transfer*, vol. 129, n°. 9, p. 1237–1245, 2007.

[24] X. Fu, R. Viskanta et J. Gore, "Measurement and correlation of volumetric heat transfer coefficients of cellular ceramics," *Experimental Thermal and Fluid Science*, vol. 17, n°. 4, p. 285–293, 1998.

[25] K. Ando, H. Hirai et Y. Sano, "An accurate experimental determination of interstitial heat transfer coefficients of ceramic foams using the single blow method," *The Open Transport Phenomena Journal*, vol. 5, p. 7–12, 2013.

[26] S. Karimian et A. Straatman, "Numerical modeling of multidirectional flow and heat transfer in graphitic foams," *Journal of heat transfer*, vol. 131, n°. 5, 2009.

[27] N. Dyck et A. Straatman, "A new approach to digital generation of spherical void phase porous media microstructures," *International Journal of Heat and Mass Transfer*, vol. 81, p. 470–477, 2015.

[28] M. Van Doormaal et J. Pharoah, "Determination of permeability in fibrous porous media using the lattice boltzmann method with application to pem fuel cells," *International journal for numerical methods in fluids*, vol. 59, n°. 1, p. 75–89, 2009.

[29] Y. Jobic, P. Kumar, F. Topin et R. Occelli, "Determining permeability tensors of porous media: A novel 'vector kinetic'numerical approach," *International Journal of Multiphase Flow*, vol. 110, p. 198–217, 2019.

[30] J. Vu et A. Straatman, "Comparison of pore-level and volume-averaged computations in highly conductive spherical-void-phase porous materials," *Transport in Porous Media*, vol. 124, n°. 2, p. 509–531, 2018.

[31] S. Haussener, P. Coray, W. LipiĹ, P. Wyss, A. Steinfeld *et al.*, "Tomography-based heat and mass transfer characterization of reticulate porous ceramics for high-temperature processing," *Journal of Heat Transfer*, vol. 132, n°. 2, p. 023305, 2010.

[32] B. Maruyama, J. Spowart, D. Hooper, H. Mullens, A. Druma, C. Druma et M. Alam, "A new technique for obtaining three-dimensional structures in pitch-based carbon foams," *Scripta materialia*, vol. 54, n°. 9, p. 1709–1713, 2006.

[33] J. Petrasch, B. Schrader, P. Wyss et A. Steinfeld, "Tomography-based determination of the effective thermal conductivity of fluid-saturated reticulate porous ceramics," *Journal of heat transfer*, vol. 130, n°. 3, p. 032602, 2008.

[34] J. Petrasch, F. Meier, H. Friess et A. Steinfeld, "Tomography based determination of permeability, dupuit–forchheimer coefficient, and interfacial heat transfer coefficient in reticulate porous ceramics," *International Journal of Heat and Fluid Flow*, vol. 29, n°. 1, p. 315–326, 2008.

[35] P. Ranut, E. Nobile et L. Mancini, "High resolution microtomography-based cfd simulation of flow and heat transfer in aluminum metal foams," *Applied thermal engineering*, vol. 69, n°. 1-2, p. 230–240, 2014.

[36] K. Bodla, J. Murthy et S. Garimella, "Microtomography-based simulation of transport through open-cell metal foams," *Numerical Heat Transfer, Part A: Applications*, vol. 58, n°. 7, p. 527–544, 2010.

[37] C. Soulaine, F. Gjetvaj, C. Garing, S. Roman, A. Russian, P. Gouze et H. Tchelepi, "The impact of sub-resolution porosity of x-ray microtomography images on the permeability," *Transport in porous media*, vol. 113, n°. 1, p. 227–243, 2016.

[38] M. Piller, G. Schena, M. Nolich, S. Favretto, F. Radaelli et E. Rossi, "Analysis of hydraulic permeability in porous media: from high resolution x-ray tomography to direct numerical simulation," *Transport in porous media*, vol. 80, n°. 1, p. 57, 2009.

[39] K. Gerke, M. Karsanina et E. Skvortsova, "Description and reconstruction of the soil pore space using correlation functions," *Eurasian soil science*, vol. 45, n°. 9, p. 861–872, 2012.

[40] R. Guibert, P. Horgue, G. Debenest et M. Quintard, "A comparison of various methods for the numerical evaluation of porous media permeability tensors from pore-scale geometry," *Mathematical Geosciences*, vol. 48, n°. 3, p. 329–347, 2016.

[41] K. Gerke, M. Karsanina et R. Katsman, "Calculation of tensorial flow properties on pore level: Exploring the influence of boundary conditions on the permeability of three-dimensional stochastic reconstructions," *Physical Review E*, vol. 100, n°. 5, p. 053312, 2019.

[42] J. Kozeny, "Ueber kapillare leitung des wassers im boden," *Sitzungsber Akad. Wiss., Wien, 136(2a): 271-306*, 1927.

[43] A. Bhattacharya, V. V. Calmidi et R. L. Mahajan, "Thermophysical properties of high porosity metal foams," *International journal of heat and mass transfer*, vol. 45, n°. 5, p. 1017–1031, 2002.

[44] K. Kamiuto et S. Yee, "Heat transfer correlations for open-cellular porous materials," *International Communications in Heat and Mass Transfer*, vol. 32, n°. 7, p. 947–953, 2005.

[45] K. N. Heck, S. Garcia-Segura, P. Westerhoff et M. S. Wong, "Catalytic converters for water treatment," *Accounts of chemical research*, vol. 52, n°. 4, p. 906–915, 2019.

[46] A. Mikelić, "Homogenization theory and applications to filtration through porous media," dans *Filtration in porous media and industrial application*. Springer, 2000, p. 127–214.

[47] A. Salim et S. Lim, "Review of recent metamaterial microfluidic sensors," *Sensors*, vol. 18, n°. 1, p. 232, 2018.

[48] R. Farajzadeh, A. Andrianov, R. Krastev, G. Hirasaki et W. Rossen, "Foam–oil interaction in porous media: implications for foam assisted enhanced oil recovery," *Advances in colloid and interface science*, vol. 183, p. 1–13, 2012.

[49] A. Ragauskas, C. Williams, B. Davison, G. Britovsek, J. Cairney, C. Eckert, W. Frederick, J. Hallett, D. Leak, C. Liotta *et al.*, "The path forward for biofuels and biomaterials," *science*, vol. 311, n°. 5760, p. 484–489, 2006.

[50] F. Broust, P. Girard et L. Van de Steene, "Biocarburants de seconde génération et bioraffinerie," *Techniques de l'Ingénieur*, 2013.

[51] H. Yang, R. Yan, H. Chen, D. Lee et C. Zheng, "Characteristics of hemicellulose, cellulose and lignin pyrolysis," *Fuel*, vol. 86, n°. 12-13, p. 1781–1788, 2007.

[52] J. Blondeau et H. Jeanmart, "Biomass pyrolysis at high temperatures: Prediction of gaseous species yields from an anisotropic particle," *Biomass and bioenergy*, vol. 41, p. 107–121, 2012.

[53] C. Bamford, J. Crank et D. Malan, "The combustion of wood. part i," dans *Mathematical Proceedings of the Cambridge Philosophical Society*, vol. 42, n°. 2. Cambridge University Press, 1946, p. 166–182.

[54] T. Nunn, J. Howard, J. Longwell et W. Peters, "Product compositions and kinetics in the rapid pyrolysis of milled wood lignin," *Industrial & engineering chemistry process design and development*, vol. 24, n°. 3, p. 844–852, 1985.

[55] C. Di Blasi, "Modeling chemical and physical processes of wood and biomass pyrolysis," *Progress in energy and combustion science*, vol. 34, n°. 1, p. 47–90, 2008.

[56] W. Chan, M. Kelbon et B. Krieger, "Modelling and experimental verification of physical and chemical processes during pyrolysis of a large biomass particle," *Fuel*, vol. 64, n°. 11, p. 1505–1513, 1985.

[57] R. Miller et J. Bellan, "A generalized biomass pyrolysis model based on superimposed cellulose, hemicelluloseand liqnin kinetics," *Combustion science and technology*, vol. 126, n°. 1-6, p. 97–137, 1997.

[58] E. Ranzi, A. Cuoci, T. Faravelli, A. Frassoldati, G. Migliavacca, S. Pierucci et S. Sommariva, "Chemical kinetics of biomass pyrolysis," *Energy & Fuels*, vol. 22, n°. 6, p. 4292–4300, 2008.

[59] B. Östman, D. Brandon et H. Frantzich, "Fire safety engineering in timber buildings," *Fire safety journal*, vol. 91, p. 11–20, 2017.

[60] R. Friedman, "Fire safety in spacecraft," *Fire and Materials*, vol. 20, n°. 5, p. 235–243, 1996.

[61] A. Mouritz et A. Gibson, *Fire properties of polymer composite materials*. Springer Science & Business Media, 2007, vol. 143.

[62] C. Huchette, P. Lapeyronnie, A. Hurmane, J. Rannou, V. Biasi et G. Leplat, "Influence de la dégradation thermique des cmo sur les propriétés mécaniques effectives," dans *Journées Nationales sur les Composites 2017*, 2017.

[63] A. Dasari, Z. Yu, G. Cai et Y. Mai, "Recent developments in the fire retardancy of polymeric materials," *Progress in Polymer Science*, vol. 38, n°. 9, p. 1357–1387, 2013.

[64] M. Delichatsios, B. Paroz et A. Bhargava, "Flammability properties for charring materials," *Fire Safety Journal*, vol. 38, n°. 3, p. 219–228, 2003.

[65] T. Fateh, F. Richard, B. Batiot, T. Rogaume, J. Luche et J. Zaida, "Characterization of the burning behavior and gaseous emissions of pine needles in a cone calorimeter–ftir apparatus," *Fire Safety Journal*, vol. 82, p. 91–100, 2016.

[66] R. White et M. Dietenberger, "Fire safety," *Wood handbook: wood as an engineering material. Madison, WI: USDA Forest Service, Forest Products Laboratory, 1999. General technical report FPL; GTR-113: Pages 17.1-17.16*, vol. 113, 1999.

[67] P. Schrooyen, "Numerical simulation of aerothermal flows through ablative thermal protection systems," Thèse de doctorat, PhD thesis, 2015.

[68] M. Wright, R. Beck, K. Edquist, D. Driver, S. Sepka, E. Slimko et W. Willcockson, "Sizing and margins assessment of mars science laboratory aeroshell thermal protection system," *Journal of Spacecraft and Rockets*, vol. 51, n°. 4, p. 1125–1138, 2014.

[69] M. Stackpoole, S. Sepka, I. Cozmuta et D. Kontinos, "Post-flight evaluation of stardust sample return capsule forebody heatshield material," dans *46th AIAA Aerospace Sciences Meeting and Exhibit*, 2008, p. 1202.

[70] H. K. Tran, C. Johnson, D. Rasky, F. Hui, M.-T. Hsu, T. Chen, Y. Chen, D. Paragas et L. Kobayashi, "Phenolic impregnated carbon ablators pica as thermal protection system for discovery missions," *NASA TM-110440, NASA, Washington, DC*, 1997.

[71] H. Ritter, P. Portela, K. Keller, J. Bouilly et S. Burnage, "Development of a european ablative material for heatshields of sample return missions," dans *6th European Workshop on Thermal Protection Systems and Hot Structures, Stuttgart, Germany*, vol. 99, 2009.

[72] J. Lachaud, T. Magin, I. Cozmuta et N. Mansour, "A short review of ablative-material response models and simulation tools," dans *7th aerothermodynamics symposium*, 2011.

[73] J. Lachaud et N. Mansour, "Porous-material analysis toolbox based on openfoam and applications," *Journal of Thermophysics and Heat Transfer*, vol. 28, n°. 2, p. 191–202, 2014.

[74] J. Lachaud, T. van Eekelen, J. Scoggins, T. Magin et N. Mansour, "Detailed chemical equilibrium model for porous ablative materials," *International Journal of Heat and Mass Transfer*, vol. 90, p. 1034–1045, 2015.

[75] J. Lachaud, J. Scoggins, T. Magin, M. Meyer et N. Mansour, "A generic local thermal equilibrium model for porous reactive materials submitted to high temperatures," *International Journal of Heat and Mass Transfer*, vol. 108, p. 1406–1417, 2017.

[76] S. I. Stoliarov, S. Crowley, R. E. Lyon et G. T. Linteris, "Prediction of the burning rates of non-charring polymers," *Combustion and Flame*, vol. 156, n°. 5, p. 1068–1083, 2009.

[77] C. Lautenberger et C. Fernandez-Pello, "A model for the oxidative pyrolysis of wood," *Combustion and Flame*, vol. 156, n°. 8, p. 1503–1513, 2009.

[78] V. Biasi, "Modélisation thermique de la dégradation d'un matériau composite soumis au feu," Thèse de doctorat, INSTITUT SUPERIEUR DE L'AERONAUTIQUE ET DE L'ESPACE (ISAE), 2014.

[79] G. Gentile, P. E. A. Debiagi, A. Cuoci, A. Frassoldati, E. Ranzi et T. Faravelli, "A computational framework for the pyrolysis of anisotropic biomass particles," *Chemical Engineering Journal*, vol. 321, p. 458–473, 2017.

[80] J. Ratte, F. Marias, J. Vaxelaire et P. Bernada, "Mathematical modelling of slow pyrolysis of a particle of treated wood waste," *Journal of hazardous materials*, vol. 170, n°. 2-3, p. 1023–1040, 2009.

[81] V. Pozzobon, S. Salvador et J. J. Bézian, "Biomass gasification under high solar heat flux: Advanced modelling," *Fuel*, vol. 214, p. 300–313, 2018.

[82] A. Van Eekelen et J. Lachaud, "Numerical validation of an effective radiation heat transfer model for fiber preforms," *Journal of Spacecraft and Rockets*, vol. 48, n°. 3, p. 534–537, 2011.

[83] A. Amar, N. Calvert et B. Kirk, "Development and verification of the charring ablating thermal protection implicit system solver," dans *49th AIAA Aerospace Sciences Meeting including the New Horizons Forum and Aerospace Exposition*, 2011, p. 144.

[84] J. B. Scoggins et T. E. Magin, "Development of mutation++: Multicomponent thermodynamic and transport properties for ionized plasmas written in c++," dans *11th AIAA/ASME joint thermophysics and heat transfer conference*, 2014, p. 2966.

[85] J. D. Anderson, *Hypersonic and high temperature gas dynamics*. Aiaa, 2000.

[86] M. E. Gurtin, *An introduction to continuum mechanics*. Academic press, 1982.

[87] M. Brochure. (2017) Calcarb rigid carbon thermal insulation. Https://www.mersen.com/sites/default/files/publications-media/3-gs-calcarb-grade-cbcf-18-2000-mersen.pdf.

[88] J. Mustard, M. Adler, A. Allwood, D. Bass, D. Beaty, J. Bell, W. Brinckerhoff, M. Carr, D. Des Marais, B. Brake *et al.*, "Report of the mars 2020 science definition team," *Mars Explor. Progr. Anal. Gr*, vol. 150, p. 155–205, 2013.

[89] L. Shaolin, A. Azita et L. Jean, "Experimental investigation of heat transfer in calcarb: one or two temperature model ?" dans *2nd International Conference on Flight Vehicles, Aerothermodynamics and Re-entry Missions Engineering (FAR)*, 2022.

[90] M. Agnaou, D. Lasseux et A. Ahmadi, "Origin of the inertial deviation from darcy's law: An investigation from a microscopic flow analysis on two-dimensional model structures," *Physical Review E*, vol. 96, n°. 4, p. 043105, 2017.

[91] A. Dybbs et R. Edwards, "A new look at porous media fluid mechanics—darcy to turbulent," dans *Fundamentals of transport phenomena in porous media*. Springer, 1984, p. 199–256.

[92] D. A. Kontinos et M. J. Wright, "Introduction: Atmospheric entry of the stardust sample return capsule," *Journal of Spacecraft and Rockets*, vol. 47, n°. 5, p. 705–707, 2010.

[93] J. B. Meurisse, J. Lachaud, F. Panerai, C. Tang et N. N. Mansour, "Multidimensional material response simulations of a full-scale tiled ablative heatshield," *Aerospace Science and Technology*, vol. 76, p. 497–511, 2018.

[94] N. Christian, "Impacts de l'énergie sur l'environnement illustration sur quelques exemples," *Techniques de l'ingénieur Énergie : économie et environnement*, vol. base documentaire : TIB593DUO, n°. be7900, 2017.

[95] O. Edenhofer, R. Pichs-Madruga, Y. Sokona, K. Seyboth, S. Kadner, T. Zwickel, P. Eickemeier, G. Hansen, S. Schlömer, C. von Stechow *et al.*, *Renewable energy sources and climate change mitigation: Special report of the intergovernmental panel on climate change*. Cambridge University Press, 2011.

[96] A. Martin et I. D. Boyd, "Modeling of heat transfer attenuation by ablative gases during the stardust reentry," *Journal of Thermophysics and Heat Transfer*, vol. 29, n°. 3, p. 450–466, 2015.

[97] N. Puiroux, M. Prat et M. Quintard, "Non-equilibrium theories for macroscale heat transfer: ablative composite layer systems," *International Journal of Thermal Sciences*, vol. 43, n°. 6, p. 541–554, 2004.

[98] B. S. Venkatachari, G. Cheng, R. Koomullil et A. Ayasoufi, "Computational tools for re-entry aerothermodynamics: Part ii. surface ablation," dans *46th AIAA Aerospace Sciences Meeting and Exhibit*, 2008, p. 1218.

[99] G. Blanquart, P. Pepiot-Desjardins et H. Pitsch, "Chemical mechanism for high temperature combustion of engine relevant fuels with emphasis on soot precursors," *Combustion and Flame*, vol. 156, n°. 3, p. 588–607, 2009.

[100] E. Sanchez-Palencia, "Homogenization method for the study of composite media," dans *Asymptotic Analysis II—*. Springer, 1983, p. 192–214.

[101] J. B. Scoggins et T. E. Magin, "Gibbs function continuation for linearly constrained multiphase equilibria," *Combustion and Flame*, vol. 162, n°. 12, p. 4514–4522, 2015.

[102] S. Whitaker, "Flow in porous media i: A theoretical derivation of darcy's law," *Transport in porous media*, vol. 1, n°. 1, p. 3–25, 1986.

[103] K. A. Trumble, I. Cozmuta, S. Sepka, P. Jenniskens et M. Winter, "Postflight aerothermal analysis of the stardust sample return capsule," *Journal of Spacecraft and Rockets*, vol. 47, n°. 5, p. 765–774, 2010.

[104] G. Cox et J. Moss, "Fire science and aircraft safety," dans *AGARD Conference Proceedings*, n°. 467, 1989.

[105] F. Global. Firefoam. [En ligne]. Disponible: http://code.google.com/p/firefoam-dev/

[106] Y. Z. Li, C. Huang, J. Anderson, R. Svensson, H. Ingason, B. Husted, M. Runefors et J. Wahlqvist, "Verification, validation and evaluation of firefoam as a tool for performance design," 2017.

[107] R. Zamorano, "Firefoam (cfd solver) validation in compartment fire scenario using high resolution data," Thèse de doctorat, PhD thesis, 2018.

[108] A. Trouvé et Y. Wang, "Large eddy simulation of compartment fires," *International Journal of Computational Fluid Dynamics*, vol. 24, n°. 10, p. 449–466, 2010.

[109] A. Favre, "Turbulence: Space-time statistical properties and behavior in supersonic flows," *The Physics of fluids*, vol. 26, n°. 10, p. 2851–2863, 1983.

[110] J. H. Ferziger, M. Perić et R. L. Street, *Computational methods for fluid dynamics*. Springer, 2002, vol. 3.

[111] G. Erlebacher, M. Y. Hussaini, C. G. Speziale et T. A. Zang, "Toward the large-eddy simulation of compressible turbulent flows," *Journal of fluid mechanics*, vol. 238, p. 155–185, 1992.

[112] D. Siderius, "Nist standard reference simulation website-srd 173," *National Institute of Standards and Technology*, 2017.

[113] B. E. Poling, J. M. Prausnitz et J. P. O'connell, *Properties of gases and liquids*. McGraw-Hill Education, 2001.

[114] H. Xiao et P. Jenny, "A consistent dual-mesh framework for hybrid les/rans modeling," *Journal of Computational Physics*, vol. 231, n°. 4, p. 1848–1865, 2012.

[115] R. Sierens, J. Demuynck, M. d. Paepe et S. Verhelst, "Heat transfer comparison between methane and hydrogen in a spark ignited engine," dans *18th World Hydrogen Energy Conference 2010 - WHEC 2010*, 2010.

[116] P. Mandin et J. Most, "Characterization of the puffing phenomenon on a pool fire," *Fire Safety Science*, vol. 6, p. 1137–1148, 2000.

[117] C. L. Beyler, "Fire plumes and ceiling jets," *Fire safety journal*, vol. 11, n°. 1-2, p. 53–75, 1986.

[118] H. Pretrel et L. Audouin, "Periodic puffing instabilities of buoyant large-scale pool fires in a confined compartment," *Journal of fire sciences*, vol. 31, n°. 3, p. 197–210, 2013.

[119] B. Wood, X. He et S. Apte, "Modeling turbulent flows in porous media," *Annual Review of Fluid Mechanics*, vol. 52, p. 171–203, 2020.

[120] P. Forchheimer, "Wasserbewegung durch boden," *Z. Ver. Deutsch, Ing.*, vol. 45, p. 1782–1788, 1901.

[121] P. Kumar et F. Topin, "Investigation of fluid flow properties in open cell foams: Darcy and weak inertia regimes," *Chemical Engineering Science*, vol. 116, p. 793–805, 2014.

[122] S. Whitaker, "The forchheimer equation: a theoretical development," *Transport in Porous media*, vol. 25, n°. 1, p. 27–61, 1996.

[123] A. Ashari, T. Bucher et H. V. Tafreshi, "A semi-analytical model for simulating fluid transport in multi-layered fibrous sheets made up of solid and porous fibers," *Computational materials science*, vol. 50, n°. 2, p. 378–390, 2010.

[124] A. Derossi, K. Gerke, M. Karsanina, B. Nicolai, P. Verboven et C. Severini, "Mimicking 3d food microstructure using limited statistical information from 2d cross-sectional image," *Journal of food engineering*, vol. 241, p. 116–126, 2019.

[125] H. Gerke, "Preferential flow descriptions for structured soils," *Journal of Plant Nutrition and Soil Science*, vol. 169, n°. 3, p. 382–400, 2006.

[126] M. Sahimi, *Flow and transport in porous media and fractured rock: from classical methods to modern approaches*. John Wiley & Sons, 2011.

[127] T. Tranter, J. Gostick, A. Burns et W. Gale, "Capillary hysteresis in neutrally wettable fibrous media: a pore network study of a fuel cell electrode," *Transport in porous media*, vol. 121, n°. 3, p. 597–620, 2018.

[128] Q. Xiong, C. Joseph, K. Schmeide et A. Jivkov, "Measurement and modelling of reactive transport in geological barriers for nuclear waste containment," *Physical Chemistry Chemical Physics*, vol. 17, n°. 45, p. 30 577–30 589, 2015.

[129] E. Moreira, M. Innocentini et J. Coury, "Permeability of ceramic foams to compressible and incompressible flow," *Journal of the European Ceramic Society*, vol. 24, n°. 10-11, p. 3209–3218, 2004.

[130] F. Panerai, J. White, T. Cochell, O. Schroeder, N. Mansour, M. Wright et A. Martin, "Experimental measurements of the permeability of fibrous carbon at high-temperature," *International Journal of Heat and Mass Transfer*, vol. 101, p. 267–273, 2016.

[131] P. Renard, A. Genty et F. Stauffer, "Laboratory determination of the full permeability tensor," *Journal of Geophysical Research: Solid Earth*, vol. 106, n°. B11, p. 26 443–26 452, 2001.

[132] K. M. Gerke, T. O. Sizonenko, M. V. Karsanina, E. V. Lavrukhin, V. V. Abashkin et D. V. Korost, "Improving watershed-based pore-network extraction method using maximum inscribed ball pore-body positioning," *Advances in Water Resources*, vol. 140, p. 103576, 2020.

[133] K. M. Gerke, R. V. Vasilyev, S. Khirevich, D. Collins, M. V. Karsanina, T. O. Sizonenko, D. V. Korost, S. Lamontagne et D. Mallants, "Finite-difference method stokes solver (fdmss) for 3d pore geometries: Software development, validation and case studies," *Computers & geosciences*, vol. 114, p. 41–58, 2018.

[134] Z. A. Khan, A. Elkamel et J. T. Gostick, "Efficient extraction of pore networks from massive tomograms via geometric domain decomposition," *Advances in Water Resources*, vol. 145, p. 103734, 2020.

[135] P. H. Valvatne et M. J. Blunt, "Predictive pore-scale modeling of two-phase flow in mixed wet media," *Water resources research*, vol. 40, n°. 7, 2004.

[136] C. Davy et P. Adler, "Three-scale analysis of the permeability of a natural shale," *Physical Review E*, vol. 96, n°. 6, p. 063116, 2017.

[137] M. Ali, R. Umer, K. Khan et W. Cantwell, "Application of x-ray computed tomography for the virtual permeability prediction of fiber reinforcements for liquid composite molding processes: A review," *Composites Science and Technology*, vol. 184, p. 107828, 2019.

[138] E. Landis et D. Keane, "X-ray microtomography," *Materials characterization*, vol. 61, n°. 12, p. 1305–1316, 2010.

[139] K. Gerke, D. Korost, R. Vasilyev, M. Karsanina et V. Tarasovskii, "Studying structure and determining permeability of materials based on x-ray microtomography data (using porous ceramics as an example)," *Inorganic Materials*, vol. 51, n°. 9, p. 951–957, 2015.

[140] F. Panerai, J. Ferguson, J. Lachaud, A. Martin, M. Gasch et N. Mansour, "Micro-tomography based analysis of thermal conductivity, diffusivity and oxidation behavior of rigid and flexible fibrous insulators," *International Journal of Heat and Mass Transfer*, vol. 108, p. 801–811, 2017.

[141] G. Pickup, P. Ringrose, J. Jensen et K. Sorbie, "Permeability tensors for sedimentary structures," *Mathematical Geology*, vol. 26, n°. 2, p. 227–250, 1994.

[142] S. Jaganathan, H. V. Tafreshi et B. Pourdeyhimi, "Two-scale modeling approach to predict permeability of fibrous media," *Journal of Engineered Fibers and Fabrics*, vol. 3, n°. 2, p. 155892500800300208, 2008.

[143] E. Masad, A. Al Omari et H.-C. Chen, "Computations of permeability tensor coefficients and anisotropy of asphalt concrete based on microstructure simulation of fluid flow," *Computational Materials Science*, vol. 40, n°. 4, p. 449–459, 2007.

[144] A. Wiegmann, "Computation of the permeability of porous materials from their microstructure by fff-stokes," *Bericht des Fraunhofer ITWM*, vol. 129, 2007.

[145] H. Andrä, N. Combaret, J. Dvorkin, E. Glatt, J. Han, M. Kabel, Y. Keehm, F. Krzikalla, M. Lee, C. Madonna *et al.*, "Digital rock physics benchmarks—part i: Imaging and segmentation," *Computers & Geosciences*, vol. 50, p. 25–32, 2013.

[146] D. Bernard, Ø. Nielsen, L. Salvo et P. Cloetens, "Permeability assessment by 3d interdendritic flow simulations on microtomography mappings of al–cu alloys," *Materials Science and Engineering: A*, vol. 392, n°. 1-2, p. 112–120, 2005.

[147] J. Barrere, O. Gipouloux et S. Whitaker, "On the closure problem for darcy's law," *Transport in Porous Media*, vol. 7, n°. 3, p. 209–222, 1992.

[148] C. Manwart, U. Aaltosalmi, A. Koponen, R. Hilfer et J. Timonen, "Lattice-boltzmann and finite-difference simulations for the permeability for three-dimensional porous media," *Physical Review E*, vol. 66, n°. 1, p. 016702, 2002.

[149] A. Liakopoulos, "Darcy's coefficient of permeability as symmetric tensor of second rank," *Hydrological Sciences Journal*, vol. 10, n°. 3, p. 41–48, 1965.

[150] M. Quintard, "Introduction to heat and mass transport in porous media," *Porous media interaction with high temperature and high speed ows, STO-AVT-261. VKI*, p. 33, 2015.

[151] F. module by Simpleware. Http://www.simpleware.com/.

[152] J. Ahrens, B. Geveci et C. Law, "Paraview: An end-user tool for large data visualization," *The visualization handbook*, vol. 717, 2005.

[153] R. Issa, "Solution of the implicitly discretised fluid flow equations by operator-splitting," *Journal of computational physics*, vol. 62, n°. 1, p. 40–65, 1986.

[154] S. Patankar et D. Spalding, "A calculation procedure for heat, mass and momentum transfer in three-dimensional parabolic flows," dans *Numerical prediction of flow, heat transfer, turbulence and combustion*. Elsevier, 1983, p. 54–73.

[155] J. Lachaud et J. Meurisse. Http://pato.ac/.

[156] J. Almedeij, "Drag coefficient of flow around a sphere: Matching asymptotically the wide trend," *Powder Technology*, vol. 186, n°. 3, p. 218–223, 2008.

[157] G. Bagheri et C. Bonadonna, "On the drag of freely falling non-spherical particles," *Powder Technology*, vol. 301, p. 526–544, 2016.

[158] M. Mikhailov et A. Freire, "The drag coefficient of a sphere: An approximation using shanks transform," *Powder technology*, vol. 237, p. 432–435, 2013.

[159] W. Gray, "A derivation of the equations for multi-phase transport," *Chemical Engineering Science*, vol. 30, n°. 2, p. 229–233, 1975.

[160] Y. Anguy, D. Bernard et R. Ehrlich, "The local change of scale method for modelling flow in natural porous media (i): Numerical tools," *Advances in water resources*, vol. 17, n°. 6, p. 337–351, 1994.

[161] S. E. Kentish, C. A. Scholes et G. W. Stevens, "Carbon dioxide separation through polymeric membrane systems for flue gas applications," *Recent Patents on Chemical Engineering*, vol. 1, n°. 1, p. 52–66, 2008.

[162] C. Cercignani, "The boltzmann equation," dans *The Boltzmann equation and its applications*. Springer, 1988, p. 40–103.

[163] R. K. Agarwal, K.-Y. Yun et R. Balakrishnan, "Beyond navier–stokes: Burnett equations for flows in the continuum–transition regime," *Physics of Fluids*, vol. 13, n°. 10, p. 3061–3085, 2001.

[164] F. Sharipov, "Data on the velocity slip and temperature jump coefficients [gas mass, heat and momentum transfer]," dans *5th International Conference on Thermal and Mechanical Simulation and Experiments in Microelectronics and Microsystems, 2004. EuroSimE 2004. Proceedings of the*. IEEE, 2004, p. 243–249.

[165] S. Roy, R. Raju, H. Chuang, B. Cruden et M. Meyyappan, "Modeling gas flow through microchannels and nanopores," *Journal of applied physics*, vol. 93, n°. 8, p. 4870–4879, 2003.

[166] J. Maxwell, "On stresses in rarefied gases arising from inequalities of temperature the scientific papers of james clerk maxwell," 1879.

[167] L. Klinkenberg *et al.*, "The permeability of porous media to liquids and gases," dans *Drilling and production practice*. American Petroleum Institute, 1941.

[168] D. Lasseux et F. J. Valdés-Parada, "On the developments of darcy's law to include inertial and slip effects," *Comptes Rendus Mécanique*, vol. 345, n°. 9, p. 660–669, 2017.

[169] C. Charles, C. Descamps et G. L. Vignoles, "Low pressure gas transfer in fibrous media with progressive infiltration: correlation between different transfer modes," *International Journal of Heat and Mass Transfer*, vol. 182, p. 121954, 2022.

[170] C. White, T. J. Scanlon et R. E. Brown, "Permeability of ablative materials under rarefied gas conditions," *Journal of Spacecraft and Rockets*, vol. 53, n°. 1, p. 134–142, 2016.

[171] A. Kalarakis, V. Michalis, E. Skouras et V. Burganos, "Mesoscopic simulation of rarefied flow in narrow channels and porous media," *Transport in porous media*, vol. 94, n°. 1, p. 385–398, 2012.

[172] T. Oshima, S. Yonemura et T. Tokumasu, "A numerical study for transport phenomena of nanoscale gas flow in porous media," dans *AIP Conference Proceedings*, vol. 1501, n°. 1. American Institute of Physics, 2012, p. 809–815.

[173] J. Li et A. S. Sultan, "Klinkenberg slippage effect in the permeability computations of shale gas by the pore-scale simulations," *Journal of natural gas science and engineering*, vol. 48, p. 197–202, 2017.

[174] R. Jambunathan, D. A. Levin, A. Borner, J. C. Ferguson et F. Panerai, "Prediction of gas transport properties through fibrous carbon preform microstructures using direct simulation monte carlo," *International Journal of Heat and Mass Transfer*, vol. 130, p. 923–937, 2019.

[175] S. Hosseini et H. V. Tafreshi, "Modeling permeability of 3-d nanofiber media in slip flow regime," *Chemical Engineering Science*, vol. 65, n°. 6, p. 2249–2254, 2010.

[176] P. Krakowska et P. Madejski, "Research on fluid flow and permeability in low porous rock sample using laboratory and computational techniques," *Energies*, vol. 12, n°. 24, p. 4684, 2019.

[177] P. Madejski, P. Krakowska, E. Puskarczyk, M. Habrat et M. Jędrychowski, "Permeability determination in tight rock sample using novel method based on partial slip modelling and x-ray tomography data," *International Journal of Numerical Methods for Heat & Fluid Flow*, 2019.

[178] M. Nojoomizadeh, A. D'Orazio, A. Karimipour, M. Afrand et M. Goodarzi, "Investigation of permeability effect on slip velocity and temperature jump boundary conditions for fmwnt/water nanofluid flow and heat transfer inside a microchannel filled by a porous media," *Physica E: Low-dimensional Systems and Nanostructures*, vol. 97, p. 226–238, 2018.

[179] H. Darcy, *Les Fontaines publiques de la ville de Dijon. Exposition et application des principes à suivre et des formules à employer dans les questions de distribution d'eau, etc.* V. Dalamont, 1856.

[180] Z. Chai, J. Lu, B. Shi et Z. Guo, "Gas slippage effect on the permeability of circular cylinders in a square array," *International Journal of Heat and Mass Transfer*, vol. 54, n°. 13-14, p. 3009–3014, 2011.

[181] C. White, M. K. Borg, T. J. Scanlon, S. M. Longshaw, B. John, D. R. Emerson et J. M. Reese, "dsmcfoam+: An openfoam based direct simulation monte carlo solver," *Computer Physics Communications*, vol. 224, p. 22–43, 2018.

[182] G. Pulci, J. Tirillò, F. Marra, F. Fossati, C. Bartuli et T. Valente, "Carbon–phenolic ablative materials for re-entry space vehicles: Manufacturing and properties," *Composites Part A: Applied Science and Manufacturing*, vol. 41, n°. 10, p. 1483–1490, 2010.

[183] M. Natali, J. M. Kenny et L. Torre, "Science and technology of polymeric ablative materials for thermal protection systems and propulsion devices: A review," *Progress in Materials Science*, vol. 84, p. 192–275, 2016.

[184] X. Hu et M. Gholizadeh, "Biomass pyrolysis: A review of the process development and challenges from initial researches up to the commercialisation stage," *Journal of Energy Chemistry*, vol. 39, p. 109–143, 2019.

[185] V. Petrov, "Combined radiation and conduction heat transfer in high temperature fiber thermal insulation," *International Journal of Heat and Mass Transfer*, vol. 40, n°. 9, p. 2241–2247, 1997.

[186] G. Fau, N. Gascoin, P. Gillard, M. Bouchez et J. Steelant, "Fuel pyrolysis through porous media: Coke formation and coupled effect on permeability," *Journal of Analytical and Applied Pyrolysis*, vol. 95, p. 180–188, 2012.

[187] G. F. Sykes, *Thermal cracking of phenolic-nylon pyrolysis products on passing through a heated char*. National Aeronautics and Space Administration, 1970.

[188] H. Scandelli, A. Ahmadi, C. Levet et J. Lachaud, "Review and comparison of numerical strategies to estimate anisotropic permeability tensors from micro-tomography images," *International Journal of Heat and Fluid Flow*, 2021.

[189] D. Vortmeyer et R. Schaefer, "Equivalence of one-and two-phase models for heat transfer processes in packed beds: one dimensional theory," *Chemical Engineering Science*, vol. 29, n°. 2, p. 485–491, 1974.

[190] T. Kanit, S. Forest, I. Galliet, V. Mounoury et D. Jeulin, "Determination of the size of the representative volume element for random composites: statistical and numerical approach," *International Journal of solids and structures*, vol. 40, n°. 13-14, p. 3647–3679, 2003.

[191] K. Vafai et A. Amiri, "Non-darcian effects in confined forced convective flows," *Transport phenomena in porous media*, vol. 1, p. 313–329, 1998.

[192] F. Kuwahara, M. Shirota et A. Nakayama, "A numerical study of interfacial convective heat transfer coefficient in two-energy equation model for convection in porous media," *International journal of heat and mass transfer*, vol. 44, n°. 6, p. 1153–1159, 2001.

[193] M. Quintard, M. Kaviany et S. Whitaker, "Two-medium treatment of heat transfer in porous media: numerical results for effective properties," *Advances in water resources*, vol. 20, n°. 2-3, p. 77–94, 1997.

[194] R. G. Carbonell et S. Whitaker, "Heat and mass transfer in porous media," dans *Fundamentals of transport phenomena in porous media*. Springer, 1984, p. 121–198.

[195] S. Kim et S. Jang, "Effects of the darcy number, the prandtl number, and the reynolds number on local thermal non-equilibrium," *International Journal of Heat and Mass Transfer*, vol. 45, n°. 19, p. 3885–3896, 2002.

[196] X. Zhang et W. Liu, "New criterion for local thermal equilibrium in porous media," *Journal of thermophysics and heat transfer*, vol. 22, n°. 4, p. 649–653, 2008.

[197] M. Kaviany, *Principles of heat transfer in porous media*. Springer Science & Business Media, 2012.

[198] M. Quintard et S. Whitaker, "One-and two-equation models for transient diffusion processes in two-phase systems," dans *Advances in heat transfer*. Elsevier, 1993, vol. 23, p. 369–464.

[199] F. Dórea et M. De Lemos, "Simulation of laminar impinging jet on a porous medium with a thermal non-equilibrium model," *International Journal of Heat and Mass Transfer*, vol. 53, n°. 23-24, p. 5089–5101, 2010.

[200] H. Xu, L. Gong, C. Zhao, Y. Yang et Z. Xu, "Analytical considerations of local thermal non-equilibrium conditions for thermal transport in metal foams," *International Journal of Thermal Sciences*, vol. 95, p. 73–87, 2015.

[201] S. Hamidi, T. Heinze, B. Galvan et S. Miller, "Critical review of the local thermal equilibrium assumption in heterogeneous porous media: dependence on permeability and porosity contrasts," *Applied Thermal Engineering*, vol. 147, p. 962–971, 2019.

[202] M. Saito et M. de Lemos, "A macroscopic two-energy equation model for turbulent flow and heat transfer in highly porous media," *International Journal of Heat and Mass Transfer*, vol. 53, n°. 11-12, p. 2424–2433, 2010.

[203] D. Gao, F. Tian, Z. Chen et D. Zhang, "An improved lattice boltzmann method for solid-liquid phase change in porous media under local thermal non-equilibrium conditions," *International Journal of Heat and Mass Transfer*, vol. 110, p. 58–62, 2017.

[204] P. Jiang et Z. Ren, "Numerical investigation of forced convection heat transfer in porous media using a thermal non-equilibrium model," *International Journal of Heat and Fluid Flow*, vol. 22, n°. 1, p. 102–110, 2001.

[205] C. Wang, M. Mobedi et F. Kuwahara, "Analysis of local thermal non-equilibrium condition for unsteady heat transfer in porous media with closed cells: Sparrow number," *International Journal of Mechanical Sciences*, vol. 157, p. 13–24, 2019.

[206] M. Cimmino et B. Baliga, "Evaluation of the interfacial conduction heat transfer coefficient in two-temperature macroscopic models of homogenous porous media using a fully developed unsteady microscopic model in periodic unit cells," *Numerical Heat Transfer, Part B: Fundamentals*, vol. 71, n°. 3, p. 236–252, 2017.

[207] F. Teruel et L. Díaz, "Calculation of the interfacial heat transfer coefficient in porous media employing numerical simulations," *International Journal of Heat and Mass Transfer*, vol. 60, p. 406–412, 2013.

[208] S. Sabet, M. Mobedi, M. Barisik et A. Nakayama, "Numerical determination of interfacial heat transfer coefficient for an aligned dual scale porous medium," *International Journal of Numerical Methods for Heat & Fluid Flow*, 2018.

[209] M. Zafari, M. Panjepour, M. D. Emami et M. Meratian, "Microtomography-based numerical simulation of fluid flow and heat transfer in open cell metal foams," *Applied Thermal Engineering*, vol. 80, p. 347–354, 2015.

[210] A. Nakayama, F. Kuwahara, T. Umemoto et T. Hayashi, "Heat and fluid flow within an anisotropic porous medium," *J. Heat Transfer*, vol. 124, n°. 4, p. 746–753, 2002.

[211] C. Truesdell et R. Toupin, "The classical field theories," dans *Principles of classical mechanics and field theory/Prinzipien der Klassischen Mechanik und Feldtheorie*. Springer, 1960, p. 226–858.

[212] J. Petrasch, B. Schrader, P. Wyss et A. Steinfeld, "Tomography-based determination of the effective thermal conductivity of fluid-saturated reticulate porous ceramics," *Journal of heat transfer*, vol. 130, n°. 3, 2008.

[213] H. Celik, M. Mobedi, O. Manca et U. Ozkol, "A pore scale analysis for determination of interfacial convective heat transfer coefficient for thin periodic porous media under mixed convection," *International Journal of Numerical Methods for Heat & Fluid Flow*, 2017.

[214] F. Kuwahara, A. Nakayama et H. Koyama, "A numerical study of thermal dispersion in porous media," *Journal of Heat Transfer*, vol. 118, 1996.

[215] M. Saito et M. de Lemos, "Interfacial heat transfer coefficient for non-equilibrium convective transport in porous media," *International Communications in Heat and Mass Transfer*, vol. 32, n°. 5, p. 666–676, 2005.

[216] A. Nakayama, F. Kuwahara et T. Hayashi, "Numerical modelling for three-dimensional heat and fluid flow through a bank of cylinders in yaw," *Journal of Fluid Mechanics*, vol. 498, p. 139, 2004.

[217] J. C. Ferguson, F. Panerai, A. Borner et N. N. Mansour, "Puma: The porous microstructure analysis software," *SoftwareX*, vol. 7, p. 81–87, 2018.

[218] T. Ahmed, *Reservoir engineering handbook*. Gulf professional publishing, 2018.

[219] M. Grant, *Geothermal reservoir engineering*. Elsevier, 2013.

[220] A. Verruijt, *Theory of groundwater flow*. Macmillan International Higher Education, 2016.

[221] S. P. Walker, K. Daryabeigi, J. A. Samareh et S. C. Armand, "Preliminary development of a multifunctional hot structure heat shield," dans *55th AIAA/ASMe/ASCE/AHS/SC Structures, Structural Dynamics, and Materials Conference*, 2014, p. 0350.

[222] K. Edquist, A. Dyakonov, M. Wright et C. Tang, "Aerothermodynamic design of the mars science laboratory heatshield," dans *41st AIAA Thermophysics Conference*, 2009, p. 4075.

[223] D. Lasseux, F. J. Valdés-Parada et F. Bellet, "Macroscopic model for unsteady flow in porous media," *Journal of Fluid Mechanics*, vol. 862, p. 283–311, 2019.

[224] A. Bourgeat et A. Mikelić, "Homogenization of a polymer flow through a porous medium," *Nonlinear Analysis: Theory, Methods & Applications*, vol. 26, n°. 7, p. 1221–1253, 1996.

[225] R. Moghaddam et M. Jamiolahmady, "Slip flow in porous media," *Fuel*, vol. 173, p. 298–310, 2016.

[226] J.-L. Auriault, "Transport in porous media: upscaling by multiscale asymptotic expansions," dans *Applied micromechanics of porous materials*. Springer, 2005, p. 3–56.

[227] K. Ando et H. Onda, "Mechanism for deformation of wood as a honeycomb structure i: effect of anatomy on the initial deformation process during radial compression," *Journal of wood science*, vol. 45, n°. 2, p. 120–126, 1999.

[228] M. J. Hagge et K. M. Bryden, "Modeling the impact of shrinkage on the pyrolysis of dry biomass," *Chemical Engineering Science*, vol. 57, n°. 14, p. 2811–2823, 2002.

[229] C. Di Blasi, "Heat, momentum and mass transport through a shrinking biomass particle exposed to thermal radiation," *Chemical engineering science*, vol. 51, n°. 7, p. 1121–1132, 1996.

[230] M. Sreekanth, B. Prasad, A. K. Kolar, H. Thunman et B. Leckner, "Stresses in a cylindrical wood particle undergoing devolatilization in a hot bubbling fluidized bed," *Energy & fuels*, vol. 22, n°. 3, p. 1549–1559, 2008.

[231] R. W. Lewis, R. W. Lewis et B. Schrefler, *The finite element method in the static and dynamic deformation and consolidation of porous media*. John Wiley & Sons, 1998.

[232] O. Iliev, A. Mikelić et P. Popov, "On upscaling certain flows in deformable porous media," *Multiscale Modeling & Simulation*, vol. 7, n°. 1, p. 93–123, 2008.

[233] M. Bornert, T. Bretheau et P. Gilormini, *Homogénéisation en mécanique des matériaux, Tome 1: Matériaux aléatoires élastiques et milieux périodiques*. Hermes science, 2001.

[234] J. Davies et P. Leach, "First-order generalised beam theory," *Journal of Constructional Steel Research*, vol. 31, n°. 2-3, p. 187–220, 1994.

[235] J. Zhang et M. Ashby, "The out-of-plane properties of honeycombs," *International journal of mechanical sciences*, vol. 34, n°. 6, p. 475–489, 1992.

[236] W. S. Burton et A. Noor, "Assessment of continuum models for sandwich panel honeycomb cores," *Computer methods in applied mechanics and engineering*, vol. 145, n°. 3-4, p. 341–360, 1997.

[237] X. F. Xu et P. Qiao, "Homogenized elastic properties of honeycomb sandwich with skin effect," *International Journal of Solids and Structures*, vol. 39, n°. 8, p. 2153–2188, 2002.

[238] C. Schwingshackl, G. Aglietti et P. Cunningham, "Determination of honeycomb material properties: existing theories and an alternative dynamic approach," *Journal of Aerospace Engineering*, vol. 19, n°. 3, p. 177–183, 2006.

[239] E. J. Barbero, *Finite element analysis of composite materials*. CRC press, 2007.

[240] A. Catapano et M. Montemurro, "A multi-scale approach for the optimum design of sandwich plates with honeycomb core. part i: homogenisation of core properties," *Composite structures*, vol. 118, p. 664–676, 2014.

[241] W. Voigt, "Ueber die beziehung zwischen den beiden elasticitätsconstanten isotroper körper," *Annalen der physik*, vol. 274, n°. 12, p. 573–587, 1889.

[242] P. Turner et R. Thomason, *Correlation Between Strength Properties in Standard Test Specimens and Molded Phenolic Parts*. National Advisory Committee for Aeronautics, 1946, n°. 1005.

[243] V. Levin, V. Rumyantsev, I. Chubinskaya, N. Aleksandrov et I. Zhakov, "A linear electron accelerator for medical purposes," *Soviet Atomic Energy*, vol. 23, n°. 5, p. 1224–1226, 1967.

[244] B. W. Rosen et Z. Hashin, "Effective thermal expansion coefficients and specific heats of composite materials," *International Journal of Engineering Science*, vol. 8, n°. 2, p. 157–173, 1970.

[245] R. A. Schapery, "Thermal expansion coefficients of composite materials based on energy principles," *Journal of Composite materials*, vol. 2, n°. 3, p. 380–404, 1968.

[246] B. Budiansky, "Thermal and thermoelastic properties of isotropic composites," *Journal of composite Materials*, vol. 4, n°. 3, p. 286–295, 1970.

[247] N. Chamberlain, "Derivation of expansion coefficients for a fibre reinforced composite," *BAC Report SON (P)*, vol. 33, p. 23, 1968.

[248] C. Karch, "Micromechanical analysis of thermal expansion coefficients," *Modeling and Numerical Simulation of Material Science*, vol. 2014, 2014.

[249] M. Delucia, A. Catapano, M. Montemurro et J. Pailhes, "Determination of the effective thermoelastic properties of cork-based agglomerates," *Journal of Reinforced Plastics and Composites*, vol. 38, n°. 16, p. 760–776, 2019.

[250] Ž. Tuković, A. Ivanković et A. Karač, "Finite-volume stress analysis in multi-material linear elastic body," *International journal for numerical methods in engineering*, vol. 93, n°. 4, p. 400–419, 2013.

[251] D. Gisen, "Generation of a 3d mesh using snappyhexmesh featuring anisotropic refinement and near-wall layers," dans *ICHE 2014. Proceedings of the 11th International Conference on Hydroscience & Engineering*, 2014, p. 983–990.

[252] F. Howes et S. Whitaker, "The spatial averaging theorem revisited," *Chemical engineering science*, vol. 40, n°. 8, p. 1387–1392, 1985.

# Annexe A

# Derivation of the Porous Media Macroscopic Equations by the Volume Averaging Technique

## Nomenclature

*Latin Letters*

| | |
|---|---|
| $a_v$ | specific surface $m^2\ m^{-3}$ |
| $\underline{\underline{B}}$ | mapping tensor |
| $\boldsymbol{b}_{\sigma\sigma}, \boldsymbol{b}_{\beta\sigma}, \boldsymbol{b}_{\sigma\beta}, \boldsymbol{b}_{\beta\beta}$ | mapping vectors |
| $\underline{\underline{C}}$ | tensor defined in the development of the closure problem |
| $c_p$ | specific heat at constant pressure $[J\ kg^{-1}\ K^{-1}]$ |
| $\boldsymbol{c}_{\sigma\sigma}, \boldsymbol{c}_{\beta\sigma}, \boldsymbol{c}_{\sigma\beta}, \boldsymbol{c}_{\beta\beta}$ | transport vectors defined in the development of the closure problem |
| $\underline{\underline{G}}$ | function to deal with the the boundary condition |
| $\boldsymbol{g}$ | gravitational field $[m\ s^{-2}]$ |
| $h$ | heat transfer coefficient $[W\ m^{-2}\ K^{-1}]$ |
| $h_v$ | volumetric heat transfer coefficient $[W\ m^{-3}\ K^{-1}]$ |
| $\underline{\underline{K}}$ | permeability tensor $[m^2]$ |
| $\underline{\underline{k}}_{\sigma\sigma}, \underline{\underline{k}}_{\beta\sigma}, \underline{\underline{k}}_{\sigma\beta}, \underline{\underline{k}}_{\beta\beta}$ | thermal conductivity tensors |
| $k$ | thermal conductivity coefficient $[W\ m^{-1}\ K^{-1}]$ |
| $l, L$ | microscopic and macroscopic scales characteristic lengths $[m]$ |
| $\boldsymbol{n}$ | surface normal |
| $p$ | pressure $[Pa]$ |
| $r$ | representative element volume dimension $[m]$ |
| $S$ | interface area $[m^2]$ |
| $t$ | time $[s]$ |
| $\mathcal{T}$ | time scale $[s]$ |

## Nomenclature

| | |
|---|---|
| $T$ | temperature $[K]$ |
| $\boldsymbol{v}$ | convective velocity $[m\ s^{-1}]$ |
| $\boldsymbol{v}_{\sigma\sigma}, \boldsymbol{v}_{\beta\sigma}, \boldsymbol{v}_{\sigma\beta}, \boldsymbol{v}_{\beta\beta}$ | transport vectors |
| $V$ | averaging volume $[m^3]$ |
| $\boldsymbol{w}$ | interface velocity $[m\ s^{-1}]$ |

*Greek Letters*

| | |
|---|---|
| $\boldsymbol{\delta}$ | Dirac distribution function |
| $\epsilon$ | volume fraction |
| $\mu$ | dynamic viscosity $[Pa\ s]$ |
| $\xi$ | arbitrary function |
| $\rho$ | density $[kg\ m^{-3}]$ |
| $\psi$ | generic variable |
| $\Phi_\beta, \Phi_\sigma, \Omega_{\beta\sigma}$ | functions defined in the development of the closure problem |
| $\boldsymbol{\psi}$ | arbitrary function |

*Subscripts and Superscripts*

| | |
|---|---|
| 0 | change of variable |
| $\beta$ | fluid phase |
| $\sigma$ | solid phase |

*Notation*

| | |
|---|---|
| $\partial V$ | boundary of the domain |
| $\langle\rangle$ | intrinsic average |
| $\langle\rangle^\beta$ | phase average |
| $\sim$ | deviation term |

*Adimensional Groups*

| | |
|---|---|
| Kn | Knudsen number |
| Re | Reynolds number |

*Acronyms*

| | |
|---|---|
| REV | Representative Elementary Volume |

The purpose of this appendix is to derive the macroscopic equations for porous media using the volume averaging technique. A single-phase incompressible flow ($\beta$-phase) interacting with a rigid, non

reactive porous medium ($\sigma$-phase) is considered. This problem is represented in Fig. A.1.

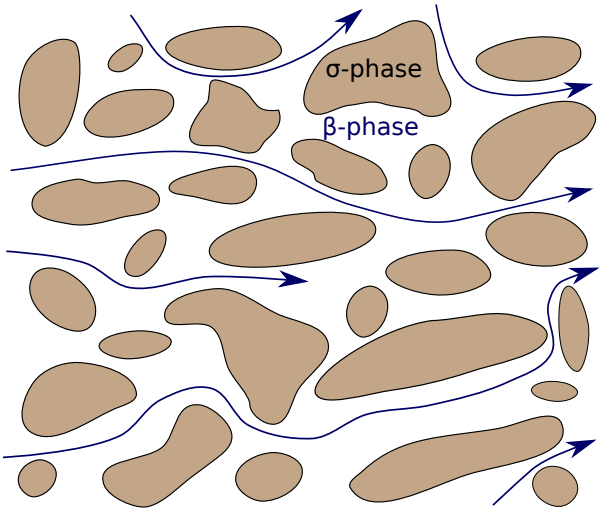


FIGURE A.1 – Averaging problem considered. A single-phase incompressible flow ($\beta$-phase) interacting with a rigid, non reactive porous medium ($\sigma$-phase) is considered. The volume averaging technique is applied.

The method of volume averaging is a technique used to derive continuum equations for multiphase systems. This means that equations valid within a particular phase can be spatially smoothed and lead to equations valid everywhere. In this way, the description of the problem moves from a pore-scale level, with all the complexity of geometry and boundary conditions, to a macro-scale level described by locally averaged equations. This concept is schematized in Fig. A.2. In the macroscopic description, the properties of a generic point are the averaged of the properties of a REV centered on it. The volume, to be representative, must be characterized by a characteristic length $r$ such that

$$l_\sigma, l_\beta \ll r \ll L \tag{A.1}$$

where $l_\beta$ and $l_\sigma$ are the characteristic lengths of the $\beta$ and $\sigma$ phases, and $L$ is the characteristic lenght of the macroscopic domain. This inequality is nothing more than a convenient restriction that is often satisfied by many systems of practical importance.

Some definitions and theorems need to be introduced. There are two types of volume averaging. The first is the **phase average**, defined as

$$\langle \psi_\beta \rangle = \frac{1}{V} \int_{V_\beta} \psi_\beta \, dV \tag{A.2}$$

where $\psi_\beta$ is a generic variable of the $\beta$ phase and $V_\beta$ represents the volume of the $\beta$-phase contained within the averaging volume $V$. In the case $\psi_\beta$ is a constant within the domain, the phase average $\langle \psi_\beta \rangle$ differs to $\psi_\beta$. For this reason, it is often more convenient to use the **intrinsic phase average**

$$\langle \psi_\beta \rangle^\beta = \frac{1}{V_\beta} \int_{V_\beta} \psi_\beta \, dV \tag{A.3}$$

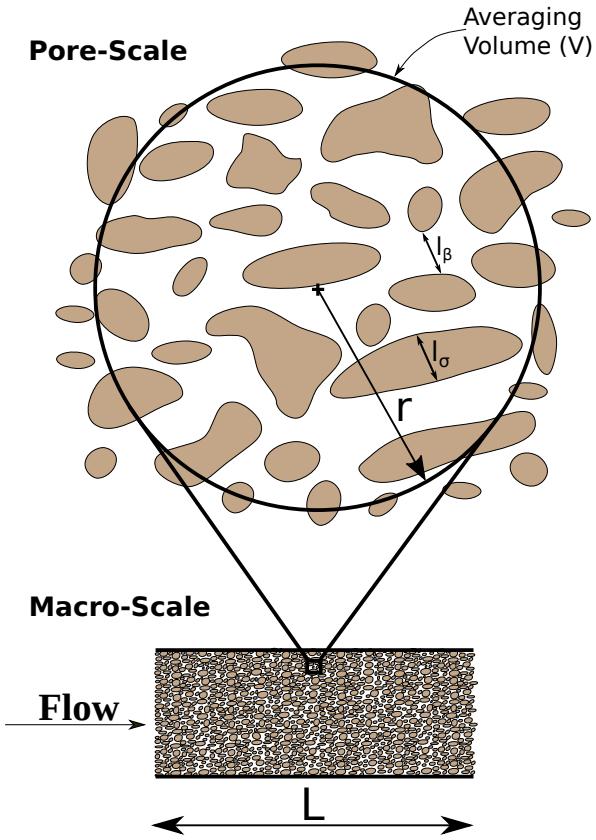


FIGURE A.2 – Pore and macro scales of the problem. At the macro-scale, the properties of a generic point are the averaged of the properties of a REV centered on it.

which is more representative of the conditions in the $\beta$-phase. The two averages are related by the following relationship

$$\langle \psi_\beta \rangle = \epsilon_\beta \langle \psi_\beta \rangle^\beta \tag{A.4}$$

where $\epsilon_\beta$ is the volume fraction of the related phase: $\epsilon_\beta = V_\beta / V$. In the case of two phases, solid and flow, the volume fraction of the flow phase is defined as the porosity of the medium.

The development of the volume averaging method is based on three averaging theorems. The first one is an application of the generic Reynolds transport theorem [211] and it is used to move the temporal derivation out of the spatial averaging. By considering a generic field $\psi$

$$\left\langle \partial_t \psi_\beta \right\rangle = \partial_t \langle \psi_\beta \rangle - \frac{1}{V} \int_{S_{\beta\sigma}} \psi_\beta \, \boldsymbol{w}_{\beta\sigma} \cdot \boldsymbol{n}_{\beta\sigma} dS \tag{A.5}$$

where $\boldsymbol{w_{\beta\sigma}}$ denotes the velocity of the interface. Since the solid phase is assumed to be rigid, $\boldsymbol{w_{\beta\sigma}} = 0$, and the theorem can be rewritten as

$$\left\langle \partial_t \psi_\beta \right\rangle = \partial_t \langle \psi_\beta \rangle \tag{A.6}$$

The second theorem moves the gradient operator out of the spatial averaging [252]

$$\langle \partial_{\boldsymbol{x}} \psi_\beta \rangle = \partial_{\boldsymbol{x}} \langle \psi_\beta \rangle + \frac{1}{V} \int_{S_{\beta\sigma}} \psi_\beta \, \boldsymbol{n}_{\beta\sigma} dS \tag{A.7}$$

The third theorem moves the divergence operator out of the spatial averaging [252]

$$\langle \partial_{\boldsymbol{x}} \cdot \boldsymbol{\psi_\beta} \rangle = \partial_{\boldsymbol{x}} \cdot \langle \boldsymbol{\psi_\beta} \rangle + \frac{1}{V} \int_{S_{\beta\sigma}} \boldsymbol{n}_{\beta\sigma} \cdot \boldsymbol{\psi_\beta} \, dS \tag{A.8}$$

The last theorem to mention is the Gray's decomposition [159], which allows a generic variable to be decomposed as the sum of its mean plus a deviation contribution

$$\psi_\beta = \langle \psi_\beta \rangle^\beta + \tilde{\psi_\beta} \tag{A.9}$$

In the problem of interest, an incompressible, continuum ($Kn \ll 1$) and creeping ($Re \ll 1$) flow is considered interacting with a rigid and non-reactive solid. At the pore-scale, within volume V, the following system solves the problem

$$\begin{cases}
\partial_{\boldsymbol{x}} \cdot \boldsymbol{v}_\beta = 0 & in\ V_\beta \\
\rho_\beta \partial_t \boldsymbol{v}_\beta - \mu_\beta \partial^2_{\boldsymbol{x}} \boldsymbol{v}_\beta = -\partial_{\boldsymbol{x}} p_\beta + \rho_\beta \boldsymbol{g} & in\ V_\beta \\
\rho_\beta \, c_{p,\beta} \partial_t T_\beta + \rho_\beta \, c_{p,\beta} \boldsymbol{v}_\beta \cdot \partial_{\boldsymbol{x}} T_\beta = \partial_{\boldsymbol{x}} \cdot (k_\beta \partial_{\boldsymbol{x}} T_\beta) & in\ V_\beta \\
\rho_\sigma \, c_{p,\sigma} \partial_t T_\sigma = \partial_{\boldsymbol{x}} \cdot (k_\sigma \partial_{\boldsymbol{x}} T_\sigma) & in\ V_\beta \\
BC1: \ \boldsymbol{v}_\beta = 0 & at\ S_{\beta\sigma} \\
BC2: \ \boldsymbol{v}_\beta = \boldsymbol{v}_1(\boldsymbol{x}, t) & at\ \partial V_\beta \\
BC3: \ T_\beta = T_\sigma & at\ S_{\beta\sigma} \\
BC4: \ \boldsymbol{n}_{\beta\sigma} \cdot k_\beta \partial_{\boldsymbol{x}} T_\beta = \boldsymbol{n}_{\beta\sigma} \cdot k_\sigma \partial_{\boldsymbol{x}} T_\sigma & at\ S_{\beta\sigma} \\
BC5: \ T_\beta = T_{\beta,1}(\boldsymbol{x}, t) & at\ \partial V_\beta \\
BC6: \ T_\sigma = T_{\sigma,1}(\boldsymbol{x}, t) & at\ \partial V_\sigma \\
iC1: \ \boldsymbol{v}(t=0) = \boldsymbol{v}_{t=0}(\boldsymbol{x}) & in\ V_\beta \\
iC2: \ T_\beta(t=0) = T_{\beta,0} & in\ V_\beta \\
iC3: \ T_\sigma(t=0) = T_{\sigma,0} & in\ V_\sigma
\end{cases} \tag{A.10}$$

## A.1 Continuity Averaged Equation

From Eq. (A.10), the pore-scale continuity equation and the respective boundary condition are extracted

$$\begin{cases} \partial_{\boldsymbol{x}} \cdot \boldsymbol{v}_\beta = 0 & \\ BC1: \quad \boldsymbol{v}_\beta = 0 & \text{at } S_{\beta\sigma} \end{cases} \tag{A.11}$$

The first step of the technique involves the application of the averaging operator

$$\langle \partial_{\boldsymbol{x}} \cdot \boldsymbol{v}_\beta \rangle = 0 \tag{A.12}$$

Then, the terms in the equation are developed. In this case, the averaging theorem for the divergence operator Eq. (A.8) is applied

$$\partial_{\boldsymbol{x}} \cdot \langle \boldsymbol{v}_\beta \rangle + \frac{1}{V} \cancel{\int_{S_{\beta\sigma}} \rho_\beta \boldsymbol{v}_\beta \cdot \boldsymbol{n}_{\beta\sigma} dS} = 0 \tag{A.13}$$

where the term cancels due to BC1 of Eq. (A.11). The averaged continuity equation results as follows

$$\partial_{\boldsymbol{x}} \cdot \langle \boldsymbol{v}_\beta \rangle = 0 \tag{A.14}$$

## A.2 Momentum Equation

From Eq. (A.10), the pore-scale momentum equation and the respective boundary conditions are extracted

$$\begin{cases} \rho_\beta \partial_t \boldsymbol{v}_\beta - \mu_\beta \partial_{\boldsymbol{x}}^2 \boldsymbol{v}_\beta = -\partial_{\boldsymbol{x}} p_\beta + \rho_\beta \boldsymbol{g} & \text{in } V_\beta \\ BC1: \quad \boldsymbol{v}_\beta = 0 & \text{at } S_{\beta\sigma} \\ BC2: \quad \boldsymbol{v}_\beta = \boldsymbol{v}_1(\boldsymbol{x}, t) & \text{at } \partial V_\beta \\ iC1: \quad \boldsymbol{v}_\beta(t=0) = \boldsymbol{v}_{t=0}(\boldsymbol{x}) & \text{in } V_\beta \end{cases} \tag{A.15}$$

The equation is averaged

$$\Big\langle \rho_\beta \partial_t \boldsymbol{v}_\beta - \mu_\beta \partial_{\boldsymbol{x}}^2 \boldsymbol{v}_\beta \Big\rangle = \langle -\partial_{\boldsymbol{x}} p_\beta + \rho_\beta \boldsymbol{g} \rangle \tag{A.16}$$

Due to the linearity property of the integral operator, the average of the sums is the sum of the averages

$$\Big\langle \rho_\beta \partial_t \boldsymbol{v}_\beta \Big\rangle - \langle \mu_\beta \partial_{\boldsymbol{x}}^2 \boldsymbol{v}_\beta \rangle = -\langle \partial_{\boldsymbol{x}} p_\beta \rangle + \langle \rho_\beta \boldsymbol{g} \rangle \tag{A.17}$$

Each term must be developed. The density inside the REV is assumed homogeneous. The averaging theorem of the time derivative, Eq. (A.6), is applied to the transient term

$$\Big\langle \rho_\beta \partial_t \boldsymbol{v}_\beta \Big\rangle = \rho_\beta \Big\langle \partial_t \boldsymbol{v}_\beta \Big\rangle = \rho_\beta \partial_t \langle \boldsymbol{v}_\beta \rangle \tag{A.18}$$

The averaged theorems Eq. (A.7) and Eq. (A.8) are applied to the second term of Eq. (A.17),

$$\langle \mu_\beta \partial_{\boldsymbol{x}}^2 \boldsymbol{v}_\beta \rangle = \mu_\beta \Big[ \partial_{\boldsymbol{x}} \cdot \langle \partial_{\boldsymbol{x}} \boldsymbol{v}_\beta \rangle + \frac{1}{V} \int_{S_{\beta\sigma}} \boldsymbol{n}_{\beta\sigma} \cdot \partial_{\boldsymbol{x}} \boldsymbol{v}_\beta \, dS \Big] = \mu_\beta \Big[ \partial_{\boldsymbol{x}}^2 \langle \boldsymbol{v}_\beta \rangle + \\ + \frac{1}{V} \int_{S_{\beta\sigma}} \boldsymbol{n}_{\beta\sigma} \cdot \partial_{\boldsymbol{x}} \boldsymbol{v}_\beta \, dS + \cancel{\frac{1}{V} \int_{S_{\beta\sigma}} \boldsymbol{v}_\beta \boldsymbol{n}_{\beta\sigma} dS} \Big] \tag{A.19}$$

where the viscosity is assumed to be uniform inside the REV and BC1 of Eq. (A.15) has been considered. Gravity is assumed to be an uniform vector. Thus, the body force term in Eq. (A.17) simplifies to

$$\langle \rho_\beta \boldsymbol{g} \rangle = \rho_\beta \boldsymbol{g} \langle 1 \rangle = \rho_\beta \boldsymbol{g} \frac{1}{V} \int_{V_\beta} 1 dV = \rho_\beta \boldsymbol{g} \frac{V_\beta}{V} = \rho_\beta \epsilon_\beta \boldsymbol{g} \tag{A.20}$$

The averaging theorem of the gradient, Eq. (A.7), is applied to the pressure term

$$\langle \partial_{\boldsymbol{x}} p_\beta \rangle = \partial_{\boldsymbol{x}} \langle p_\beta \rangle + \frac{1}{V} \int_{S_{\beta\sigma}} p_\beta \boldsymbol{n}_{\beta\sigma} dS = \epsilon_\beta \partial_{\boldsymbol{x}} \langle p_\beta \rangle^\beta + \langle p_\beta \rangle^\beta \partial_{\boldsymbol{x}} \epsilon_\beta + \frac{1}{V} \int_{S_{\beta\sigma}} p_\beta \boldsymbol{n}_{\beta\sigma} dS \tag{A.21}$$

All the terms, once developed, are substituted back in the averaged momentum equation, Eq. (A.17)

$$\rho_\beta \partial_t \langle \boldsymbol{v}_\beta \rangle - \mu_\beta \Big[ \partial_{\boldsymbol{x}}^2 \langle \boldsymbol{v}_\beta \rangle + \frac{1}{V} \int_{S_{\beta\sigma}} \boldsymbol{n}_{\beta\sigma} \cdot \partial_{\boldsymbol{x}} \tilde{\boldsymbol{v}}_\beta dS \Big] = -\epsilon_\beta \partial_{\boldsymbol{x}} \langle p_\beta \rangle^\beta - \langle p_\beta \rangle^\beta \partial_{\boldsymbol{x}} \epsilon_\beta + \\ - \frac{1}{V} \int_{S_{\beta\sigma}} p_\beta \boldsymbol{n}_{\beta\sigma} dS + \epsilon_\beta \rho_\beta \boldsymbol{g} \tag{A.22}$$

The Gray's decomposition, Eq. (A.9), of the pressure field reads

$$p_\beta = \langle p_\beta \rangle^\beta + \tilde{p}_\beta \tag{A.23}$$

This decomposition is applied to the integral term on the second-hand side of Eq. (A.22)

$$\frac{1}{V} \int_{S_{\beta\sigma}} p_\beta \boldsymbol{n}_{\beta\sigma} dS = \frac{1}{V} \int_{S_{\beta\sigma}} \langle p_\beta \rangle^\beta \boldsymbol{n}_{\beta\sigma} dS + \frac{1}{V} \int_{S_{\beta\sigma}} \tilde{p}_\beta \boldsymbol{n}_{\beta\sigma} dS \tag{A.24}$$

The average of the pressure, $\langle p_\beta \rangle^\beta$, is a constant quantity with respect to the integration over the interface are $S_{\beta\sigma}$. It can be then moved out from the integral under the assumption of scales separation (Eq. (A.1)) inside the domain (see Section A.4)

$$\frac{1}{V} \int_{S_{\beta\sigma}} \langle p_\beta \rangle^\beta \boldsymbol{n}_{\beta\sigma} dS = \langle p_\beta \rangle^\beta \frac{1}{V} \int_{S_{\beta\sigma}} \boldsymbol{n}_{\beta\sigma} dS \tag{A.25}$$

The developed term is substituted back into Eq. (A.24)

$$\frac{1}{V} \int_{S_{\beta\sigma}} p_\beta \boldsymbol{n}_{\beta\sigma} dS = \langle p_\beta \rangle^\beta \frac{1}{V} \int_{S_{\beta\sigma}} \boldsymbol{n}_{\beta\sigma} dS + \frac{1}{V} \int_{S_{\beta\sigma}} \tilde{p}_\beta \boldsymbol{n}_{\beta\sigma} \tag{A.26}$$

An expression is required to proceed with the development of Eq. (A.26). When $\psi = 1$, the mediation theorem related to the gradient, Eq. (A.7), writes

$$\cancel{\langle \partial_{\boldsymbol{x}} 1 \rangle} = \partial_{\boldsymbol{x}} \langle 1 \rangle + \frac{1}{V} \int_{S_{\beta\sigma}} 1 \, \boldsymbol{n}_{\beta\sigma} dS \tag{A.27}$$

"1" is a constant and it is moved out from the averaging term

$$0 = \partial_{\boldsymbol{x}}\epsilon_\beta + \frac{1}{V}\int_{S_{\beta\sigma}} \boldsymbol{n}_{\beta\sigma} dS \tag{A.28}$$

This expression is used in the development of Eq. (A.26)

$$\frac{1}{V}\int_{S_{\beta\sigma}} p_\beta \boldsymbol{n}_{\beta\sigma} dS = -\langle p_\beta\rangle^\beta \partial_{\boldsymbol{x}}\epsilon_\beta + \frac{1}{V}\int_{S_{\beta\sigma}} \tilde{p}_\beta \boldsymbol{n}_{\beta\sigma} dS \tag{A.29}$$

This term is substituted back in the averaged momentum equation Eq. (A.22)

$$\rho_\beta \partial_t \langle \boldsymbol{v}_\beta\rangle - \mu_\beta\Big[\partial^2_{\boldsymbol{x}}\langle \boldsymbol{v}_\beta\rangle + \frac{1}{V}\int_{S_{\beta\sigma}} \boldsymbol{n}_{\beta\sigma}\cdot\partial_{\boldsymbol{x}}\tilde{\boldsymbol{v}}_\beta dS\Big] = -\epsilon_\beta\partial_{\boldsymbol{x}}\langle p_\beta\rangle^\beta - \frac{1}{V}\int_{S_{\beta\sigma}} \tilde{p}_\beta \boldsymbol{n}_{\beta\sigma} dS + \epsilon_\beta\rho_\beta \boldsymbol{g} \tag{A.30}$$

The Grey's decomposition, Eq. (A.9), of the velocity field reads

$$\boldsymbol{v}_\beta = \langle \boldsymbol{v}_\beta\rangle^\beta + \tilde{\boldsymbol{v}}_\beta \tag{A.31}$$

This decomposition is applied to the velocity field inside the integral term on the first-hand side of Eq. (A.30)

$$\frac{1}{V}\int_{S_{\beta\sigma}} \partial_{\boldsymbol{x}}\boldsymbol{n}_{\beta\sigma}\cdot\boldsymbol{v}_\beta dS = -\partial_{\boldsymbol{x}}\epsilon_\beta\cdot\partial_{\boldsymbol{x}}\langle \boldsymbol{v}_\beta\rangle^\beta + \frac{1}{V}\int_{S_{\beta\sigma}} \boldsymbol{n}_{\beta\sigma}\cdot\partial_{\boldsymbol{x}}\tilde{\boldsymbol{v}}_\beta dS \tag{A.32}$$

At the pore-scale level, the $\partial_{\boldsymbol{x}}\langle \boldsymbol{v}_\beta\rangle^\beta$ term is constant and it moves out from the integral. The integral term becomes

$$\frac{1}{V}\int_{S_{\beta\sigma}} \partial_{\boldsymbol{x}}\boldsymbol{n}_{\beta\sigma}\cdot\boldsymbol{v}_\beta dS = \frac{1}{\epsilon_\beta}\langle \boldsymbol{v}_\beta\rangle^\beta\partial^2_{\boldsymbol{x}}\epsilon_\beta - \frac{1}{\epsilon_\beta}\partial_{\boldsymbol{x}}\epsilon_\beta\cdot\partial_{\boldsymbol{x}}\langle \boldsymbol{v}_\beta\rangle^\beta \tag{A.33}$$

The term is substituted back into the averaged momentum equation Eq. (A.30)

$$\rho_\beta\partial_t\langle \boldsymbol{v}_\beta\rangle^\beta - \mu_\beta\Big[\partial^2_{\boldsymbol{x}}\langle \boldsymbol{v}_\beta\rangle^\beta + \frac{1}{\epsilon_\beta}\langle \boldsymbol{v}_\beta\rangle^\beta\partial^2_{\boldsymbol{x}}\epsilon_\beta - \frac{1}{\epsilon_\beta}\partial_{\boldsymbol{x}}\epsilon_\beta\cdot\partial_{\boldsymbol{x}}\langle \boldsymbol{v}_\beta\rangle^\beta\Big] = -\partial_{\boldsymbol{x}}\langle p_\beta\rangle^\beta - \frac{1}{V_\beta}\int_{S_{\beta\sigma}} \tilde{p}_\beta\boldsymbol{n}_{\beta\sigma}dS +$$

$$+\rho_\beta\boldsymbol{g} + \frac{\mu_\beta}{V_\beta}\int_{S_{\beta\sigma}} \boldsymbol{n}_{\beta\sigma}\cdot\partial_{\boldsymbol{x}}\tilde{\boldsymbol{v}}_\beta dS \tag{A.34}$$

The terms inside the square brackets are negligible under the assumption of scales separation (see Section A.4). The averaged momentum equation simplifies to

$$\rho_\beta\partial_t\langle \boldsymbol{v}_\beta\rangle^\beta = -\partial_{\boldsymbol{x}}\langle p_\beta\rangle^\beta + \rho_\beta\boldsymbol{g} - \frac{1}{V_\beta}\int_{S_{\beta\sigma}} \tilde{p}_\beta\boldsymbol{n}_{\beta\sigma}dS + \frac{\mu_\beta}{V_\beta}\int_{S_{\beta\sigma}} \boldsymbol{n}_{\beta\sigma}\cdot\partial_{\boldsymbol{x}}\tilde{\boldsymbol{v}}_\beta dS \tag{A.35}$$

### A.2.1 Closure Problem

To close the problem, the deviation terms $\tilde{p}_\beta$ and $\tilde{\boldsymbol{v}}_\beta$ must be determined in terms of the dependent variables $\langle p_\beta\rangle^\beta$ and $\langle \boldsymbol{v}_\beta\rangle^\beta$, that is, some governing differential equations must be derived for both $\tilde{p}_\beta$ and $\tilde{\boldsymbol{v}}_\beta$.

The length scale separation assumption (A.1) implies that the time scale associated with the pore-scale equations ($\mathcal{T} = (l_\beta, l_\sigma)/|\boldsymbol{v}|$) is much smaller than the time scale associated with the averaged

equations ($\langle \mathcal{T} \rangle = L/|\langle \boldsymbol{v} \rangle|$). A quasi-stationary representation of the deviation fields as a function of the mean fields is introduced.
The Gray's decomposition, Eq. (A.9), is applied to the velocity and pressure fields in the pore-scale governing equations, Eq (A.15)

$$\begin{cases} \partial_{\boldsymbol{x}} \cdot \tilde{\boldsymbol{v}}_\beta = -\partial_{\boldsymbol{x}} \cdot \langle \boldsymbol{v}_\beta \rangle^\beta \\ -\partial_{\boldsymbol{x}} \tilde{p}_\beta + \mu_\beta \partial^2_{\boldsymbol{x}} \tilde{\boldsymbol{v}}_\beta = \partial_{\boldsymbol{x}} \langle p_\beta \rangle^\beta - \rho_\beta \boldsymbol{g} - \mu_\beta \partial^2_{\boldsymbol{x}} \langle \boldsymbol{v}_\beta \rangle^\beta \\ BC1 \;\; \tilde{\boldsymbol{v}}_\beta = -\langle \boldsymbol{v}_\beta \rangle^\beta \qquad\qquad at \; S_{\beta\sigma} \\ BC2 \;\; \tilde{\boldsymbol{v}}_\beta = \boldsymbol{v}_1(\boldsymbol{x}, t) - \langle \boldsymbol{v}_\beta \rangle^\beta \qquad at \; \partial V_\beta \end{cases} \tag{A.36}$$

All transient terms are neglected since the aim is to express the deviation terms (faster dynamic) as a function of the averaged ones (slower dynamic). This system of equations represents a boundary value problem for $\tilde{p}_\beta$ and $\tilde{\boldsymbol{v}}_\beta$ where the averaged quantities $\langle p_\beta \rangle^\beta$ and $\langle \boldsymbol{v}_\beta \rangle^\beta$ are the source terms.
This system is further developed. The source term in the continuity equation for $\tilde{\boldsymbol{v}}_\beta$ (see Section A.4) is neglected. Thus

$$\partial_{\boldsymbol{x}} \cdot \tilde{\boldsymbol{v}}_\beta = 0 \tag{A.37}$$

The momentum equation of the deviation system is averaged

$$\frac{1}{V} \int_{V_\beta} [ - \partial_{\boldsymbol{x}} \tilde{p}_\beta + \mu_\beta \partial^2_{\boldsymbol{x}} \tilde{\boldsymbol{v}}_\beta ] dV = \frac{1}{V} \int_{V_\beta} [\partial_{\boldsymbol{x}} \langle p_\beta \rangle^\beta - \rho_\beta \boldsymbol{g} - \mu_\beta \partial^2_{\boldsymbol{x}} \langle \boldsymbol{v}_\beta \rangle^\beta ] \tag{A.38}$$

By multiplying all the terms for the volume $V$ and by moving out of the integral the terms on the second-hand side, the momentum equations becomes

$$\frac{1}{V_\beta} \int_{V_\beta} [ - \partial_{\boldsymbol{x}} \tilde{p}_\beta + \mu_\beta \partial^2_{\boldsymbol{x}} \tilde{\boldsymbol{v}}_\beta ] dV = \partial_{\boldsymbol{x}} \langle p_\beta \rangle^\beta - \rho_\beta \boldsymbol{g} - \mu_\beta \partial^2_{\boldsymbol{x}} \langle \boldsymbol{v}_\beta \rangle^\beta \tag{A.39}$$

By comparing this equation to the momentum equation defined in the system of Eqs. (A.36)

$$-\partial_{\boldsymbol{x}} \tilde{p}_\beta + \mu_\beta \partial^2_{\boldsymbol{x}} \tilde{\boldsymbol{v}}_\beta = \frac{1}{V_\beta} \int_{V_\beta} [ - \partial_{\boldsymbol{x}} \tilde{p}_\beta + \mu_\beta \partial^2_{\boldsymbol{x}} \tilde{\boldsymbol{v}}_\beta ] dV \tag{A.40}$$

The system of Eqs. (A.36) becomes

$$\begin{cases} \partial_{\boldsymbol{x}} \cdot \tilde{\boldsymbol{v}}_\beta = 0 \\ -\partial_{\boldsymbol{x}} \tilde{p}_\beta + \mu_\beta \partial^2_{\boldsymbol{x}} \tilde{\boldsymbol{v}}_\beta = \frac{1}{V_\beta} \int_{V_\beta} \left( - \partial_{\boldsymbol{x}} \tilde{p}_\beta + \mu_\beta \partial^2_{\boldsymbol{x}} \tilde{\boldsymbol{v}}_\beta \right) dV \\ BC1 \;\; \tilde{\boldsymbol{v}}_\beta = -\langle \boldsymbol{v}_\beta \rangle^\beta \qquad\qquad at \; S_{\beta\sigma} \\ BC2 \;\; \tilde{\boldsymbol{v}}_\beta = \underline{\underline{G}} \cdot \langle \boldsymbol{v}_\beta \rangle^\beta \qquad\qquad at \; \partial V_\beta \\ \langle \tilde{\boldsymbol{v}}_\beta \rangle = \langle \tilde{p}_\beta \rangle = 0 \end{cases} \tag{A.41}$$

Where BC2 is rewritten by introducing the function $\underline{\underline{G}}$ and two conditions on the deviation terms are introduced. They derive from the average of the Gray's decomposition: $\langle \boldsymbol{v} \rangle = \langle \langle \boldsymbol{v} \rangle \rangle + \langle \tilde{\boldsymbol{v}} \rangle \Rightarrow \langle \tilde{\boldsymbol{v}} \rangle = 0$ and $\langle p \rangle = \langle \langle p \rangle \rangle + \langle \tilde{p} \rangle \Rightarrow \langle \tilde{p} \rangle = 0$. In this way, BC2 with the two conditions on the deviation terms provide a formulation equivalent to that of Eq. (A.36), as the function $\underline{\underline{G}}$ can maps the values of $\langle \boldsymbol{v}_\beta \rangle^\beta$ such that $\underline{\underline{G}} \cdot \langle \boldsymbol{v}_{\boldsymbol{\beta}} \rangle^\beta = \boldsymbol{v}_1(\boldsymbol{x}, \boldsymbol{t}) - \langle \boldsymbol{v}_\beta \rangle^\beta$.
The system of equations is linear, so its solutions (the perturbation fields) are linear functions of the independent variables (the averaged fields). Furthermore, the independent variables influence the system through the boundary conditions. In particular, only the averaged velocity $\langle \boldsymbol{v}_\beta \rangle^\beta$ affects the problem. Based on these observations, the following generic solution for the system is proposed

$$\tilde{\boldsymbol{v}}_\beta = \underline{\underline{B}} \cdot \langle \boldsymbol{v}_\beta \rangle^\beta + \boldsymbol{\psi} \tag{A.42}$$

$$\tilde{p}_\beta = \mu_\beta \boldsymbol{b} \cdot \langle \boldsymbol{v}_\beta \rangle^\beta + \mu_\beta \xi \tag{A.43}$$

where $\boldsymbol{\psi}$ and $\xi$ are two completely arbitrary functions and the viscosity term is added to simplify the next steps. Thanks to the arbitrary functions, the mapping functions $\underline{\underline{B}}$ and $\boldsymbol{b}$ can be specified in any way. The classic way is by defining the same boundary value problem as for the deviation terms Eq. (A.41): $\boldsymbol{b}$ takes the place of $\tilde{p}_\beta$ and $\underline{\underline{B}}$ the place of $\tilde{\boldsymbol{v}}_\beta$

$$\begin{cases} \partial_{\boldsymbol{x}} \cdot \underline{\underline{B}} = 0 \\ -\partial_{\boldsymbol{x}} \boldsymbol{b} + \partial^2_{\boldsymbol{x}} \underline{\underline{B}} = \dfrac{1}{V_\beta} \int_{V_\beta} [ - \partial_{\boldsymbol{x}} \boldsymbol{b} + \partial^2_{\boldsymbol{x}} \underline{\underline{B}}] dV \\ BC1 \;\; \underline{\underline{B}} = -\underline{\underline{I}} \qquad\qquad at \; S_{\beta\sigma} \\ BC2 \;\; \underline{\underline{B}} = \underline{\underline{G}} \qquad\qquad at \; \partial V_\beta \\ \langle \underline{\underline{B}} \rangle^\beta = \langle \boldsymbol{b} \rangle^\beta = 0 \end{cases} \tag{A.44}$$

To close the problem, the functions $\boldsymbol{\psi}$ and $\xi$ need to be defined. Their boundary value problem is obtained from the boundary value problem for the deviation terms Eq. (A.41) by considering Eqs. (A.42) and (A.43). The continuity equation reads

$$\partial_{\boldsymbol{x}} \cdot \tilde{\boldsymbol{v}}_\beta = \partial_{\boldsymbol{x}} \cdot (\underline{\underline{B}} \cdot \langle \boldsymbol{v}_\beta \rangle^\beta + \boldsymbol{\psi}) = \partial_{\boldsymbol{x}} \cdot (\underline{\underline{B}} \cdot \langle \boldsymbol{v}_\beta \rangle^\beta) + \partial_{\boldsymbol{x}} \cdot \boldsymbol{\psi} = 0 \tag{A.45}$$

The following vectorial property can be used

$$\partial_{\boldsymbol{x}} \cdot (\underline{\underline{B}} \cdot \langle \boldsymbol{v}_\beta \rangle^\beta) = \cancel{\langle \boldsymbol{v}_\beta \rangle^\beta \cdot (\partial_{\boldsymbol{x}} \cdot \underline{\underline{B}})} + \underline{\underline{B}}^T \cdot \partial_{\boldsymbol{x}} \langle \boldsymbol{v}_\beta \rangle^\beta \tag{A.46}$$

where the term on the second-hand side neglects due to the choice of the closure problem of $\underline{\underline{B}}$, Eq. (A.44). Thus, the continuity equation (Eq. (A.45)) becomes

$$\partial_{\boldsymbol{x}} \cdot \boldsymbol{\psi} = -\underline{\underline{B}}^T \cdot \partial_{\boldsymbol{x}} \langle \boldsymbol{v}_\beta \rangle^\beta \tag{A.47}$$

The momentum equation reads

$$-\partial_{\boldsymbol{x}}(\mu_\beta \boldsymbol{b} \cdot \langle \boldsymbol{v}_\beta \rangle^\beta) - \partial_{\boldsymbol{x}}(\mu_\beta \xi) + \mu_\beta \partial^2_{\boldsymbol{x}} (\underline{\underline{B}} \cdot \langle \boldsymbol{v}_\beta \rangle^\beta) + \mu_\beta \partial^2_{\boldsymbol{x}} \boldsymbol{\psi} = \frac{1}{V_\beta} \int_{V_\beta} [ - \partial_{\boldsymbol{x}}(\mu_\beta \boldsymbol{b} \cdot \langle \boldsymbol{v}_\beta \rangle^\beta) +$$

$$-\partial_{\boldsymbol{x}}(\mu_\beta \xi) + \mu_\beta \partial^2_{\boldsymbol{x}}(\underline{\underline{B}} \cdot \langle \boldsymbol{v}_\beta \rangle^\beta) + \mu_\beta \partial^2_{\boldsymbol{x}} \boldsymbol{\psi}] dV \tag{A.48}$$

Two vectorial identities are needed

$$\partial_{\boldsymbol{x}}(\boldsymbol{b} \cdot \langle \boldsymbol{v}_\beta \rangle^\beta) = \partial_{\boldsymbol{x}} \boldsymbol{b} \cdot \langle \boldsymbol{v}_\beta \rangle^\beta + \partial_{\boldsymbol{x}} \langle \boldsymbol{v}_\beta \rangle^\beta \cdot \boldsymbol{b} \tag{A.49}$$

$$\partial^2_{\boldsymbol{x}}(\underline{\underline{B}} \cdot \langle \boldsymbol{v}_\beta \rangle^\beta) = \underline{\underline{B}} \cdot \partial^2_{\boldsymbol{x}} \langle \boldsymbol{v}_\beta \rangle^\beta + 2\partial_{\boldsymbol{x}} \underline{\underline{B}}^T (\partial_{\boldsymbol{x}} \langle \boldsymbol{v}_\beta \rangle^\beta)^T + \langle \boldsymbol{v}_\beta \rangle^\beta \cdot \partial^2_{\boldsymbol{x}} \underline{\underline{B}} \tag{A.50}$$

by dividing everything for the viscosity coefficient, $\mu$, the momentum equation (Eq. (A.48)) develops as

$$-\partial_{\boldsymbol{x}} \boldsymbol{b} \cdot \langle \boldsymbol{v}_\beta \rangle^\beta - \partial_{\boldsymbol{x}} \langle \boldsymbol{v}_\beta \rangle^\beta \cdot \boldsymbol{b} - \partial_{\boldsymbol{x}} \xi + \underline{\underline{B}} \cdot \partial^2_{\boldsymbol{x}} \langle \boldsymbol{v}_\beta \rangle^\beta + 2\partial_{\boldsymbol{x}} \underline{\underline{B}}^T (\partial_{\boldsymbol{x}} \langle \boldsymbol{v}_\beta \rangle^\beta)^T + \langle \boldsymbol{v}_\beta \rangle^\beta \cdot \partial^2_{\boldsymbol{x}} \underline{\underline{B}} + \partial^2_{\boldsymbol{x}} \boldsymbol{\psi} =$$

$$= \frac{1}{V_\beta} \int_{V_\beta} \left[ -\partial_{\boldsymbol{x}} \boldsymbol{b} \cdot \langle \boldsymbol{v}_\beta \rangle^\beta - \partial_{\boldsymbol{x}} \langle \boldsymbol{v}_\beta \rangle^\beta \cdot \boldsymbol{b} - \partial_{\boldsymbol{x}} \xi + \underline{\underline{B}} \cdot \partial^2_{\boldsymbol{x}} \langle \boldsymbol{v}_\beta \rangle^\beta + 2\partial_{\boldsymbol{x}} \underline{\underline{B}}^T (\partial_{\boldsymbol{x}} \langle \boldsymbol{v}_\beta \rangle^\beta)^T + \langle \boldsymbol{v}_\beta \rangle^\beta \cdot \partial^2_{\boldsymbol{x}} \underline{\underline{B}} + \partial^2_{\boldsymbol{x}} \boldsymbol{\psi} \right] \tag{A.51}$$

This equation can be rearranged as

$$\partial^2_{\boldsymbol{x}} \boldsymbol{\psi} - \partial_{\boldsymbol{x}} \xi = \frac{1}{V_\beta} \int_{V_\beta} \left[ \partial^2_{\boldsymbol{x}} \boldsymbol{\psi} - \partial_{\boldsymbol{x}} \xi \right] + \partial_{\boldsymbol{x}} \langle \boldsymbol{v}_\beta \rangle^\beta \cdot \boldsymbol{b} + (\partial_{\boldsymbol{x}} \boldsymbol{b} - \partial^2_{\boldsymbol{x}} \underline{\underline{B}}) \cdot \langle \boldsymbol{v}_\beta \rangle^\beta - 2\partial_{\boldsymbol{x}} \underline{\underline{B}}^T (\partial_{\boldsymbol{x}} \langle \boldsymbol{v}_\beta \rangle^\beta)^T +$$

$$- \underline{\underline{B}} \cdot \partial^2_{\boldsymbol{x}} \langle \boldsymbol{v}_\beta \rangle^\beta - \frac{1}{V_\beta} \int_{V_\beta} \left[ (\partial_{\boldsymbol{x}} \boldsymbol{b} - \partial^2_{\boldsymbol{x}} \underline{\underline{B}}) \cdot \langle \boldsymbol{v}_\beta \rangle^\beta \right] + \frac{1}{V_\beta} \int_{V_\beta} \left[ 2\partial_{\boldsymbol{x}} \underline{\underline{B}}^T (\partial_{\boldsymbol{x}} \langle \boldsymbol{v}_\beta \rangle^\beta)^T - \partial_{\boldsymbol{x}} \langle \boldsymbol{v}_\beta \rangle^\beta \cdot \boldsymbol{b} + \underline{\underline{B}} \cdot \partial^2_{\boldsymbol{x}} \langle \boldsymbol{v}_\beta \rangle^\beta \right] \tag{A.52}$$

where different terms neglect and the equation can be further simplified by considering the closure problem of the mapping functions $\underline{\underline{B}}$ and $\boldsymbol{b}$ Eq. (A.44). Finally, the boundary value problem for $\boldsymbol{\psi}$ and $\xi$ writes

$$\begin{cases} \partial_{\boldsymbol{x}} \cdot \boldsymbol{\psi} = -\underline{\underline{B}}^T \cdot \partial_{\boldsymbol{x}} \langle \boldsymbol{v}_\beta \rangle^\beta \\ \partial^2_{\boldsymbol{x}} \boldsymbol{\psi} - \partial_{\boldsymbol{x}} \xi = \frac{1}{V_\beta} \int_{V_\beta} \left[ \partial^2_{\boldsymbol{x}} \boldsymbol{\psi} - \partial_{\boldsymbol{x}} \xi \right] + \partial_{\boldsymbol{x}} \langle \boldsymbol{v}_\beta \rangle^\beta \cdot \boldsymbol{b} - 2(\partial_{\boldsymbol{x}} \langle \boldsymbol{v}_\beta \rangle^\beta)^T \left[ \partial_{\boldsymbol{x}} \underline{\underline{B}}^T - \langle \partial_{\boldsymbol{x}} \underline{\underline{B}}^T \rangle^\beta \right] - \underline{\underline{B}} \cdot \partial^2_{\boldsymbol{x}} \langle \boldsymbol{v}_\beta \rangle^\beta \\ BC1 \;\; \boldsymbol{\psi} = 0 \qquad\qquad at \; S_{\beta\sigma} \\ BC2 \;\; \boldsymbol{\psi} = 0 \qquad\qquad at \; \partial V_\beta \\ \langle \xi \rangle^\beta = \langle \boldsymbol{\psi} \rangle^\beta = 0 \end{cases} \tag{A.53}$$

A magnitude analysis (see Section A.4) shows that the terms $\boldsymbol{\psi}$ and $\xi$ are negligible compared to the mapping terms. Thus, the velocity and pressure perturbations can be expressed as

$$\tilde{\boldsymbol{v}}_\beta = \underline{\underline{B}} \cdot \langle \boldsymbol{v}_\beta \rangle^\beta \tag{A.54}$$

$$\tilde{p}_\beta = \mu_\beta \boldsymbol{b} \cdot \langle \boldsymbol{v}_\beta \rangle^\beta \tag{A.55}$$

The permeability tensor is derived from the boundary values problem of $\underline{\underline{B}}$ and $\boldsymbol{b}$, Eq. (A.44). For such purpose, the velocity and pressure perturbation terms are substitutes inside the averaged momentum equation, Eq. (A.35), leading to

$$\rho_\beta \partial_t \langle \boldsymbol{v}_\beta \rangle^\beta = -\partial_{\boldsymbol{x}} \langle p_\beta \rangle^\beta + \rho_\beta \boldsymbol{g} - \frac{1}{V_\beta} \int_{S_{\beta\sigma}} (\mu_\beta \boldsymbol{b} \cdot \langle \boldsymbol{v}_\beta \rangle^\beta) \boldsymbol{n}_{\beta\sigma} dS + \frac{\mu_\beta}{V_\beta} \int_{S_{\beta\sigma}} \boldsymbol{n}_{\beta\sigma} \cdot \partial_{\boldsymbol{x}} (\underline{\underline{B}} \cdot \langle \boldsymbol{v}_\beta \rangle^\beta) dS \tag{A.56}$$

The two integral terms are developed by considering an uniform averaged velocity field. The first integral term becomes

$$\frac{1}{V_\beta} \int_{S_{\beta\sigma}} \boldsymbol{n}_{\beta\sigma} \boldsymbol{b} \cdot \langle \boldsymbol{v}_\beta \rangle^\beta dS = \Big[ \frac{1}{V_\beta} \int_{S_{\beta\sigma}} \boldsymbol{b} \boldsymbol{n}_{\beta\sigma} dS \Big] \cdot \langle \boldsymbol{v}_\beta \rangle^\beta = 0 \tag{A.57}$$

The second integral term develops

$$\frac{1}{V_\beta} \int_{S_{\beta\sigma}} \boldsymbol{n}_{\beta\sigma} \cdot \partial_{\boldsymbol{x}} (\underline{\underline{B}} \cdot \langle \boldsymbol{v}_\beta \rangle^\beta) dS = \frac{1}{V_\beta} \int_{S_{\beta\sigma}} \Big[ \boldsymbol{n}_{\beta\sigma} \cdot \partial_{\boldsymbol{x}} \underline{\underline{B}} \cdot \langle \boldsymbol{v}_\beta \rangle^\beta + \cancel{\boldsymbol{n}_{\beta\sigma} \cdot \underline{\underline{B}} \cdot \partial_{\boldsymbol{x}} \langle \boldsymbol{v}_\beta \rangle^\beta} \Big] dS =$$

$$= \Big[ \frac{1}{V_\beta} \int_{S_{\beta\sigma}} \boldsymbol{n}_{\beta\sigma} \cdot \partial_{\boldsymbol{x}} \underline{\underline{B}} dS \Big] \cdot \langle \boldsymbol{v}_\beta \rangle^\beta \tag{A.58}$$

Eq. (A.56) is rearranged as follows

$$\rho_\beta \partial_t \langle \boldsymbol{v}_\beta \rangle^\beta = -\partial_{\boldsymbol{x}} \langle p_\beta \rangle^\beta + \rho_\beta \boldsymbol{g} + \Big[ \frac{\mu_\beta}{V_\beta} \int_{S_{\beta\sigma}} \boldsymbol{n}_{\beta\sigma} \cdot (\partial_{\boldsymbol{x}} \underline{\underline{B}} - \underline{\underline{I}} \boldsymbol{b}) dS \Big] \cdot \langle \boldsymbol{v}_\beta \rangle^\beta \tag{A.59}$$

The integral term can be defined as

$$\underline{\underline{C}} = -\frac{1}{V_\beta} \int_{S_{\beta\sigma}} \boldsymbol{n}_{\beta\sigma} \cdot (\partial_{\boldsymbol{x}} \underline{\underline{B}} - \underline{\underline{I}} \boldsymbol{b}) dS \tag{A.60}$$

The averaged momentum equation becomes

$$\rho_\beta \partial_t \langle \boldsymbol{v}_\beta \rangle^\beta = -\partial_{\boldsymbol{x}} \langle p_\beta \rangle^\beta + \rho_\beta \boldsymbol{g} - \mu_\beta \underline{\underline{C}} \cdot \langle \boldsymbol{v}_\beta \rangle^\beta \tag{A.61}$$

and can be rearranged as

$$\frac{\rho_\beta}{\epsilon_\beta \mu_\beta} \underline{\underline{K}} \partial_t \langle \boldsymbol{v}_\beta \rangle + \langle \boldsymbol{v}_\beta \rangle = -\frac{\underline{\underline{K}}}{\mu_\beta} \cdot \Big[ \partial_{\boldsymbol{x}} \langle p_\beta \rangle^\beta - \rho_\beta \boldsymbol{g} \Big] \tag{A.62}$$

where $\underline{\underline{K}} = \epsilon_\beta \underline{\underline{C}}^{-1}$. By considering a steady-state flow, Darcy's law is achieved

$$\langle \boldsymbol{v}_\beta \rangle = -\frac{\underline{\underline{K}}}{\mu_\beta} \cdot \Big[ \partial_{\boldsymbol{x}} \langle p_\beta \rangle^\beta - \rho_\beta \boldsymbol{g} \Big] \tag{A.63}$$

### A.2.2 Periodic Domain

The values of the mapping variables are obtained by solving the closure problem of Eq. (A.44). Once known, the permeability tensor can be deduced from Eq. (A.60). Thus, theoretically the problem is solved, but in practice there is still the issue arising from the boundary condition BC2: the mapping variable $\underline{\underline{B}}$ is set to be equal to a certain function $\underline{\underline{G}}$ representing the perturbation velocity at the inlet and outlet of the domain. This function is not known, so the problem can not be solved. The only way to proceed is by making the further assumption of periodic domain. The boundary problem, Eq. (A.44), becomes

$$\begin{cases} \partial_{\boldsymbol{x}} \cdot \underline{\underline{B}} = 0 \\ -\partial_{\boldsymbol{x}} \boldsymbol{b} + \partial^2_{\boldsymbol{x}} \underline{\underline{B}} = \dfrac{1}{V_\beta} \int_{V_\beta} [\, -\partial_{\boldsymbol{x}} \boldsymbol{b} + \partial^2_{\boldsymbol{x}} \underline{\underline{B}}] dV \\ BC1 \;\; \underline{\underline{B}} = -\underline{\underline{I}} & at\ S_{\beta\sigma} \\ BC2 \;\; \underline{\underline{B}}(\boldsymbol{r} + l_i) = \underline{\underline{B}}(\boldsymbol{r}) \quad \boldsymbol{b}(\boldsymbol{r} + l_i) = \boldsymbol{b}(\boldsymbol{r}) \;\; i = 1,2,3 & at\ \partial V_\beta \\ \langle \underline{\underline{B}} \rangle^\beta = \langle \boldsymbol{b} \rangle^\beta = 0 \end{cases} \tag{A.64}$$

The integral term on the second-hand side of the momentum equation is developed as

$$\int_{V_\beta} [\, -\partial_{\boldsymbol{x}} \boldsymbol{b} + \partial^2_{\boldsymbol{x}} \underline{\underline{B}}] dV = \int_{V_\beta} \partial_{\boldsymbol{x}} \cdot [\, -\boldsymbol{b} \underline{\underline{I}} + \partial_{\boldsymbol{x}} \underline{\underline{B}}] dV = \int_{S_{\sigma\beta}} [\, -\boldsymbol{b} \underline{\underline{I}} + \partial_{\boldsymbol{x}} \underline{\underline{B}}] \cdot \boldsymbol{n}_{\boldsymbol{\sigma\beta}} dS = V_\beta \epsilon_\beta \underline{\underline{K}}^{-1} \tag{A.65}$$

The following transformation is introduced

$$\boldsymbol{d} = \epsilon_\beta^{-1} \boldsymbol{b} \cdot \underline{\underline{K}}\,, \quad \underline{\underline{D}} = \epsilon_\beta^{-1} (\underline{\underline{B}} + \underline{\underline{I}}) \cdot \underline{\underline{K}} \tag{A.66}$$

As highlighted in Eq. (A.60), the permeability tensor derives from an averaging operation within the volume. It is therefore a uniform averaged quantity representing the volume of interest. Its gradient within the volume is equal to zero. With this in mind, the following relationships can be stated

$$\partial_{\boldsymbol{x}} \cdot \underline{\underline{D}} = 0 \tag{A.67}$$

$$\partial_{\boldsymbol{x}} \boldsymbol{d} = \epsilon^{-1} \partial_{\boldsymbol{x}} \boldsymbol{b} \cdot \underline{\underline{K}} \tag{A.68}$$

$$\underline{\underline{B}} = \epsilon \underline{\underline{D}} \cdot \underline{\underline{K}}^{-1} \tag{A.69}$$

$$\partial^2_{\boldsymbol{x}} \underline{\underline{B}} = \epsilon \partial^2_{\boldsymbol{x}} \underline{\underline{D}} \cdot \underline{\underline{K}}^{-1} \tag{A.70}$$

The periodic closure problem Eq. (A.64) is further developed as follows

$$\begin{cases} \partial_{\boldsymbol{x}} \cdot \underline{\underline{D}} = 0 \\ -\partial_{\boldsymbol{x}} \boldsymbol{d} + \partial_{\boldsymbol{x}}^2 \underline{\underline{D}} + \underline{\underline{I}} = 0 \\ BC1 \;\; \underline{\underline{D}} = 0 & at\ S_{\beta\sigma} \\ BC2 \;\; \underline{\underline{D}}(\boldsymbol{r} + l_i) = \underline{\underline{D}}(\boldsymbol{r}) \quad \boldsymbol{d}(\boldsymbol{r} + l_i) = \boldsymbol{d}(\boldsymbol{r}) \;\; i = 1,2,3 & at\ \partial V_\beta \\ \langle \underline{\underline{D}} \rangle^\beta = \epsilon_\beta^{-1} \underline{\underline{K}} \end{cases} \tag{A.71}$$

The solution of this system can be carried out with any numerical code capable of solving the Stokes equations.

## A.3 Energy Equation

From Eq. (A.10), the pore-scale energy equations and the respective boundary conditions are extracted

$$\begin{cases} (\rho\, c_p)_\beta \partial_t T_\beta + (\rho\, c_p)_\beta \boldsymbol{v}_\beta \cdot \partial_{\boldsymbol{x}} T_\beta = \partial_{\boldsymbol{x}} \cdot (k_\beta \partial_{\boldsymbol{x}} T_\beta) & in\ V_\beta \\ (\rho\, c_p)_\sigma \partial_t T_\sigma = \partial_{\boldsymbol{x}} \cdot (k_\sigma \partial_{\boldsymbol{x}} T_\sigma) & in\ V_\sigma \\ BC1: \;\; T_\beta = T_\sigma & at\ S_{\beta\sigma} \\ BC2: \;\; \boldsymbol{n}_{\beta\sigma} \cdot k_\beta \partial_{\boldsymbol{x}} T_\beta = \boldsymbol{n}_{\beta\sigma} \cdot k_\sigma \partial_{\boldsymbol{x}} T_\sigma & at\ S_{\beta\sigma} \end{cases} \tag{A.72}$$

In the following development, only the equation for the $\beta$ phase is showed. The same conclusions apply to the $\sigma$ phase.

The procedure starts with the averaging of the equation

$$\left\langle (\rho\, c_p)_\beta \partial_t T_\beta \right\rangle + \left\langle (\rho\, c_p)_\beta \boldsymbol{v}_\beta \cdot \partial_{\boldsymbol{x}} T_\beta \right\rangle = \left\langle \partial_{\boldsymbol{x}} \cdot (k_\beta \partial_{\boldsymbol{x}} T_\beta) \right\rangle \tag{A.73}$$

Each term is now developed. The averaging theorem related to time derivative, Eq. (A.6), is applied to the transient term

$$\left\langle (\rho\, c_p)_\beta \partial_t T_\beta \right\rangle = (\rho\, c_p)_\beta \partial_t \langle T_\beta \rangle = \epsilon_\beta (\rho\, c_p)_\beta \partial_t \langle T_\beta \rangle^\beta \tag{A.74}$$

The second term of the averaged energy equation, Eq. (A.73), is now considered

$$\left\langle (\rho\, c_p)_\beta \boldsymbol{v}_\beta \cdot \partial_{\boldsymbol{x}} T_\beta \right\rangle = (\rho\, c_p)_\beta \left\langle \boldsymbol{v}_\beta \cdot \partial_{\boldsymbol{x}} T_\beta \right\rangle \tag{A.75}$$

The scalar product between the velocity and the temperature gradient is rewritten by considering the properties of the divergence operator

$$\boldsymbol{v}_\beta \cdot \partial_{\boldsymbol{x}} T_\beta = \partial_{\boldsymbol{x}} \cdot (T_\beta \boldsymbol{v}_\beta) - \cancel{T_\beta\, \partial_{\boldsymbol{x}} \cdot \boldsymbol{v}_\beta} = \partial_{\boldsymbol{x}} \cdot (T_\beta \boldsymbol{v}_\beta) \tag{A.76}$$

where the incompressibility constraint ($\partial_{\boldsymbol{x}} \cdot \boldsymbol{v}_\beta = 0$) is taken into account. The averaging theorem of the divergence, Eq. (A.8), is applied to the term

$$(\rho\, c_p)_\beta \left\langle \boldsymbol{v}_\beta \cdot \partial_{\boldsymbol{x}} T_\beta \right\rangle = (\rho\, c_p)_\beta \left[ \partial_{\boldsymbol{x}} \cdot \langle T_\beta \boldsymbol{v}_\beta \rangle + \frac{1}{V} \cancel{\int_{S_{\beta\sigma}} T_\beta \boldsymbol{v}_\beta \cdot \boldsymbol{n}_{\beta\sigma} dS} \right] \tag{A.77}$$

where the last term is equal to zero since the flow is assumed to be in the continuum regime, thus no-slip conditions apply at the boundaries. The Grays' decomposition, Eq. (A.9), is applied to the temperature field

$$\partial_{\boldsymbol{x}} \cdot \langle T_\beta \boldsymbol{v}_\beta \rangle = \partial_{\boldsymbol{x}} \cdot \left[ \langle \langle T_\beta \rangle^\beta \langle \boldsymbol{v}_\beta \rangle^\beta \rangle + \langle \langle T_\beta \rangle^\beta \tilde{\boldsymbol{v}_\beta} \rangle + \langle \tilde{T_\beta} \langle \boldsymbol{v}_\beta \rangle^\beta \rangle + \langle \tilde{T_\beta} \tilde{\boldsymbol{v}_\beta} \rangle \right] \tag{A.78}$$

From a magnitude analysis it follows that the deviation quantities scale down as $1/l_\beta$, while the averaged quantities scale down as $1/L$. Due to the assumption of scales separation, the deviation quantities are neglected. Moreover, the averaging quantities can be moved out of the averaging operator

$$\partial_{\boldsymbol{x}} \cdot \langle T_\beta \boldsymbol{v}_\beta \rangle = \partial_{\boldsymbol{x}} \cdot \left[ \langle T_\beta \rangle^\beta \langle \boldsymbol{v}_\beta \rangle^\beta \langle 1 \rangle + \langle T_\beta \rangle^\beta \langle \tilde{\boldsymbol{v}_\beta} \rangle + \langle \tilde{T_\beta} \rangle \langle \boldsymbol{v}_\beta \rangle^\beta + \langle \tilde{T_\beta} \tilde{\boldsymbol{v}_\beta} \rangle \right] \tag{A.79}$$

where $\langle 1 \rangle$ is by definition: $\langle 1 \rangle = \frac{1}{V} \int_{V_\beta} dV = \epsilon_\beta$. The average of the spatial deviation, under the scale separation assumption, is set equal to zero $\langle \tilde{\psi_\beta} \rangle = 0$. In this way, the divergence term becomes

$$\partial_{\boldsymbol{x}} \cdot \langle T_\beta \boldsymbol{v}_\beta \rangle = \partial_{\boldsymbol{x}} \cdot \left[ \epsilon_\beta \langle T_\beta \rangle^\beta \langle \boldsymbol{v}_\beta \rangle^\beta + \langle \tilde{T_\beta} \tilde{\boldsymbol{v}_\beta} \rangle \right] = \epsilon_\beta \left[ \cancel{\langle T_\beta \rangle^\beta \partial_{\boldsymbol{x}} \cdot \langle \boldsymbol{v}_\beta \rangle^\beta} + \langle \boldsymbol{v}_\beta \rangle^\beta \cdot \partial_{\boldsymbol{x}} \langle T_\beta \rangle^\beta \right] + \partial_{\boldsymbol{x}} \cdot \langle \tilde{T_\beta} \tilde{\boldsymbol{v}_\beta} \rangle \tag{A.80}$$

where the properties of the divergence operator are used and the averaged incompressibility constraint considered. The second term of Eq. (A.73) results as follows

$$\left\langle (\rho\, c_p)_\beta \boldsymbol{v}_\beta \cdot \partial_{\boldsymbol{x}} T_\beta \right\rangle = (\rho\, c_p)_\beta \left[ \langle \boldsymbol{v}_\beta \rangle \cdot \partial_{\boldsymbol{x}} \langle T_\beta \rangle^\beta + \partial_{\boldsymbol{x}} \cdot \langle \tilde{T_\beta} \tilde{\boldsymbol{v}_\beta} \rangle \right] \tag{A.81}$$

The averaging theorem related to the divergence, Eq. (A.8), is applied to the divergence term of the second hand-side of the equation

$$\partial_{\boldsymbol{x}} \cdot \langle \tilde{T_\beta} \tilde{\boldsymbol{v}_\beta} \rangle = \langle \partial_{\boldsymbol{x}} \cdot \left( \tilde{T_\beta} \tilde{\boldsymbol{v}_\beta} \right) \rangle = \langle \tilde{\boldsymbol{v}_\beta} \cdot \partial_{\boldsymbol{x}} \tilde{T_\beta} \rangle \tag{A.82}$$

since the velocity deviation and its divergence are equal to zero at the boundary.
The last term of the averaged energy equation, Eq. (A.73), is now considered. The averaging theorem for the divergence, Eq. (A.8), is applied twice. The first time the equation reads

$$\left\langle \partial_{\boldsymbol{x}} \cdot (k_\beta \partial_{\boldsymbol{x}} T_\beta) \right\rangle = \partial_{\boldsymbol{x}} \cdot \left( k_\beta \langle \partial_{\boldsymbol{x}} T_\beta \rangle \right) + \frac{1}{V} \int_{S_{\beta\sigma}} k_\beta \partial_{\boldsymbol{x}} T_\beta \cdot \boldsymbol{n}_{\beta\sigma} dS \tag{A.83}$$

and the second time

$$\left\langle \partial_{\boldsymbol{x}} \cdot (k_\beta \partial_{\boldsymbol{x}} T_\beta) \right\rangle = \partial_{\boldsymbol{x}} \cdot \left[ k_\beta \left( \partial_{\boldsymbol{x}} \langle T_\beta \rangle + \frac{1}{V} \int_{S_{\beta\sigma}} T_\beta \boldsymbol{n}_{\beta\sigma} dS \right) \right] + \frac{1}{V} \int_{S_{\beta\sigma}} k_\beta \partial_{\boldsymbol{x}} T_\beta \cdot \boldsymbol{n}_{\beta\sigma} dS \tag{A.84}$$

The Grey's decomposition, Eq. (A.9), is introduced for the temperature field. The gradient of the temperature is equal to zero at the interface (BC1 of Eq. (A.72)) and the gradient of the averaged temperature is equal to zero in the domain. The development of the term proceeds as follows

$$\left\langle \partial_{\boldsymbol{x}} \cdot (k_\beta \partial_{\boldsymbol{x}} T_\beta) \right\rangle = \partial_{\boldsymbol{x}} \cdot \left[ k_\beta \left( \epsilon_\beta \partial_{\boldsymbol{x}} \langle T_\beta \rangle^\beta + \frac{1}{V} \int_{S_{\beta\sigma}} \tilde{T_\beta} \boldsymbol{n}_{\beta\sigma} dS \right) \right] + \frac{1}{V} \int_{S_{\beta\sigma}} k_\beta \partial_{\boldsymbol{x}} \tilde{T_\beta} \cdot \boldsymbol{n}_{\beta\sigma} dS \tag{A.85}$$

All the terms of the averaged energy equation, Eq. (A.73), are completely developed and are now replaced in the starting equation

$$\epsilon_\beta(\rho\, c_p)_\beta \partial_t \langle T_\beta\rangle^\beta + (\rho\, c_p)_\beta \langle \boldsymbol{v}_\beta\rangle \cdot \partial_{\boldsymbol{x}} \langle T_\beta\rangle^\beta + (\rho\, c_p)_\beta \langle \tilde{\boldsymbol{v}_\beta} \cdot \partial_{\boldsymbol{x}} \tilde{T_\beta}\rangle =$$

$$= \partial_{\boldsymbol{x}} \cdot \Big[k_\beta \Big(\epsilon_\beta \partial_{\boldsymbol{x}} \langle T_\beta\rangle^\beta + \frac{1}{V}\int_{S_{\beta\sigma}} \tilde{T_\beta} \boldsymbol{n}_{\beta\sigma} dS\Big)\Big] + \frac{1}{V}\int_{S_{\beta\sigma}} k_\beta \partial_{\boldsymbol{x}} \tilde{T_\beta} \cdot \boldsymbol{n}_{\beta\sigma} dS \tag{A.86}$$

A boundary value problem for the spatial deviation temperatures $\tilde{T_\beta}$ must be developed to obtain a closed form for the energy equation. For such purpose, Eq. (A.86) is divided by $\epsilon_\beta$ and subtracted to the pore-scale system of equations (Eq. (A.72)). Similar steps are done for the $\sigma$ phase. The following system is obtained

$$\begin{cases} (\rho\, c_p)_\beta \partial_t \tilde{T_\beta} + (\rho\, c_p)_\beta \tilde{\boldsymbol{v}_\beta} \cdot \partial_{\boldsymbol{x}} \langle T_\beta\rangle^\beta + (\rho\, c_p)_\beta \boldsymbol{v}_\beta \cdot \partial_{\boldsymbol{x}} \tilde{T_\beta} = \partial_{\boldsymbol{x}} \cdot (k_\beta \partial_{\boldsymbol{x}} \tilde{T_\beta}) + \\ \qquad -\epsilon_\beta^{-1} \partial_{\boldsymbol{x}} \cdot \Big(k_\beta \frac{1}{V}\int_{S_{\beta\sigma}} \tilde{T_\beta} \boldsymbol{n}_{\beta\sigma} dS\Big) - \epsilon_\beta^{-1} k_\beta \frac{1}{V}\int_{S_{\beta\sigma}} \partial_{\boldsymbol{x}} \tilde{T_\beta} \cdot \boldsymbol{n}_{\beta\sigma} dS \\ (\rho\, c_p)_\sigma \partial_t \tilde{T_\sigma} = \partial_{\boldsymbol{x}} \cdot (k_\sigma \partial_{\boldsymbol{x}} \tilde{T_\sigma}) - \epsilon_\sigma^{-1} \partial_{\boldsymbol{x}} \cdot \Big(k_\sigma \frac{1}{V}\int_{S_{\sigma\beta}} \tilde{T_\sigma} \boldsymbol{n}_{\boldsymbol{\sigma\beta}} dS\Big) - \epsilon_\beta^{-1} k_\sigma \frac{1}{V}\int_{S_{\sigma\beta}} \partial_{\boldsymbol{x}} \tilde{T_\sigma} \cdot \boldsymbol{n}_{\boldsymbol{\sigma\beta}} dS \\ BC1: \quad \tilde{T_\beta} = \tilde{T_\sigma} - (\langle \tilde{T_\beta}\rangle^\beta - \langle \tilde{T_\sigma}\rangle^\sigma) \qquad \text{at } S_{\beta\sigma} \\ BC2: \quad \boldsymbol{n}_{\beta\sigma} \cdot k_\beta \partial_{\boldsymbol{x}} \tilde{T_\beta} + \boldsymbol{n}_{\beta\sigma} \cdot k_\beta \partial_{\boldsymbol{x}} \langle T_\beta\rangle^\beta = \boldsymbol{n}_{\beta\sigma} \cdot k_\sigma \partial_{\boldsymbol{x}} \tilde{T_\sigma} + \boldsymbol{n}_{\beta\sigma} \cdot k_\sigma \partial_{\boldsymbol{x}} \langle T_\sigma\rangle^\sigma \qquad \text{at } S_{\beta\sigma} \end{cases} \tag{A.87}$$

### A.3.1 Closure Variable

In order to close the problem, the deviation variables ($\tilde{T_\beta}$, $\tilde{T_\sigma}$) must be determined in terms of the independent ones ($\langle T_\beta\rangle$, $\langle T_\sigma\rangle$). The problem is linear, so it is possible to express a generic linear dependence of the deviation variables as a function of the averaged ones. Moreover, both variables depend on the averaged variables and their gradient. Furthermore, due to the scale separation assumption, a quasi-steady relationships (the averaged fields are time-dependant, while the deviation fields are stationary) can be introduced. Based on these observations, the following generic expressions can be introduced

$$\tilde{T_\beta} = \boldsymbol{b_{\beta\beta}} \cdot \partial_{\boldsymbol{x}} \langle T_\beta\rangle^\beta + \boldsymbol{b_{\beta\sigma}} \cdot \partial_{\boldsymbol{x}} \langle T_\sigma\rangle^\sigma - s_\beta(\langle T_\beta\rangle^\beta - \langle T_\sigma\rangle^\sigma) + \xi_\beta 0 \tag{A.88}$$

$$\tilde{T_\sigma} = \boldsymbol{b_{\sigma\beta}} \cdot \partial_{\boldsymbol{x}} \langle T_\beta\rangle^\beta + \boldsymbol{b_{\sigma\sigma}} \cdot \partial_{\boldsymbol{x}} \langle T_\sigma\rangle^\sigma + s_\sigma(\langle T_\sigma\rangle^\sigma - \langle T_\beta\rangle^\beta) + \xi_\sigma \tag{A.89}$$

where $\xi_\beta$ and $\xi_\sigma$ are two arbitrary functions and $\boldsymbol{b}_{\sigma\sigma}$, $\boldsymbol{b}_{\beta\beta}$, $\boldsymbol{b}_{\sigma\beta}$, and $\boldsymbol{b}_{\beta\sigma}$ are the mapping variables. Both the mapping variables and arbitrary functions must be closed in terms of a plausible set of boundary value problems. Assuming the domain to be periodic and substituting the two expressions of the deviation terms (without the arbitrary functions since, as discussed later, they can be neglected) within Eq. (A.86), it is possible to obtain

$$\epsilon_\beta(\rho\, c_p)_\beta \partial_t \langle T_\beta\rangle^\beta + (\rho\, c_p)_\beta \langle \boldsymbol{v}_\beta\rangle \cdot \partial_{\boldsymbol{x}} \langle T_\beta\rangle^\beta + (\rho\, c_p)_\beta \Big\langle \tilde{\boldsymbol{v}_\beta} \cdot \partial_{\boldsymbol{x}} [\boldsymbol{b_{\beta\beta}} \cdot \partial_{\boldsymbol{x}} \langle T_\beta\rangle^\beta + \boldsymbol{b_{\beta\sigma}} \cdot \partial_{\boldsymbol{x}} \langle T_\sigma\rangle^\sigma +$$

$$-s_\beta(\langle T_\beta\rangle^\beta - \langle T_\sigma\rangle^\sigma)]\Big\rangle = \partial_{\boldsymbol{x}}\cdot\Big[k_\beta\Big(\epsilon_\beta\partial_{\boldsymbol{x}}\langle T_\beta\rangle^\beta + \frac{1}{V}\int_{S_{\beta\sigma}}[\boldsymbol{b_{\beta\beta}}\cdot\partial_{\boldsymbol{x}}\langle T_\beta\rangle^\beta + \boldsymbol{b_{\beta\sigma}}\cdot\partial_{\boldsymbol{x}}\langle T_\sigma\rangle^\sigma +$$

$$-s_\beta(\langle T_\beta\rangle^\beta - \langle T_\sigma\rangle^\sigma)]\boldsymbol{n}_{\beta\sigma}dS\Big)\Big] + \frac{1}{V}\int_{S_{\beta\sigma}} k_\beta\partial_{\boldsymbol{x}}[\boldsymbol{b_{\beta\beta}}\cdot\partial_{\boldsymbol{x}}\langle T_\beta\rangle^\beta + \boldsymbol{b_{\beta\sigma}}\cdot\partial_{\boldsymbol{x}}\langle T_\sigma\rangle^\sigma +$$

$$-s_\beta(\langle T_\beta\rangle^\beta - \langle T_\sigma\rangle^\sigma)]\cdot\boldsymbol{n}_{\beta\sigma}dS \tag{A.90}$$

This equation can be reorganised and written in a more compact form as follows

$$\epsilon_\beta(\rho\, c_p)_\beta\partial_t\langle T_\beta\rangle^\beta + (\rho\, c_p)_\beta\langle\boldsymbol{v}_\beta\rangle\cdot\partial_{\boldsymbol{x}}\langle T_\beta\rangle^\beta - \boldsymbol{v}_{\beta\beta}\cdot\partial_{\boldsymbol{x}}\langle T_\beta\rangle^\beta - \boldsymbol{v}_{\beta\sigma}\cdot\partial_{\boldsymbol{x}}\langle T_\sigma\rangle^\sigma =$$

$$= \partial_{\boldsymbol{x}}\cdot(\underline{\underline{K}}_{\beta\beta}\cdot\partial_{\boldsymbol{x}}\langle T_\beta\rangle^\beta + \underline{\underline{K}}_{\beta\sigma}\cdot\partial_{\boldsymbol{x}}\langle T_\sigma\rangle^\sigma) - a_v h(\langle T_\beta\rangle^\beta - \langle T_\sigma\rangle^\sigma) \tag{A.91}$$

Analogously, for the $\sigma$ phase

$$\epsilon_\sigma(\rho\, c_p)_\sigma\partial_t\langle T_\sigma\rangle^\sigma - \boldsymbol{v}_{\sigma\beta}\cdot\partial_{\boldsymbol{x}}\langle T_\beta\rangle^\beta - \boldsymbol{v}_{\sigma\sigma}\cdot\partial_{\boldsymbol{x}}\langle T_\sigma\rangle^\sigma =$$

$$= \partial_{\boldsymbol{x}}\cdot(\underline{\underline{K}}_{\sigma\beta}\cdot\partial_{\boldsymbol{x}}\langle T_\beta\rangle^\beta - \underline{\underline{K}}_{\sigma\sigma}\cdot\partial_{\boldsymbol{x}}\langle T_\sigma\rangle^\sigma) - a_v h(\langle T_\sigma\rangle^\sigma - \langle T_\beta\rangle^\beta) \tag{A.92}$$

Where the transport coefficients $\boldsymbol{v}_{\beta\sigma}$, $\boldsymbol{v}_{\beta\beta}$, $\boldsymbol{v}_{\sigma\beta}$, and $\boldsymbol{v}_{\sigma\sigma}$, the conductivity tensors $\underline{\underline{K}}_{\beta\beta}$, $\underline{\underline{K}}_{\beta\sigma}$, $\underline{\underline{K}}_{\sigma\beta}$, and $\underline{\underline{K}}_{\sigma\sigma}$, and the heat transfer coefficient $h$, are determined by the mapping variables

$$\underline{\underline{K}}_{\beta\beta} = k_\beta(\epsilon_\beta\underline{\underline{I}} + \langle\boldsymbol{n}_{\beta\sigma}\boldsymbol{b}_{\beta\beta}\boldsymbol{\delta}_{\beta\sigma}\rangle) - (\rho c_p)_\beta\langle\tilde{\boldsymbol{v}}_\beta\boldsymbol{b}_{\beta\beta}\rangle \tag{A.93}$$

$$\underline{\underline{K}}_{\beta\sigma} = k_\beta\langle\boldsymbol{n}_{\beta\sigma}\boldsymbol{b}_{\beta\sigma}\boldsymbol{\delta}_{\beta\sigma}\rangle - (\rho c_p)_\beta\langle\tilde{\boldsymbol{v}}_\beta\boldsymbol{b}_{\beta\sigma}\rangle \tag{A.94}$$

$$\underline{\underline{K}}_{\sigma\beta} = k_\sigma\langle\boldsymbol{n}_{\sigma\beta}\boldsymbol{b}_{\sigma\beta}\boldsymbol{\delta}_{\beta\sigma}\rangle \tag{A.95}$$

$$\underline{\underline{K}}_{\sigma\sigma} = k_\sigma(\epsilon_\sigma\underline{\underline{I}} + \langle\boldsymbol{n}_{\sigma\beta}\boldsymbol{b}_{\sigma\sigma}\boldsymbol{\delta}_{\beta\sigma}\rangle) \tag{A.96}$$

$$\boldsymbol{v}_{\beta\beta} = \boldsymbol{c}_{\beta\beta} - k_\beta\langle\boldsymbol{n}_{\beta\sigma}s_\beta\boldsymbol{\delta}_{\beta\sigma}\rangle + (\rho c_p)_\beta\langle\tilde{\boldsymbol{v}}_\beta s_\beta\rangle \tag{A.97}$$

$$\boldsymbol{v}_{\beta\sigma} = \boldsymbol{c}_{\beta\sigma} + k_\beta\langle\boldsymbol{n}_{\beta\sigma}s_\beta\boldsymbol{\delta}_{\beta\sigma}\rangle - (\rho c_p)_\beta\langle\tilde{\boldsymbol{v}}_\beta s_\beta\rangle \tag{A.98}$$

$$\boldsymbol{v}_{\sigma\beta} = \boldsymbol{c}_{\sigma\beta} - k_\sigma\langle\boldsymbol{n}_{\sigma\beta}s_\sigma\boldsymbol{\delta}_{\beta\sigma}\rangle \tag{A.99}$$

$$\boldsymbol{v}_{\sigma\sigma} = \boldsymbol{c}_{\sigma\sigma} - k_\sigma\langle\boldsymbol{n}_{\sigma\beta}s_\sigma\boldsymbol{\delta}_{\beta\sigma}\rangle \tag{A.100}$$

$$h_\beta = h_\sigma = \langle\boldsymbol{n}_{\beta\sigma}\cdot k_\beta\partial_{\boldsymbol{x}}s_\beta\boldsymbol{\delta}_{\beta\sigma}\rangle = a_v h \tag{A.101}$$

where:

$$\boldsymbol{c}_{\beta\beta} = \langle \boldsymbol{n}_{\beta\sigma} \cdot k_\beta \partial_{\boldsymbol{x}} \boldsymbol{b}_{\beta\beta} \boldsymbol{\delta}_{\beta\sigma} \rangle \tag{A.102}$$

$$\boldsymbol{c}_{\sigma\beta} = \langle \boldsymbol{n}_{\sigma\beta} \cdot k_\sigma \partial_{\boldsymbol{x}} \boldsymbol{b}_{\sigma\beta} \boldsymbol{\delta}_{\beta\sigma} \rangle \tag{A.103}$$

$$\boldsymbol{c}_{\beta\sigma} = \langle \boldsymbol{n}_{\beta\sigma} \cdot k_\beta \partial_{\boldsymbol{x}} \boldsymbol{b}_{\beta\sigma} \boldsymbol{\delta}_{\beta\sigma} \rangle \tag{A.104}$$

$$\boldsymbol{c}_{\sigma\sigma} = \langle \boldsymbol{n}_{\sigma\beta} \cdot k_\sigma \partial_{\boldsymbol{x}} \boldsymbol{b}_{\sigma\sigma} \boldsymbol{\delta}_{\beta\sigma} \rangle \tag{A.105}$$

The mapping variables require the definition of some closure problems. Thanks to the arbitrary functions, the closure problems for the mapping variables can be specified in any way. The classic way is by defining the same boundary value problems as for the variation terms (Eq. (A.87)). For $\boldsymbol{b}_{\beta\beta}$ and $\boldsymbol{b}_{\sigma\beta}$ the closure problem is defined as follows

$$\begin{cases} (\rho c_p)_\beta \tilde{\boldsymbol{v}}_\beta + (\rho c_p)_\beta \boldsymbol{v}_\beta \cdot \partial_{\boldsymbol{x}} \boldsymbol{b}_{\beta\beta} = k_\beta \partial^2_{\boldsymbol{x}} \boldsymbol{b}_{\beta\beta} - \epsilon_\beta^{-1} \boldsymbol{c}_{\beta\beta} \ , & in \ V_\beta \\ B.C.1 \quad \boldsymbol{n}_{\beta\sigma} \cdot k_\beta \partial_{\boldsymbol{x}} \boldsymbol{b}_{\beta\beta} + \boldsymbol{n}_{\beta\sigma} k_\beta = \boldsymbol{n}_{\beta\sigma} \cdot k_\sigma \partial_{\boldsymbol{x}} \boldsymbol{b}_{\sigma\beta} \ , & at \ S_{\beta\sigma} \\ B.C.2 \quad \boldsymbol{b}_{\beta\beta} = \boldsymbol{b}_{\sigma\beta} \ , & at \ S_{\beta\sigma} \\ 0 = k_\sigma \partial^2_{\boldsymbol{x}} \boldsymbol{b}_{\sigma\beta} - \epsilon_\sigma^{-1} \boldsymbol{c}_{\sigma\beta} \ , & in \ V_\sigma \\ \boldsymbol{b}_{\beta\beta}(\boldsymbol{r} + l_i) = \boldsymbol{b}_{\beta\beta}(\boldsymbol{r}) & \\ \boldsymbol{b}_{\sigma\beta}(\boldsymbol{r} + l_i) = \boldsymbol{b}_{\sigma\beta}(\boldsymbol{r}) \ , & i = 1,2,3 \\ \langle \boldsymbol{b}_{\beta\beta} \rangle = 0 \ , \quad \langle \boldsymbol{b}_{\sigma\beta} \rangle = 0 & \\ \boldsymbol{c}_{\beta\beta} = \langle \boldsymbol{n}_{\beta\sigma} \cdot k_\beta \partial_{\boldsymbol{x}} \boldsymbol{b}_{\beta\beta} \boldsymbol{\delta}_{\beta\sigma} \rangle & \\ \boldsymbol{c}_{\sigma\beta} = \langle \boldsymbol{n}_{\beta\sigma} \cdot k_\sigma \partial_{\boldsymbol{x}} \boldsymbol{b}_{\sigma\beta} \boldsymbol{\delta}_{\beta\sigma} \rangle = -\boldsymbol{c}_{\beta\beta} & \end{cases} \tag{A.106}$$

where $\boldsymbol{\delta}$ is the Dirac distribution associated with the interface $S_{\beta\delta}$. For $\boldsymbol{b}_{\beta\sigma}$ and $\boldsymbol{b}_{\sigma\sigma}$ the closure problem reads

$$\begin{cases} (\rho c_p)_\beta \boldsymbol{v}_\beta \cdot \partial_{\boldsymbol{x}} \boldsymbol{b}_{\beta\sigma} = k_\beta \partial^2_{\boldsymbol{x}} \boldsymbol{b}_{\beta\sigma} - \epsilon_\beta^{-1} \boldsymbol{c}_{\beta\sigma} \ , & in \ V_\beta \\ B.C.1 \quad \boldsymbol{n}_{\beta\sigma} \cdot k_\beta \partial_{\boldsymbol{x}} \boldsymbol{b}_{\beta\sigma} = \boldsymbol{n}_{\beta\sigma} \cdot k_\sigma \partial_{\boldsymbol{x}} \boldsymbol{b}_{\sigma\sigma} + \boldsymbol{n}_{\beta\sigma} k_\sigma \ , & at \ S_{\beta\sigma} \\ B.C.2 \quad \boldsymbol{b}_{\beta\sigma} = \boldsymbol{b}_{\sigma\sigma} \ , & at \ S_{\beta\sigma} \\ 0 = k_\sigma \partial^2_{\boldsymbol{x}} \boldsymbol{b}_{\sigma\sigma} - \epsilon_\sigma^{-1} \boldsymbol{c}_{\sigma\sigma} \ , & in \ V_\sigma \\ \boldsymbol{b}_{\beta\sigma}(\boldsymbol{r} + l_i) = \boldsymbol{b}_{\beta\sigma}(\boldsymbol{r}) & \\ \boldsymbol{b}_{\sigma\sigma}(\boldsymbol{r} + l_i) = \boldsymbol{b}_{\sigma\sigma}(\boldsymbol{r}) \ , & i = 1,2,3 \\ \langle \boldsymbol{b}_{\beta\sigma} \rangle = 0 \ , \quad \langle \boldsymbol{b}_{\sigma\sigma} \rangle = 0 & \\ \boldsymbol{c}_{\beta\sigma} = \langle \boldsymbol{n}_{\beta\sigma} \cdot k_\beta \partial_{\boldsymbol{x}} \boldsymbol{b}_{\beta\sigma} \boldsymbol{\delta}_{\beta\sigma} \rangle & \\ \boldsymbol{c}_{\sigma\sigma} = \langle \boldsymbol{n}_{\sigma\beta} \cdot k_\sigma \partial_{\boldsymbol{x}} \boldsymbol{b}_{\sigma\sigma} \boldsymbol{\delta}_{\beta\sigma} \rangle = -\boldsymbol{c}_{\beta\sigma} & \end{cases} \tag{A.107}$$

The closure problem for the two scalar fields $s_\beta$ and $s_\sigma$ is as follows

$$\begin{cases} (\rho c_p)_\beta \boldsymbol{v}_\beta \cdot \partial_{\boldsymbol{x}} s_\beta = k_\beta \partial^2_{\boldsymbol{x}} s_\beta - \epsilon_\beta^{-1} h_\beta \ , & in \ V_\beta \\ B.C.1 \quad \boldsymbol{n}_{\beta\sigma} \cdot k_\beta \partial_{\boldsymbol{x}} s_\beta = \boldsymbol{n}_{\beta\sigma} \cdot k_\sigma \partial_{\boldsymbol{x}} s_\beta \ , & at \ S_{\beta\sigma} \\ B.C.2 \quad s_\beta = 1 + s_\sigma \ , & at \ S_{\beta\sigma} \\ 0 = k_\sigma \partial^2_{\boldsymbol{x}} s_\beta + \epsilon_\sigma^{-1} h_\sigma \ , & in \ V_\sigma \\ s_\beta(\boldsymbol{r} + l_i) = s_\beta(\boldsymbol{r}) \ , \quad s_\sigma(\boldsymbol{r} + l_i) = s_\sigma(\boldsymbol{r}) \ , & i = 1,2,3 \\ \langle s_\beta \rangle = 0 \ , \quad \langle s_\sigma \rangle = 0 \end{cases} \tag{A.108}$$

The two arbitrary functions $\xi_\beta$ and $\xi_\sigma$ have to be defined. The two equations for the spatial deviation temperatures (Eqs. (A.88) and (A.89)) are substituted into the boundary value problem for the spatial deviation temperature $\tilde{T}_\beta$ (Eq. (A.87)). The following closure is defined

$$\begin{cases} k_\beta \partial^2_{\boldsymbol{x}} \xi_\beta = \epsilon_\beta^{-1} \langle \boldsymbol{n}_{\beta\sigma} k_\beta \cdot \partial_{\boldsymbol{x}} \xi_\beta \boldsymbol{\delta}_{\beta\sigma} \rangle + \Phi_\beta \\ B.C.1 \quad \boldsymbol{n}_{\beta\sigma} \cdot k_\beta \partial_{\boldsymbol{x}} \xi_\beta = \boldsymbol{n}_{\beta\sigma} \cdot k_\sigma \xi_\sigma + \Omega_{\beta\sigma} \ , & at \ S_{\beta\sigma} \\ B.C.2 \quad \xi_\beta = \xi_\sigma \ , & at \ S_{\beta\sigma} \\ k_\sigma \partial^2_{\boldsymbol{x}} \xi_\sigma = \epsilon_\sigma^{-1} \langle \boldsymbol{n}_{\sigma\beta} k_\beta \cdot \partial_{\boldsymbol{x}} \xi_\sigma \boldsymbol{\delta}_{\beta\sigma} \rangle + \Phi_\sigma \end{cases} \tag{A.109}$$

where $\Phi_\beta$, $\Phi_\sigma$, and $\Omega_{\beta\sigma}$ are three functions that depend on the mapping variables, geometry, thermal properties, and temperature fields. However, it is possible to show [15] that the contribution of the two arbitrary functions to the temperature deviation fields is negligible with respect to the contribution of the mapping variables. Hence, $\xi_\beta$ and $\xi_\sigma$ can be neglected in the equations.

It should be remarked that the quasi-steady assumption for the deviation terms holds as long as the time dependent mechanisms are not important. Otherwise, additional source terms in the temperature deviation equations must be included. This two-equations model is fully compatible with the one-equation model, in which: $\langle T_\sigma \rangle^\sigma = \langle T_\beta \rangle^\beta = \langle T \rangle$ and $\underline{\underline{K}}_{\text{eff}} = \underline{\underline{K}}_{\beta\beta} + \underline{\underline{K}}_{\beta\sigma} + \underline{\underline{K}}_{\sigma\beta} + \underline{\underline{K}}_{\sigma\sigma}$.
All the mapping variables must be determined before solving the macroscopic equations. However, this implies solving the three closure problems involving the integrals of the solution as source terms. Although this is not a problem when solving the closure problems on one-dimensional unit cells, a special procedure can be adapted to avoid such integro-differential equations in the general case. A change of variables is required. For the first closure problem, the following variables are introduced

$$\boldsymbol{b}_{\beta\beta} = \boldsymbol{b}^0_{I\beta} + \underline{\underline{B}}_{I\beta} \boldsymbol{c}_{\sigma\beta} \ ; \quad \boldsymbol{b}_{\sigma\beta} = \boldsymbol{b}^0_{I\sigma} + \underline{\underline{B}}_{I\sigma} \boldsymbol{c}_{\sigma\beta} \tag{A.110}$$

$\boldsymbol{b}^0_{I\beta}$ and $\boldsymbol{b}^0_{I\sigma}$ satisfy the following problem

$$\begin{cases} (\rho c_p)_\beta \tilde{\boldsymbol{v}}_\beta + (\rho c_p)_\beta \boldsymbol{v}_\beta \cdot \partial_{\boldsymbol{x}} \boldsymbol{b}^0_{I\beta} = k_\beta \partial^2_{\boldsymbol{x}} \boldsymbol{b}^0_{I\beta} \ , & in \ V_\beta \\ B.C.1 \quad \boldsymbol{n}_{\beta\sigma} \cdot k_\beta \partial_{\boldsymbol{x}} \boldsymbol{b}^0_{I\beta} + \boldsymbol{n}_{\beta\sigma} k_\beta = \boldsymbol{n}_{\beta\sigma} \cdot k_\sigma \partial_{\boldsymbol{x}} \boldsymbol{b}^0_{I\beta} \ , & at \ S_{\beta\sigma} \\ B.C.2 \quad \boldsymbol{b}^0_{I\beta} = \boldsymbol{b}^0_{I\sigma} \ , & at \ S_{\beta\sigma} \\ 0 = k_\sigma \partial^2_{\boldsymbol{x}} \boldsymbol{b}^0_{I\sigma} \ , & in \ V_\sigma \\ \boldsymbol{b}^0_{I\beta}(\boldsymbol{r} + l_i) = \boldsymbol{b}^0_{I\beta}(\boldsymbol{r}) \ , \quad \boldsymbol{b}^0_{I\sigma}(\boldsymbol{r} + l_i) = \boldsymbol{b}^0_{I\sigma}(\boldsymbol{r}) \ , & i = 1,2,3 \\ \langle \boldsymbol{b}^0_{I\beta} \rangle + \langle \boldsymbol{b}^0_{I\sigma} \rangle = 0 \end{cases} \tag{A.111}$$

$\underline{\underline{B}}_{I\beta}$ and $\underline{\underline{B}}_{I\sigma}$ satisfy the following problem

$$\begin{cases} (\rho c_p)_\beta \boldsymbol{v}_\beta \cdot \partial_{\boldsymbol{x}} \underline{\underline{B}}_{I\beta} = k_\beta \partial^2_{\boldsymbol{x}} \underline{\underline{B}}_{I\beta} + \epsilon_\beta^{-1} \, , & in \;\; V_\beta \\ B.C.1 \quad \boldsymbol{n}_{\beta\sigma} \cdot k_\beta \partial_{\boldsymbol{x}} \underline{\underline{B}}_{I\beta} = \boldsymbol{n}_{\beta\sigma} \cdot k_\sigma \partial_{\boldsymbol{x}} \underline{\underline{B}}_{I\sigma} \, , & at \;\; S_{\beta\sigma} \\ B.C.2 \quad \underline{\underline{B}}_{I\beta} = \underline{\underline{B}}_{I\sigma} \, , & at \;\; S_{\beta\sigma} \\ 0 = k_\sigma \partial^2_{\boldsymbol{x}} \underline{\underline{B}}_{I\sigma} - \epsilon_\sigma^{-1} \, , & in \;\; V_\sigma \\ \underline{\underline{B}}_{I\beta}(\boldsymbol{r} + l_i) = \underline{\underline{B}}_{I\beta}(\boldsymbol{r}) \, , \quad \underline{\underline{B}}_{I\sigma}(\boldsymbol{r} + l_i) = \underline{\underline{B}}_{I\sigma}(\boldsymbol{r}) \, , & i = 1,2,3 \\ \langle \underline{\underline{B}}_{I\beta} \rangle + \langle \underline{\underline{B}}_{I\sigma} \rangle = 0 \end{cases} \tag{A.112}$$

And:

$$\boldsymbol{c}_{\sigma\beta} = -\frac{\langle \boldsymbol{b}^0_{I\beta} \rangle^\beta}{\langle \underline{\underline{B}}_{I\beta} \rangle^\beta} \tag{A.113}$$

The mapping variables can thus be evaluated without solving integro-differential equations. Similar variables are introduced for the second closure problem

$$\boldsymbol{b}_{\beta\sigma} = \boldsymbol{b}^0_{II\beta} + \underline{\underline{B}}_{II\beta} \boldsymbol{c}_{\beta\sigma} \; ; \quad \boldsymbol{b}_{\sigma\sigma} = \boldsymbol{b}^0_{II\sigma} + \underline{\underline{B}}_{II\sigma} \boldsymbol{c}_{\beta\sigma} \tag{A.114}$$

$\boldsymbol{b}^0_{II\beta}$ and $\boldsymbol{b}^0_{II\sigma}$ satisfy the following problem

$$\begin{cases} (\rho c_p)_\beta \boldsymbol{v}_\beta \cdot \partial_{\boldsymbol{x}} \boldsymbol{b}^0_{II\beta} = k_\beta \partial^2_{\boldsymbol{x}} \boldsymbol{b}^0_{II\beta} \, , & in \;\; V_\beta \\ B.C.1 \quad \boldsymbol{n}_{\beta\sigma} \cdot k_\beta \partial_{\boldsymbol{x}} \boldsymbol{b}^0_{II\beta} = \boldsymbol{n}_{\beta\sigma} \cdot k_\sigma \partial_{\boldsymbol{x}} \boldsymbol{b}^0_{II\beta} + \boldsymbol{n}_{\beta\sigma} k_\sigma \, , & at \;\; S_{\beta\sigma} \\ B.C.2 \quad \boldsymbol{b}^0_{II\beta} = \boldsymbol{b}^0_{II\sigma} \, , & at \;\; S_{\beta\sigma} \\ 0 = k_\sigma \partial^2_{\boldsymbol{x}} \boldsymbol{b}^0_{II\sigma} \, , & in \;\; V_\sigma \\ \boldsymbol{b}^0_{II\beta}(\boldsymbol{r} + l_i) = \boldsymbol{b}^0_{II\beta}(\boldsymbol{r}) \, , \quad \boldsymbol{b}^0_{II\sigma}(\boldsymbol{r} + l_i) = \boldsymbol{b}^0_{II\sigma}(\boldsymbol{r}) \, , & i = 1,2,3 \\ \langle \boldsymbol{b}^0_{II\beta} \rangle + \langle \boldsymbol{b}^0_{II\sigma} \rangle = 0 \end{cases}$$

$\underline{\underline{B}}_{II\beta}$ and $\underline{\underline{B}}_{II\sigma}$ satisfy the following problem

$$\begin{cases} (\rho c_p)_\beta \boldsymbol{v}_\beta \cdot \partial_{\boldsymbol{x}} \underline{\underline{B}}_{II\beta} = k_\beta \partial^2_{\boldsymbol{x}} \underline{\underline{B}}_{II\beta} + \epsilon_\beta^{-1} \, , & in \;\; V_\beta \\ B.C.1 \quad \boldsymbol{n}_{\beta\sigma} \cdot k_\beta \partial_{\boldsymbol{x}} \underline{\underline{B}}_{II\beta} = \boldsymbol{n}_{\beta\sigma} \cdot k_\sigma \partial_{\boldsymbol{x}} \underline{\underline{B}}_{II\sigma} \, , & at \;\; S_{\beta\sigma} \\ B.C.2 \quad \underline{\underline{B}}_{II\beta} = \underline{\underline{B}}_{II\sigma} \, , & at \;\; S_{\beta\sigma} \\ 0 = k_\sigma \partial^2_{\boldsymbol{x}} \underline{\underline{B}}_{II\sigma} - \epsilon_\sigma^{-1} \, , & in \;\; V_\sigma \\ \underline{\underline{B}}_{II\beta}(\boldsymbol{r} + l_i) = \underline{\underline{B}}_{II\beta}(\boldsymbol{r}) \, , \quad \underline{\underline{B}}_{II\sigma}(\boldsymbol{r} + l_i) = \underline{\underline{B}}_{II\sigma}(\boldsymbol{r}) \, , & i = 1,2,3 \\ \langle \underline{\underline{B}}_{II\beta} \rangle + \langle \underline{\underline{B}}_{II\sigma} \rangle = 0 \end{cases} \tag{A.115}$$

and

$$\boldsymbol{c}_{\beta\sigma} = -\frac{\langle \boldsymbol{b}^0_{II\beta} \rangle^\beta}{\langle \underline{\underline{B}}_{II\beta} \rangle^\beta} \tag{A.116}$$

For the third problem, the following variables are introduced

$$s_\beta = a_v h s^0_\beta \; ; \quad s_\sigma = -1 + a_v h s^0_\sigma \tag{A.117}$$

$s_\beta$ and $s_\sigma$ are associated with the following problem

$$\begin{cases} (\rho c_p)_\beta \boldsymbol{v}_\beta \cdot \partial_{\boldsymbol{x}} s^0_\beta = k_\beta \partial^2_{\boldsymbol{x}} s^0_\beta \,, & in \;\; V_\beta \\ B.C.1 \quad \boldsymbol{n}_{\beta\sigma} \cdot k_\beta \partial_{\boldsymbol{x}} s^0_\beta = \boldsymbol{n}_{\beta\sigma} \cdot k_\sigma \partial_{\boldsymbol{x}} s^0_\beta \,, & at \;\; S_{\beta\sigma} \\ B.C.2 \quad s^0_\beta = s^0_\sigma \,, & at \;\; S_{\beta\sigma} \\ 0 = k_\sigma \partial^2_{\boldsymbol{x}} s^0_\beta + \epsilon^{-1}_\sigma \,, & in \;\; V_\sigma \\ s^0_\beta(\boldsymbol{r} + l_i) = s^0_\beta(\boldsymbol{r}) \,,\; s^0_\sigma(\boldsymbol{r} + l_i) = s^0_\sigma(\boldsymbol{r}) \,, & i = 1,2,3 \\ \langle s^0_\beta \rangle^\beta = 0 \end{cases} \tag{A.118}$$

where the volumetric exchange coefficient is given by

$$h_v = a_v h = \frac{1}{\langle s^0_\sigma \rangle^\beta} \tag{A.119}$$

## A.4 Remarks: Magnitude Analysis for the Derivation of the Momentum Averaged Equation

The assumption of scale separation has been used several times in the derivation of the averaged equations to simplify certain terms. More details on this are given in this section.

The main concept to consider is that it is possible to associate the length scale of the averaged quantities, $\epsilon_\beta$, $\langle p_\beta \rangle^\beta$, and $\langle \boldsymbol{v}_\beta \rangle^\beta$, to the macroscopic length scale $L$ (see Fig. A.2); while the non-averaged and the deviation quantities, $\tilde{p}_\beta$ and $\tilde{\boldsymbol{v}}_\beta$ have to be associated to the phase scale $l_\beta$ (or $l_\sigma$) (see Fig. A.2). In this way, a magnitude analysis can be performed. The analysis is here performed in a qualitative way. A more detailed analysis can be found in the literature [15, 194].
The magnitude analysis is introduced four times in the derivation of the averaged momentum equation. Each case is now explained.

1) Each time an averaged quantity is moved out from the averaging operator. This operation is performed several times during the development. A generic case is the following

$$\frac{1}{V} \int_{S_{\beta\sigma}} \langle p_\beta \rangle^\beta \boldsymbol{n}_{\beta\sigma} dS = \langle p_\beta \rangle^\beta \frac{1}{V} \int_{S_{\beta\sigma}} \boldsymbol{n}_{\beta\sigma} dS$$

The integral term considers the average pressure field at each point of the interface area between the two phases. In other words, a REV is centered on each point on the interface to measure the average pressure field. The REV is characterized by a lenght scale $L$, so the averaged pressure scales down with $L$. The interface area is characterized by a scale length $l$. Thus, conceptually, several points at a scale length $l$ are considered to measure a field that scales down with $L$. The averaged pressure is therefore uniform, provided the assumption of scale separation holds.

2) Eq. (A.34) reads

$$-\partial_{\boldsymbol{x}}\langle p_\beta\rangle^\beta + \rho_\beta \boldsymbol{g} + \mu_\beta\Big[\partial^2_{\boldsymbol{x}}\langle \boldsymbol{v}_\beta\rangle^\beta + \frac{1}{\epsilon_\beta}\langle \boldsymbol{v}_\beta\rangle^\beta \partial^2_{\boldsymbol{x}}\epsilon_\beta - \frac{1}{\epsilon_\beta}\partial_{\boldsymbol{x}}\epsilon_\beta \cdot \partial_{\boldsymbol{x}}\langle \boldsymbol{v}_\beta\rangle^\beta\Big] - \frac{1}{V_\beta}\int_{S_{\beta\sigma}} \tilde{p}_\beta \boldsymbol{n}_{\beta\sigma} dS +$$

$$+\frac{\mu_\beta}{V_\beta}\int_{S_{\beta\sigma}} \partial_{\boldsymbol{x}}\tilde{\boldsymbol{v}}_\beta \cdot \boldsymbol{n}_{\beta\sigma} dS = 0$$

Four viscous terms characterize this equation. From a magnitude analysis, it can be showed that three of them are negligible in relation to the fourth. The terms enclosed in the square brackets scale down by the same quantity

$$\mu_\beta \partial^2_{\boldsymbol{x}}\langle \boldsymbol{v}_\beta\rangle^\beta = \boldsymbol{O}\Big(\mu_\beta \langle \boldsymbol{v}_\beta\rangle^\beta / L^2\Big)$$

$$\frac{1}{\epsilon_\beta}\mu_\beta \langle \boldsymbol{v}_\beta\rangle^\beta \partial^2_{\boldsymbol{x}}\epsilon_\beta = \boldsymbol{O}\Big(\mu_\beta \langle \boldsymbol{v}_\beta\rangle^\beta / L^2\Big)$$

$$\frac{1}{\epsilon_\beta}\mu_\beta \partial_{\boldsymbol{x}}\epsilon_\beta \cdot \partial_{\boldsymbol{x}}\langle \boldsymbol{v}_\beta\rangle^\beta = \boldsymbol{O}\Big(\mu_\beta \langle \boldsymbol{v}_\beta\rangle^\beta / L^2\Big)$$

The fourth viscous term scale down by a different quantity

$$\frac{\mu_\beta}{V_\beta}\int_{S_{\beta\sigma}} \partial_{\boldsymbol{x}}\tilde{\boldsymbol{v}}_\beta \cdot \boldsymbol{n}_{\beta\sigma} dS = \boldsymbol{O}\Big(\frac{S_{\beta\sigma}}{V_\beta}\mu_\beta \langle \tilde{\boldsymbol{v}}_\beta\rangle^\beta / l_\beta\Big) = \boldsymbol{O}\Big(\mu_\beta \langle \tilde{\boldsymbol{v}}_\beta\rangle^\beta / (l_\beta * l_r)\Big)$$

Based on the assumption of scale separation, Eq. (A.1), the ratio of the two scaling quantities leads to

$$\frac{\Big(\mu_\beta \langle \boldsymbol{v}_\beta\rangle^\beta / L^2\Big)}{\Big(\mu_\beta \langle \tilde{\boldsymbol{v}}_\beta\rangle^\beta / (l_\beta * l_r)\Big)} \approx \frac{\Big(l_\beta * l_r\Big)}{\Big(L^2\Big)} \approx 0$$

As a consequence of this, the three viscous terms in the square brackets in Eq. (A.34) are neglected

3) The second equation of Eq. (A.36) reads

$$\partial_{\boldsymbol{x}} \cdot \tilde{\boldsymbol{v}}_\beta = -\partial_{\boldsymbol{x}} \cdot \langle \boldsymbol{v}_\beta\rangle^\beta$$

The magnitude analysis of the two terms leads to

$$\partial_{\boldsymbol{x}} \cdot \tilde{\boldsymbol{v}}_\beta = \boldsymbol{O}\Big(\langle \tilde{\boldsymbol{v}}_\beta\rangle^\beta / l_\beta\Big)$$

$$\partial_{\boldsymbol{x}} \cdot \langle \boldsymbol{v}_\beta\rangle^\beta = \boldsymbol{O}\Big(\langle \boldsymbol{v}_\beta\rangle^\beta / L\Big)$$

Under the assumption of scale separation, the source term becomes negligible in the continuity equation for $\tilde{\boldsymbol{v}}_\beta$.

4) The boundary value problem of the arbitrary functions $\boldsymbol{\psi}$ and $\xi$, Eq. (A.53), reads

$$\begin{cases} \partial_{\boldsymbol{x}} \cdot \boldsymbol{\psi} = -\underline{\underline{B}}^T \cdot \partial_{\boldsymbol{x}} \langle \boldsymbol{v}_\beta \rangle^\beta \\ \partial^2_{\boldsymbol{x}} \boldsymbol{\psi} - \partial_{\boldsymbol{x}} \xi = \frac{1}{V_\beta} \int_{V_\beta} \left[ \partial^2_{\boldsymbol{x}} \boldsymbol{\psi} - \partial_{\boldsymbol{x}} \xi \right] + \partial_{\boldsymbol{x}} \langle \boldsymbol{v}_\beta \rangle^\beta \cdot \boldsymbol{b} - 2(\partial_{\boldsymbol{x}} \langle \boldsymbol{v}_\beta \rangle^\beta)^T \left[ \partial_{\boldsymbol{x}} \underline{\underline{B}}^T - \langle \partial_{\boldsymbol{x}} \underline{\underline{B}}^T \rangle^\beta \right] - \underline{\underline{B}} \cdot \partial^2_{\boldsymbol{x}} \langle \boldsymbol{v}_\beta \rangle^\beta \\ BC1 \;\; \boldsymbol{\psi} = 0 \qquad\qquad at \; S_{\beta\sigma} \\ BC2 \;\; \boldsymbol{\psi} = 0 \qquad\qquad at \; \partial V_\beta \\ \langle \xi \rangle^\beta = \langle \boldsymbol{\psi} \rangle^\beta = 0 \end{cases} \tag{A.120}$$

Their magnitude can be estimated as follows

$$\boldsymbol{O}\Big(\frac{\boldsymbol{\psi}}{l_\beta}\Big) = \boldsymbol{O}\Big(\frac{\underline{\underline{B}} \cdot \langle \boldsymbol{v}_\beta \rangle^\beta}{L}\Big) \quad \Rightarrow \quad \boldsymbol{O}\Big(\boldsymbol{\psi}\Big) = \boldsymbol{O}\Big(\underline{\underline{B}} \cdot \langle \boldsymbol{v}_\beta \rangle^\beta \frac{l_\beta}{L}\Big)$$

$$\boldsymbol{O}\Big(\frac{\boldsymbol{\psi}}{l_\beta^2}, \frac{\xi}{l_\beta}\Big) = \boldsymbol{O}\Big(\frac{\underline{\underline{B}} \cdot \langle \boldsymbol{v}_\beta \rangle^\beta}{l_\beta L}, \frac{\boldsymbol{b} \cdot \langle \boldsymbol{v}_\beta \rangle^\beta}{L}, \frac{\underline{\underline{B}} \cdot \langle \boldsymbol{v}_\beta \rangle^\beta}{L^2}\Big) \quad \Rightarrow$$

$$\Rightarrow \quad \boldsymbol{O}\Big(\boldsymbol{\psi}\Big) = \boldsymbol{O}\Big(\underline{\underline{B}} \cdot \langle \boldsymbol{v}_\beta \rangle^\beta \frac{l_\beta}{L}, \boldsymbol{b} \cdot \langle \boldsymbol{v}_\beta \rangle^\beta \frac{l_\beta^2}{L}, \underline{\underline{B}} \cdot \langle \boldsymbol{v}_\beta \rangle^\beta \frac{l_\beta^2}{L^2}\Big) \; ;$$

$$\Rightarrow \quad \boldsymbol{O}\Big(\xi\Big) = \boldsymbol{O}\Big(\underline{\underline{B}} \cdot \langle \boldsymbol{v}_\beta \rangle^\beta \frac{1}{L}, \boldsymbol{b} \cdot \langle \boldsymbol{v}_\beta \rangle^\beta \frac{l_\beta}{L}, \underline{\underline{B}} \cdot \langle \boldsymbol{v}_\beta \rangle^\beta \frac{l_\beta}{L^2}\Big)$$

These arbitrary functions are introduced to generalize the mapping of the deviation fields $\tilde{\boldsymbol{v}}_\beta$ and $\tilde{p}_\beta$ (Eq. (A.42) and Eq. (A.43)), defined as

$$\tilde{\boldsymbol{v}}_\beta = \underline{\underline{B}} \cdot \langle \boldsymbol{v}_\beta \rangle^\beta + \boldsymbol{\psi}$$

$$\tilde{p}_\beta = \mu_\beta \boldsymbol{b} \cdot \langle \boldsymbol{v}_\beta \rangle^\beta + \mu_\beta \xi$$

A magnitude analysis of these equations results in

$$\tilde{\boldsymbol{v}}_\beta = \boldsymbol{O}\Big(\frac{\underline{\underline{B}} \cdot \langle \boldsymbol{v}_\beta \rangle^\beta}{l_\beta}\Big) + \boldsymbol{O}\Big(\boldsymbol{\psi}\Big)$$

$$\tilde{p}_\beta = \boldsymbol{O}\Big(\frac{\mu_\beta \boldsymbol{b} \cdot \langle \boldsymbol{v}_\beta \rangle^\beta}{l_\beta}\Big) + \boldsymbol{O}\Big(\mu_\beta \xi\Big)$$

For the velocity deviation, the first term scales down as $1/l_\beta$ and the second one scales down as $l_\beta/L$, at its best. For the pressure deviation, the first term scales down as $1/l_\beta$ and the second term scales down as $1/L$, at its best. The contribution of the arbitrary functions to the deviation terms can be neglected, provided the scale separation assumption holds.

Hermes SCANDELLI

# Multiscale modeling of reactive porous materials interacting with high-temperature flows in support of the biomass, space, and fire communities

**Résumé:** De nombreuses technologies en développement reposent sur des matériaux poreux : échangeurs de chaleur pour les concentrateurs solaires, processus de production de biocarburants, stockage d'énergie de nouvelle génération comme les piles à combustible et les supercondensateurs, boucliers thermiques des véhicules spatiaux, etc. Les ingénieurs chimistes et les chercheurs à l'avant-garde de leur propre domaine et à la pointe de l'innovation du 21e siècle bénéficieraient grandement de développements fondamentaux en matière de transfert de chaleur et de masse pour renforcer les modèles phénoménologiques spécifiques aux applications. L'objectif de ce projet de thèse est de contribuer au développement d'un cadre théorique et numérique générique pour évaluer et modéliser les échanges de masse, de quantité de mouvement, et de chaleur entre une structure solide élastique et réactive interagissant avec un environnement à haute température. Les principales applications ciblées sont la conversion thermique de la biomasse en biocarburant, la prédiction du comportement du feu dans un environnement fermé, et la conception de boucliers thermiques pour les véhicules d'entrée. L'étude se compose de deux parties interdépendantes reposant sur une approche multi-échelle: (1) des simulations numériques sont effectuées à l'échelle macroscopique pour aborder les applications ciblées où la description du matériau est couplée à l'environnement externe; (2) des simulations numériques directes sont effectuées à l'échelle microscopique sur des images numérisées afin de définir des stratégies numériques pour l'évaluation des propriétés effectives.
Les contributions théorique et les fonctionnalités numériques développées au cours de la thèse ont été intégrées dans le logiciel Porous material Analysis Toolbox based on OpenFoam (PATO) distribué sous licence open source NASA.

**Mots clés:** Matériaux poreux, Simulation CFD, Propriétés macroscopiques, Conversion de biomasse, Bouclier thermique, Sécurité incendie.

**Abstract:** Numerous technologies in development rely on porous materials: heat exchangers for solar concentrators, biofuel production processes, new generation energy storage as fuel cells and supercapacitors, space vehicle heat shields, etc. Chemical engineers and researchers at the forefront of their own fields and leading 21st century innovation would greatly benefit from fundamental developments in heat and mass transfer to reinforce application-specific phenomenological models. The objective of this PhD project is to contribute to the development of a generic theoretical and numerical framework to assess and model mass, momentum, and heat exchanges between an elastic and reactive solid structure interacting with a high temperature environment. The primary applications targeted are the thermal conversion of biomass into biofuel, the prediction of fire behavior in a closed environment, and the design of heat shield for atmospheric entry vehicles. The study consists of two interrelated parts relying on a multi-scale approach: (1) numerical simulations are performed on a macroscopic scale to address the targetted applications where the material description is coupled with the external environment; (2) direct numerical simulations are carried out at the microscopic scale on digitalized images to define numerical strategies for the evaluation of the effective properties.
The theoretical and numerical contributions of the PhD have been implemented in the Porous material Analysis Toolbox based on OpenFoam (PATO) released open source by NASA.

**Keywords:** Porous media, CFD simulation, Macroscopic properties, Biomass conversion, Heat shield, Fire safety.